Thèse de Doctorat

Marie CATHELAIN

Mémoire présenté en vue de l'obtention du
grade de Docteur de l'Ecole Centrale de Nantes
sous le label de L'Université Nantes Angers Le Mans

École doctorale : Sciences pour l'Ingénieur, Géosciences, Architecture

Discipline : Mécanique des Milieux Fluides
Unité de recherche : *Laboratoire de Recherche en Hydrodynamique, Energétique et Environnement Atmosphérique*

Soutenue le 4 janvier 2017

Développement d'un modèle de simulation déterministe pour l'étude du couplage entre un écoulement atmosphérique et un état de mer.

Development of a deterministic numerical model for the study of the coupling between an atmospheric flow and a sea state.

JURY

Président **:**	
Rapporteurs :	**Sandrine AUBRUN**, Maître de Conférences, Université d'Orléans **Jean-Luc REDELSPERGER**, Directeur de Recherche au CNRS, Ifremer
Examinateurs :	**Fabrice ARDHUIN,** Directeur de Recherche au CNRS, Ifremer **Isabelle CALMET**, Maître de Conférences, Ecole Centrale Nantes
Invité(s) :	**Christine DE JOUETTE**, Directrice technique, Adwen France
Directeur de Thèse :	**Pierre FERRANT**, Professeur des Universités, Ecole Centrale Nantes
Co-encadrant de Thèse :	**Yves PERIGNON**, Ingénieur de recherche, Ecole Centrale Nantes

Acknowledgements

These are the acknowledgements.

Contents

List of Figures

List of Tables

Nomenclature

Acronyms

ABL	Atmospheric Boundary Layer
ABS	American Bureau of Shipping
API	American Petroleum Institute
BASE	Baltic Sea swell experiment
BV	Bureau Veritas
CBLAST	Coupled Boundary Layers Air-Sea Transfer
CFL	Courant-Friedrichs-Lewy number
COARE	Coupled Ocean Atmosphere Response Experiment
CFD	Computational Fluid Dynamics
CPU	Central Processing Unit
DNS	Direct Numerical Simulation
DNV	Det Norske Veritas
ECN	Ecole Centrale de Nantes
FFT	Fast Fourier Transform
GCL	Geometric Conservation Law
GL	Germanischer Lloyd
GW	gigawatts
HOS	High-Order Spectral
IEC	International Electrotechnical Commission
ISO	International Organization for Standardization
JONSWAP	JOint North Sea WAve Project
LES	Large-Eddy Simulation
HOS	High-Order Spectral
IEC	International Electrotechnical Commission
ISO	International Organization for Standardization
JONSWAP	JOint North Sea WAve Project
LES	Large-Eddy Simulation
MABL	Marine Atmospheric Boundary Layer
MPI	Message Passing Interface
NREL	National Renewable Energy Laboratory
PBL	Planetary Boundary Layer
RANS	Reynolds Averaged Navier-Stokes equations

RECOFF	Recommendations for design of offshore wind turbines
RED	Rough Evaporation Duct experiment
RK	Runge-Kutta
SAR	Synthetic Aperture Radar
SCOPE	San Clemente Ocean Probing Experiment
SGS	Sub-Grid Scale
TKE	Turbulence Kinetic Energy

Mathematical notations

a	wave amplitude
a_{ij}^h, a_{ij}^ϕ	modal amplitudes of the velocity potential and wave elevation
ak	wave steepness
$c(t)$	Bernoulli constant
C_D	drag coefficient
C_g	group velocity of the wave
C_k, C_ε	constants in the parametrisation of SGS model
$\mathcal{C}_p$	specific heat at constant pressure
C_p	phase velocity of the wave at the peak
D	water domain
e	SGS energy
E	dimensionless wave energy density
f (f_p)	(peak) wave frequency
F_p	form drag, or pressure stress
g	gravitational acceleration
G	directionality function of the wave spectrum
h	wave elevation
H_s	significant wave height
I_{ref}	turbulence intensity at 15 m.s^{-1}
$\mathcal{J}$	Jacobian of the mapping transformation
k (k_p)	(peak) wavenumber
k	turbulence kinetic energy
L	Obukhov length
M	HOS order of non-linearities
N_x, N_y	number of grid points in x and y-directions

p^*	fluctuating pressure normalised by the air density
P	pressure
P_{atm}	atmospheric pressure
P_0	reference pressure
$\partial\mathcal{P}/\partial x_i$	large-scale external pressure gradient
q	specific humidity
R	ideal gas constant
Re	Reynolds number
S_h	variance spectral density
S_{ij}	resolved scale strain rate
t	time
T	temperature
T (T_p)	(peak) wave period
u_*	friction velocity
u_+	velocity solution in the air
u_-	velocity solution in the water
u_{junction}	velocity in the viscous boundary layer
u_{orbital}	orbital velocity of the water wave
$u_{\text{potential}}$	potential velocity in the air
$\overline{u'w'}$	vertical turbulent flux of horizontal momentum
(U, V, W)	velocity vector
(U_f, V_f, W_f)	contravariant flux velocity
$\mathbf{U}_{\text{ref}}$	velocity of the relative frame of reference of a monochromatic wave
U_{10}	reference wind speed at 10 m
U_∞	velocity outside the viscous boundary layer
V_{ref}	reference wind speed average over 10 min at hub height
$\overline{w'\theta'}$	vertical turbulent heat flux
W_v	wall shear stress work
(x, y, z)	physical coordinates
y_+	dimensionless distance to the wall
z_0	roughness length
z_{0_s}	roughness for a smooth surface
z_{0_w}	roughness for surface waves
z_i	top of the MABL (base of the temperature inversion layer)
z_t	vertical grid speed of the mesh
Z_L	height of the LES computational domain

α	power law exponent
α_c	Charnock parameter
β	wave growth rate parameter
β_b	buoyancy parameter
γ^r	extra peak enhancement factor in JONSWAP spectrum
Γ_d	dry adiabatic lapse rate
δ	thickness of the viscous air boundary layer
δ_{ij}	Kronecker delta
Δ	filter length scale
Δz_0	height of the first cell of the mesh
ε	viscous dissipation
ϵ_{ijk}	Levi-Civita symbol
θ	wind-wave misalignement angle
Θ	potential temperature
Θ_v	virtual potential temperature
κ	von Karman constant
λ (λ_p)	(peak) wavelength
μ	viscous dissipation coefficient
μ_{Dore}	Dore coefficient
ν_a	kinematic viscosity of the air
ν_t	turbulent viscosity
(ξ, η, ζ)	curvilinear computational coordinates
ρ_a	air density
ρ_{w}	water density
τ_{Reynolds}	Reynolds stress
τ_{tot}	total stress at the sea surface
τ_{turb}	turbulent shear stress
τ_{visc}	viscous stress
τ_{wall}	wall shear stress
τ_{wave}	wave-induced stress
ϕ	velocity potential
ϕ^S	velocity potential at the free surface
Φ	directional wave spectrum
Φ_M	dimensionless wind shear in the surface layer
χ	wave age based on the reference wind speed at 10 m
ψ	wave spectrum
Ψ_M	surface layer stability correction term for momentum
ω (ω_p)	(peak) angular frequency

$\boldsymbol{\Omega}$	angular velocity vector
Δ	Laplacian operator
∇	del operator

Résumé de la thèse

Dans le contexte d'une exploitation croissante de l'énergie du vent offshore et du développement de modèles océano-météorologiques de plus en plus précis, la mise en place de méthodes numériques visant à une description plus fine des propriétés turbulentes de la couche limite atmosphérique marine sera notamment une étape déterminante dans la réduction des coûts et l'optimisation des structures pour des rendements de récupération d'énergie améliorés. La France a pour objectif de porter la puissance de son parc éolien en mer à 6000 MW de puissance éolienne en mer d'ici 2020. L'installation de 500 MW est d'ores et déjà planifiée par des concessions de parcs offshore d'éoliennes posées comptant de 60 à 100 machines. Des solutions technologiques sont également en développement pour l'installation de parcs de machines flottantes afin d'étendre les zones d'implantation potentielles au delà de quelques dizaines de mètres de profondeur d'eau. Du fait de la taille croissante des machines et de leur implantation future dans des sites dont les caractéristiques atmosphériques s'apparenteront de moins en moins à des zones de mers fermées et plus à des domaines océaniques, la description adaptée des conditions atmosphériques de couche limite océanique va représenter un enjeu croissant. En ce sens les normes actuelles héritées de l'éolien terrestre ne prennent pas ou peu en compte les spécificités océaniques, à savoir principalement la forte capacité thermique océanique, et le couplage spécifique entre la surface libre et l'écoulement atmosphérique. Que ce soit pour l'estimation de la ressource et de la production, ou pour le dimensionnement des machines, les implications de telles hypothèses simplificatrices peuvent ne pas être anodines (Kalvig et al., 2014).

Une description plus appropriée de la couche limite atmosphérique nécessite entre autre de dépasser le formalisme statistique à l'œuvre dans la modélisation du couplage et de l'interaction océan-atmosphère tant en météorologie qu'en science du climat (Chen et al. (2013), Fan et al. (2012)). Une meilleure description des processus liés aux échanges de quantité de mouvement passe alors par une description spécifique des évolutions d'écoulements aux échelles de temps et d'espace qui leur sont propres. Les questions non résolues sont en outre nombreuses dans la simple description du couplage vent vague ; on peut notamment mentionner parmi celles-ci l'extension verticale de la couche limite atmosphérique directement impactée par les vagues sous-jacentes, le

rôle de la houle, la validité de théories de similarités type Monin-Obukhov pour la prédiction de flux de surfaces, la corrélation entre vagues et vents pour des états de mers différents, etc. Le simple mécanisme de croissance des vagues sous l'action du vent est sujet à de nombreux débats. Si des mesures in-situ peuvent apporter des éclairages importants, elles n'incluent pas jusque là une description déterministe de la corrélation entre champ de pression et profil de surface libre, du fait des échelles et du caractère instationnaire des écoulements à caractériser.

Une étude préliminaire a été réalisée sur la dissipation visqueuse de la houle par la contrainte de cisaillement atmosphérique induite par la houle dans le cas d'un écoulement d'air initialement au repos. La rétroaction de la couche visqueuse atmosphérique cisaillée, forcée par une houle idéalisée (linéaire, unidirectionnelle et monochromatique) a été simulée à l'aide d'un modèle numérique de type RANS (Alessandrini and Delhommeau, 1999). ICARE est habituellement utilisé pour des applications navales et hydrodynamiques et il a été modifié pour une toute nouvelle application atmosphérique: l'idée était de développer un outil performant et évolutif, capable d'aborder une complexité croissante de la représentation d'une partie de la physique du système océan-atmosphère.

Dans cet effort de meilleure description et représentation de la couche limite atmosphérique en domaine océanique, l'Ecole Centrale de Nantes et ses partenaires du LabexMER (Laboratoire d'Océanographie Physique notamment) ont initié une collaboration avec P. Sullivan du NCAR (Boulder, USA) spécialisé dans la modélisation de la turbulence de couche limite atmosphérique et océanique. Dans le cadre de cette thèse menée au Laboratoire de recherche en Hydrodynamique, Energétique et Environnement Atmosphérique (LHEEA, ECN) sur la simulation couplée atmosphère turbulente – état de mer, un code Large Eddy Simulation (LES) massivement parallèle pour la simulation des écoulements atmosphériques incompressibles sous hypothèse de Boussinesq (Sullivan et al., 2008) a été couplé à un code spectral d'états de mer non-linéaires HOS (High Order Spectral Method, West et al (1987), Bonnefoy et al. (2010)). Le modèle atmosphérique repose sur une simulation des grandes échelles qui définit un nombre d'onde de coupure audelà duquel l'énergie due aux petits mouvements tourbillonnaires est prise en compte par un modèle de sous-maille. Une approximation majeure est faite dans la résolution des équations de Navier-Stokes: on néglige l'influence des variations de température et de la flottabilité en considérant une atmosphère neutre. L'étude bibliographique montre que, à la fois, la stratification atmosphérique et les vagues ont un impact sur la couche limite atmosphérique marine. Cependant, considérer ces effets de façon indépendante constitue un premier pas dans la compréhension de ces phénomènes. Ainsi seul l'effet des vagues sera étudié dans ces travaux. La méthode HOS, développée à l'ECN depuis 2002, constitue une des méthodes les plus efficaces pour simuler l'évolution non-linéaire d'états de mer complexes (Ducrozet et al., 2012). Sur la base d'une méthode potentielle et d'une approche spectrale de résolution des conditions de surface libre, elle est un moyen efficace de propager de manière déterministe et sur plusieurs heures tous types de conditions de vagues sur des surfaces de plusieurs centaines de kilomètres carrés (Ducrozet et al., 2008). Dans le cadre du couplage LES-HOS, elle constitue un outil particulièrement rapide et efficace afin de fournir des conditions aux limites couplées et dont les temps de calcul caractéristiques restent négligeables devant la charge imposée par le code LES. Le couplage implémenté repose sur une communication entre les deux codes basée sur l'échange d'informations telles que l'élévation de surface libre et les vitesses orbitales pour le modèle de vague et la pression atmosphérique à la surface libre pour le modèle LES. Ces échanges ont lieu à chaque itération temporelle, le pas de temps étant imposé par la simulation atmosphérique, et une gestion spécifique de la mise à jour de la solution potentielle de l'état de mer est implémentée lors des sous-itérations du schéma RK3. L'eau ayant une masse volumique beaucoup plus importante que l'air, l'échelle de temps nécessaire à l'état de mer pour évoluer sous le forçage du vent est beaucoup plus grande que les échelles temporelles d'advection et de renouvellement (turnover time scale) des tourbillons turbulents. On considère alors qu'une unique itération temporelle est nécessaire au couplage entre les deux codes.

Différents cas d'application sont mis en place afin d'étudier les interactions vent-vagues. On définit l'âge de vague comme étant le rapport entre la vitesse de phase de la vague et la vitesse de frottement du vent, avec un rapport à l'équilibre autour de $C_p/u_* \approx 15 - 20$. Premièrement, on considère des cas de forçage de la simulation atmosphérique par le modèle de vague (on ne prend pas en compte la rétroaction de la pression sur l'état de mer): un cas de conditions fortes de vent sur une mer du vent (petit âge de vague

$C_p/u_* < 10$), un cas de houle se propageant dans une zone de vent faible ($C_p/u_* = 60$) et un cas de génération d'un jet de vent par la houle ($C_p/u_* = 120$). Ce jet de vent induit par la houle invalide les modèles de vent tels que la loi logarithmique couramment préconisée par les normes internationales. Finalement, une étude préliminaire est réalisée sur le couplage entre les deux codes. En l'absence de modèle de dissipation au sein du modèle HOS, la prise en compte du terme de forçage par la pression empêche la stabilité de la simulation. Un filtrage du signal de pression atmosphérique est introduit afin de dissiper les hautes fréquences. Dans de telles conditions, les simulations couplées durent de 20 à 100 périodes de vague. Des tests plus poussés seront nécessaires car la dissipation introduite ici n'est évidemment pas physique et la paramétrisation de la dissipation de l'énergie constitue une des questions fondamentales dans l'étude du système couplé vent-vague.

Introduction

Within the context of a growing exploitation of the offshore wind energy and the development of metocean models, a refined description of this resource is a key issue. Solar radiation and Earth's rotation are the driving forces of the thermodynamics of the atmosphere. The discontinuities of the thermal properties (i.e. heat absorption/dissipation) of the ground play an important role in local weather. The oceans contribute to regulate the temperature in the lower part of the atmosphere: just the top few metres of the ocean have a heat capacity equivalent to that of the whole atmosphere! Earth's rotation and variations in atmospheric temperature create motion of cold/warm air parcels that generates low/high pressure centres and thus wind systems. The atmosphere is in large part responsible for the oceanic circulation via the generation of waves and currents. However, contributions are not quite that simple. The ocean-atmosphere system is indeed a complex system governed by two-way interactions and the assessment of the offshore wind resource must be considered within the whole coupled ocean-atmosphere system.

Offshore wind energy is a supplement and a growth driver for onshore wind energy. The wind being stronger and steadier offshore rather than onshore represents a competitive advantage. According to the European Wind Energy Association (EWEA), the installed wind power capacity will reach 40 gigawatts (GW) in Europe in 2020, the equivalent of the household consumption in France. In France, the objectives for installed capacity in 2020 are 19 GW for onshore wind energy (with a current installed capacity of 6 GW) and 6 GW for offshore wind energy in accordance with the objectives outlined by the Ministry of Ecology, Sustainable Development and Energy. Although offshore wind technology has significant similarities with onshore wind technology, offshore wind is still considered as an immature industry in France especially since the offshore environment addresses very specific problems. The assessment and the forecasting of wind resource are key points in the different development stages of a wind farm (Kalvig et al., 2014). The resource estimate on a specific site is crucial for assessing its economic potential and it allows to select appropriate technology solutions for this site. Wind turbines and wind farm layout can be designed at best thanks to a more advanced understanding of the wind features at a local or regional scale. During installation and decommissioning phases, forecasting accurate meteorological conditions is necessary to identify the appropriate time windows for the weather-sensitive operations. During the exploitation of the farm, metocean conditions need to be predicted to optimise the operation of the farm, to anticipate maintenance work and to assess the power that will be fed into the grid.

Currently, design standards and methodologies are similar to those applied for the design of onshore wind turbines. Two major factors have been identified in the literature as key drivers in ocean-atmosphere interactions: the atmospheric thermal stability or instability due to the large heat capacity of the ocean (Kristjansson et al., 2011) and the wave-induced effects (especially the dynamic roughness of the oceanic surface). IEC 61400-3 standard, *Wind Turbines Part 3: Design Requirements for Offshore Wind Turbines*, relies on parametric relationships of the wind profile and the surface roughness. Ocean waves are generally thought to act as a drag on the surface wind, which is related to a downward momentum transferred from the atmosphere into the waves. However, field campaigns and numerical modelling have suggested that momentum can also be transferred upward in case of long wavelength waves propagating faster than the surface wind: this upward momentum transfer causes the surface wind to accelerate. The existence of low-level wave-driven wind jets is the evidence that the marine atmospheric boundary layer (MABL) is influenced by the dynamic offshore surface. Moreover, parametric laws tend to overestimate the wind velocity at 30-40 metres above the sea surface (Kalvig et al., 2014). The surface roughness is, on the other hand, generally evaluated through an empirical expression, the Charnock's relation. This expression does not fully take into account the interaction of the sea state with the wind profile and with the turbulence in the atmospheric boundary layer (ABL).

The aim of this PhD thesis is to develop a deterministic numerical model for the coupling between an atmospheric flow and a sea state. The PhD work is part of an overall framework (i.e. ocean-atmosphere interactions) and is based on a multidisciplinary approach that includes hydrodynamics, atmospheric sciences and computing science. As a hydrodynamicist, a significant part of my bibliographical study focused on the mechanisms driving the atmospheric boundary layer to address gaps in my knowledge of this specific thematics. The bibliographical work in Chapter 1 will show that both the atmospheric stratification and the waves have an impact on the marine atmospheric boundary layer. However, considering independently theses effects will constitute a first step in understanding the ocean-atmosphere interactions: the PhD work will then focus on the wave effects. A preliminary study in Chapter 2 investigates the viscous dissipation of the swell by the wave-induced atmospheric shear stress in the case of a initially still airflow (i.e. no mean wind). Gaining insight into the atmospheric dissipation phenomena related to the swell propagation will provide an improvement of the wave prediction models in which dissipation is not taken into account. In order to investigate the laminar-to-turbulence dynamics of the air boundary layer, numerical simulations will be conducted with a modified version of ICARE, a computational code that has been developed for hydrodynamic applications at the Hydrodynamics, Energetics and Atmospheric Environment Laboratory (LHEEA) in Ecole Centrale de Nantes, France. Towards overcoming the current case modelled in ICARE (i.e. 1D idealised monochromatic waves propagating in a domain with no mean windfield modelled with a RANS turbulent approach), a coupling is implemented between an atmospheric Large-Eddy Simulation and a spectral code that solves the non-linear evolution of sea states. The atmospheric code has been graciously provided by Peter Sullivan from the National Center for Atmospheric Research, USA. Numerical details about these two codes and the implemented coupling are specified in Chapter 3. The influence of a sea state on the overlying airflow will be numerically investigated through three cases in Chapter 4: wind forcing over young waves, a swell underlying a light wind and a case of generation of a wave-induce wind. An exploratory study will be conducted on the coupling, meaning that the sea state will evolve under wind pressure forcing. Finally, the pre-conclusion chapter will place into perspective the logarithmic wind profile commonly used to predict the vertical wind profile in the governing standards.

Résumé du chapitre 1

Ce chapitre introduit les concepts généraux des sciences de l'atmosphère dans le cadre du système océan-atmosphère. L'étude des interactions océan-atmosphère est complexe et nécessite une approche multidisciplinaire. Les propriétés thermodynamiques de ces deux milieux sont très différentes, notamment au niveau de leur capacité thermique, et cela introduit un déséquilibre marqué dans la rétroaction d'un fluide au forçage de l'autre: en première approximation, la rétroaction de l'océan au forçage de l'atmosphère est en général étudiée, alors que l'impact des variations horizontales et temporelles de la couche supérieure de l'océan sur l'atmosphère est négligé. Toutefois, il est important de comprendre et de modéliser ce système dans son ensemble, en incluant notamment les modifications de l'état de mer. Afin de mettre en place une description appropriée de la couche limite atmosphérique marine, il est nécessaire de dépasser, entre autres, le formalisme statistique actuellement à l'oeuvre dans la modélisation du couplage océan-atmosphère en météorologie et en science du climat (Chen et al. (2013), Fan et al. (2012)). Une meilleure description des processus relatifs aux transferts de quantité de mouvement repose donc sur une description spécifique des évolutions des écoulements à leurs propres échelles de temps et d'espace. De plus, de nombreuses questions restent non résolues dans le cadre du couplage vent-vague, dont: l'extension verticale de la couche limite atmosphérique qui est directement impactée par les vagues sous-jacentes, l'influence de la houle, la validité des théories de similarités telles que la théorie de Monin-Obukhov pour la prédiction des flux de surface, ainsi que la corrélation entre le vent et les vagues.

Chapter 1

Geophysical processes in the marine atmospheric boundary layers

This chapter introduces some general concepts about atmospheric sciences within the context of the ocean-atmosphere system. The study of the ocean-atmosphere interactions is complex and requires a multidisciplinary approach. The very different thermodynamic properties of the ocean and the atmosphere (especially the heat capacity) introduce a strong asymmetry in the feedback from one fluid to the forcing of the other fluid: in a first approximation, the ocean feedback to the atmospheric forcing is usually studied, and the impact of horizontal and temporal variations of the upper ocean on the atmosphere is neglected. Yet it is the whole coupled system, including the modifications of the sea surface state, that needs to be understood and modelled. A proper description of the MABL needs, among others, to overcome the statistical formalism currently established in the modelling of the ocean-atmosphere coupling and interactions in meteorology as well as in climate science (Chen et al. (2013), Fan et al. (2012)). A better description of the processes related to the momentum transfers thus relies on a specific description of the flows evolutions at their own time and space scales. Moreover, numerous are the unresolved questions within the framework of the wind-wave coupling with for instance: the vertical extension of the ABL which is directly impacted by the underlying waves, the influence of the swell, the validity of similarity theories such as Monin-Obukhov theory in the prediction of surface fluxes, the correlation between wind and waves.

1.1 Atmospheric boundary layer

In fluid dynamics, a boundary layer is the transition zone between a body and a surrounding fluid in which frictional drag associated with the surface of the body is significant. In atmospheric sciences, a similar definition is widely adopted. The ABL is the layer of fluid directly above the earth's surface in which significant fluxes of momentum, heat and/or moisture are carried by turbulent motions whose horizontal and vertical scales are on the order of the boundary layer depth, and whose circulation timescale is a few hours or less (Garratt, 1994). Stull (1988) defines the boundary layer as "that part of troposphere that is directly influenced by the presence of the earth's surface, and responds to surface forcings with a timescale of about an hour or less". The ABL thickness can extend from hundred metres to a few kilometres and its structure evolves with the diurnal cycle as shown in Figure 1.1.

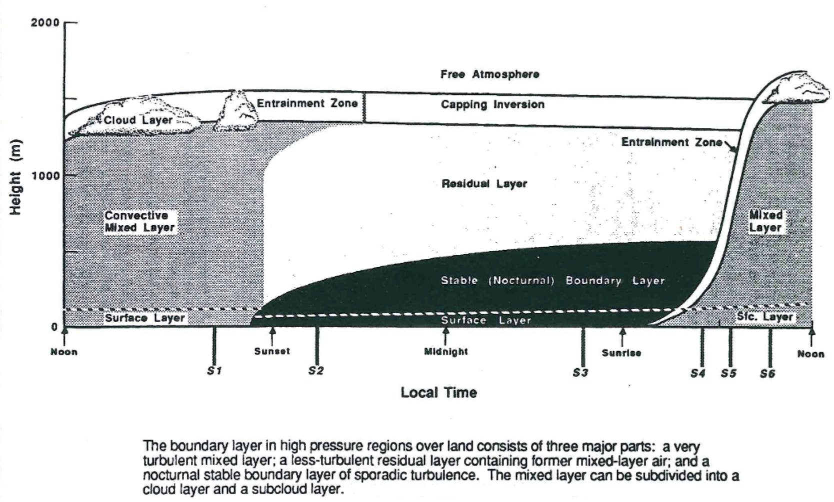

Figure 1.1: The diurnal cycle of the atmosphere structure by Stull (1988).

The motion in the atmosphere is governed by a set of equations, known as the Navier-Stokes equations. These equations reflect the conservation of mass and of momentum and can be written as (Stull, 1988):

$$
\begin{aligned}
&\frac{\partial \rho_a}{\partial t} + \frac{\partial \rho_a U_j}{\partial x_j} = 0 \\
&\frac{\partial U_i}{\partial t} + U_j \frac{\partial U_i}{\partial x_j} = -\delta_{i3} g - 2\epsilon_{ijk}\Omega_j U_k - \frac{1}{\rho_a}\frac{\partial P}{\partial x_i} + \frac{1}{\rho_a}\frac{\partial \tau_{ij}}{\partial x_j}
\end{aligned}
\tag{1.1}
$$

I II III IV V VI

with ρ_a the air density, $(i, j, k) \in (1, 2, 3)^3$ the indices representing the three components of the corresponding vector, the velocity vector $\mathbf{U}$ for example, and:

- Term I describes storage of momentum.
- Term II represents advection.
- Term III allows gravity to act vertically (buoyancy) with g the gravitational acceleration and δ_{ij} the Kronecker delta.
- Term IV represents the Coriolis effects (influence of earth's rotation) with ϵ_{ijk} the Levi-Civita symbol and Ω the angular velocity vector.
- Term V describes the pressure-gradient forces with P the pressure.
- Term VI describes the influence of viscous stress τ_{ij}.

At the top of the ABL, the wind speed is the result of the balance between pressure and Coriolis forces. This wind is called geostrophic wind, it is orthogonal to the pressure gradient and not affected by the surface. This region is sometimes called the "free atmosphere". Coming closer to the surface, the equilibrium between pressure gradient and Coriolis forces is broken by a drag force due to the presence of roughness at the earth's surface. The wind flow will therefore be weaker and its direction will turn toward low-pressure zones. This phenomena is called Eckman spiral. At the surface, the mean wind speed reduces to zero over land at a height z_0, called the roughness length, which is related to the roughness characteristics of the ground (Stull, 1988): it is not a physical length, but can be considered as a length scale of the roughness of the surface. Over water, the wind matches the speed of the surface waves and the surface currents. Hence, over land or over water, a wind shear develops over the depth of the ABL and dynamically produces turbulence. This mechanical turbulence produces a flux of momentum from the atmosphere to the surface of the earth. Depending on the vertical temperature gradient, a heat flux can occur within the ABL. This phenomenon is explained in Subsection 1.1.1. Close to the surface, the fluxes of heat and momentum are nearly constant with height: this feature thus defines the surface layer (Stull, 1988). In this layer, frictional effects are dominant compared to pressure-gradient and Coriolis forces.

The ABL flow is highly influenced by the surface forcings, such as frictional drag, evaporation and transpiration, heat transfer, pollutant emission, and ground induced flow modification. Mean wind is responsible for the horizontal transport of quantities such as moisture, heat, momentum, and pollutants, whereas transport in the vertical is dominated by turbulence. A common approach for studying turbulence relies on splitting variables, such as wind speed and temperature, into two parts. It is the Reynolds decomposition: a mean part representing the effects of the mean variables, and a perturbation part describing the turbulence effect that is superimposed on the mean variables. The overbar denotes ensemble (time) average and the prime notation indicates perturbation from the average:

$$U = \bar{U} + u' \tag{1.2}$$

Usually turbulence consists of eddies of many different sizes superimposed onto the mean flow. Turbulence is several orders of magnitude more effective at transporting quantities than is molecular diffusivity (Stull, 1988). Turbulence allows the boundary layer to respond to changing surface forcings. Driving forces such as buoyancy and stability are presented, and parametrisation of the surface layer is introduced with the Monin-Obukhov similarity theory.

1.1.1 Buoyancy and stability

Buoyancy is one of the driving forces for turbulence in the ABL (Stull, 1988). As mentioned previously, buoyancy is determined by the vertical gradient of temperature. The temperature profile of the atmosphere is a result of the interaction between radiation and convection. The incoming radiation from the sun is absorbed and reflected by clouds and the earth's surface. Moreover, according to the first law of thermodynamics, a rising (sinking) parcel will cool (warm) if there is no additional energy source such as condensation of water vapour: this follows a dry adiabatic process. Convection comes to equilibrium when a parcel of air at a given altitude has the same density as the surrounding air at the same elevation.

In the ABL, under a hydrostatic equilibrium state, a parcel of air affected by a dry adiabatic process has the following pressure variation:

$$\frac{dP}{dz} = -\rho_a g, \tag{1.3}$$

and the following temperature variation:

$$\frac{dT}{dz} = -\frac{g}{\mathcal{C}_p} = -\Gamma_d, \tag{1.4}$$

$\mathcal{C}_p$ being the specific heat at constant pressure for dry air and Γ_d the dry adiabatic lapse rate. Γ_d is about 9.8°C per kilometre. An atmospheric layer with such a temperature variation is called neutral for dry air. In that case, the potential temperature defined as

$$\Theta = T\left(\frac{P_0}{P}\right)^{R/\mathcal{C}_p}, \tag{1.5}$$

with R the ideal gas constant and P_0 a reference pressure, is constant and can be approximated by

$$\Theta \approx T + \left(\frac{g}{\mathcal{C}_p}\right) z. \tag{1.6}$$

The potential temperature is an adjusted temperature that discounts the pressure (compressibility) effect. In other words, it represents the temperature that an air parcel would have if it were brought adiabatically to a reference pressure P_0. The atmosphere usually does not have a temperature distribution that fits the dry adiabatic lapse rate. Indeed, air normally contains water vapour, and condensation or evaporation occurs in the air. Latent heat is released by condensation and consumed by evaporation: this alters the adiabatic lapse rate. The modified lapse rate is called the moist or saturated adiabatic lapse rate and is typically about 6.5°C per kilometre. Adiabatic lapse rates are commonly different to the surrounding vertical change in temperature at a given time in a given location, known as the environmental lapse rate. It is influenced by patterns of heating, cooling and mixing, and the past history of an air mass (Stull, 1988). A new variable is introduced in order to deal with the fact that potential temperature is derived based on the assumption of dry air. Indeed, the presence of water influences the density: the density of water vapour is lower than the density of dry air. To get this in one variable, the virtual potential temperature is introduced. It is defined as

$$\Theta_v = \Theta \left(1 + 0.608q\right), \tag{1.7}$$

where $q = \rho_v / \left(\rho_d + \rho_v\right)$ is the specific humidity, ρ_v the density of water vapour and ρ_d the density of dry air. In other words, two air samples with the same virtual temperature have the same density, regardless of their actual temperature or relative humidity (Stull, 1988).

The stability of air masses depends on the relative values of the environmental lapse rate and the adiabatic lapse rate of the air parcel as shown in Figure 1.2. Static stability is often mentioned as a measure of the capability for buoyant convection. "Static" means "having no motion": this type of stability does not depend on the wind. Air is statically unstable when a warm air (less dense) underlies a cold air (denser). The flow responds to this instability by supporting convective circulations such as thermals that allow buoyant air to rise to the top of the unstable layer, stabilising by that means the fluid. In the real boundary layer, there are so many triggers (hills, buildings, trees...) to get thermals started that convection is usually insured (Stull, 1988). In terms of lapse rate, air is unstable when the environmental lapse rate is greater than the adiabatic lapse rate. Uplifted air cools relatively slowly, and will thus be warmer and less dense than its new surroundings along the adiabatic lapse rate. It will therefore continue to rise. On the other hand, air is stable when the environmental lapse rate is smaller than the adiabatic lapse rate. A parcel of air being uplifted will cool to lower temperatures than its new surroundings. The air parcel will be denser than the surrounding air and will tend to fall back to its original level.

Stull (1988) points out that the measurement of the local lapse rate alone is not sufficient to determine the static stability. Either knowledge of the whole virtual potential temperature profile, $\bar{\Theta}_v$, is needed or the measurement of the turbulent buoyancy flux, $\overline{w'\theta'_v}$, must be made. Stability can then be evaluated through the potential temperature variation and its vertical turbulent flux (Wyngaard, 2010). With the Reynolds decomposition $\Theta = \bar{\Theta} + \theta'$, averaging the temperature balance equation in a turbulent boundary

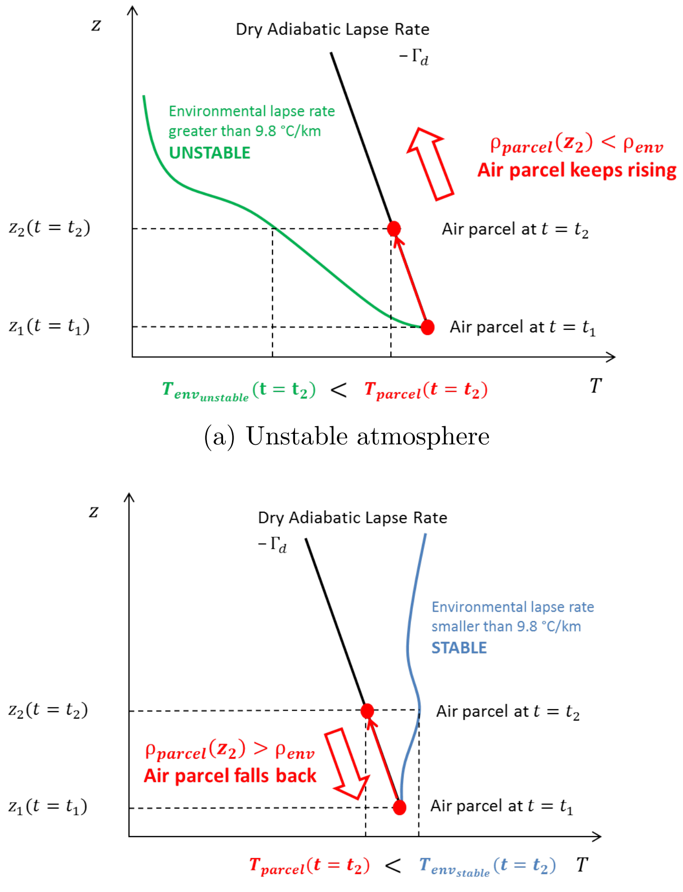

(a) Unstable atmosphere

(b) Stable atmosphere

Figure 1.2: Temperature variation over height (Calmet, 2015). *(a) Unstable atmosphere with environmental lapse rate greater than dry adiabatic lapse rate. An air parcel being displaced from height z_1 to height z_2 will keep rising as its temperature is greater than the ambient temperature. (b) Stable atmosphere with environmental lapse rate smaller than dry adiabatic lapse rate. An air parcel being displaced from height z_1 to height z_2 will fall to its original position as its temperature is smaller than the ambient temperature.*

layer leads to:

$$\frac{\partial \bar{\Theta}}{\partial t} + \bar{U}_i \frac{\partial \bar{\Theta}}{\partial x_i} + \frac{\partial \overline{u_i'\theta'}}{\partial x_i} = \frac{\mu_\theta}{\rho_a C_p} \frac{\partial^2 \bar{\Theta}}{\partial x_i \partial x_i}. \tag{1.8}$$

The molecular diffusion is negligible except in the diffusive sublayer near the surface. If we consider horizontal homogeneity, meaning that statistics do not vary in the horizontal, then $\bar{U}_i = \left[\bar{U}(z,t), 0, 0\right]$ and $\bar{\Theta} = \bar{\Theta}(z,t)$. The previous equation therefore yields:

$$\frac{\partial \bar{\Theta}}{\partial t} = -\frac{\partial \overline{u_i'\theta'}}{\partial x_i} = -\frac{\partial \overline{w'\theta'}}{\partial z}. \tag{1.9}$$

The time rate of cooling or warming of the air is due to the divergence of the vertical turbulent heat flux $\overline{w'\theta'}$. In a neutral boundary layer, the dominant turbulent kinetic energy (TKE) generation mechanism is mechanical or dynamic, associated with wind shear and surface stress, and the buoyant production of TKE based on the vertical heat flux is really small. In overcast conditions with strong winds but little temperature difference between the air and the surface, the boundary layer is often close to neutral stability. During fair weather conditions over land, the boundary layer close to the ground is rarely neutral. If $\overline{w'\theta'}$ at earth's surface is positive, then the whole boundary layer is said to be unstable or convective. It corresponds to a typical daytime with clear-weather. The buoyant production of TKE adds up to the dynamic production of TKE. Vertical turbulent temperature flux $\overline{w'\theta'}$ and mean temperature $\bar{\Theta}$ profiles during typical daytime are sketched in Figure 1.3. If $\overline{w'\theta'}$ is negative at the surface, then the boundary layer is said to be stable. It characterises the boundary layer during calm nights or over ice. The stable thermal stratification counteracts the motions induced by mechanical turbulence and limits the turbulence diffusion processes. This evolution of convective and stable layers during the course of a day is also illustrated in Figure 1.1.

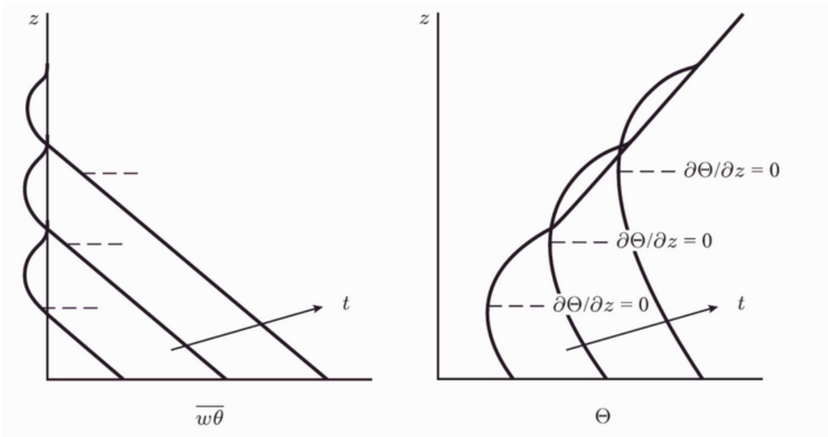

Figure 1.3: Profiles of vertical turbulent temperature flux $\overline{w'\theta'}$ (*left*) and mean temperature $\bar{\Theta}$ (*right*) in a growing convective boundary layer (Wyngaard, 2010).

1.1.2 Similarity theories: the Monin-Obukhov similarity

The knowledge obtained from similarity theory is applied in many fields of natural and engineering science, among others in fluid mechanics. In this field, similarity considerations are often used for providing insight into the flow phenomena and for the generalisation of results. Indeed, for a number of situations, the lack of comprehensive knowledge of the governing physics prevents the scientists from deriving laws based on first principles. In atmospheric sciences, boundary layer observations frequently show consistent and repeatable characteristics, suggesting that empirical relationships can be established for the variables of interest. Dimensional analysis and similarity theory provide a way to organise and group the relevant variables, and eventually provide guidelines on how to design experiments to gain the most information (Stull, 1988). One of the most common classes of similarity scaling is the Monin-Obukhov similarity. It is usually applied to the surface layer. The surface layer is the part of the boundary layer where the fluxes vary by less than 10% of their magnitude with height: this layer is said to be a constant-flux layer. The wind speed slows down and become zero close to the ground due to the frictional drag, while the pressure gradient forces cause the wind to increase with height. In statically neutral conditions, the mean wind speed can be expressed as

$$\bar{U}(z) = \frac{u_*}{\kappa} \ln\left(\frac{z}{z_0}\right). \tag{1.10}$$

This equation comes from the Buckingham Pi Theory by which two dimensionless variables have been established: $\bar{U}/u_*$ and z/z_0 with u_*, the friction velocity and z_0, the roughness length. κ is the von Karman constant. The friction velocity, u_*, is defined as

$$\begin{aligned} u_*^2 &\equiv \left[\overline{u'w'_s}^2 + \overline{v'w'_s}^2\right]^{1/2} \\ &= \left|\tau_{\text{Reynolds}}\right| / \overline{\rho_a}, \end{aligned} \tag{1.11}$$

with τ_{Reynolds} being the Reynolds stress. This stress accounts for turbulent fluctuations in the fluid momentum. The roughness length, z_0, is defined as the height where the wind speed becomes zero. It is related to the roughness characteristics of the underlying surface, specific to this surface and does not change with the wind speed, stability, or stress. Typical values are indicated in Figure 1.4.

An alternative derivation of the log wind profile is possible using the mixing length theory (Prandtl, 1961). This theory states that the momentum flux in the surface layer can be written as

$$\overline{u'w'} = -\kappa^2 z^2 \left|\frac{\partial \bar{U}}{\partial z}\right| \frac{\partial \bar{U}}{\partial z}. \tag{1.12}$$

Since the surface layer is assumed to be a constant layer, the momentum flux is approximately constant with height, $\overline{u'w'}(z) = \overline{u'w'}(z = z_0) = u_*^2$. Substituting this into the mixing length expression and taking the square root of the whole equation gives:

$$\frac{\partial \bar{U}}{\partial z} = \frac{u_*}{\kappa z}. \tag{1.13}$$

Integrating over height from $z = z_0$ where $\bar{U} = 0$ to any height z gives the equation (1.10).

From the expression of the log wind profile, a dimensionless wind shear, Φ_M, can be defined. This wind shear is equal to unity in the neutral surface layer:

$$\Phi_M = \left(\frac{\kappa z}{u_*}\right) \frac{\partial \bar{U}}{\partial z} = 1. \tag{1.14}$$

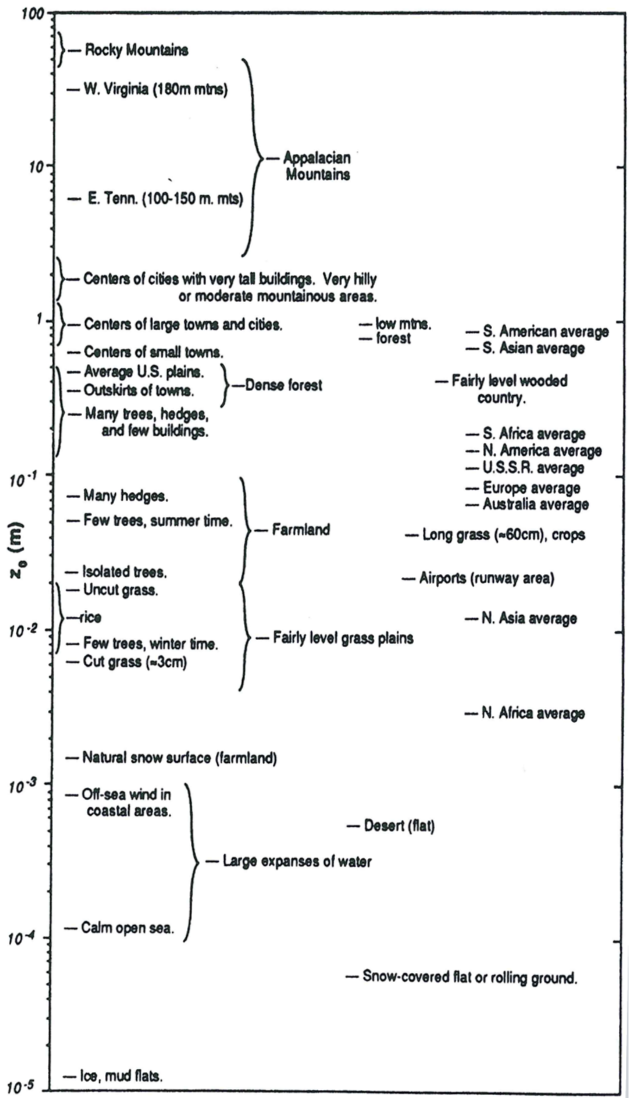

Figure 1.4: Roughness lengths for typical terrain types according to Stull (1988).

The mean wind speed expression (1.10) can be extended to include non-neutral surface layers. The Monin-Obukhov similarity theory generalises the mixing length theory in non-neutral conditions by using so-called "universal functions" of dimensionless height to characterise vertical distributions of mean flow and temperature. The Obukhov length, L, is a characteristic length scale of surface layer turbulence derived by Obukhov (1971). It is used for non-dimensional scaling of the height. This length parameter characterises the relative contributions to TKE from buoyant production and shear production. It is defined as

$$L = -\frac{u_*^3}{\kappa \frac{g}{\theta_v} \overline{w'\theta_v'}}. \tag{1.15}$$

The Obukhov length acts as a criterion for the static stability of the surface layer. When $L < 0$, the surface layer is statically unstable, and when $L > 0$, it is statically stable. The absolute magnitude of L indicates the deviation from statically neutral state, with smaller $|L|$ values corresponding to buoyant processes dominating the production of turbulent kinetic energy compared with shear production. By definition, under neutral conditions, $L \to \infty$. A stability function, which corresponds to the dimensionless wind shear (cf Equation (1.14)), has been empirically determined by Businger et al. (1971) and Dyer (1974) who independently estimated:

$$\begin{aligned} &= 1 + \left(\frac{4.7z}{L}\right) && \text{for } \frac{z}{L} > 0 \quad \text{(stable)} \\ \Phi_M &= 1 && \text{for } \frac{z}{L} = 0 \quad \text{(neutral)} \\ &= \left[1 - \left(\frac{15z}{L}\right)\right]^{-1/4} && \text{for } \frac{z}{L} < 0 \quad \text{(unstable).} \end{aligned} \tag{1.16}$$

The Businger-Dyer relationships can be integrated over height to yield the wind speed profiles:

$$\bar{U} = \frac{u_*}{\kappa}\left[\ln\left(\frac{z}{z_0}\right) + \psi_M\left(\frac{z}{L}\right)\right] \tag{1.17}$$

where the function ψ_M is given for stable conditions $(z/L > 0)$ by:

$$\psi_M\left(\frac{z}{L}\right) = \frac{4.7z}{L} \tag{1.18}$$

and for unstable conditions $(z/L < 0)$ by:

$$\psi_M\left(\frac{z}{L}\right) = -2\ln\left[\frac{1+x}{2}\right] - \ln\left[\frac{1+x^2}{2}\right] + 2\tan^{-1}(x) - \frac{\pi}{2} \tag{1.19}$$

where $x = [1 - (15z/L)]^{1/4}$. This last equation was presented by Paulson (1970), although alternative expressions that are more easily solved numerically were presented by Nickerson and Smiley (1975) and Benoit (1977). The so-called Businger-Dyer stability correction functions $\Phi_M\left(\frac{z}{L}\right)$ have proved

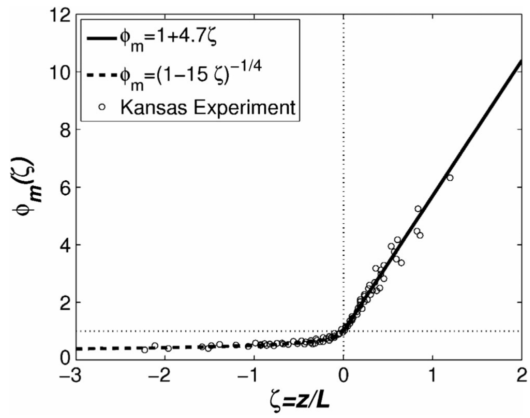

Figure 1.5: Determination of $\Phi_M(z/L)$ from the Kansas experiment (Katul et al., 2011).

successful in fitting numerous experiments including the results of the classic Kansas experiments shown in Figure 1.5 (Katul et al., 2011).

The design of offshore wind turbines relies heavily on standard procedures that have been defined for onshore wind turbines. As a result, simplifications regarding the marine boundary layer are made: neutral stratification and a flat, smooth and static sea surface are commonly used as assumptions in wind energy calculations.

1.2 Boundary layer simplifications in the international guidelines

A standard is an established norm or requirement in regard to technical systems. It is usually a document developed from best practices and research, which establishes engineering or technical criteria, design methods, processes and practices. This document is used by consensus of the stakeholders.

During the early 1990s, the International Electrotechnical Commission (IEC) introduced international standards for the wind energy industry. Until 2009, offshore wind turbines were designed according to national design rules and international standards for the onshore wind industry. The principal standard for wind turbine structural design requirements is the IEC 61400-1, *Wind turbines - Part1: Design Requirements*. This standard addresses numerous key project aspects, including safety, site condition assessment, design evaluation of turbines, blades and support structures, manufacturing, transportation, installation, commissioning and operation: all these aspects are directly affected by the external environmental conditions. One aim of the standard is therefore to provide a comprehensive definition of the turbulent wind environment from an engineering point of view.

In 2009, the IEC and its Technical Committee 88, which focuses on wind energy generation systems, established an offshore wind turbine standard, *Wind turbines - Part 3: Design Requirements for Offshore Wind Turbines*, IEC 61400-3, in connection with IEC 61400-1. It was intended to address requirements for offshore wind turbines that were not previously covered. IEC 61400-3 assumes that the turbine will be certified to a set of design classes specified in IEC 61400-1 with regard to the engineering integrity of the rotor-nacelle assembly. It is a usual approach within the guidelines to define a reference and average wind speed for certain classes together with parameters for different turbulence regimes. Nevertheless, IEC 61400-3 states that the structural integrity should not be compromised by the offshore site-specific external conditions. IEC 61400-1 describes three wind turbine classes and "a further wind turbine class, class S, is defined for use when special wind or other external conditions are required by the designer and/or the customer. In addition to wind speed and turbulence intensity, which define the wind turbine classes, several other important parameters, notably marine conditions, are required to specify completely the external conditions to be used in the design of an offshore wind turbine" (IEC 61400-1). These additional parameters are extreme wind speed averaged over three seconds and the extreme wave height, normal marine conditions and extreme marine conditions, and normal, severe and extreme sea state. Table I.1 specifies the basic parameters defining the wind turbine classes. The parameter values apply at the hub height, V_{ref} being the reference wind speed average over 10 min, I_{ref} the expected value of the turbulence intensity at 15 m.s^{-1} and A, B and C designate the category for higher, medium and lower turbulence characteristics respectively.

Wind turbine class		I	II	III	S
V_{ref}	(m/s)	50	42.5	37.5	Values specified by the designer
A	I_{ref}	0.16			
B	I_{ref}	0.14			
C	I_{ref}	0.12			

Table 1.1: Basic parameters for wind turbine classes in IEC 61400-1.

Previous structural standards and guidelines for offshore oil and gas structures, including those developed by the American Petroleum Institute (API), the International Organization for Standardization (ISO), Det Norske Veritas (DNV) and Germanischer Lloyd (GL), were used as the basis for the new IEC 61400-3 requirements. Indeed, standards and guidelines are international, national or industry-specific. IEC and ISO are international standard organisations, and API an industry-specific standard: although it is not specific to the wind industry, it covers the design and construction of offshore structures. The most relevant design standards for the offshore wind industry are:

- IEC 61400-1, *Wind turbines - Part 1: Design requirements*
- IEC 61400-3-1, *Wind turbines - Part 3-1: Design requirements for offshore wind turbine*s (forecast publication date: 2016-11)

– IEC 61400-3-2, *Wind turbines - Part 3-2: Design requirements for floating offshore wind turbines* (forecast publication date: 2017-01)

– IEC 61400-22, *Wind turbines — Part 22: Conformity testing and certification*

– ISO 19900, *General requirements for offshore structures*

– ISO 19902, *Fixed steel offshore structures*

– ISO 19902, *Fixed steel offshore structures*

– ISO 19903, *Fixed concrete offshore structures*

– ISO 19904-1, *Floating offshore structures - monohulls, semisubmersibles and spars*

– ISO 19904-2, *Floating offshore structures - tension leg platforms*

– API Series 2, *Offshore structures*

A guideline is a recommended practice document established by a classification society. It consists of recommended (non-mandatory) controls that help to support standards or serve as a reference when no applicable standard is in place. The most relevant guidelines in offshore wind industry are:

– American Bureau of Shipping (ABS): ABS 176, *Guide for building and classing offshore wind turbine installations* (2010)

– ABS 195, *Guide for building and classing floating offshore wind turbine installations* (2015)

– Bureau Veritas (BV): BV-NI 572 DT R01 E, *Classification and certification of floating offshore wind turbines* (2015)

– Det Norske Veritas: DNV-OS-J101, *Design of offshore wind turbine structures*

– Germanischer Lloyd: GL2, *Guideline for the certification of offshore wind turbines* (2012)

In Europe, a European-funded project, *Recommendations for design of Offshore Wind Turbines* (RECOFF), included comparisons of these various standards and assessed their suitability for wind turbine design. The RECOFF study concluded that for the vast majority of support structure requirements, standards such as those of API and ISO could be used. Offshore wind turbines are, however, subject to wind and wave stochastic loadings that are nearly equal in importance with respect to the dynamic excitation of the wind turbine (Musial and Ram, 2010). In the United States, the National Renewable Energy Laboratory (NREL) pointed out in a technical report that there are inherent differences in atmospheric, oceanic, and lake conditions between Europe and the United States (Sirnivas et al., 2014). For example, hurricanes and extra-tropical cyclones correspond to severe storms whose characteristics and return periods can affect wind development and drive different key design and operational criteria. Such events, as well as freshwater ice, are not commonly treated in Europe. Therefore international offshore wind standards and guidelines do not provide specific guidance for offshore wind project design in the United States.

As stated in the IEC 61400-3, the designer has to specify values for the parameters defining the wind turbine class S, such as reference wind speed average over 10 min at the hub height and the turbulence intensity. If a site-specific metocean database is available, data can be used in order to perform the analysis for the load cases specified in the standards. This site-specific database can be established from offshore measurements, or by hindcasting (numerical model integration of a historical period when no observations have been assimilated) (Obhrai et al., 2012). Concerning the duration of the measurements, the IEC standards suggest that it should be long enough to obtain reliable parameters but they do not specify a time period. The GL guidelines state that a time period of six months is required, but it should account for the seasonal variations if they have an impact on the wind conditions. The DNV standard recommends that the 10-minute mean value of wind speed should be obtained from several years of data. When no database is available or when wind speed data are available for heights other than the reference height, the standards recommend different wind profile models to evaluate the vertical structure of the marine boundary layer. The wind speed at 10 metres is often used as the reference height in all the standards. The assumed wind profile is eventually used to define the average vertical wind shear across the rotor swept area.

1.2.1 Simplified models for wind profile estimations

IEC 61400-3 refers to IEC 61400-1 for the estimation of the wind speed using the power law:

$$U(z) = U_{\text{hub}} \left(\frac{z}{z_{\text{hub}}} \right)^{\alpha} \tag{1.20}$$

The mean profile, $U(z)$, denotes the average wind speed as a function of height, z, over the still water level, U_{hub} is the wind speed at the hub height, z_{hub}, and α is the power law exponent. For normal wind conditions at off-shore locations, α is set to 0.14. The GL guideline also refers to Equation (1.20) for wind speed estimations. This model assumes the neutral stability based on a constant roughness length of 0.002 m over the sea. The power law in Equation (1.20) has no real theoretical basis: it is just known to fit the logarithmic wind profile. Compared to the logarithmic law, the power law can easily be integrated over a height: this profile is widely used for engineering purposes. Despite the empirical variation of α to take into consideration a specific roughness, this law does not really account for any roughness effects due to the waves and thermals effects due to the atmospheric stability.

In strong wind conditions, the most accurate theoretical expression is the logarithmic law. It was originally derived from the turbulent boundary layer on a flat plate by Prandtl (1932) and it has been found to be valid in an unmodified form in strong wind conditions in the ABL near the surface. Under neutral conditions and in the surface layer, the Monin-Obukhov similarity theory leads to the logarithmic wind profile as stated in Subsection 1.1.2:

$$U(z) = \frac{u_*}{\kappa} \ln \left(\frac{z}{z_0} \right). \tag{1.21}$$

DNV guidelines note that the logarithmic wind profile should be modified in order to include the stability corrections Ψ_M as stated in Subsection 1.1.2 (Obhrai et al., 2012).

1.2.2 Parametrisation of the sea surface roughness

In the logarithmic wind profile, the roughness length z_0 accounts for the roughness characteristics of the terrain. It represents the height above the surface where the mean velocity is zero when extrapolated towards the surface using the Monin-Obukhov theory (Stull, 1988). Above the sea surface, the roughness length is expressed through Charnock's relation:

$$z_0 = \frac{\alpha_c u_*^2}{g}, \tag{1.22}$$

where the empirical constant α_c is the Charnock parameter (Charnock, 1955). Charnock (1955) argued that the short gravity waves are mainly responsible for the momentum transfer from air to ocean. Measurements resulted in an estimate of the Charnock parameter: $\alpha_c = 0.0112$. According to Stull (1988), $\alpha_c = 0.016$. This relationship expresses the dependence of the roughness on the surface stress through the friction velocity. Stronger wind produces higher waves due to stronger wind stresses, which results in a greater roughness length (Obhrai et al., 2012). In IEC 61400-3, $\alpha_c = 0.011$ is recommended for open sea and $\alpha_c = 0.034$ for near coastal waters (IEC 61400-3).

To sum up, the governing standards and international guidelines for the offshore wind industry rely on standards and methodologies that have first been addressed to the onshore wind industry. The design of a turbine is based on specified design load cases and on turbine classes that were initially defined over land in terms of average and extreme wind speed, and turbulence. Log law, or power law, is commonly used to predict the vertical wind profile and waves are regarded as a roughness length included in the log law. This sea surface roughness is estimated through the Charnock's relation based on a constant that may have different values. But there is no consideration about how the waves interact with the wind and how it can affect the wind profile. Moreover, the logarithmic wind profile is only valid in the surface layer under neutral atmospheric stratification. Field experiments and numerical simulations reveal that atmospheric stability and wave effects, including the dynamic sea surface roughness, are two major factors affecting flow over sea.

1.3 Influence of the waves on the atmospheric layer

Transfers of momentum, heat and mass between the earth's ocean and atmosphere play an important role in weather and climate. For example, energy from the wind blowing over the surface of the ocean produces waves and currents. The problem of wind-wave interaction is a challenging research topic. Predicting the evolution of sea states under wind forcing in the ocean through atmosphere-ocean coupled systems requires a fundamental understanding of the mechanisms of wind-wave interaction. Moreover, ocean waves are generally thought to act as a drag on the surface wind with a downward momentum transfer from the atmosphere into the waves. Recent observations during conditions where long wavelength waves propagate faster than the wind have reported that momentum can also be transferred from the waves into the atmosphere. This upward momentum transfer leads to an acceleration of the wind near the free surface and the occurrence of low-level wind jets. Currently, the ocean-atmosphere models only allow the momentum transfer to be directed from the atmosphere to the ocean. Due to the complexity of the physics, our current understanding of the problem remains quite incomplete.

1.3.1 Wave generation

The wind-generated waves are surface waves that result from the wind blowing over an area of fluid surface. In the ocean, theses waves are directly generated and affected by local winds and their generation is influenced by some factors as the wind speed (wind strength), its direction, the fetch (uninterrupted distance over which the wind blows without significant change in direction), the wind duration and the water depth. The longer the fetch and the faster the wind speed, the more wind energy is imparted to the water surface and the larger the resulting sea state will be (see Figure 1.6). Assuming linear theory (i.e. small steepness, dispersive waves), the wave field can be seen as a superposition of random waves of various periods, lengths and amplitudes. The free surface elevation can be described by its variance: the discrete variance (or energy) spectral density (i.e. $S_h(f) = \frac{1/2a(f)^2}{\Delta f}$ (m^2.s) with $a(f)$ the amplitude of the wave at frequency f) describes how energy is distributed over frequencies. Several parametric formulations for synthetic wave spectra have been proposed by researchers and they depend on a number of parameters such as wind speed, fetch, etc. One example of wave energy spectrum is the parametric Pierson-Moskowitz spectrum presented in Figure 1.6: it gives a quite realistic estimate of a fully developed sea (i.e. the waves have eventually reached a point of equilibrium with the wind) even if its existence remains theoretical. The distribution of the wave spectral density (i.e. the variance of the wave elevation) is plotted over frequency and the five curves represent the wave spectra for different wind speeds measured at 19.5 m above the sea surface in the North Atlantic (Moskowitz, 1964). The peak wave frequency, f_p, is defined as the wave frequency with the highest energy, as well as the peak wave period, $T_p = 1/f_p$, and, if linear waves in deep water are considered, the peak wavenumber, k_p, is defined through the dispersion relation:

$$\omega_p^2 = gk_p \tag{1.23}$$

with $\omega_p = 2\pi/T_p$ the peak angular frequency. Peak wavelength is then de-

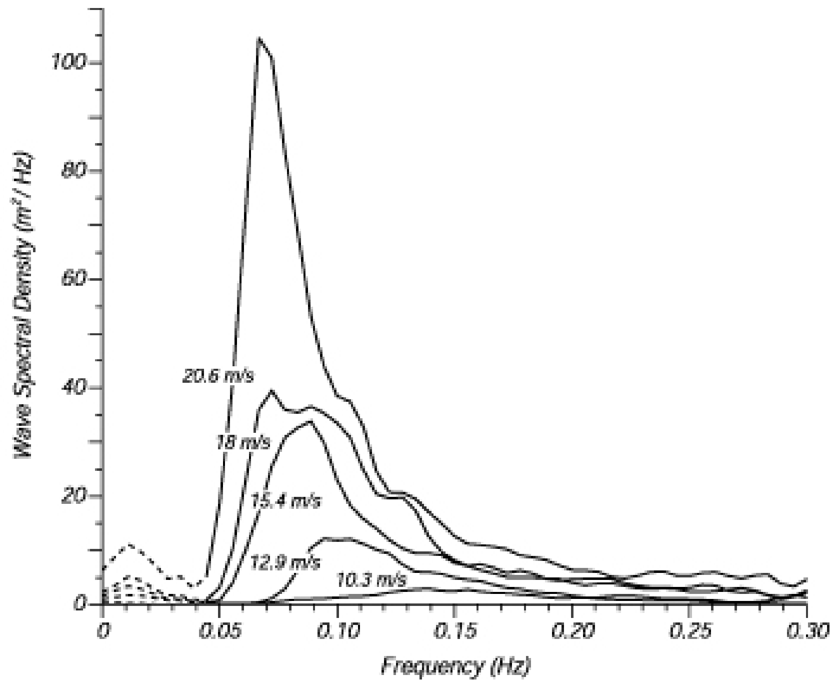

Figure 1.6: Wave spectra of a fully developed sea for different wind speeds according to Moskowitz (1964).

fined as $\lambda_p = 2\pi/k_p$.

The first attempt to introduce the concept of wave generation was in 1874 by Lord Kelvin. He described wave growth through a mechanism called the Kelvin-Helmholtz instability. This mechanism has been given up as an explanation for surface waves, but is accepted today as one of the main causes of clear-air turbulence (Sekioka, 1970).

In 1925, Jeffreys (1925) assumed that air flowing over ocean surface was sheltered by the waves on their lee side. He introduced the first plausible mechanism in order to explain the phase shift of the atmospheric pressure necessary to the energy transfer from wind to waves. An instability can appear at the interface between two fluids experiencing a difference in velocities. Small capillary waves are thus generated by a sudden increase in the wind velocity due to this instability. The wave growth is then due to flow separation. This separation occurs downstream of the crest with a reattachment upstream the following wave: this is called the separated sheltering mechanism. The growth rates related to this mechanism were nevertheless not in accordance with laboratory measurements on water waves: the pressure difference was much too small to account for the observed growth rates.

In the 1950s, Miles (1957) and Phillips (1957) provided the basis of our theoretical understanding of wind-wave generation. Their independent and complementary works focused on the dynamic wind-wave interaction depending on the pressure field at the surface. Phillips considered the resonant forcing of surface waves by turbulent pressure fluctuations in the wind field: the turbulent atmospheric pressure fluctuations are unrelated to waves and are advected over the sea surface at some velocity related to the wind speed. Resonance mechanism accounts for the excitation and the initial growth of waves on an undisturbed water surface. This mechanism leads to a linear growth rate of capillary waves, but it is weak and can only account for the early stages of wave generation. According to Miles (1957), wave growth is due to the resonant interaction between the wave-induced pressure fluctuations and the free surface waves. Miles' approach assumes that the atmospheric flow over a wave is inviscid and turbulence only serves to maintain the shear flow (quasi-laminar approach): the turbulence does not participate explicitly in the momentum transfer to sea surface. The deformations of the critical layer, where the wind speed is equal to the phase velocity of the wave, induce a variation in the pressure field which is out of phase with the surface wave. Work occurs and waves grow exponentially. Indeed the wave-induced pressure fluctuations lead to the generation of a turbulent layer of variable thickness at the critical height. A physical explanation of the energy transfer in terms of the vortex forces acting on the fluid particles near the critical layer has been given by Lighthill (1962). Experimental studies showed that this critical layer mechanism predicts energy transfers that are similar (sometimes lower) to energy transfers observed in wave tanks. But Miles' theory is mainly criticised because non-linear effects, such as wave-mean flow interactions, are not considered and it ignores the effects of turbulence on the wave-induced motion: it neglects a possible change of wind profile while the ocean waves are evolving (Janssen, 2004).

More recently, there have been several attempts to overcome these shortcomings by means of numerical modelling of the turbulent boundary layer flow over a moving water surface, e.g. Townsend (1972), Gent and Taylor (1976), Chalikov (1978), and no resonance mechanism was found to occur. It has been shown that wave-induced turbulence is responsible for the pressure phase shift leading to an energy transfer from wind to waves. It should be noted that growth rates predicted by these different theories strongly depend on the closure of turbulence models. Jacobs (1987) and van Duin and Janssen (1992) used a mixing length model to calculate the modulations of the Reynolds stress caused by the wave-induced motions. They pointed out that this approach is not justified for low-frequency waves which interact with large eddies whose eddy-turnover time may become larger than the period of the waves: indeed, mixing-length modelling assumes that the momentum transport caused by turbulence is the fastest process in the fluid. Gent and Taylor (1976) and Chalikov (1978) used a one-equation e-model (with e the turbulent kinetic energy). Owing to their simplicity, the turbulence schemes based on the eddy viscosity concept, such as the mixing length model, have been widely used in the past. Mastenbroek et al. (1996) showed that the local equilibrium assumption underpinning the eddy viscosity models does not hold in the airflow over waves. In the bulk of the flow, the advection of the turbulence disturbs the local balance of production and dissipation that is essential for the eddy viscosity models to be valid. Belcher and Hunt (1993) also pointed out that mixing-length modelling is inadequate for slow waves. Far away from the surface, turbulence is slow with respect to the wave, so that again, large eddies do not have sufficient time to transport momentum. They identified an inner layer and an outer layer in the airflow over waves: the turbulence in the layer close to the wave surface called the inner region is considered to be in equilibrium with local velocity gradients and a simple mixing length model can be used. Above this layer, in the outer region, the advection of turbulence cannot be neglected any more. The distortion effects of turbulent eddies are described by the rapid distortion theory (Batchelor and Proudman, 1954). Belcher and Hunt (1993) applied this theory to shear flows over waves propagating slowly compared to the wind. They identified a non-separated sheltering effect associated with the thickening of the boundary layer on the leeward side of the wave. This thickening of the boundary layer leads to an asymmetric pressure and then to the growth of the wave. Cohen and Belcher (1999) extended this theory to flows over fast waves. These studies complete the theory of Miles and give a theoretical explanation to the growth of slow waves and to the damping of fast waves under wind forcing.

A sea state actually results from the combined effects of these locally wind-generated waves and swells. Swell waves are the remains of wind waves that have moved away from the area where they were generated. They are long waves that contain a lot of energy and are able to travel long distances (thousands of kilometres). Their energy should be conserved or weakly dissipated, but little information is available. Ardhuin et al. (2009) observed that steep swells can lose a significant fraction of their energy, up to 65%, over 2800 km. The state of development, or maturity, of the waves is usually defined by the wave age:

$$\chi = \frac{C_p}{U_{10}} \tag{1.24}$$

where C_p is the phase speed at the spectral peak, $C_p = \omega_p/k_p$. U_{10} corresponds to the wind speed measured at 10 m above the mean free surface. This parameter enables to split the wind sea which is actively generated by the wind (young, or developing, waves) from the swell on which the wind does nearly have no effect (old, or mature, waves). Donelan et al. (1992) have shown that wave growth stops, or at least becomes slower, for $\chi > 1.2$ which confirms the analysis from Pierson and Moskowitz (1964). Wave age can also be defined by wind velocities at other reference height, for example wind speed at 8m height U_8 (Smedman et al., 1999) (Högström et al., 1999), at a height equal to the wavelength U_λ (Nilsson et al., 2012), or by the geostrophic wind U_g (Sullivan et al., 2008). Sullivan et al. (2008) also define the wave age as $C_p/(U_{10}\cos\theta)$ in case of waves propagating in a different direction than the wind, with θ the wind-wave misalignment angle. Another definition of the wave age also relies on the friction velocity, C_p/u_*: Cohen and Belcher (1999) predict fast waves, or swell, when C_p/u_* is larger than 20, and Sullivan and McWilliams (2010) note that wind and waves reach equilibrium at $C_p/u_* \approx 30$. Typical values of wave age range from $C_p/u_* = 5$ to several hundred (Emeis, 2013): in 2005, in the North Sea near the major offshore wind farms, the FINO1 research platform has measured an average wave age of 55.3.

The wave effects are commonly thought to have a limited impact on the ABL and they are usually considered in terms of aerodynamic roughness height. This roughness height is typically treated as a constant or as a function of the wind stress through the Charnock's relation, regardless its dependency on the sea state. Field observations and numerical modelling have shown that the influence of the waves on the ABL might be stronger.

1.3.2 Wave boundary layer

The wave boundary layer is the lowest part of the constant-flux atmospheric layer where the wave-induced fluctuations are very substantial. According to Chalikov and Rainchik (2011), the height of the wave boundary layer is in the range of the significant height, i.e. a few metres, and the Monin-Obhukhov theory is verified above. However, the wave boundary layer may extend higher for light winds (Grachev and Fairall, 2001).

1.3.2.1 Wave-induced momentum flux

Within the wave boundary layer, the motion is influenced by the waves and, since the wave boundary layer is responsible for wave drag, its structure changes the dynamic of the entire constant-flux layer. Previous studies of the boundary layer over the ocean were based mostly on the theory of a boundary layer above an infinite flat and rigid surface. The influence of the waves was interpreted in terms of roughness. One significant difference between the airflow above the sea compared to the air flow over land is the dynamic motion of the sea surface. Indeed, the profiles of wind velocity and stress over sea waves deviate from similar situations over land due to the fact that the surface waves modulate the velocity and the pressure perturbations coming from the surface. Over surface waves, the total wind velocity can then be separated into three parts: the mean, turbulent, and wave-induced components of the flow (Phillips, 1966). This wave-induced motion gives an additional Reynolds stress to the turbulent and the viscous stresses:

$$\tau_{\text{tot}}(z) = \tau_{\text{turb}}(z) + \tau_{\text{wave}}(z) + \tau_{\text{visc}}(z) \tag{1.25}$$

where τ_{tot} is the total stress at the sea surface, τ_{turb} the turbulent shear stress, τ_{wave} the wave-induced stress, and τ_{visc} the viscous stress (Hanley and Belcher, 2008). The viscous stress is usually assumed to be negligible in the wave boundary layer as it is only important in the $O\,(1)$ mm viscous sublayer above the surface. The influence of the waves disappear with height and, well above the surface, $\tau_{\text{wave}} = 0$. The wave boundary layer is hence that part of the atmosphere where the wave-induced stress is a significant part of the total stress. The stress at the surface is the tangential force per unit area exerted by the wind on the surface. It results in a transfer of horizontal momentum between the air and sea via vertical momentum flux (Grachev and Fairall, 2001):

$$\begin{aligned}
\tau_{\text{tot}} &= -\rho_a \left(\langle uw \rangle \, \mathbf{i} + \langle vw \rangle \, \mathbf{j}\right) \\
\tau_{\text{turb}} &= -\rho_a \left(\langle u'w' \rangle \, \mathbf{i} + \langle v'w' \rangle \, \mathbf{j}\right) \\
\tau_{\text{wave}} &= -\rho_a \left(\langle \tilde{u}\tilde{w} \rangle \, \mathbf{i} + \langle \tilde{v}\tilde{w} \rangle \, \mathbf{j}\right),
\end{aligned} \tag{1.26}$$

where angle brackets are time and/or spatial averaging operators, the primes and the tildes denote turbulent and wave-induced fluctuations (respectively) of the (u, v, w) velocity components, and $\mathbf{i}$ and $\mathbf{j}$ are the longitudinal and lateral unit vectors. The stress is thus a horizontal vector whereas its magnitude is the vertical momentum flux and can be seen as directed upward or downward. The wave-induced momentum flux, τ_{wave}, is described by the pressure-wave slope correlation at the surface (Hare et al., 1997): it is also called the form drag. Janssen (1989) showed that τ_{wave} may be described at the free surface h by the wave spectrum $S(\omega)$:

$$\tau_{\text{wave}}\,(h) = \rho_w \int_0^{+\infty} \beta g C_p^{-1} S(\omega) \mathrm{d}\omega, \tag{1.27}$$

where ρ_w is the water density, $\omega = 2\pi f$ the angular frequency, and β the dimensionless wind-wave interaction parameter (or wave growth parameter). The wave-induced momentum flux shows strong dependence on wave age. Sullivan et al. (2000) demonstrated that the wave effects depend on the wave age and the wave slope in a region confined in $kz < 1$. For young waves (small wave age), the wave-induced momentum flux is directed downward, i.e. $\tau_{\text{wave}} > 0$, and the surface roughness z_0 tends to increase: the vertical velocity profile shows a longer logarithmic region. While increasing the wave age, the surface roughness z_0 tends to decrease and τ_{wave} decreases, reaches zero, and reverses sign: $\tau_{\text{wave}} < 0$. Since the turbulence momentum flux τ_{turb} is always positive, the increase of the wave age tends to enhance the negative portion of the total momentum flux, and, at some point, leads to a sign reversal of τ_{tot}. This sign reversal indicates a transfer momentum from the ocean to the atmosphere.

1.3.2.2 Parametrisation of the wind stress

From a modeller's point of view, it is natural to try to identify relevant parameters in order to describe physical phenomena with a relation between these parameters. The air-sea coupling in the atmospheric numerical models is usually parametrised in terms of the drag coefficient C_D for a given wind stress (Edson, 2008):

$$\tau = \rho_a u_*^2 = \rho_a C_D U^2, \tag{1.28}$$

where U is the wind speed measured at a certain height. The atmospheric numerical models and their parametrisation are often based on numerous field experiments in various oceanic areas, such as the COARE (Coupled Ocean Atmosphere Response experiment) model (Fairall et al., 2003). As reviewed by Komen et al. (1998), correct parametrisation of the drag over ocean has a significant impact on a synoptic scale and on the climate. But in the literature, different experiments give contradictory results. The choice of the reference wind speed has obviously an impact on the quantitative and qualitative properties of C_D. Many publications refer to a wind speed measured at the height of 10 m. Nevertheless, the dynamic understanding of this height in the marine boundary layer is rather vague and despite enormous efforts, the scatter of experimental data is very significant and a consistent parametrisation for $C_{D_{10}}$ has not been established. For a fixed wind speed at 10 m height, Donelan (1982) found that the drag coefficient may vary by a factor 2 depending on the sea state. Hwang (2004) introduced the $\lambda/2$ reference height in order to define the drag coefficient $C_{D_{\lambda/2}}$: he considered that the dynamic influence of the waves decay exponentially with height, and that the decay rate is inversely proportional to the wavelength λ. Babanin et al. (2012) argue that the wind speed does not determine such coupling, but the momentum and energy fluxes. Some measurements have confirmed the dependence of the drag coefficient on wave age (Donelan, 1982) (Smith et al., 1992), but many studies demonstrate that the drag coefficient can be significantly influenced by swell waves (Drennan et al. (1999), Kudryavtsev and Makin (2004), Högström et al. (2009)).

1.3.2.3 Influence of the sea surface roughness

The surface roughness of the sea is low compared to land surfaces. However, the roughness is not constant with wind speed unlike the roughness over land surfaces, but depends on the underlying wave field, which in turn depends on wind speed, upstream fetch, water depth, etc. Different models have been proposed to describe these dependencies.

Under neutral conditions, the drag coefficient, $C_{D_{10}}$, is usually given by

$$C_{D_N} = \left(\frac{\kappa}{\ln(10/z_0)}\right)^2$$

with z_0 the roughness length over waves. For open sea sites, z_0 is often assumed to be a constant (0.2 mm). In the literature (Smith (1988), Fairall et al. (1996)), the sea surface roughness length z_0 is often parametrised as

$$z_0 = z_{0_s} + z_{0_w}. \tag{1.29}$$

Here, z_{0_s} is the roughness for a smooth surface, $z_{0_s} = 0.11\nu_a/u_*$ with ν_a being the kinematic viscosity of the air. z_{0_s} is often assumed to be negligible compared to z_{0_w}. z_{0_w} is the roughness corresponding to the surface waves: previous studies showed that short waves are responsible for the roughness (Makin et al., 1995), and are often assumed to be in equilibrium with the local wind. The typical parametrisation scheme for the sea surface roughness z_{0_w} is based on Charnock's relation $z_{0_w} = \alpha u_*^2/g$, in which the Charnock parameter α varies in different experiments. Many experimental investigations indicated that the sea surface roughness is related to wind wave features. Taylor and Yelland (2001) proved that sea surface roughness is related to wave steepness, whereas Oost et al. (2002) reported that it could be related to wave age and frictional speed. For example, Komen et al. (1998) compared field data from Lake Ontario (Donelan, 1990) and from the Humidity Exchange Over the Sea (HEXOS) experiment in the North Sea (Smith et al., 1992) with estimations from the wave model WAM and showed that α increases with decreasing inverse wave age for very young waves ($u_*/C_p > 0.2$) and decreases rapidly for smaller values as suggested by observations from Lake Ontario and HEXOS. Smedman et al. (2003), Drennan et al. (2005) and Potter (2015) also showed the influence of those parameters on z_0 for pure wind seas. Yang et al. (2013) proposed a dynamic modelling of sea-surface roughness within the framework of numerical simulation. Indeed, direct numerical simulation (DNS) enables the study of airflow over waves without any turbulence modelling (Sullivan et al., 2000), (Yang and Shen, 2010). However, the applications of DNS are limited to low Reynolds number flows due to its high computation cost. There are numerous applications of the turbulence-resolving modelling with large-eddy simulation (LES) to planetary boundary layer research and climate studies (Deardorff (1973), Moeng (1984), Sullivan et al. (2008)). In LES, large eddies are explicitly solved whereas small eddies are modelled through a subgrid-scale model. Yang et al. (2013) used a dynamic modelling of the sea surface roughness necessary for the surface-layer model. In Sullivan et al. (2014), z_0 is assigned the constant value of 0.2 mm, which does not account for any dependencies on wave dynamics. To conclude, a universal parametrisation - valid for pure wind sea, mixed sea/swell or swell - remains a challenge. However, it seems that offshore wind profiles are governed more by the atmospheric stability than by the roughness length (Obhrai et al., 2012). Lange et al. (2004) showed that the choice of method for deriving z_0 offshore has little impact on the predicted mean wind speed profiles. Motta et al. (2005) compared two approaches - the 0.2mm constant z_0 and the Charnock's relation - and found that no significant differences resulted between those two approaches.

1.3.2.4 Influence of the atmospheric stability

The models for the estimation of the sea surface roughness were found to lead only to little differences. For the purpose of wind resource assessment, the assumption of a constant roughness was found to be sufficient. But studies showed the influence of the atmospheric stratification on the wind-wave interactions under certain conditions.

The design standards in offshore wind industry rely on the logarithmic law (Equation (1.10)) and the power law (Equation (1.20)) to define a wind velocity profile, but both assume homogeneous and neutral wind conditions. According to Chalikov and Rainchik (2011), the direct influence of stratification on the wind-wave interaction is negligible since the height of the wave boundary layer does not exceed the height of a dynamic sublayer in most cases. Smedman et al. (2003) studied the dependence of drag on the ocean of wave state parameters for near-neutral conditions measured in the Baltic Sea. For developing sea states, the drag (thus the roughness length) depends on wave age and the logarithmic wind law is valid. For mixed sea states and swells, the logarithmic wind profile is no longer valid and the drag coefficient depends on the wave age and on the ratio E_1/E_2 being the ratio of the energy of the relatively long waves on the short wave energy. They showed that the very young and slow waves behave like rigid roughness elements on the airflow whereas for the longer waves, a dynamic coupling with the atmospheric turbulence seems to occur. Motta et al. (2005) investigated the role of atmospheric stability on the vertical wind profile by using four-year data from three Danish offshore meteorological masts. They found that the usual diurnal variation of stability (see Figure 1.1) is extremely smoothed for open sea locations, owing to the large thermal capacity of the ocean. They noticed that the use of the stability-corrected logarithmic law results in a generalised reduction of the deviations from the observations. On the other hand, Högström et al. (2013) compared wind profiles and momentum exchange in the Baltic Sea (BASE experiment) and at a trade-wind site in the Pacific (RED experiment). During the RED experiment, slightly unstable conditions with wind speeds of moderate magnitude and swell of 1-2 m height travelling in the mean wind direction occurred. During the BASE experiment, stable conditions occurred during 25% of the time, and unstable conditions with growing sea, mixed sea and swell conditions occurred for 25% of the time each. They found that during unstable conditions and swell, the wind profile in light winds (less than 3 m.s^{-1}) shows a wind maximum at 7-8 m above the sea surface, with a quasi-constant wind speed above. This feature proves that Monin-Obukhov similarity is no longer valid and that the use of the logarithmic wind profile in such cases can result in misleading results. Moreover, they concluded with the fact that attempting to correct the wind profile for stability was not likely to improve the results.

Within the context of offshore wind industry, energy yield and fatigue damage vary when accounting for the atmospheric stability. Lange et al.

(2004) and Motta et al. (2005) showed that power output estimations improve if stability-corrected logarithmic law is considered. Concerning the fatigue damage, stable conditions contribute to higher fatigue damage than neutral conditions. By performing a time-domain analysis of the structural response of the wind turbine with data from the FINO3 platform in the North Sea, Eliassen et al. (2012) showed that the fatigue loading on the rotor blade increases by a factor of 1.4. Moreover, as the offshore wind turbines tend to be larger than those over land, precise assessment of the wind profiles over 60-100 m is needed and at these heights, tips of blades may emerge from the surface layer where the Monin-Obukhov theory is supposed to hold.

Numerous studies have shown that the effects of the wave field on the MABL were not always negligible and may have a significant impact on the airflow. Hence, air-sea interactions must be looked at from a broader perspective than the traditional overview of wind forcing waves without any feedback from the wave field on the overlying airflow, especially under swell conditions.

1.3.3 Air-sea interactions in the swell regime

The wave effects are commonly thought to be confined within a small region above the water surface and are usually considered as an aerodynamic roughness length (see Subsection 1.3.2.3). However, field observations and numerical modelling have shown that the atmospheric surface layer can be strongly disturbed by waves, especially nonlocally generated waves (i.e. swell). According to Semedo et al. (2011), the presence of swell-dominated sea states is higher than 70 % almost everywhere in the global oceans and the wave field is practically swell-dominated 100 % of the time at low latitudes.

The most striking effect of the swell on the MABL is the presence of a low-level wave-driven wind maximum (i.e. wind jet) at heights of the order of 5-10 m observed by Smedman et al. (1999). Indeed, several field campaigns showed that swell generates a wave-driven wind component: the influence of wave-induced wind affects the overall energy exchange between the sea and the atmosphere. But these observations are relatively rare and sparse. The first observation of a wave-driven wind was during indoor wave tank experiments during which Harris (1966) found that progressive waves in water drive the airflow in the direction of the wave propagation, inducing a wave-driven wind. Figure 1.7 illustrates this swell-driven wind, which is quite pronounced for a lower wind, and whose bump disappears as the wind increases.

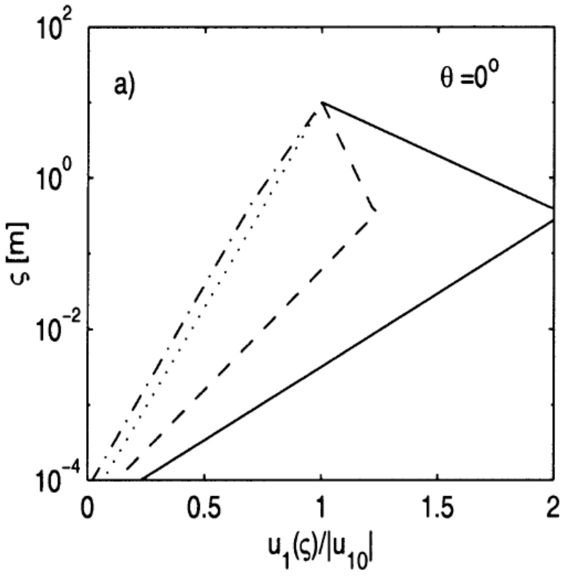

Figure 1.7: Vertical profile of the wind velocity normalised on the wind speed U_{10} in the presence of swell with the slope $ak = 0.1$ and phase velocity $C_p = 15$ m.s^{-1} (Kudryavtsev and Makin, 2004). *Solid lines:* $U_{10} = 0.5$ *m.s*$^{-1}$*; dashed:* $U_{10} = 1.0$ *m.s*$^{-1}$*; dotted:* $U_{10} = 2.0$ *m.s*$^{-1}$*; dashed-dotted:* $U_{10} = 4.0$ *m.s*$^{-1}$*.*

The presence of this wave-driven wind is correlated to an upward transport of momentum from water to air, corresponding to a negative wind stress τ and a negative drag coefficient C_D. Eddy-correlation flux observations confirmed an upward momentum flux in the Mediterranean Sea by Volkov (1970), on Lake Ontario by Drennan et al. (1999), in the Baltic Sea by Smedman et al. (1994) and in the Atlantic and Pacific Oceans by Donelan et al. (1997) and Grachev and Fairall (2001) in high wave age conditions: fast-travelling ocean swells aligned with weak wind. Figure 1.8 shows that, from 8 to 13 hours, an upward momentum flux has been observed from a height range of 0 to 200 m in the Baltic Sea. This was correlated to really weak winds (less than 2 m.s^{-1}). The physical explanation for this behaviour is that ocean waves supply momentum to the atmosphere instead of extracting momentum as they do in the case of equilibrium or increasing wind conditions. As stated in Subsection 1.3.2.1, the momentum flux above the sea surface has two major components: the positive turbulent shear stress, which is directed downward, and the swell-induced stress, which becomes negative (i.e. out of the waves) with increasing wave age. For sufficiently high wave age, the air-sea momentum flux will be directed upward as the wave-induced component becomes dominant. Computations by Hanley and Belcher (2008) indicated that the sign reversal of the total momentum flux from positive to negative occurs when the inverse wave age $U_{10}\cos\theta/C_p$ drops below the range 0.15-0.2, which agrees with oceanic observations (Grachev and Fairall, 2001). Often considered as an exotic case, the upward momentum transfer is now associated with the swell regime correlated to the light-wind-speed regime (less than 2 m.s^{-1}). According to Grachev and Fairall (2001), this wind regime occurs about 16% of the time in the equatorial west Pacific Ocean.

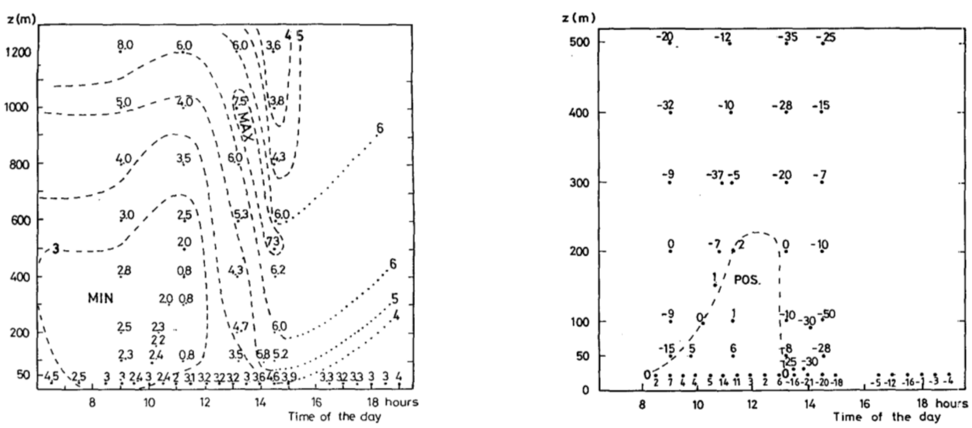

Figure 1.8: Height-time cross sections of wind speed (*left*) and streamwise momentum flux ($\times 10^3$ m^2.s^{-1}) (*right*) from 30 May 1989 based on mast and aircraft measurements (Smedman et al., 1994).

Several numerical simulations have been carried out to study the observed wave effects on the wind field during field campaigns. Sullivan et al. (2000) and Rutgersson and Sullivan (2005) modelled the airflow over idealised waves using DNS with a focus on the turbulent structure and the kinetic energy budgets. Later, LES simulations by Sullivan et al. (2008) have shown that the generation of a low-level jet results in a near collapse of turbulence in the overall ABL, beyond the upper limit of the wave boundary layer. In these conditions (here a neutrally stratified ABL was considered), the wind profile no longer follows a logarithmic shape because of the acceleration of the flow in the surface layer, thus invalidating the Monin-Obukhov similarity theory. The LES results showed good agreement with the measurements from the Coupled Boundary Layers Air-Sea Transfer (CBLAST) field campaign. As illustrated in Figure 1.9, the majority of the values of the bulk drag coefficient C_D are lower than the standard TOGA COARE parametrisation in case of high wave ages. For light winds following swell, the bulk drag coefficient C_D is about 50% lower than the values from standard parametrisations that have no coupling with the sea state, and C_D can be negative in the case of extreme light winds with an underlying fast-moving swell.

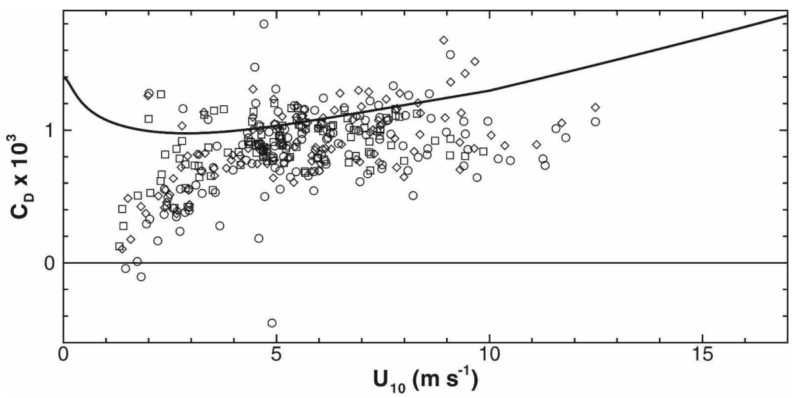

Figure 1.9: Variation of neutral drag coefficient with wind speed for wind-following waves in CBLAST (Sullivan et al., 2008). *Squares correspond to* $z = 4$ *m; diamonds:* $z = 6.5$ *m; circles:* $z = 10$ *m. Solid line is the TOGA COARE 3.0 parametrisation.*

Nilsson et al. (2012) investigated the MABL during wind-following swell and various stability conditions using LES modelling: an increase in upward momentum flux has been observed during slightly unstable or convective conditions compared to neutral state.

Measurements from field campaigns and numerical simulations have recently brought insight to the understanding of wind-wave interactions. They resulted in improved coupled atmosphere-ocean climate models (Carlsson et al., 2009) and mesoscale forecasting models (Jenkins et al., 2012), and proved that wave-induced winds have an effect on offshore wind resource assessment. Recently, several studies addressed this issue within the framework of the applications in wind energy. Yang et al. (2014) carried out a numerical study based on the modelling of an offshore wind farm through a hybrid numerical simulation combining an atmospheric LES model and a spectral model for the wave propagation. AlSam et al. (2015) studied the influence of sea waves on offshore wind turbine aerodynamics by using large-eddy simulations and actuator-line techniques: they focused on the old sea with high wave ages ($C_p/u_* = 45$, 60 and 90) and showed that the swell-induced stress reduces the total wind stress resulting in higher wind velocity, less wind shear and lower turbulence intensity level. They showed that for a same hub height wind speed, the turbine power extraction rate is increased by $[3-8]\,\%$ when the presence of swell is accounted for.

From the perspective of investigating the influence of waves on the MABL, a deterministic model based on the coupling between an atmospheric code and a wave model has been developed during this PhD thesis. However, a preliminary study has been carried out on the swell dissipation by induced atmospheric shear stress in the case of no mean wind. This study is based on the intention of developing modular and scalable tools for the investigation of wind-wave coupled phenomena.

Résumé du chapitre 2

La modélisation du couplage dynamique du système océan-atmosphère nécessite une compréhension approfondie et quantitative des mécanismes gouvernant les interactions vent-vague: malgré de nombreuses études, le sujet reste assez complexe. Dans le cadre du développement d'un modèle numérique déterministe représentant le couplage entre un écoulement atmosphérique et un état de mer, l'objectif de ce second chapitre est d'étudier la dissipation visqueuse de la houle par la contrainte de cisaillement atmosphérique induite par la houle dans le cas d'un écoulement d'air initialement au repos. La rétroaction de la couche visqueuse atmosphérique cisaillée, forcée par une houle idéalisée (linéaire, unidirectionnelle et monochromatique) a été simulée à l'aide d'un modèle numérique de type RANS. ICARE est habituellement utilisé pour des applications navales et hydrodynamiques et il a été modifié pour une toute nouvelle application atmosphérique: l'idée était de développer un outil performant et évolutif, capable d'aborder une complexité croissante de la représentation d'une partie de la physique du système océan-atmosphère. Entre autres, ICARE permettrait des développements numériques tels que l'utilisation de surfaces réalistes avec des états de mer irréguliers, le forçage par la pression de ces états de mer, la prise en compte d'un écoulement atmosphérique réel, la modification des modèles de turbulence..., développements qui n'auraient pas été possible avec un code commercial tel que STARCCM+.

Considérant un domaine périodique selon la direction de propagation de la vague, les propriétés de l'écoulement sous des conditions stationnaires ont été étudiées. Un ensemble de simulations numériques a été mené pour une fourchette usuelle de périodes et d'amplitudes de houle caractéristiques. On y retrouve la dépendance de l'écoulement atmosphérique au nombre de Reynolds comme pour le problème de couche limite oscillante sur plaque plane (Gundogdu and Carpinlioglu, 1999). Tandis que le travail de l'écoulement cisaillé dans des conditions laminaires montre un écart faible par rapport à l'expression analytique de Dore, on retrouve, à partir d'un Reynolds critique ($10^5 < \mathrm{Re} < 2 \times 10^5$), un état de transition vers un développement pleinement turbulent de la couche limite visqueuse cisaillée. La série de simulations numériques permet de quantifier de façon cohérente l'augmentation du travail quand la turbulence se développe au-dessus d'une fraction croissante de

la longueur d'onde. Un paramétrage de cette augmentation est exprimé en fonction du coefficient de dissipation visqueuse calculé à partir du travail du cisaillement moyenné sur une longueur d'onde. Pour le cas le plus turbulent, l'augmentation atteint moins de $3.5\mu_{\mathrm{Dore}}$ ce qui correspond à une distance caractéristique d'atténuation $1/\mu$ de l'ordre de 20 000 km pour une houle océanique. Ardhuin et al. (2009) ont déterminé à partir de leurs observations des dissipations de près de $56\mu_{\mathrm{Dore}}$. Nos calculs ne montrent pas de telles valeurs de dissipation mais nous avons négligé l'effet du vent moyen ainsi que les effets thermiques, et nous avons travaillé avec une surface non rugueuse de la mer et des vagues périodiques. Nous n'avons pas non plus analysé le travail de la contrainte de pression. En effet, le moindre déphasage par rapport à la théorie potentielle influencerait fortement le travail lié à la contrainte de pression. Ce travail n'est pas aussi facilement capté que le travail de la contrainte de cisaillement et notre configuration périodique n'est pas capable de fournir une estimation quantitative correcte de ce mécanisme.

Par conséquent, il reste à ce jour à éclaircir et étudier les autres mécanismes impliqués dans la dissipation de la houle. Considérer une circulation atmosphérique exacte et son influence sur la houle reste un défi avec les outils de calcul actuels. S'il est actuellement très difficile de modéliser l'ensemble du système couplé océan-atmosphère, on choisit de se concentrer sur les interactions vent-vagues dans la suite du document. Un couplage entre une simulation atmosphérique de type LES et un code spectral qui résout l'évolution non-linéaire d'états de mer est implémenté afin d'étudier l'impact de l'état de mer sous-jacent sur la couche limite atmosphérique marine.

Chapter 2

Swell dissipation by induced atmospheric shear stress: a case with no wind

Modelling the dynamic coupling of ocean-atmosphere systems requires a fundamental and quantitative understanding of the mechanisms governing the wind-wave interaction: despite numerous studies, this topic remains quite complex. Within the framework of the development of a deterministic numerical model representing the coupling between an atmospheric flow and a sea state, the aim of this second chapter is to investigate the viscous dissipation of the swell by the wave-induced atmospheric shear stress in the case of a initially still airflow.

Gaining insight into the atmospheric dissipation phenomena related to the swell propagation will provide an improvement of the wave prediction models in which dissipation is not taken into account. Indeed, in case of usual storms, such models currently overestimate the significant wave heights of about 20% in a radius of more than 4000 km from the centre of the storm (Collard et al., 2009). In the ocean, an idealised wave underlying a constant airflow (i.e. a constant wind) is subject to a balance between the energy injected by the wind and the dissipation losses: a constant balance of energy can be observed over very long distances. However, satellite observations of the swell (SAR measurements by Ardhuin et al. (2009)) demonstrated that an important loss in energy can occur, especially for steep waves. Stochastic wave models take into account transfer in energy such as: wind input leading to wave generation, non-linear effects, and losses due to dissipation. Many processes remain to be identified and their influence on the closure of the energy balance to be quantified: for example the interaction of swell with the turbulence in the ocean (Phillips, 1961) or the coupling with the atmosphere (Harris, 1966).

The work presented in this second chapter falls within the investigation of the viscous dissipation induced by atmospheric shear stress. The interaction between a wave-induced flow and an atmospheric flow is neglected here (i.e. the mean wind is not taken into account). Indeed, the feedback of the wave-induced atmospheric shear stress is not well quantified, especially when water orbital velocity and particle displacement reach a turbulent threshold for the motion they impose in the air side (Collard et al., 2009). The characterisation of this atmospheric turbulent regime and the magnitude of the wave-induced dissipation remain a major question to be answered. When neglecting the curvature of the surface, one can recover known results for an oscillating boundary layer on a fixed bottom (Gundogdu and Carpinlioglu, 1999). An increase in the shear stress, and thus its work on the surface, is observed and needs to be investigated in order to characterise the turbulent flow regime above waves. The detailed structure of the turbulent flow near the wavy surface is, however, hard to observe by experiment because of the complexity of the environment and there is limited information on the overall environmental parameters. Indeed, the viscous air boundary layer whose characteristic thickness is $\delta = \sqrt{2\nu/\omega} \equiv O\left(10^{-3}\text{m}\right)$ needs to be studied over a wavelength $O\left(100\text{m}\right)$ on a height of vertical displacement corresponding to an amplitude $O\left(1\text{m}\right)$. In order to investigate the laminar-to-turbulence dynamics of this boundary layer, numerical simulations have been conducted with simulation softwares handling problems governed by the Navier-Stokes equations (i.e. Computational Fluid Dynamics, or CFD). The evolution of the shear stress is investigated for a large rank of swell conditions and the increase in the wall shear stress and its associated dissipation rate due to turbulence is quantified. This study is based on the intention of developing numerical tools for the investigation of wind-wave coupled phenomena. The LHEEA's in-house code ICARE (Alessandrini and Delhommeau, 1999) is validated through a comparative study with the commercial code Star-CCM+ (Perignon et al., 2014). This study provided a proper test case for the development of a modular and scalable tool where the environment of development does not prevent access to the sources and enables the numerical implementation of key aspects such as the remeshing, the turbulence model and the coupling with other codes (e.g. wave model).

2.1 Theoretical solution for small amplitudes

While studying the problem of a swell propagating under a viscous atmospheric layer at rest, the oceanic layer can be considered as a strong forcing on the atmospheric layer, and the atmospheric layer as a weak forcing on the free surface. Here is detailed a study of a sheared atmospheric flow in order to evaluate the feedback of the large-scale forcing on an idealised wave. For simplicity reasons, the wave is considered as unidirectional and monochromatic. As stated before, a first simplification can be done with the surface curvature being neglected (Collard et al., 2009) if amplitudes are small compared to wavelengths. A Reynolds number based on the double velocity and double displacement is introduced by analogy with oscillatory boundary layer on a flat plate:

$$Re = \frac{4u_{\text{orbital}}a}{\nu}, \tag{2.1}$$

u_{orbital} and a being respectively the amplitude of the surface velocity and the amplitude of the displacement h. For linear waves in infinite depth, one can consider the solution of the Euler equation:

$$h\left(\mathbf{x}, t\right) = a \cos\left(\mathbf{k} \cdot \mathbf{x} - \omega t\right) \tag{2.2}$$

and the velocity below the free surface is:

$$\begin{aligned} u_{\text{orbital}}\left(\mathbf{x}, t\right) &= a\omega \cos\left(\mathbf{k} \cdot \mathbf{x} - \omega t\right) \\ w_{\text{orbital}}\left(\mathbf{x}, t\right) &= a\omega \sin\left(\mathbf{k} \cdot \mathbf{x} - \omega t\right) \end{aligned} \tag{2.3}$$

with $\omega = 2\pi/T$ the angular frequency and $\vec{k}$ the wavenumber.

The flow is supposed to be turbulent above $Re \approx 10^5$ (Jensen et al., 1989) and the atmospheric shear stress at the free surface is then expected to deviate from the analytical laminar solution of Dore (1978). The laminar solution can be written as the sum of a potential flow and a viscous sublayer which connects the velocity profiles between both media. The viscous layer in the water can be neglected since the water inertia is larger than the air and large wavelengths are considered here. The Euler solution for the atmospheric velocity profile verifies the same solution of potential flow as in the oceanic layer:

$$\begin{aligned} u_{\text{potential}}(\mathbf{x}, z, t) &= -a\omega e^{-k(z-h)} \cos(\mathbf{k}\cdot\mathbf{x} - \omega t) \\ w_{\text{potential}}(\mathbf{x}, z, t) &= -a\omega e^{-k(z-h)} \sin(\mathbf{k}\cdot\mathbf{x} - \omega t), \end{aligned} \tag{2.4}$$

with a connection to the oceanic layer through a viscous boundary layer:

$$u_{\text{junction}} = 2a\omega \exp(-z_+) \cos(\mathbf{k}\cdot\mathbf{x} - \omega t), \tag{2.5}$$

with

$$z_+ = \frac{z-h}{\sqrt{2\nu/\omega}}. \tag{2.6}$$

The mean work of the wall shear stress W_v under laminar conditions is defined as:

$$W_v = \left\langle \rho_a \nu u_+ (z = h) \left.\frac{\partial u_+}{\partial z}\right|_{z=h} \right\rangle, \tag{2.7}$$

u_+ being the sum of the potential solution and the junction solution in the air.
This work normalised by the linear power of the wave gives the viscous dissipation coefficient:

$$\mu = -\frac{W_v}{C_g \rho_w g a^2/2} \tag{2.8}$$

with C_g the group velocity of the wave. Replacing the analytical formulation of the wall shear stress under laminar conditions yields the "Dore coefficient":

$$\mu_{\text{Dore}} = -\frac{\omega^2}{gC_g}\frac{\rho_a}{\rho_w}\sqrt{2\nu\omega}. \tag{2.9}$$

This analytical expression rectifies by a factor 2 the equation A8 from Collard et al. (2009) and the equation 5 from Ardhuin et al. (2009). While studying the turbulent air flow, a low-Reynolds asymptote is expected, wave steepness and Reynolds number being subject to the aforementioned hypotheses. However, since the oceanic swell conditions often exceed the turbulent threshold of theoretical Reynolds, the characterisation of the dissipation coefficient for a large range of flow regimes needs to be investigated.

2.2 Numerical model

2.2.1 Geometry

One of the challenges of the numerical modelling of the atmospheric shear stress above the waves is the detailed representation of the flow in the vicinity of the moving free surface. In an absolute frame of reference, the displacement of the free surface requires a meshing process which is expensive in terms of CPU (i.e., central processing unit) time and precision. In case of swell, especially unidirectional and monochromatic wave, the flow modelling is easier. Solving the flow in a frame of reference linked to the displacement of the crest of the wave (i.e., a frame moving at the phase velocity of the monochromatic wave, C_ϕ, compared to the absolute frame) leads to simpler governing equations and boundary conditions, and the most interesting advantage is that no remeshing is needed. The relative frame of reference is moving with a constant linear velocity in the x-direction, $\mathbf{U}_{ref} = \mathbf{C}_p$, and the phase of the wave elevation in this frame is simplified to a space function satisfying $\mathbf{k}\cdot\mathbf{x} - \omega t = \mathbf{k}\cdot(\mathbf{x}_{ref} + \mathbf{C}_p t) - \omega t = \mathbf{k}\cdot\mathbf{x}_{ref}$. Under the hypothesis of a strong forcing of the ocean on the atmospheric boundary layer and a weak feedback on the other hand, the fluid domain can be limited to the atmosphere, with a suitable boundary condition in accordance with the oceanic forcing and the motion of the reference frame attached to the crest.

The wave elevation is set periodic in the x-direction (Equation (2.2)). Numerical simulations have been carried out in a domain of a wavelength λ of the order of 100 metres. The transverse extension is set to be $\lambda/16$ for practical reasons: a sensitivity analysis has shown that there is no influence of the width, and with the chosen width, several simulations of turbulent flow can be undertaken with a reasonable mesh size for the largest wavelengths considered here. The vertical extension is set to $H = \lambda/4$.

A kinematic boundary condition is applied at the top and bottom boundaries, satisfying:

– the condition of forcing by the orbital velocity at the bottom (cf Equation 2.3):

$$\mathbf{u}_{-} = u_{\text{orbital}}\mathbf{i} + w_{\text{orbital}}\mathbf{k} - \mathbf{U}_{ref},$$

– the potential solution at the top (cf Equation 2.4):

$$\mathbf{u}_{+}\left(z=H\right)=u_{\text{potential}}\left(z=H\right)\mathbf{i}+w_{\text{potential}}\left(z=H\right)\mathbf{k}-\mathbf{U}_{ref}.$$

Lateral boundaries are defined as symmetry boundary conditions (i.e., scalar fluxes set to zero).

In the atmospheric fluid domain, the initial condition of a still air in the absolute frame of reference is easily transposable to the relative frame with an initial velocity, $-\mathbf{U}_{ref}$, associated with the condition of an inlet mass flow at the upstream boundary of the domain. A periodic condition is imposed at upstream and downstream boundaries.

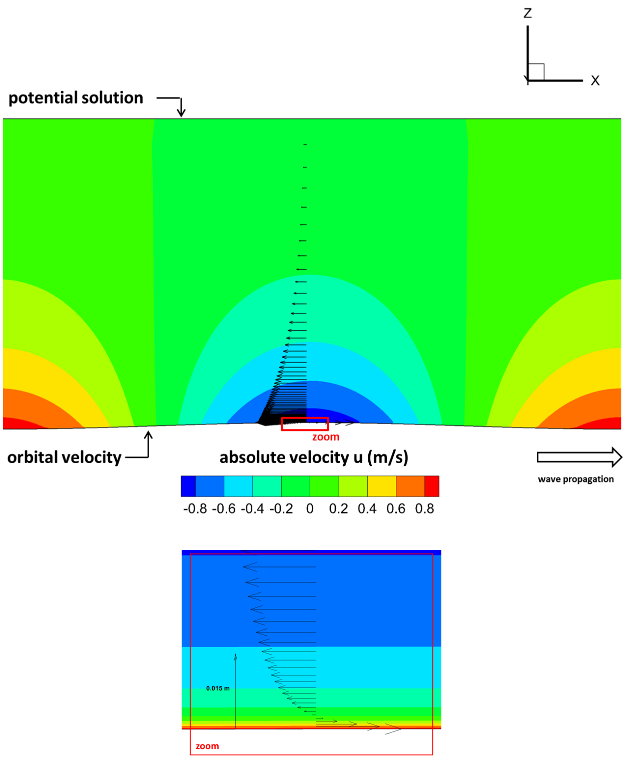

Figure 2.1: Absolute velocity field in the central section of the air domain and its vertical profile at the wave crest for a wave of period $T = 17.5$ s and amplitude $a = 2.55$ m ($Re = 5 \times 10^5$) (*top*). Detailed field in the vicinity of the free surface (*bottom*). Note that the XZ ratio is not respected.

2.2.2 Solver

The modelling strategy and the choice of turbulence closure are related to the nature of the studied flow. For this specific case of a viscous sheared flow, a Reynolds-Averaged Navier Stokes (RANS) approach seems to be appropriate for the modelling of the near-wall area with reasonable CPU costs. Moreover, in the relative frame of reference previously described, the mean flow is supposed to reach a stationary state: stationary RANS simulations can then be carried out (Perignon et al., 2014).

ICARE is a hydrodynamic computational code that solves Navier-Stokes equations with free surface equations. It has been developed in LHEEA laboratory in the 1990s for resistance, propulsion, manoeuvrability and seakeeping applications. The first idea was to use this in-house tool in order to investigate the viscous airflow above the waves. Despite its hydrodynamic applications, this code solves Navier-Stokes equations which govern the motion of a viscous fluid, and after various modifications, it has been transformed in order to address the specific problem of the swell dissipation by induced atmospheric shear stress.

2.2.2.1 Hypotheses and equations

In ICARE, the fluid is supposed to be incompressible. The continuity equation yielding the mass conservation is reflected in the fact that the divergence of the velocity field $\mathbf{U}$ becomes zero:

$$\frac{D\rho}{Dt} + \rho \mathrm{div}\mathbf{U} = 0 \qquad \Rightarrow \qquad \mathrm{div}\mathbf{U} = 0 \tag{2.10}$$

In the Navier-Stokes equation (see Equation 1.1), term IV is neglected: as the domain is of the order of one wavelength $O\,(100)$m, the Coriolis effect is not significant. Term VI representing the viscous stress can be written as:

$$\tau_{ij} = 2\mu \left(\frac{\partial U_i}{\partial x_j} + \frac{\partial U_j}{\partial x_i} \right) \tag{2.11}$$

since the fluid behaves as a Newtonian fluid, i.e. the deformations and the stresses are related within an incompressible fluid. The viscosity μ is a property of the fluid and the kinematic viscosity ν is defined as:

$$\nu = \frac{\mu}{\rho}. \tag{2.12}$$

As mentioned in the previous chapter, it is convenient to analyse the flow in two parts, a mean component and a fluctuating component. Thus an instantaneous quantity can be written as:

$$U = \bar{U} + u'. \tag{2.13}$$

This Reynolds decomposition leads to the following Reynolds-Averaged Navier-Stokes equation, where the overline notation is omitted:

$$\frac{\partial U_i}{\partial t} + U_j \frac{\partial U_i}{\partial x_j} = -\frac{1}{\rho}\frac{\partial P}{\partial x_i} + \frac{1}{\rho}\frac{\partial \tau_{ij}}{\partial x_j} - \frac{\partial \overline{u_i' u_j'}}{\partial x_j} \tag{2.14}$$

Closing the RANS equation requires modelling the Reynolds stress $\overline{u_i' u_j'}$ in order to solve the mean part of the velocity. Thus, the correlations of the fluctuating velocities $\overline{u_i' u_j'}$ are expressed through a Newtonian type closure, often referred as an "eddy" or "turbulent" viscosity model:

$$\overline{u_i' u_j'} = \frac{2}{3}k - \nu_t \left(\frac{\partial U_i}{\partial x_j} + \frac{\partial U_j}{\partial x_i} \right). \tag{2.15}$$

This turbulence closure involves a turbulent viscosity ν_t and the TKE $k = \frac{1}{2}\overline{u_i' u_j'}$. A transport equation for k is then necessary to close the whole system. A $k - \omega$ turbulence model is implemented in ICARE.

Eventually, the RANS equation becomes:

$$\frac{\partial U_i}{\partial t} + U_j \frac{\partial U_i}{\partial x_j} = -\frac{1}{\rho}\frac{\partial p}{\partial x_i} + (\nu + \nu_t)\frac{\partial^2 U_i}{\partial x_j \partial x_j} + \left(\frac{\partial U_i}{\partial x_j} + \frac{\partial U_j}{\partial x_i} \right)\frac{\partial \nu_t}{\partial x_j} \tag{2.16}$$

with the "pressure" term $p = P + \rho g z + \frac{2}{3}\rho k$.

From a numerical point of view, RANS equations are written into convective form with a partial transformation from the Cartesian space (x_1, x_2, x_3) to a curvilinear space (ξ_1, ξ_2, ξ_3), which follows the deformation of the free surface at each time. The equations are discretised using a finite-difference method, and implicit and second-order discretisation schemes in time and space. A structured mesh following the free surface is implemented.

The Cartesian components of velocity, turbulence kinetic energy and turbulence dissipation rate are located at the nodes of this mesh, whereas the pressure is located at the centre of the cells. The Rhie and Chow method (Rhie and Chow, 1983) is implemented in order to get, from the continuity equation, an equation on the pressure p and to eliminate the chequer-board pressure problem by introducing a momentum interpolation at the cell faces. More details on the numerical implementation in ICARE can be found in Alessandrini and Delhommeau (1999).

2.2.2.2 Modifications introduced in ICARE for modelling an airflow

As stated in the previous section, ICARE is a hydrodynamic computational code that has been developed for naval applications. In order to address the modelling of an airflow above waves, it is natural to consider the water surface as the rigid body and the air as the fluid. No physical modifications have been actually introduced inside the equations. The main change occurs in the module calculating the metrics: while the (x, y, z) system was considered with a z-axis directed downward, the new system has been reversed with a z-axis directed upward. New boundary conditions have also been implemented in order to model our specific problem as specified in 2.2.1:

- periodicity has been implemented in x and y-direction,
- orbital velocity $\mathbf{u}_-$ and potential solution $\mathbf{u}_+$ have been implemented at the bottom and top boundaries (cf equations 2.3 and 2.4).

2.2.2.3 Flux across the free surface

As stated at the beginning of this chapter, we focus on an Airy wave, which is monochromatic and unidirectional, and has the following properties:

$$\begin{aligned} h\left(\mathbf{x}, t\right) &= a \cos\left(\mathbf{k} \cdot \mathbf{x} - \omega t\right) \\ u_{\text{orbital}}\left(\mathbf{x}, t\right) &= a\omega \cos\left(\mathbf{k} \cdot \mathbf{x} - \omega t\right) \\ w_{\text{orbital}}\left(\mathbf{x}, t\right) &= a\omega \sin\left(\mathbf{k} \cdot \mathbf{x} - \omega t\right) \end{aligned}$$

Considering a flow with a free surface, the following free surface boundary conditions must be satisfied:

- the kinematic condition expresses the fact that there is no material flux across the free surface:

$$\frac{\partial h}{\partial t} + u_{\text{orbital}} \frac{\partial h}{\partial x} - w_{\text{orbital}} = 0 \qquad \text{on} \quad z = h\left(\mathbf{x}, t\right), \tag{2.17}$$

– the dynamic condition expresses the fact that the pressure is constant across the free surface interface.

Here the kinematic boundary condition is not satisfied as is. Indeed, if we write out the equations:

$$
\begin{aligned}
&\frac{\partial h}{\partial t} + u_{\text{orbital}}\frac{\partial h}{\partial x} - w_{\text{orbital}} \\
&= a\omega \sin(\mathbf{k}\cdot\mathbf{x} - \omega t) - a^2\omega\cos(\mathbf{k}\cdot\mathbf{x} - \omega t)\sin(\mathbf{k}\cdot\mathbf{x} - \omega t) - a\omega\sin(\mathbf{k}\cdot\mathbf{x} - \omega t) \\
&= -a^2\omega\cos(\mathbf{k}\cdot\mathbf{x} - \omega t)\sin(\mathbf{k}\cdot\mathbf{x} - \omega t) \\
&\neq 0.
\end{aligned}
$$

Thus, a new wave condition needs to be implemented as a boundary condition or the fluxes at the free surface must be numerically removed. Three simulations with two kinds of boundary condition are compared:

1. one simulation is set with the usual velocity components for a Airy wave (i.e. u_{orbital} and w_{orbital}),
2. one simulation is set with the usual velocity components for a Airy wave, but fluxes at the free surface are neglected and set to zero in the numerical equations,
3. one simulation is set with a corrected velocity component (i.e. u_{orbital} and $w_{\text{orbital}} - a^2\omega\cos(\mathbf{k}\cdot\mathbf{x} + \omega t)\sin(\mathbf{k}\cdot\mathbf{x} - \omega t)$).

Figure 2.2 shows the comparison of the usual vertical component of an Airy wave and the "no flux"-corrected vertical component. Red line is the first simulation specified above, green line is the second one where fluxes at free surface have been numerically removed and blue line is the third one where the correction on the vertical component is implemented in order to get no physical fluxes at the free surface. Simulations 1 and 2 have the exact same Dirichlet boundary conditions (i.e. u_{orbital} and w_{orbital}). A very small difference appears when implementing the corrected vertical component of the Airy wave.

The most striking evidence that the presence of fluxes at the free surface plays an important role can be noted on Figure 2.3. This figure displays the vertical derivative of the horizontal component of the velocity $\partial U/\partial z$ at the free surface for the three simulations plus the analytical solution calculated

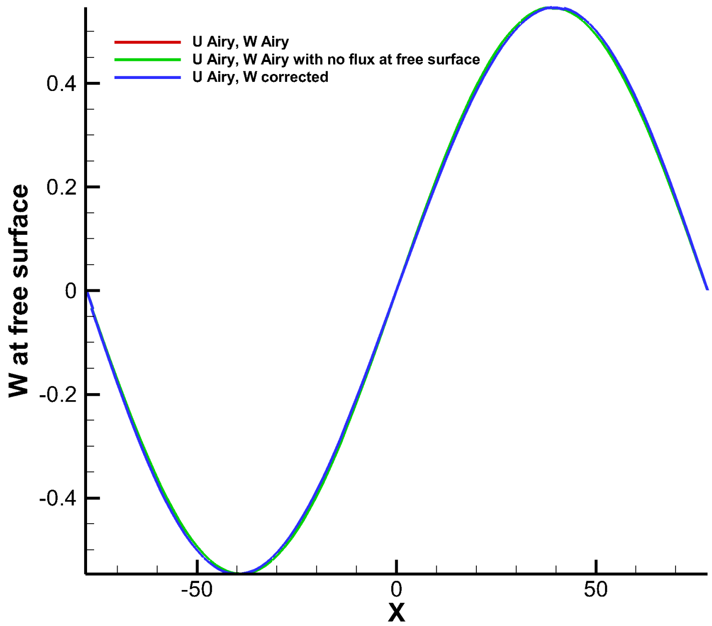

Figure 2.2: Comparison of the vertical component of an Airy wave and the "no flux"-corrected vertical component for a wave of period $T = 10$ s and amplitude $a = 0.87$ m ($Re = 1 \times 10^5$). Note that the wave crest is located at $X = 0$.

from u_{junction} in the air at the free surface. As it was mentioned previously, the work of the wall shear stress depends on this quantity (equation 2.7) and influences the estimation of the viscous dissipation coefficient (equation 2.8). It is thus necessary to correctly model the airflow and the influence of the wave in the vicinity of the free surface.

Imposing an Airy wave at the lower boundary leads to an odd shape of $\partial U/\partial z$ along x at the free surface (red curve). If the fluxes are numerically removed at free surface in order to satisfy the kinematic boundary condition, then the shape of the derivative is closer to the analytical solution (green curve). The trend is really similar when imposing a wave whose vertical velocity satisfies the "no flux across the surface" condition (blue curve). It can be noted that the amplitude of the curves are slightly larger for the numerical models compared to the analytical solution, but the phase is satisfied. It can be due to the near-wall treatment and the turbulence model used in the

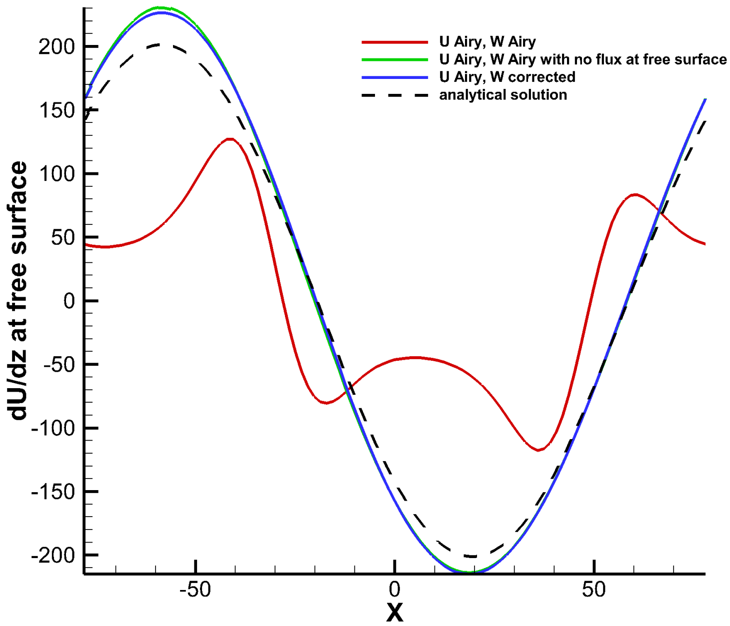

Figure 2.3: Comparison of the vertical derivative of the horizontal component of the velocity in the air at the free surface for a wave of period $T = 10$ s and amplitude $a = 0.87$ m ($Re = 1 \times 10^5$). Note that the wave crest is located in $X = 0$.

numerical simulation.

In Figure 2.4, the vertical profile of the horizontal component of the velocity of the airflow is plotted in the vicinity of the wave crest. The difference in $\partial U/\partial z$ at the free surface has a significant impact in the layer near the free surface.

Afterwards, all the simulations are then conducted considering a slightly modified wave condition: the vertical component of the wave orbital velocity is modified in order to take into account the fact that no fluxes across the interface is required to model the viscous air-sea boundary layer. Under such modified wave boundary conditions, the numerical simulations give good results. It has been demonstrated that Airy waves do not satisfy the free surface boundary condition: in order to overcome this specific problem, non-linear monochromatic waves will be modelled with the Rienecker&Fenton

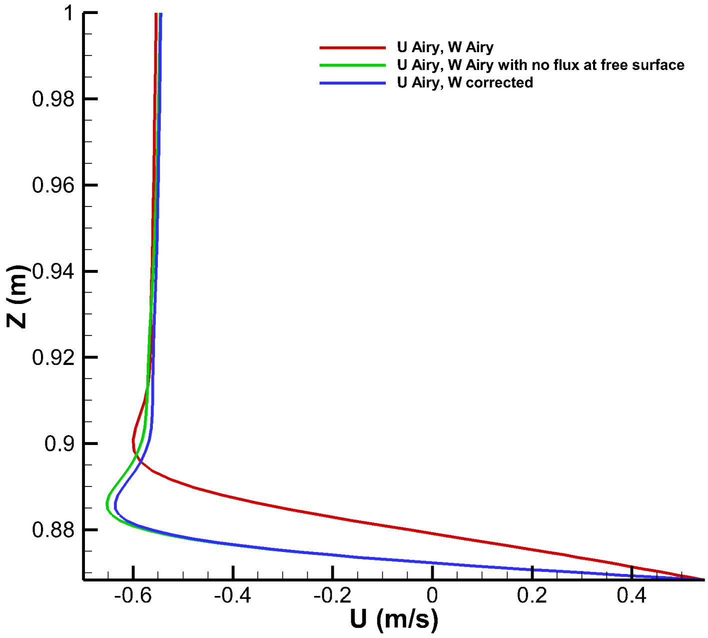

Figure 2.4: Detailed vertical profile of the horizontal component of the velocity in the air in the vicinity of the wave crest for a wave of period $T = 10$ s and amplitude $a = 0.87$ m ($Re = 1 \times 10^5$).

method (Rienecker and Fenton, 1981) in the following chapters by solving for the non-linear free surface conditions.

2.2.3 Near-wall specifications and meshing approach

The aim of this numerical modelling is to examine the properties of the viscous air-sea boundary layer driven by an idealised swell in order to characterise the induced atmospheric flow regime and its associated viscous dissipation over swell. In this numerical modelling, the free surface (i.e. bottom boundary) is seen as a wall moving at the phase velocity of the wave regarding the airflow. The presence of walls or surfaces allows the existence of turbulence even in the absence of density fluctuations. Indeed, vorticity can actually be generated at surfaces by an on-coming flow, which is suddenly brought to rest, or to tend to the velocity phase in this case, to satisfy the no-slip condition. A boundary layer grows near the surface and the vorticity generated can then be diffused, transported and amplified.

In the case of a laminar flow, the laminar boundary layer is characterised by huge velocity gradients and viscous forces, and is defined by its thickness δ. The velocity can be described by:

$$U = U_\infty f\left(\frac{y}{\delta}\right), \tag{2.18}$$

with U_∞ the velocity outside the boundary layer and y the distance normal to the surface. Outside the boundary layer, the flow is considered as inviscid.

In the case of a turbulent flow, the laminar boundary layer becomes turbulent as shown in Figure 2.5:

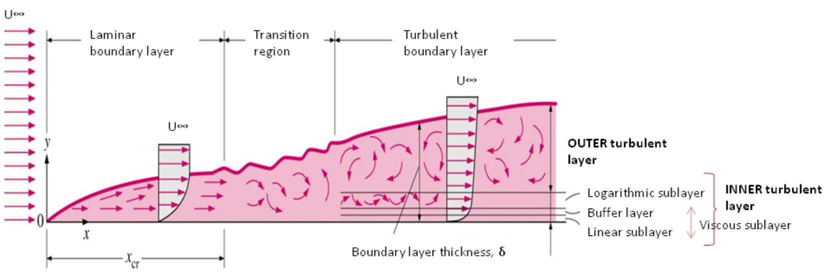

Figure 2.5: Developing turbulent boundary layer on a flat plate (Solliec, 2013).

Two parameters are used to characterise the turbulent boundary layer:

– the inner velocity scale, or friction velocity:

$$u_* = \sqrt{\frac{\tau_{\text{wall}}}{\rho}} \tag{2.19}$$

with τ_{wall} the wall shear stress,

– a new length scale, the dimensionless distance to the wall:

$$y_+ = \frac{y u_*}{\nu} \tag{2.20}$$

The total shear stress is defined by the sum of the viscous (Navier) stress and the turbulent (Reynolds) stress:

$$\frac{\tau}{\rho} = \nu \frac{\partial \bar{U}}{\partial y} - \overline{u'v'}$$

At the wall, the turbulent stress is zero and the total shear stress equals the viscous stress. The wall shear stress is therefore defined by

$$\tau_{\text{wall}} \equiv \mu \frac{\partial U}{\partial y}\bigg|_{y=0}.$$

The turbulent boundary layer is characterised by two zones as shown in Figure 2.5:

1. The inner or viscous turbulent boundary layer represents 20% of the total thickness. The flow is governed by the boundary conditions at the wall, the turbulent stress is small compared to the viscous one. The shear stress is almost constant in this region. The velocity profile is described by a wall function. The inner boundary layer is defined by:
   - the viscous sublayer (1% of the total thickness):
     - the linear sublayer (y_+ <3): the viscous stress dominates the Reynolds stress and the flow is laminar. The velocity is defined by a universal law

       $$\frac{\bar{U}(y)}{u_*} = \frac{y u_*}{\nu}$$

     - the buffer layer (3< y_+ <30): the Reynolds stress begins to evolve. There is no universal law describing the velocity in this layer.
   - the logarithmic sublayer (30< y_+ <500): the velocity follows a logarithmic law of the wall $\frac{U}{u_*} = \frac{1}{\kappa}\ln(y_+) + C$ with κ the von Karman constant. The Reynolds stress dominates.

2. the outer turbulent boundary layer represents 80% of the total thickness. The velocity gradient normal to the surface is small and the velocity profile depends on the fluid and flow characteristics. The velocity defect law is

   $$\frac{U_\infty - \bar{U}(y)}{u_*} = \frac{1}{\kappa}\ln\left(\frac{y}{\delta}\right) + B$$

   with B a non-universal constant.

In CFD, it is possible to specify the wall treatment in RANS models. While using a "high"-Re RANS model, the viscous sublayer is modelled by one cell where a wall function is implemented (see Figure 2.6). The value of y_+ at the top of this first cell should be 30. If a "low"-Re RANS model is implemented, no wall function is used to resolve the flow near the wall. A really fine mesh is therefore necessary near the wall. A value of one at the top of the first cell is usually required for y_+.

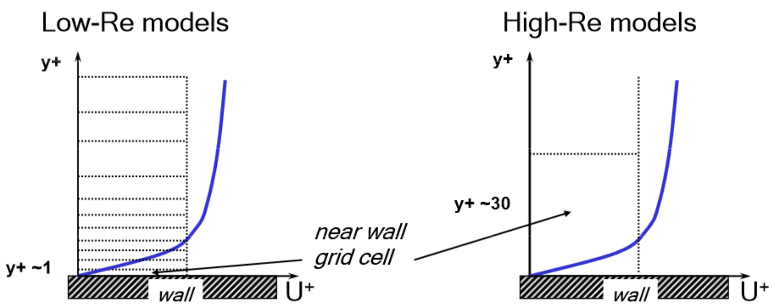

Figure 2.6: Mesh near the wall for a low-Re RANS model and a high-Re RANS model.

In order to correctly model the shear in the vicinity of the free surface, the currently implemented $k-\omega$ turbulence model is activated with the option "low-Reynolds". $y_+ \approx 1$ is used as a posteriori criterion in order to validate the mesh refinement.

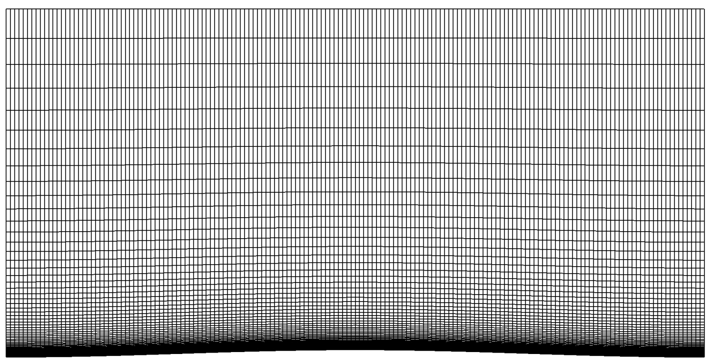

Figure 2.7: Structured mesh.

A mesh convergence study has been carried out. Three criteria have been selected:

- $y_+ \approx 1$ imposes the height of the first cell at the free surface,
- as mentioned in 2.1, a connection occurs between the oceanic layer and the potential airflow through the viscous layer (see the velocity profile in Figure 2.1) and an acceleration/deceleration of the wind is observed compared to a log profile: a certain number of cells is imposed in this area where the junction occurs,
- the mesh is graded in geometric progression: the common ratio is set to be less than 1.1.

For example, the mesh convergence for the case presented in Figure 2.1 ($T = 17.5$ s and $a = 2.55$ m) gives:

- the height of the first cell $\Delta z_0 \approx 5 \times 10^{-4}$ m,
- 50-60 cells discretise the height where an acceleration/deceleration of the wind is observed at the crest of the wave (Figure 2.8),
- the grading ratio is 1.088.

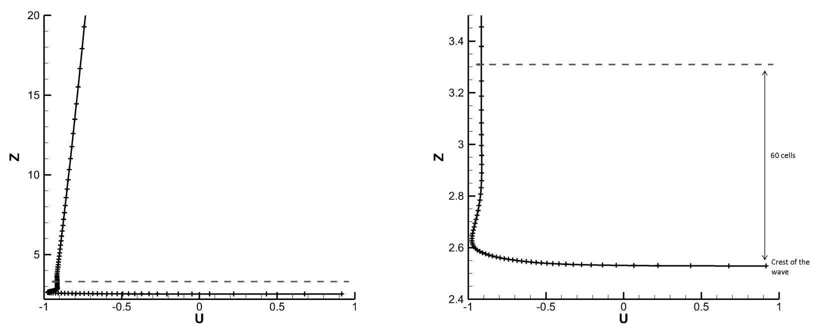

Figure 2.8: Detailed vertical profile of the horizontal velocity U at the crest of the wave ($T = 17.5$ s and $a = 2.55$ m). Symbols are the vertical nodes of the grid. Gray dashed line marks the 0.8 m-height above the crest.

2.3 Air-sea interface modelling

A set of simulations has been carried out in order to evaluate the features of the airflow in an infinite homogeneous domain. Similar simulations have been carried out by Perignon et al. (2014) using the commercial CFD code, StarCCM+. The numerical domain has a length of one wavelength and its upstream and downstream boundaries are periodic. 36 numerical simulations are conducted, corresponding to airflows with Reynolds numbers in the range of 0.1×10^5 to 12×10^5 overlying waves whose period ranges from 10 to 17.5 s, in order to characterise the behaviour of the flow.

	T (s)	10.0	12.5	15.0	17.5
	λ (m)	156	244	351	478
$Re = 0.1 \times 10^5$	a (m)	0.28	0.31	0.34	0.36
	u_{orbital} (m/s)	0.17	0.16	0.14	0.13
	ak	0.01	0.008	0.006	0.005
$Re = 5 \times 10^5$	a (m)	1.93	2.15	2.35	2.55
	u_{orbital} (m/s)	1.21	1.08	0.98	0.91
	ak	0.078	0.055	0.042	0.034
$Re = 12 \times 10^5$	a (m)	3.00	3.30	3.60	4.00
	u_{orbital} (m/s)	1.88	1.66	1.51	1.43
	ak	0.12	0.08	0.06	0.05

Table 2.1: Characteristics quantities for $Re = 0.1 \times 10^5$, 5×10^5, and 12×10^5 simulations for four setup of different wave periods.

For a given Reynolds number (for example, $Re = 0.1 \times 10^5$, 5×10^5 or 12×10^5 - Table 2.1), the wave steepness ak of the lower boundary layer varies with the wavelength. All the simulations therefore provide an estimation of the airflow characterisation by the previously defined Reynolds number in Equation 2.1. Stationary RANS simulations have been carried out until 1000 iterations and the time convergence has been a posteriori verified considering the residuals. Convergence in space has also been verified and the first cell of the mesh above the free surface and the grid spacing satisfies $y_+ > 1$ at high Reynolds numbers as mentioned in the previous section.

2.3.1 Characterisation of the work of the wall shear stress

Similarly to the characterisation of the oscillation flow on a flat plate (Jensen et al., 1989), the wall shear stress along a wavelength (or during an oscillatory period in Jensen et al. (1989)) shows a laminar-turbulent transition in the sheared flow. The region in the vicinity of the lower boundary is supposed to be the most Reynolds-Number-dependent part of the flow. The wall shear stress and its work above a moving free surface are indeed sensitive quantities for the study of the flow characterisation. Normalising the work of the total shear stress by the characteristic amplitude of the Dore expression ($a\omega^2\sqrt{\omega}$ in Equation 2.9) and plotting this quantity against the relative position x along the wavelength exhibits a scalability at any given Reynolds number in Figure 2.9.

Whereas simulations for $Re = 0.1 \times 10^5$ show a good agreement with the Dore analytical expression (black line), the transition to turbulence in the airflow seems to appear around $Re = 0.5 \times 10^5$. A very similar study has been carried out by Perignon et al. (2014) with the commercial CFD code, StarCCM+ (Figure 2.10). In their study, the Airy wave propagates along negative x direction. The mesh is a polyhedral grid with a prismatic layer in vicinity of the free surface whose height and number of prismatic cells verify the $y_+ > 1$ condition. A low-Reynolds $k-\varepsilon$ turbulence model is implemented with the low-y_+ option active.

In Perignon et al. (2014), the transition to turbulence appears later at $Re = 2 \times 10^5$. This transition exhibits a strong deviation compared to the

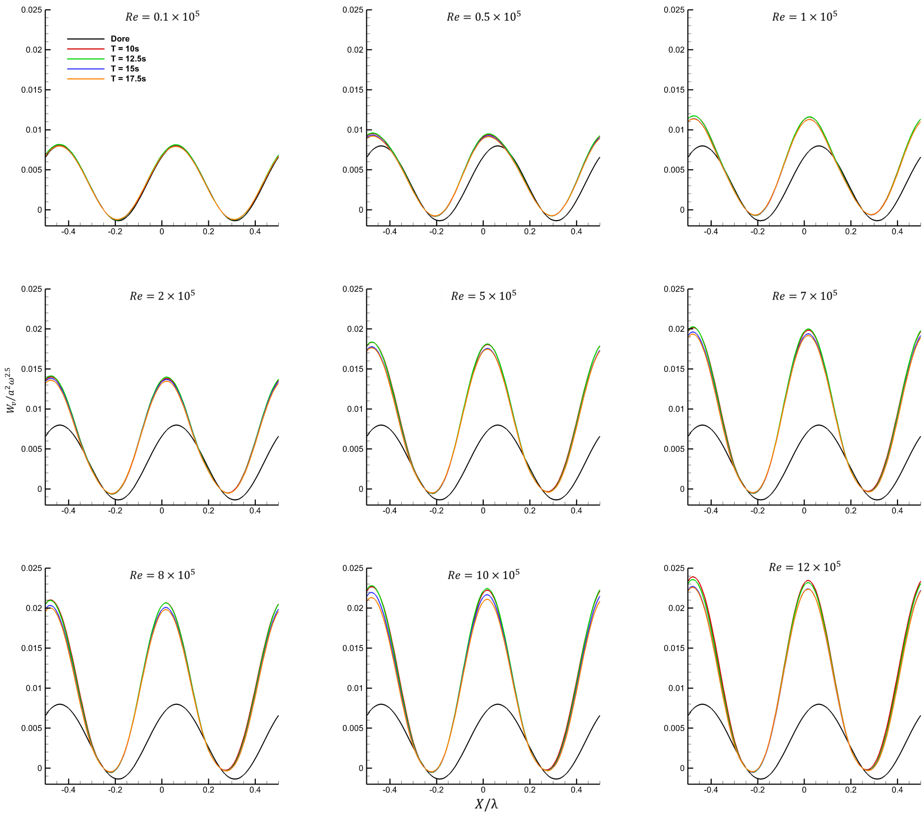

Figure 2.9: Evolution of the normalised work of the wall shear stress at the free surface over the relative position X/λ, from laminar ($Re = 0.1 \times 10^5$) to fully developed turbulent cases ($Re = 12 \times 10^5$) for four waves periods (coloured lines). The laminar analytical solution (black line) is plotted as a reference.

laminar solution over two quarters of wavelength. This effect is in good agreement with the observations from Jensen et al. (1989) and the DNS simulations from Spalart and Baldwin (1989) in which the transition starts between $Re = 1.6 \times 10^5$ and $Re = 2.9 \times 10^5$ for the oscillatory flat plate. The turbulence initiation appears upstream the maximum of the horizontal orbital velocity and affects the work of the shear until the horizontal orbital velocity reverses sign. When the Reynolds number increases, the initiation of the turbulent behaviour is shifted downstream. This initiation of turbulence does not seem to occur in the simulations carried out with ICARE and the transition occurs for lower Reynolds numbers ($Re = 0.5 \times 10^5$). The laminar-turbulent transition is indeed very sensitive to the turbulence model

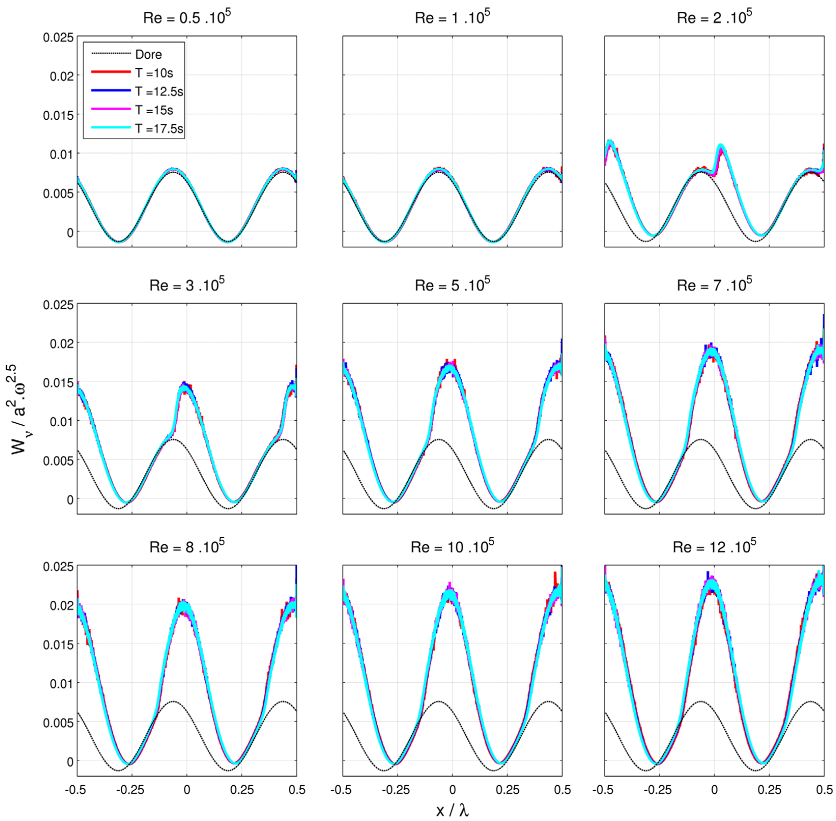

Figure 2.10: Evolution of the normalised work of the wall shear stress at the free surface over the relative position X/λ with the computational code StarCCM+, from laminar ($Re = 0.5 \times 10^5$) to fully developed turbulent cases ($Re = 12 \times 10^5$) for four waves periods (coloured lines). The laminar analytical solution (black line) is plotted as a reference. The wave is propagating along negative x direction.

and different turbulence models are implemented in both codes. But apart from this specific point, the features of the evolution of the work of the wall shear stress are fairly consistent in both computational codes. These dimensionless plots also show the influence at low order of the wave steepness over the properties of the turbulent shear. For a given Reynolds number, and for different steepnesses at each wavelength, the deviation of the work of the shear stress seems negligible. Perignon et al. (2014) investigated the influence of the domain length on the work of the shear stress and a really low sensitivity to the length of the periodic domain has been found.

2.3.2 Parametrisation of dissipation rates in turbulent flows

The mean work of the wall shear stress over the length of the computational domain (i.e. one wavelength λ) normalised by the energy of the wave defines the viscous dissipation coefficient μ according to Equation (2.8). The previous RANS simulations give an estimation of this coefficient for different flow regimes. The ratio between this coefficient and the laminar analytical coefficient μ_{Dore} (Equation (2.9)) is plotted over Reynolds number in Figure 2.11.

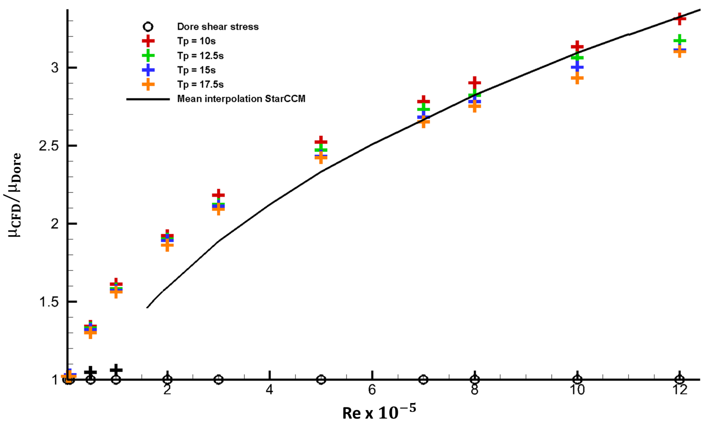

Figure 2.11: Evolution of the viscous dissipation coefficient normalised by the Dore coefficient over the Reynolds number. Coloured cross symbols represent the ICARE simulations while black symbols and black line is the mean interpolation of StarCCM+ simulations.

As mentioned before, one can recover the gap in the initiation of the laminar-turbulent transition between the simulations carried out with ICARE and StarCCM+. The deviation of the RANS laminar coefficients compared to the Dore laminar coefficients shows a slight overestimation of 2% for the case $Re = 0.1 \times 10^5$ with ICARE and 3.8% and 8.4% for cases $Re = 0.5 \times 10^5$ and $Re = 1 \times 10^5$ with StarCCM+. From simulations, where the transition occurs, to fully turbulent simulations, the computed dissipation coefficients deviate from the low Reynolds number laminar asymptote as expected. One can also notice that the higher the Reynolds number is, the larger is the discrepancy between the wave periods, which might be due to the difference in wave steepness.

Even if Ardhuin et al. (2009) supposed that turbulent shear can be responsible for a wave dissipation of order $56\mu_{\mathrm{Dore}}$, the shear stress computed here contributes to a dissipation of $3.5\mu_{\mathrm{Dore}}$. Perignon et al. (2014) showed that the dissipation rate can be approximated by:

$$\mu = \begin{cases} \mu_v & , \mathrm{Re} \leq 1.5 \times 10^5 \\ 1.42\mu_v \left(\frac{\mathrm{Re}}{1.5\times10^5}\right)^{0.41} & , \mathrm{Re} > 1.5 \times 10^5. \end{cases} \tag{2.21}$$

Assuming that the hypotheses considered in this study, i.e. oceanic and atmospheric conditions, are valid, it is obvious that the dissipation related to the turbulent shear stress is not the only mechanism responsible in the dissipation rates observed by Ardhuin et al. (2009).

The description of a fully realistic airflow above swell in the ocean, including the coupling between the turbulent sheared flow in the vicinity of the free surface and an atmospheric circulation was not the point of this first study. Indeed, even light wind conditions involve a coupling mechanism between the wave-induced shear and the wind shear which requires a more detailed analysis in terms of numerical modelling, and theoretical extension of Kudryavtsev and Makin (2004). The following chapters will present another numerical configuration in order to take into consideration the sensitivity of some of these current hypotheses.

2.3.3 Discussion and conclusions

The feedback of the atmospheric sheared viscous layer driven by a monochromatic 1D idealised wave has been investigated with an in-house RANS computational model. To sum up, the idea behind the modification of ICARE from its usual hydrodynamic applications to a new atmospheric application is to develop an effective and evolving tool that would be able to address an increasing complexity of the representation of a part of the ocean-atmosphere physics. Among others, the use of ICARE would allow numerical developments such as the use of realistic water surfaces with irregular sea states, pressure forcing of these sea states, inclusion of a real atmospheric flow (i.e.

wind), tuning of turbulence models..., developments that will not be possible with the use of a commercial code such as StarCCM+.

The properties of the flow under stationary conditions have been studied within a periodic domain along the wave direction. A set of numerical simulations has been carried out for a common range of wave periods and amplitudes. In the same way as the case of an oscillatory boundary layer flow over a flat plate, the study shows a dependence on Reynolds number of this specific wave-induced airflow. Whereas the computed shear work under laminar conditions reveals a weak deviation compared to the Dore analytical expression, a transitional state grows, leading to a fully turbulent boundary layer. The initial stage of the transition based on a critical Reynolds number depends on the turbulence model: StarCCM+ and its low-Reynolds $k-\varepsilon$ model reveals a transitional state around $10^5 < Re < 2 \times 10^5$, while for ICARE and its $k-\omega$ model, this initial stage of transition has not been observed even if a turbulent behaviour of the boundary layer occurs after $Re = 0.5 \times 10^5$. The set of numerical simulations provides a consistent quantification of the increase in work when the turbulence is developing over an increasing fraction of wavelength (in StarCCM+). A parametrisation of this increase is expressed through the viscous dissipation coefficient calculated from the mean work of the shear stress over a wavelength. For the most turbulent case (i.e. $Re = 12 \times 10^5$), the increase reaches less than $3.5\mu_{\mathrm{Dore}}$ which corresponds to a e-folding decay ($1/\mu$) of the order of 20 000 km for an oceanic swell. Ardhuin et al. (2009) determined, from their observations, dissipations of about $56\mu_{\mathrm{Dore}}$. In the model presented here, either the effect of the mean wind has been neglected or thermal effects and roughness effects since smooth idealised periodic waves have been considered. Pressure work has not been investigated either while it seems that any phase shift from the potential theory would greatly influence the work related to the pressure stress. This work is not as easily detectable as the work of the shear stress and the periodic configuration is not able to provide an accurate quantitative estimation of this mechanism (this configuration is similar to a pressure drop in an infinite pipe).

Therefore, to date, other mechanisms involved in the swell dissipation still remain to be investigated. Considering a proper atmospheric circulation and its actual influence on the swell remains a challenge with the current computational tools. If it is currently highly difficult to model a whole atmosphere-ocean coupled system, a focus on the wind-wave interactions is proposed in the next chapters: a coupling between an atmospheric Large-Eddy Simulation (LES) and a spectral code that solves the non-linear evolution of sea states is implemented in order to investigate the impact of the underlying sea state on the marine atmospheric boundary layer.

Résumé du chapitre 3

La prédiction de l'évolution des états de mer due au forçage par le vent nécessite une compréhension fondamentale des mécanismes d'interactions vent-vagues. Le transfert d'énergie influençant l'écoulement atmosphérique turbulent a lieu à travers le travail relatif aux contraintes surfaciques incluant les variations de pression corrélées à la pente de la vague et les variations de contrainte de cisaillement corrélées à la vitesse orbitale. Parallèlement, la dynamique de la vague est affectée par les conditions de vent en entrée principalement à travers le forçage de la pression à la surface de l'eau. On pense généralement que les vagues océaniques ralentissent le vent en surface en agissant comme une traînée, ce qui se manifeste par un transfert de quantité de mouvement descendant: actuellement, les modèles océan-atmosphère permettent seulement un transfert de quantité de mouvement dirigé vers le bas, de l'atmosphère vers l'océan. Des observations récentes (Grachev and Fairall, 2001) ont rapporté que la quantité de mouvement peut aussi être transférée des vagues vers l'atmosphère. Notre compréhension actuelle reste assez parcellaire due à la complexité de la physique.

Ce chapitre présente l'outil numérique qui a été implémenté afin d'étudier les interactions vent-vagues. Dans une première partie, le modèle potentiel de vague est introduit avec le modèle High-Order Spectral. Les conditions de surface libre résolues par HOS permettent de résoudre les interactions non-linéaires et l'évolution des vagues, mais les hypothèses de fluide parfait puis d'écoulement potentiel sont incompatibles avec l'étude d'une couche limite du côté eau, qui sera alors négligée par la suite. En parallèle de la pression qui force l'état de mer, la contrainte tangentielle est responsable de la formation d'une couche cisaillée dans la couche limite atmosphérique marine. Cependant, cette contrainte de cisaillement ne peut pas être transmise au modèle de vague dû à l'hypothèse d'écoulement potentiel dans l'eau. De plus, la dissipation d'énergie en chaleur est très faible pour des ondes de gravité, et pour des vagues de période supérieure à 1.3 s, l'effet de la viscosité de l'air est plus important.

La deuxième partie détaille le modèle numérique de l'écoulement via une modélisation des grandes échelles (LES). L'utilisation de ce code CFD a été rendue possible grâce à un séjour d'un mois au National Center for Atmo-

spheric Research aux Etats-Unis. Peter Sullivan a offert son expertise et son code de simulation (Sullivan et al., 2014) pour ce couplage LES-HOS. Dans un souci de simplification et afin de fournir un premier code pour l'étude du couplage entre le code atmosphérique et le code HOS développé au LHEEA, le domaine atmosphérique est modélisé par des conditions de soufflerie avec une masse d'air considérée comme neutre. C'est une hypothèse majeure de négliger les effets de la stratification atmosphérique et les effets de flottabilité, surtout dans le cas de très faibles vents (Grachev and Fairall, 2001). Cependant, cela constitue un premier pas dans la compréhension numérique des interactions vent-vagues.

La troisième partie introduit le couplage numérique qui a été implémenté entre les deux codes. Ce couplage repose sur une procédure de communication comme illustré dans la Figure 3.5. Le code atmosphérique a besoin de l'élévation de surface libre à chaque pas de temps afin de faire évoluer le maillage au cours du temps, ainsi que de la vitesse orbitale de la vague comme condition limite. Cette vitesse orbitale doit satisfaire la condition de non-flux à la surface libre. De plus, au cours d'un pas de temps temporel (3 sous-pas de temps RK), l'élévation de surface libre est requise au sous-pas de temps futur afin de déterminer la vitesse verticale de déplacement des noeuds du maillage. En retour, l'état de mer évolue, se propageant et grossissant sous le forçage de la pression du vent dans le modèle HOS.

Chapter 3

Modelling of wind-wave interactions

Predicting the evolution of sea states under wind forcing in the ocean through atmosphere-ocean coupled systems requires a fundamental understanding of the mechanisms of wind-wave interaction. The energy transfer influencing the turbulent airflow occurs through the work related to the stresses at the surface involving the variations of the pressure correlated to the wave slope and the variations of the shear stress correlated to the orbital velocity. In the meantime, the wave dynamics is affected by the wind input mainly through the pressure forcing at the water surface. Ocean waves are generally thought to act as a drag on the surface wind with a downward momentum transfer: currently, the ocean-atmosphere models only allow the momentum transfer to be directed from the atmosphere to the ocean. Recent observations during conditions where long wavelength waves propagate faster than the wind have reported that momentum can also be transferred from the waves into the atmosphere. Due to the complexity of the physics, our current understanding remains quite incomplete.

This chapter details the numerical tool that has been implemented to study the wind-wave interactions. In a first part, the potential wave model is introduced with the High-Order Spectral model. The assumptions of perfect fluid and potential flow enable to solve the non-linear interactions and evolution of the waves, but they are not compatible with the study of a boundary layer in the water, which will be neglected thereafter. The tangential shear stress, which is responsible for the formation of a stress layer in the MABL will not be assimilated in the wave model. Moreover, the conversion of mechanical energy to heat is related to the work of the shear stress on the orbital velocity (Ardhuin, 2012): this dissipation is very small for gravity waves, and for waves with periods larger than 1.3 s ($\lambda \approx 2.6$ m), the effect of the air viscosity is more important. The second part details the numerical modelling of the airflow through LES. The use of this CFD code has been made possible by a one-month stay in May 2015 at the National Center for Atmospheric Research in Colorado, USA. Peter Sullivan kindly offered his expertise and his PBL code (Sullivan et al., 2014) for this LES-HOS coupling. With the aim of simplification and in order to provide a first tool to study the two-way coupling between his atmospheric code and the HOS code developed in the LHEEA laboratory, the air domain is considered as a neutral air mass in a wind channel. It is a major assumption to neglect the effects of the atmospheric stratification and the buoyancy, especially in the case of very light winds (Grachev and Fairall, 2001). However, considering independently the effects of the waves and the atmospheric stratification constitutes a first step in the numerical understanding of the wind-wave interactions. The third section introduces the numerical coupling that has been implemented between the HOS wave model and the LES atmospheric code.

3.1 Wave model

3.1.1 Principle and formulation

We describe here the assumptions underpinning the usual models of wave propagation. A closed wave tank or the open sea is represented by a fluid domain D. The coordinates system is expressed in Figure 3.1:

The fluid considered here is water and is assumed to be incompressible and inviscid. The flow is also considered as irrotational. Under these assumptions, the potential flow theory can be applied and the velocity $\mathbf{U}$ derives from a potential ϕ such as:

$$\mathbf{U}(\mathbf{x}, z, t) = \nabla\phi(\mathbf{x}, z, t)\,. \tag{3.1}$$

The continuity equation then becomes the Laplace equation:

$$\Delta\phi = 0 \qquad \text{in } D. \tag{3.2}$$

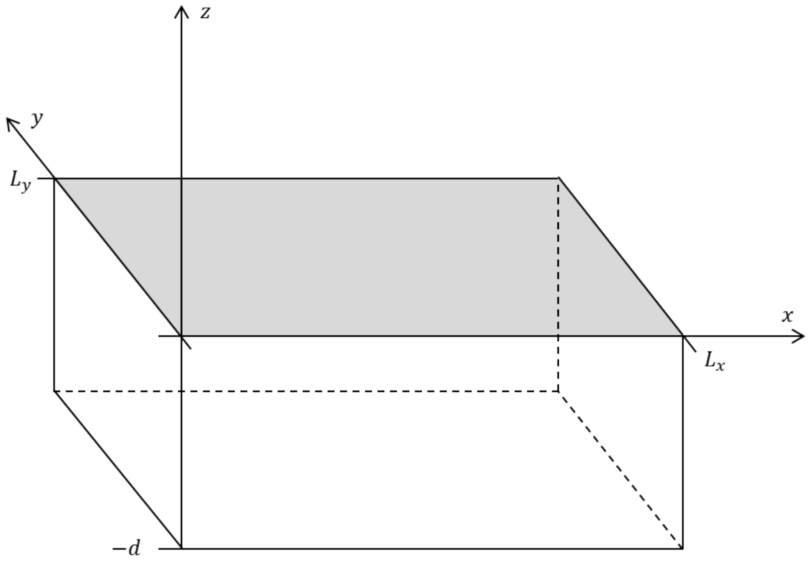

Figure 3.1: Sketch representing the numerical domain of the model. The grey surface represents the free surface of the domain.

The momentum equation can be written as the non-stationary version of Bernoulli equation:

$$\frac{P}{\rho_w} + \frac{\partial \phi}{\partial t} + gz + \frac{1}{2}\left|\nabla\phi\right|^2 = c(t) \qquad \text{in } D, \tag{3.3}$$

with $c(t)$ a time-dependent constant called the Bernoulli constant. This constant is usually set to the atmospheric pressure (i.e. the superficial stress is neglected). $\nabla\phi$ is the horizontal gradient.

At the free surface $z = h(\mathbf{x}, t)$, this equation yields:

$$\frac{P_{atm}}{\rho_w} + \frac{\partial \phi}{\partial t} + gh + \frac{1}{2}\left|\nabla\phi\right|^2 = \overline{P}_{atm} \qquad \text{at } z = h(\mathbf{x}, t), \tag{3.4}$$

with the decomposition of the atmospheric pressure such as $P_{atm} = \overline{P}_{atm} + p'_{atm}$.

The dynamic free surface boundary condition comes from this pressure continuity equation supposing that the free surface represents a univalent function (i.e. no wave breaking):

$$\frac{\partial \phi}{\partial t} = -gh - \frac{1}{2}\left|\nabla\phi\right|^2 - \frac{p'_{atm}}{\rho_w} \qquad \text{at } z = h(\mathbf{x}, t). \tag{3.5}$$

The fluctuating atmospheric pressure term is usually set to zero. It will be of key importance for the further development of the coupling between the wave model and the LES atmospheric model.

On the other hand, expressing the fact that the free surface is a material surface, the kinematic free surface boundary condition gives:

$$\frac{\partial h}{\partial t} = -\frac{\partial \phi}{\partial z} - \nabla\phi \cdot \nabla h \qquad \text{at } z = h\left(\mathbf{x}, t\right). \tag{3.6}$$

This system of equations (3.5) and (3.6) constitutes the system to be solved for the free-surface conditions. Two kinds of problems arise in the numerical treatment of the free surface boundary conditions (Ferrant, 2013):

- first of all, free-surface conditions have to be verified at a moving boundary, the location of which is unknown and part of the solution: these are the non-linearities of position;

- moreover, free-surface conditions are non-linear partial differential equations: these are the non-linearities of structure.

The boundary conditions express the conditions at the boundaries of the domain. In our specific case of the study of wind-wave interactions, we consider an open ocean with:

- a flat bottom:
$$\frac{\partial \phi}{\partial z}\left(\mathbf{x}, z = -d, t\right) = 0, \tag{3.7}$$

- periodic boundaries in x and y:

$$\begin{cases} \phi\left(x = 0, y, z, t\right) & = \phi\left(x = L_x, y, z, t\right) \\ \phi\left(x, y = 0, z, t\right) & = \phi\left(x, y = L_y, z, t\right) \\ h\left(x = 0, y, z, t\right) & = h\left(x = L_x, y, z, t\right) \\ h\left(x, y = 0, z, t\right) & = h\left(x, y = L_y, z, t\right). \end{cases} \tag{3.8}$$

3.1.2 High-Order Spectral method

The fundamental principle of resolution by spectral methods is that a numerical solution f is expressed as a finite expansion of some set of basis functions, ψ_i, such as:

$$f(x) = \sum_i a_i \psi_i(x) \,. \tag{3.9}$$

Periodic and non-periodic problems are respectively dealt with trigonometric and algebraic polynomials. Some of the methods commonly used in the literature are the Fourier collocation methods for periodic domains and the Jacobi polynomials for non-periodic domains, with the Chebyshev and Legendre polynomials as special cases. In the specific case of sea state propagation in the open ocean, the potential velocity and the free surface elevation can be written using Fourier series:

$$\begin{aligned} \phi(\mathbf{x}, z, t) &= \sum_{i=-\infty}^{+\infty} \sum_{j=-\infty}^{+\infty} a_{ij}^{\phi}(t) \exp(i\mathbf{k}_{ij} \cdot \mathbf{x}) \frac{\cosh(|\mathbf{k}_{ij}|(z+d))}{\cosh|\mathbf{k}_{ij}|h} \\ h(\mathbf{x}, z, t) &= \sum_{i=-\infty}^{+\infty} \sum_{j=-\infty}^{+\infty} a_{ij}^{h}(t) \exp(i\mathbf{k}_{ij} \cdot \mathbf{x}) \end{aligned} \tag{3.10}$$

where d is the water depth. $\mathbf{k}_{ij} = k_i\mathbf{i} + k_j\mathbf{j}$ with $k_i = 2i\pi/L_x$ and $k_j = 2i\pi/L_y$ are the wavenumbers associated with the (i, j) mode. a_{ij}^{ϕ} and a_{ij}^{h} are the modal amplitudes of the velocity potential and the wave elevation and they are the unknowns of the system of equations. Several methods can be implemented depending on the ratio between the numbers of collocation nodes (i.e. the spatial discretisation of the domain) and the numbers of selected modes (i.e. the truncation of the series of basis functions, N_x and N_y in x and y-directions). Whatever the method used, spectral methods are quite fast compared to approaches such as Boundary Element Methods for example. Moreover, the basis functions used here are orthogonal exponential functions, allowing the use of Fast Fourier Transform (FFT) algorithms, but requiring a constant spatial discretisation. Whereas a direct inversion between the physical and modal spaces requires a CPU time of the order $O(N^2)$ where $N = N_x N_y$, an inversion using FFTs has a reasonable CPU cost of $O(N \log N)$. FFT is thus a computationally efficient method with really good convergence properties.

Concerning the accuracy of the numerical solution, dissipative and dispersive errors can be numerically limited as the physical space is discretised by means of a sum of elementary functions. Theoretically, the precision then only depends on the order of truncation of the series. With pseudo-spectral methods, very high accuracy can be obtained on the collocation nodes of the domain as explained further below. Le Touzé (2003) reviewed the various spectral approaches used in the field of naval hydrodynamics. One method has been retained here, the High-Order Spectral method for irregular waves.

The High-Order Spectral (HOS) method was initially developed by West et al. (1987) and Dommermuth and Yue (1987). Its development has been the basis of successive PhD theses in the Laboratory of Fluid Mechanics (LMF) at Ecole Centrale de Nantes (ECN). The model has been evolving with the implementation of lateral tank walls, a potential modelling a real wave maker (Le Touzé, 2003 and Bonnefoy, 2005), modelling sea states in the open ocean (Ducrozet, 2007) and more recently a variable bathymetry (Gouin et al., 2016).

The basis of this model is the formulation in surface quantities of the free-surface conditions (Equations (3.5) and (3.6)) based on the spectral model developed by Zakharov (1968). In the HOS model, the free-surface conditions are written with h and the free surface potential ϕ^S defined as:

$$\phi^S(\mathbf{x}, t) = \phi(\mathbf{x}, z = h(\mathbf{x}, t), t). \tag{3.11}$$

This leads to new free-surface conditions:

$$\frac{\partial \phi^S}{\partial t} = -gh - \frac{1}{2}\left|\vec{\nabla}\phi^S\right|^2 + \frac{1}{2}\left(1 + \left|\vec{\nabla}h\right|^2\right) W^2 - \frac{p'_{atm}}{\rho_w} \qquad \text{at } z = h(\mathbf{x}, t) \tag{3.12}$$

and

$$\frac{\partial h}{\partial t} = \left(1 + \left|\vec{\nabla}h\right|^2\right) W - \nabla\phi \cdot \nabla h \qquad \text{at } z = h(\mathbf{x}, t) \tag{3.13}$$

with the vertical velocity W such as:

$$W(\mathbf{x}, t) = \frac{\partial \phi}{\partial z}(\mathbf{x}, z = h(\mathbf{x}, t), t). \tag{3.14}$$

The free surface elevation and the free surface potential are advanced in time through a time-integration scheme of order 4 (Runge Kutta - RK4) with an adaptive step size control. The quantity that remains unknown is the vertical velocity W. It should be noted that W is a bulk quantity. This quantity is evaluated through a high-order iterative process, i.e. the HOS model.

The first step consists in decomposing in power series the potential ϕ:

$$\phi\left(\mathbf{x}, z, t\right) = \sum_{m=1}^{+\infty} \phi^{(m)}\left(\mathbf{x}, z, t\right). \tag{3.15}$$

This sum is truncated at a finite value, M the order of non-linearity, i.e. the HOS order. Each potential $\phi^{(m)}$ is expanded in a Taylor series with respect to the mean water level $z = 0$, yielding a triangular set of Dirichlet problems that can be solved by means of a spectral method:

$$\phi^S\left(\mathbf{x}, t\right) = \sum_{m=1}^{M} \sum_{n=0}^{M-m} \frac{h^n}{n!} \frac{\partial^n \phi^{(m)}}{\partial z^n}\left(\mathbf{x}, z = 0, t\right). \tag{3.16}$$

The vertical velocity can then be reconstructed:

$$\frac{\partial \phi}{\partial z}\left(\mathbf{x}, z = h, t\right) = W\left(\mathbf{x}, t\right) = \sum_{m=1}^{M} \sum_{k=0}^{m-1} \frac{h^k}{k!} \frac{\partial^{k+1} \phi^{(m-k)}}{\partial z^{k+1}}\left(\mathbf{x}, z = 0, t\right). \tag{3.17}$$

Eventually the system of equations (3.12) and (3.13) can be marched in time. The method is numerically interesting with the use of FFTs which makes the computation very efficient.

3.1.3 Initialisation of the wave fields

The aforementioned model only solves the evolution of sea states whose initial conditions still remain to be defined. This essential aspect is detailed in this section. A non-linear regular wave will be initialised with the Rienecker&Fenton method, whereas an irregular sea state will be initialised as a linear superimposition of spectral components based for instance here on the JONSWAP spectrum.

3.1.3.1 Nonlinear monochromatic wave: the Rienecker and Fenton method

Rienecker and Fenton (1981) presented a method for solving non-linear water wave problems. They proposed a spectral solution to calculate the non-linear profile of the regular wave of any wave steepness. In the frame of reference of the wave, the wave has a stationary profile. From the Airy solution (i.e. the first-order Stokes wave), successive estimations are obtained with the Newton's iterative method. The potential is expressed through a direct spectral development, but unlike Equation (3.10), a stream function is used. The system unknowns are then the modal amplitudes of the stream function and the free surface elevation at the collocation nodes. The system of equations includes, besides the non-linear free-surface conditions and Laplace equation, additional equations such as the wave steepness specification or the conservation of the volume. Indeed, the wave frequency is considered as an additional unknown as its non-linear solution is different from its starting linear estimation: from the third order of the Stokes wave, the wave period is modified. More details about the numerical implementation of this method can be found in Ferrant (1996).

This approach is convenient to implement as it provides a solution for a wide range of amplitudes, wavelengths (in the limit of wave breaking) and depth (in the limit of the soliton). Figure 3.2 shows wave profiles of various wave steepness until $ak_{\text{max}} = 44.14\%$ which is very close to the Stokes limit $ak_{\text{max}} = 44.35\%$.

The quality of the generated waves only depends on the order of truncation of the series: 16 modes are usually enough to reach an accuracy of the order of the machine epsilon. For large wave steepness, more modes are needed in order to get a good accuracy. The wave steepness $ak_{\text{max}} = 44.14\%$ has been obtained with 64 modes.

The Rienecker & Fenton model enables the generation of a non-linear monochromatic wave for a large range of amplitudes, wavelengths and water depths.

3.1.3.2 Irregular wave: the JONSWAP spectrum

The initial sea state can be defined by a directional wave spectrum Φ such as:

$$\Phi\left(\omega,\theta\right) = \psi\left(\omega\right) \times G\left(\theta\right) \tag{3.18}$$

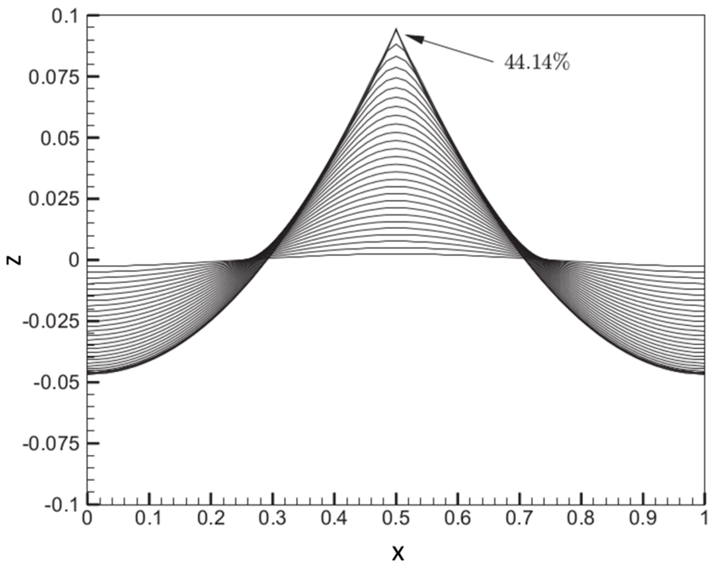

Figure 3.2: Wave profiles with successive wave steepnesses with the Rienecker & Fenton method until $ak_{\max} = 44.14\%$.

where the JONSWAP spectrum is defined as:

$$\psi(\omega) = \frac{\alpha g^2}{\omega^5} \exp\left(-\frac{5}{4}\left(\frac{\omega_p}{\omega}\right)^4\right)\gamma^r \tag{3.19}$$

with $r = \exp\left(-\frac{(\omega-\omega_p)^2}{2\sigma^2\omega_p^2}\right)$. ω_p is the angular frequency at the peak of the spectrum. The JONSWAP spectrum is defined as:

$$\alpha = 3.279E, \qquad \gamma = 3.3, \qquad \sigma = \begin{cases} 0.07 & \omega < 1 \\ 0.09 & \omega \geq 1 \end{cases}$$

with E the dimensionless energy density of the wave field. The significant wave height can be estimated by $H_s \approx 4\sqrt{E}$. For the North Sea, the usual set of parameters can be chosen as $E_{\min} = 0.0005$ and $E_{\max} = 0.005$. The JONSWAP spectrum is a Pierson-Moskowitz spectrum multiplied by an extra peak enhancement factor γ^r. Indeed, Hasselmann et al. (1973) found that the wave spectrum is never fully developed. It continues to develop through non-linear wave-wave interactions even for very long times and distances.

The directionality function can be defined by:

$$G(\theta) = \begin{cases} A_n \cos^n \theta & |\theta| \leq \dfrac{\pi}{2} \\ 0 & |\theta| > \dfrac{\pi}{2} \end{cases} \tag{3.20}$$

with θ the wave direction and

$$A_n = \begin{cases} \dfrac{(2^p!)^2}{\pi(2p)!} & \text{if } n = 2p \\ \dfrac{(2p+1)!}{2(2^p p!)^2} & \text{if } n = 2p+1. \end{cases} \tag{3.21}$$

The free surface elevation is related to the wave spectrum through the following expression on the modal amplitude:

$$\frac{1}{2}|a_{ij}^h|^2 = \Phi\left(\omega, \theta\right) \Delta k_x \Delta k_y \tag{3.22}$$

with $\Delta k_x = 2\pi/L_x$. $|a_{ij}^h(t = 0)|$ is calculated since the initial JONSWAP wave spectrum is imposed, and for any (i, j) the phases are randomly selected in $[0, 2\pi]$. The initial wave field is then built with inverse Fourier transforms.

This initialisation process corresponds to a superposition of linear components. Dommermuth (2000) demonstrated that initialising a fully non-linear computation with a linear initial wave field leads to numerical instabilities in the sea state that evolve during a transitional period (5-10 peak periods), transforming the initial stationary waves into progressive waves due to the non-linearities. He introduced a relaxation scheme allowing the use of such linear initial conditions during a transitional time period T_a:

$$\frac{\partial \phi^S}{\partial t} + gh = F\left(1 - \exp(-(t/T_a)^n)\right) \tag{3.23}$$

and

$$\frac{\partial h}{\partial t} - W^{(1)} = G\left(1 - \exp(-(t/T_a)^n)\right) \tag{3.24}$$

where F and G stand for the non-linear parts of equations 3.12 and 3.13. T_a is usually set to 10 T_p and $n = 4$.

3.2 Airflow modelling: air flowing in a wind tunnel

Large-eddy simulation (LES) represents a good compromise between DNS and RANS simulations. LES is a popular technique based on the fact that the contribution of large scales of turbulence in the process of energy and momentum transfers is directly calculated. The effect of the small scales of turbulence is, however, modelled. A LES simulation is therefore three-dimensional, non-stationary and costly in terms of CPU resources. There is an increased precision in LES compared to the RANS approach since LES attempts to provide more detailed information about non-stationary features of a flow by describing existing detached eddies, non-stationary forces, noise sources... LES is usually applied in a wide variety of engineering applications including combustion, acoustics, and simulations of the atmospheric boundary layers. Large-scale parallel computing has permitted LES simulations of turbulent planetary boundary layers (PBL) coupling small and large scales in realistic outdoor environments, for example, atmosphere-land interactions (Patton et al., 2005), boundary layers with surface water wave effects (Sullivan et al., 2014) and tropical boundary layers beneath deep convection (Moeng et al., 2009).

The principal idea behind LES is to reduce the computational cost of DNS by modelling the smallest length scales via a low-pass filtering of the Navier-Stokes equations. The large eddies of the flow are considered to be dependent on the geometry while the smaller scales tends to be more isotropic and homogeneous than the large ones. Thus modelling the subgrid-scale (SGS) motions is easier than modelling all scales within a single model as in the RANS approach. Therefore, large eddies will explicitly be solved, whereas the small eddies will implicitly be accounted through a SGS model. Mathematically, this corresponds to a separation of the quantities of interest into a resolved part and a subgrid part. This section presents the governing equations for a dry PBL under the Boussinesq approximation (Sullivan et al., 2014). The numerical code developed by Sullivan et al. (2014) has numerous applications, but requires large computational resources. With the aim of simplification and in order to provide a first tool to study the two-way coupling between the atmospheric code and a code of sea state propagation, a neutral atmosphere has been considered in a first approach. The general equations are presented in order to offer a broader perspective for the future work on this thematic, but a major simplification lies in the fact that the air domain will be considered as a neutral air mass in a wind channel, meaning no buoyancy effect and a wall-type boundary condition at the top of the domain.

3.2.1 Governing equations

The set of spatially filtered LES equations applicable to a turbulent flow in the atmospheric boundary layer under the Boussinesq equations is given below. The Cartesian velocity components are denoted by $u_i = (u, v, w)$ and θ_v is the virtual potential temperature. p^* is the fluctuating pressure normalised by the air density and deviating from the hydrostatic state $\partial\bar{p}/\partial z = -\bar{\rho}g$.

Considering an incompressible fluid of density ρ, the continuity equation is:

$$\frac{\partial u_i}{\partial x_i} = 0, \tag{3.25}$$

and the momentum equation:

$$\frac{\partial u_i}{\partial t} + \frac{\partial u_j u_i}{\partial x_j} = -\frac{\partial p^*}{\partial x_i} - 2\epsilon_{ijk}\Omega_j u_k + \delta_{i3}\beta_b\left(\theta_v - \theta_0\right) - \frac{\partial \mathcal{P}}{\partial x_i} - \frac{\partial \tau_{ij}}{\partial x_j}, \tag{3.26}$$

where the buoyancy parameter is $\beta_b = g/\theta_0$ with θ_0 the reference virtual potential temperature. The large-scale external pressure gradients normalised by the density, $\partial\mathcal{P}/\partial x_i$, drive the boundary layer winds. τ_{ij} represents the SGS momentum flux and its modelling is addressed in the following section.

Comparing this equation to Equation (1.1), we focus on the vertical component of the momentum to study the role of gravity, pressure and density:

$$\frac{Dw}{Dt} = -g - \frac{1}{\rho}\frac{\partial P}{\partial z} + \frac{\partial \tau_{3j}}{\partial x_j} \tag{3.27}$$

with Dw/Dt the total derivative of the vertical velocity. The density and pressure variables are decomposed into a mean part and a fluctuating part (i.e., $\rho = \bar{\rho} + \rho'$ and $P = \bar{p} + p'$) leading to:

$$\left(1 + \frac{\rho'}{\bar{\rho}}\right)\frac{Dw}{Dt} = -\frac{\rho'}{\bar{\rho}} - \frac{1}{\bar{\rho}}\frac{\partial p'}{\partial z} - \frac{1}{\bar{\rho}}\left[\frac{\partial \bar{p}}{\partial z} + \bar{\rho}g\right] + \frac{\partial \tau_{3j}}{\partial x_j}. \tag{3.28}$$

Considering that the air is in hydrostatic equilibrium, the term in square brackets is zero. Moreover $(1 + \rho'/\bar{\rho}) \approx 1$ since $\rho'/\bar{\rho}$ is of the order of -3.33×10^{-3} (this comes from the linearised perturbation ideal gas law where the pressure term is neglected under the shallow convection approximation (Stull, 1988)). The process of neglecting the density variations in the inertia (i.e. storage) term but retaining it in the buoyancy (i.e. gravity) term is called the Boussinesq approximation:

$$\frac{Dw}{Dt} = -\frac{\rho'}{\bar{\rho}} g - \frac{1}{\bar{\rho}} \frac{\partial p'}{\partial z} + \frac{\partial \tau_{3j}}{\partial x_j}. \tag{3.29}$$

and the buoyancy term is rewritten as $g/\theta_0 \, (\theta_v - \theta_0)$.

A transport equation on the temperature variable θ_v is implemented in the original model (Sullivan et al., 2014), but as we consider a neutral atmosphere in a first approach, the temperature variation is thus constant and the terms based on it are neglected in the momentum equation (i.e. no buoyancy term). An explanation for considering neutral atmospheric conditions lies in the fact that this thesis focuses on the processes occurring inside the thin wave boundary layer. In this context, we made an assumption concerning density stratification and Coriolis effects. In the first chapter, the bibliographical study has shown that both the atmospheric stratification and the waves have an impact on the MABL. However, considering independently these effects constitutes a first step in the understanding of such phenomena: only the wave effects will be modelled, and the effects of the temperature variations and the Coriolis force will be deactivated in the numerical model in a first stage.

3.2.2 Subgrid-scale turbulence modelling

In order to close the system of Equations (3.25) and (3.26), the SGS momentum flux τ_{ij} requires modelling in the flow and at the lower boundary. A Deardorff turbulent kinetic energy (TKE) subgrid-scale (SGS) is implemented with e the SGS energy (Moeng, 1984):

$$\frac{\partial e}{\partial t} + \frac{\partial u_i e}{\partial x_i} = -\tau_{ij} S_{ij} + \beta \tau_{3\theta} + \frac{\partial}{\partial x_j} \left(2\nu_t \frac{\partial e}{\partial x_j} \right) - \varepsilon, \tag{3.30}$$

where the time evolution of e and its advection by the resolved field depend on the shear production (with the resolved scale strain rate $S_{ij} = 1/2(\partial u_i/\partial x_j + \partial u_j/\partial x_i)$), the SGS buoyant production that will be neglected here since we consider neutral atmospheric conditions, turbulent diffusion with ν_t the subgrid-scale turbulent viscosity, and viscous dissipation ε.

The SGS turbulence model employs the Boussinesq hypothesis to parametrise the SGS momentum flux:

$$\tau_{ij} = -2\nu_t S_{ij}, \tag{3.31}$$

with the subgrid-scale turbulent viscosity $\nu_t = C_k \Delta \sqrt{e}$ and the Lilly-Kolmogorov model for the viscous dissipation:

$$\varepsilon = C_\varepsilon \frac{e^{3/2}}{\Delta}. \tag{3.32}$$

The constant C_ε is set to 0.1 (Moeng, 1984) and the filter length scale Δ is computed from the averaging cell volume. To reduce the reliance on the SGS model, a fine resolution is used near the surface. More information about the SGS model can be found in Sullivan et al. (2014). We note that the "real" viscosity of the fluid is neglected in the governing equations since high-Reynolds situations will be considered and the effects of viscosity will be modelled through the SGS turbulent viscosity.

3.2.3 Terrain-following coordinate system

The investigation of the wave boundary layer turbulence is essential to the comprehensive understanding of its impact on the mean wind profile and the estimation of sea-state dependent drag coefficients in parametrisation models. Indeed, Hara and Sullivan (2015) noted that the wind stress may deviate significantly from the bulk parametrisation when the wave field is not in equilibrium with local wind forcing and requires a sea-state dependent parametrisation with concurrent predictions of surface wave fields. Nevertheless, turbulence observations are difficult to carry out very close to moving water surfaces. Moreover, some definitions such as the definition of the wave-induced stress in terms of wave-correlated velocity components (Makin and Kudryavtsev, 1999), break down below the level of the wave crests. Hence numerical studies such as DNS and LES may be of interest because computations can then be carried out in a surface-following coordinate system over wavy surfaces. Through a coupled model formulated in a wave-following coordinate system, Chalikov and Rainchik (2011) showed that the momentum flux due to pressure acting on sloped surfaces becomes important very close to the free surface.

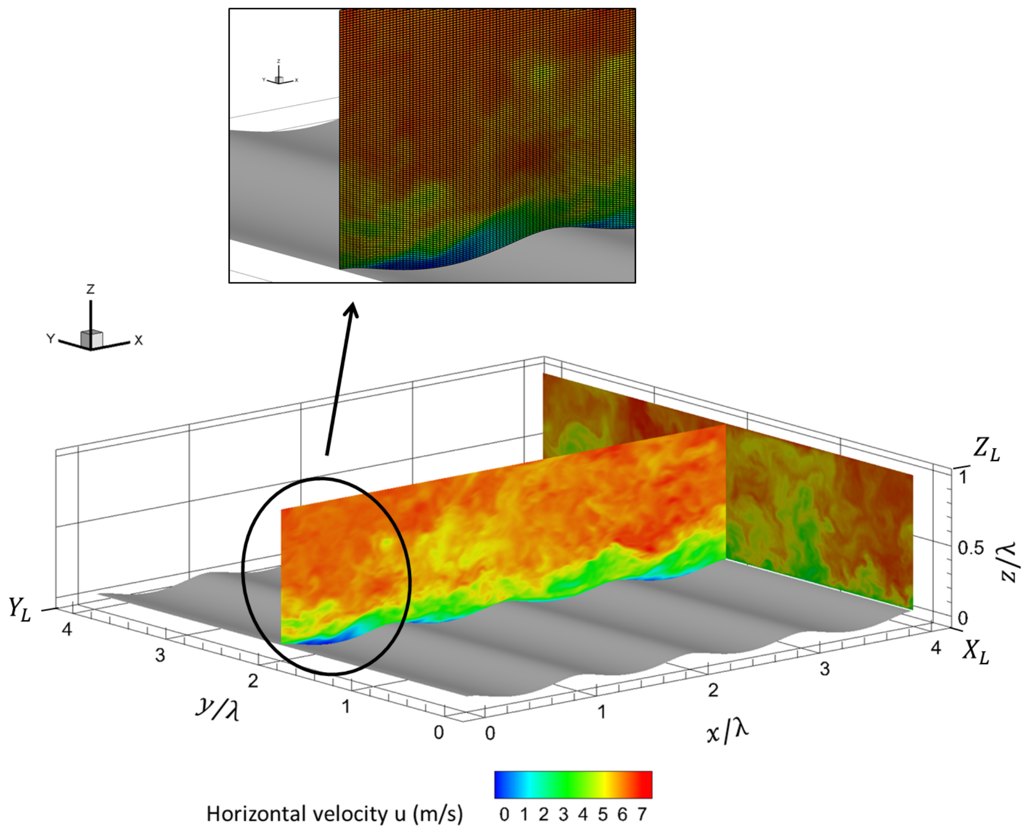

Figure 3.3: Illustration of wind turbulence over a linear monochromatic wave. Contours of instantaneous streamwise velocity u are plotted on two representative (x, z) and (y, z)-planes.

The air domain is illustrated in Figure 3.3. The coordinates are denoted as $x_{i\in\{1,2,3\}} = (x, y, z)$ where x and y are the horizontal coordinates and z is the vertical coordinate with $z = 0$ being the mean sea surface. A transformation is applied to the physical space coordinates in order to get a surface following, non-orthogonal and time varying mesh defined by a flat computational system $\xi_{i\in\{1,2,3\}} = (\xi, \eta, \zeta)$. Any three-dimensional time-dependent lower boundary with a shape $h(x, y, t)$ can thus be mapped applying the following mesh transformation:

$$\begin{cases} \tau = t, \\ \xi = \xi(x) = x, \\ \eta = \eta(y) = y, \\ \zeta = \zeta(t, x, y, z). \end{cases} \tag{3.33}$$

The vertical gridlines translate vertically following the time-dependent elevation $h(x, y, t)$ of the surface and are defined for any (x, y) location and any time by:

$$z = \zeta + h(x, y, t)\left(1 - \frac{\zeta}{Z_L}\right)^3 \tag{3.34}$$

with Z_L the height of the computational domain. With this prescription, the grid cells near the surface are squeezed (stretched) at the wave crests (troughs) by approximately 20%. At the top of the domain, the horizontal gridlines are completely flat. Figure 3.3 illustrates this surface-following mesh for a linear wave of wavelength $\lambda = 0.23$ m and wave steepness $ak = 0.2$.

The equations governing the airflow have been presented previously. These equations are expressed in the physical space, but one needs to be aware that the complete set of LES equations is actually expressed in terms of computational curvilinear coordinates under the time-dependent surface-following transformation in (3.33). The transformation is based on differentiation of compositions of functions using the chain rule. The differential metrics $\partial\xi_i/\partial x_j$ are connected to $\partial x_i/\partial\xi_j$ through the mapping transformation in (3.33):

$$\begin{cases} \zeta_t = -z_t \mathcal{J}, \\ \xi_x = \eta_y = 1, \\ \zeta_x = -z_\xi \mathcal{J}, \\ \zeta_y = -z_\eta \mathcal{J}, \\ \zeta_z = 1/z_\zeta = \mathcal{J}, \end{cases} \tag{3.35}$$

with $\mathcal{J}$ the Jacobian of the transformation. $z_t = \partial z/\partial t$ represents the grid speed, i.e. the vertical velocity of individual grid points. The metric identity (Anderson et al., 1984) is also frequently invoked:

$$\frac{\partial}{\partial\xi_j}\left(\frac{1}{\mathcal{J}}\frac{\partial\xi_j}{\partial x_i}\right) = 0. \tag{3.36}$$

3.2.4 Numerical method

3.2.4.1 Geometric conservation law

The critical importance of mesh adaptation in the numerical solution of partial differential equations is related to the difficulties with global conservation and with computation of the local volume element under time-dependent mappings that result from the boundary motion. A differential geometric conservation law is introduced and must be satisfied by the numerical discretisation so that the numerical scheme is conservative (Thomas and Lombard, 1979). This law derives from the incompressible continuity equation, and for our boundary-conforming mapping, it reduces to:

$$\frac{\partial}{\partial t}\left(\frac{1}{\mathcal{J}}\right) + \frac{\partial z_t}{\partial \zeta} = 0. \tag{3.37}$$

The GCL is automatically solved along with the flow conservation laws using conservative difference operators.

3.2.4.2 LES equations in the surface-following coordinates system

The complete set of LES equations in computational coordinates is then (Sullivan et al., 2014):

$$\begin{aligned}
\frac{\partial U_i}{\partial \xi_i} &= 0 && \text{the continuity equation,}\\
\frac{\partial}{\partial t}\left(\frac{1}{\mathcal{J}}\right) + \frac{\partial z_t}{\partial \zeta} &= 0 && \text{the geometric conservation law,}\\
\frac{\partial}{\partial t}\left(\frac{u_i}{\mathcal{J}}\right) + \frac{\partial}{\partial \xi_j}\Big((U_j - \delta_{3j} z_t) u_i\Big) &= \frac{\mathcal{F}_i}{\mathcal{J}} && \text{the momentum transport equation,}\\
\frac{\partial}{\partial t}\left(\frac{e}{\mathcal{J}}\right) + \frac{\partial}{\partial \xi_j}\Big((U_j - \delta_{3j} z_t) e\Big) &= \frac{\mathcal{R}_i}{\mathcal{J}} && \text{the SGS energy transport equation,}\\
\frac{\partial}{\partial \xi_i}\left(\frac{1}{\mathcal{J}} \frac{\partial \xi_i}{\partial x_j} \frac{\partial \xi_m}{\partial x_j} \frac{\partial p^*}{\partial \xi_m}\right) &= \mathcal{S} && \text{the pressure Poisson equation.}
\end{aligned} \tag{3.38}$$

The pressure equation represents the core of the numerical scheme. This Poisson equation results from the divergence-free flow modelled here. It comes from the combination of the continuity equation and the time-stepping scheme detailed in the further section. An iterative method is implemented in order to solve the pressure equation. More details can be found in Sullivan et al. (2014).

3.2.4.3 Spatial discretisation and time integration

The variable layout uses a collocated arrangement at the cell centres for the variables (u_i, p^*, e) in the computational mesh as specified in Figure 3.4. Collocated grids are more suitable for the implementation of general geome-

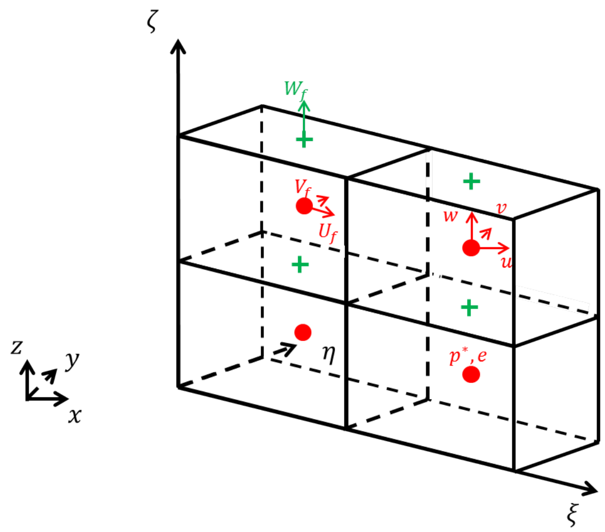

Figure 3.4: 3D sketch illustrating the layout of the cell-centred variables, the Cartesian velocity components (u, v, w) with the pressure p^* and the SGS energy e. The contravariant flux velocities U and V are cell-centred whereas W is located at a cell face.

tries and they result in a compact differencing stencil. But their use requires the enhancement of the pressure-velocity coupling. The contravariant flux velocity $\mathbf{U}_f = (U_f, V_f, W_f)$ is introduced in the momentum and SGS energy transport equations: advective terms are compactly written in strong-flux conservation form using U_i defined by:

$$U_{f_i} = \frac{u_j}{\mathcal{J}} \frac{\partial \xi_i}{\partial x_j}. \tag{3.39}$$

U_{f_i} components are normal to a surface of constant ξ_i as shown in Figure 3.4, and U_f, V_f are located at cell centres whereas W_f is located at cell faces.

This configuration tends to a staggered storage which prevents odd-even decoupling between the pressure and velocity.

The horizontal spatial derivatives in (ξ, η) computational coordinates are estimated using pseudo-spectral approximations. Vertical derivatives are discretised with centred second-order finite-difference schemes.

Concerning the time advancement, it is based on a fully explicit third-order Runge-Kutta scheme, with α_n and β_n the associated weights. This scheme uses a dynamic time stepping with a fixed Courant-Friedrichs-Lewy (CFL) number. It makes use of a fractional step method in order to enforce the incompressibility constraint: the scheme fully recognises at which point in the time integration the pressure is solved. The general rule for marching in time a cell-centred velocity variable from an old time level $(n-1)$ to a new time level (n) over a time step Δt is:

$$\left.\frac{u_i}{\mathcal{J}}\right|^{n} = \left.\frac{\hat{u}_i}{\mathcal{J}}\right|^{n-1} - \Delta t \alpha_n \frac{\partial}{\partial \xi_j} \left.\left(\frac{p^*}{\mathcal{J}} \frac{\partial \xi_j}{\partial x_i}\right)\right|^{n} \tag{3.40}$$

where the intermediate velocity $\hat{u}_i/\mathcal{J}$ at current time level $(n-1)$ is the discrete sum of the current velocity and the full right-hand-side of the momentum equation from the previous stage $(n-2)$ weighted by $\Delta t \alpha_n$ and the partial right-hand-side (i.e. minus the pressure contribution) from the current time $(n-1)$ weighted by $\Delta \beta_n$. More information about this time integration process can be found in Sullivan et al. (2014).

3.2.5 Wave propagating in a wind tunnel

This section presents the intrinsic methods implemented in the original atmospheric model in order to define a wave field that will be considered as the lower boundary of the air domain. To complete the LES model, wave information is prescribed at the bottom of the LES domain. Three information are needed:

- the wave height $h(x, y, t)$ and its spatial derivatives in order to prescribe the mesh deformation;
- the wave orbital velocities u_{orbital} and v_{orbital} which will impose the kinematics at the lower boundary;

– the time derivative h_t, i.e. the vertical boundary speed, which will be used to determine how rapidly the grid nodes in the mesh move to their new locations.

In the original LES code (i.e. before the development of the two-way coupling), the description of a surface wave field can be obtained by two ways. Firstly, the wave field can be built based on typical empirical fits of measured two-dimensional wave spectra:

$$E(k, \omega) = S(k)D(k, \theta) \tag{3.41}$$

where the amplitude $S(k)$ and directional $D(k, \theta)$ spectra depend on the magnitude of the wavenumber $k = |\mathbf{k}|$ and wave direction θ. The Pierson-Moskowitz spectrum and Donelan spectrum are implemented: these spectra are similar to the JONSWAP spectrum (Equation (3.19)) and they depend on bulk environmental parameters such as the reference average wind U_{10} at 10 m above the free surface, the phase speed at the peak of the spectrum C_p, the wave age C_p/U_{10} and the mean direction of wave propagation. The wave elevation, its orbital velocity, and time and spatial derivatives are constructed in physical space using two-dimensional FFTs to compute future values of the wave field, which are needed to construct the moving mesh and the surface boundary conditions. This leads to a wave field $h(x, y, t)$ constructed as a sum of linear waves:

$$h(\mathbf{x}, t) = \sum_k a(k) \exp\left(i\left(\mathbf{k} \cdot \mathbf{x} - \omega(k)t + \varphi\right)\right) \tag{3.42}$$

where each wave is characterised by its amplitude $a(k)$ such as

$$a^2(k) = S(k)D(k, \theta)dk_x dk_x,$$

its wave number k and its frequency $\omega(k)$, related through the linear dispersion relation $k = \omega(k)^2/g$, and a random phase φ.

Another way to obtain a surface wave field comes from wave tank experiments. In this case, a file with wave elevation and orbital velocities is read at $t = 0$ and the wavelength and phase speed are also given as an input to the LES code. Data are then interpolated into a spline function at the surface grid nodes. Fourier coefficients are eventually evaluated at $t = 0$ and they will be used in building the new shape, its orbital velocity and its time derivative at $t > 0$ assuming that the shape moves with uniform phase speed. This practice is possible when dealing with non-dispersive waves, which is the case here.

3.2.5.1 Boundary conditions

The wind and the wave fields are assumed to be spatially periodic in computational ξ-η planes. The air domain is thus modelled by a finite horizontal domain of dimensions $X_L \times Y_L$ as illustrated in Figure 3.3.

The shape of the wavy surface and its movement form the boundary conditions for the motion of the grid. The total time rate of change of the wave height is:

$$\frac{dh}{dt} = w_{\text{orbital}} = h_t + h_x u_{\text{orbital}} + h_y v_{\text{orbital}}. \tag{3.43}$$

Therefore, the boundary condition for the grid speed is:

$$z_t = h_t = w_{\text{orbital}} - h_x u_{\text{orbital}} - h_y v_{\text{orbital}} \qquad \text{at } \zeta = 0. \tag{3.44}$$

Requiring no flow across the wavy boundary also implies a boundary condition on the contravariant velocity W_f:

$$W_f - h_t = 0 \qquad \text{at } \zeta = 0. \tag{3.45}$$

At the top of the domain, gradient conditions are imposed on (u_i, e, U, V) and a "no flow through the boundary" condition requires that the vertical contravariant velocity W_f is set to:

$$W_f = z_t \qquad \text{at } \zeta = Z_L. \tag{3.46}$$

These boundary conditions represent a channel flow type simulation.

Concerning the pressure, the iteration scheme implemented to solve for the pressure term is based on a linear preconditioner and a source term $\partial U_{f_k}(p^*)/\partial \xi_k$ accounting for the divergence-free condition (Sullivan et al., 2014). The proper boundary condition at the wavy surface is $\partial p^*/\partial \zeta = 0$ for the linear part (it is the usual condition applied in a flat-wall LES). The non-orthogonality of the mesh is taken into account in the pressure boundary condition $\partial p^*/\partial \zeta$ of the source term. To evaluate the vertical pressure gradient at the first level above the wavy boundary using a 2nd-order centred finite-difference scheme, the pressure field is needed below the wavy boundary. The ghost-point pressure is thus evaluated with the equation of time advancement for the contravariant velocity W_f:

$$\left.\frac{W_f}{\mathcal{J}}\right|^n = \left.\frac{\hat{W}_{f_i}}{\mathcal{J}}\right|^{n-1} - \Delta t \alpha_n \frac{\partial}{\partial \xi_j}\left(\frac{p^*}{\mathcal{J}}\frac{\partial \xi_j}{\partial x_i}\right)\Bigg|^n \tag{3.47}$$

where W_f is known at $\zeta = 0$ as a no-flow condition is imposed at the boundary. The intermediate contravariant velocity $\hat{W}_f$ is defined by

$$\hat{U}_{f_i} = \left.\frac{\hat{u}_j}{\mathcal{J}}\right|_I \frac{\partial \xi_i}{\partial x_j} \tag{3.48}$$

where $(\cdot)|_I$ denotes an interpolated value and $\hat{u}_i$ is defined in Equation (3.40).

With the iterative scheme on the pressure, and knowing the pressure field above the water level and the horizontal pressure gradients $\partial p^*/\partial \xi$ and $\partial p^*/\partial \eta$, the system is rearranged to solve for the ghost pressure at each iteration (Sullivan et al., 2014).

3.2.5.2 Surface fluxes

Donelan (1998) showed that under high wind conditions, the ocean surface can be assumed to be in a fully rough regime where the contributions from the molecular viscous sublayer are negligible. Under these conditions, the surface fluxes of momentum can be represented in terms of law-of-the-wall relationships (Belcher and Hunt, 1998): to compute the total surface stress τ_{surface} (i.e. the surface momentum flux), Monin-Obukhov similarity theory and the bulk aerodynamic formulas are invoked:

$$\tau_{\text{surface}} = -u_*^2 = -C_D |\mathbf{u}_{\text{surface}}|^2 \tag{3.49}$$

where C_D is the bulk transfer coefficient, u_* the friction velocity and $\mathbf{u}_{\text{surface}}$ the relative wind vector at the surface, i.e. $\mathbf{u}_{\text{surface}} = \mathbf{u}_{\text{1st cell}} - \mathbf{u}_{\text{orbital}}$. It is assumed that the surface stress acts parallel to the surface and depends on the relative motion between the wind and the surface. The friction velocity is computed from the Monin-Obukhov similarity theory:

$$|\mathbf{u}_{\text{surface}}| = \frac{u_*}{\kappa} \ln\left(\frac{z_{\text{surface}}}{z_0}\right) \tag{3.50}$$

with z_0 the surface roughness and z_{surface} the normal distance from the distance to the first gridpoint. Sullivan et al. (2014) chose a fixed surface roughness of $z_0 = 2{\times}10^{-4}$ m. Yang et al. (2013) attempted to implement a dynamic modelling approach in order to reduce the sensitivity to the grid resolution.

τ_{surface} is then imposed along the wavy boundary and it accounts for the effects of the unresolved waves (i.e., small-scale, less-energetic waves that are below the cut-off scale of the LES).

3.2.6 Initialisation of the airflow

The initialisation procedure is carried out on the same domain and mesh as for the neutral wind-wave simulation, but on a flat bottom. A constant heat flux is imposed at the lower boundary of the domain, and the temperature and buoyancy variations are activated during this initialisation. The surface heat flux is set to the value 30 K.m.s^{-1}. The top of the MABL, z_i, is marked by a steep stable gradient in the potential temperature. This addition of surface heating helps to initiate the turbulence and by that means it skips the long spin-up time of a purely neutral simulation. A LES simulation is then started and runs until the turbulence reaches a near statistical equilibrium. After the initialisation process, the surface waves are introduced at the bottom of the air domain by means of a linear ramp. This strategy significantly decreases the CPU cost and also reduces the non-physical transient state due to the sudden introduction of surface waves into the air domain. A study on the influence of the initialisation on the wind-wave simulations will be carried out in the next chapter.

3.3 Coupling procedure

In order to study the interaction between wind turbulence and dynamically evolving surface waves, the two previous models, i.e. an atmospheric model based on LES approach and a wave model based on a potential flow (HOS method), are dynamically coupled.

The LES simulation of wind turbulence and the HOS simulation of sea-surface wave field are coupled using a fractional-step scheme. At each time step, the wave field is forced by the wind: the HOS advances the wave field to the next time step using the surface air pressure p_{atm} obtained from LES at the previous time step as specified in Equation (3.5). With the updated sea-surface elevation h and its orbital velocity $\mathbf{u}_{\mathrm{orbital}}$, the grid nodes of the air domain move vertically in order to map the free surface distortion, and the relative surface wind is calculated and used to compute the surface momentum fluxes in Equations (3.49) and (3.50). The LES simulation of wind turbulence then advances in time to the next time step. The water density being much larger than the air density, the airflow is supposed to see the water surface as a moving wavy wall. Indeed, Liu et al. (2003) demonstrated that the interface acts as a solid wall to the air motions for a coupled air-water turbulent Couette flow. Moreover, the time scale for the wave to evolve under the wind forcing is supposed to be much larger than the advection and turnover time scales of the turbulent eddies so that only one iteration is needed in the time marching to correctly represent the coupling (Liu et al., 2010). The small time steps being constrained by the Courant condition, the error of time integration is therefore small and having one iteration has a negligible effect on the flow physics. This procedure is repeated for every time steps as illustrated in Figure 3.5.

From a numerical point of view, the time steps are imposed by the time stepping in LES. The spatial discretisation of the free surface is also imposed to be the same in order to prevent any numerical disorders introduced by some interpolation. This choice falls in a simplification approach but it will lead to specific considerations in the HOS model that will be tackled in the following.

This procedure has also been implemented by Yang and Shen (2011): they conducted studies about interaction between wind turbulence and water wave field through DNS-HOS coupled simulation. They focused on the growth of a single wave train and a JONSWAP wave field under wind pressure forcing. They also developed a coupled DNS-DNS method, so that the effect of viscosity for both fluids can be accounted for: they examined the interaction between surface waves and interfacial waves below through the damping of water surface waves by a highly viscous mud flow at the bottom. Recently, they carried out a numerical study based on the modelling of an offshore wind farm through a hybrid numerical simulation combining an atmospheric LES model and a HOS model for the wave propagation (Yang

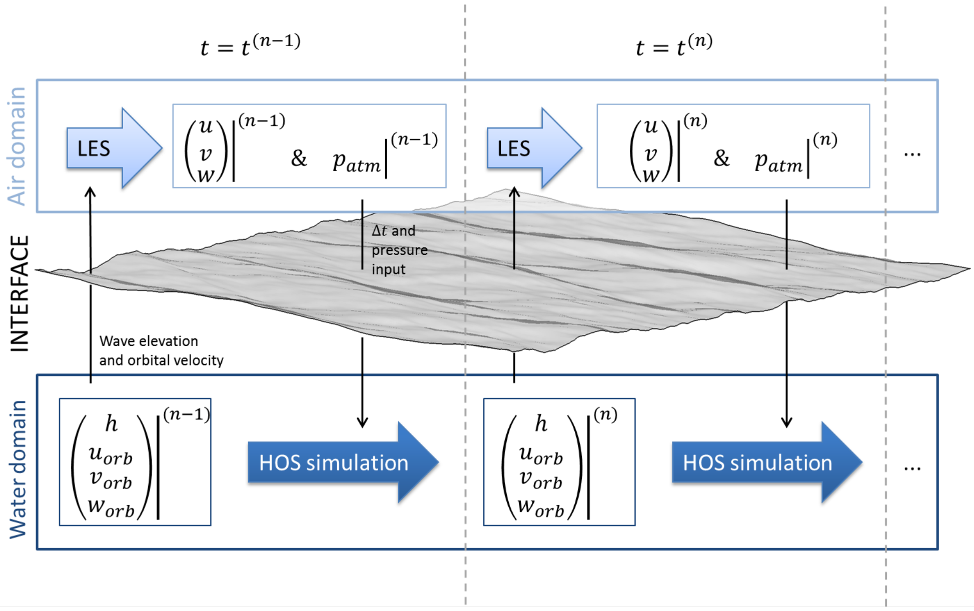

Figure 3.5: Illustrative sketch of the coupling procedure between the LES simulation of the airflow and the HOS model propagating the sea state.

et al., 2014).

3.3.1 Communication through an MPI implementation

Since the LES and HOS codes exchange information, a global parallel world is needed for the communication between the two codes. This procedure requires a Message Passing Interface (MPI) implementation. The LES code currently runs in parallel using MPI, whereas the HOS code is here used as a serial code. The global parallel world actually gather the parallel world defined in the LES code and the one-processor world of the HOS code. This global MPI communicator is named *mpi_comm_world*. The command

```
    mpi_comm_split(mpi_comm_world, color, myGlobalRank,
+                        comm_world, ierr)
```

creates a new communicator, *comm_world* based on *color* which controls the subset assignment (i.e., processes with the same color are in the same new communicator). This command is implemented in both codes with a different color for each code.

Concretely, all the communication processes are done via the global parallel world and all quantities are exchanged in physical dimensions. As mentioned above, the spatial discretisation of the free surface is the same in both codes for simplicity and rapidity reasons. The HOS processor sends the wave field information to the LES master processor via the global MPI communicator. In the LES code, the root processor broadcasts the data to the other processors. The same process is implemented when LES sends the pressure to HOS: the root processor gathers the pressure field at the free surface and sends it to the HOS processor via the global MPI communicator.

3.3.2 Wave field information

As previously detailed in 3.1, the HOS method solves the wave elevation $h(\mathbf{x}, t)$ and the free surface potential $\phi^S(\mathbf{x}, t)$: the orbital velocity $\mathbf{u}_{\text{orbital}}$ is reconstructed from the velocity potential at the free surface. A subroutine has been implemented in the LES code in order to receive the wave field information from the HOS code.

3.3.2.1 Validity of the free-surface condition

The previous section details the modelling of the airflow as a wind channel. Both upper and lower boundaries are implemented as slipping wall boundary conditions, which are reflected by the fact that there is no normal flow crossing the boundaries. At the free surface, as the HOS method solves the kinematic free surface boundary condition in Equation (3.6), this condition should be verified while being exchanged between the two codes. Special care must really be taken in order to fully respect this condition at the lower boundary in the LES code. At each time step, the spatially discretised kinematic free-surface condition is calculated inside the LES code after LES receives the wave field information from HOS, and its value is printed in the log file if it exceeds 10^{-10}. Usually, $\forall(x, y)$ and $\forall t$

$$h_t + h_x u_{\text{orbital}} + h_y v_{\text{orbital}} - w_{\text{orbital}} \approx 1 \times 10^{-15}$$

which is of the order of the machine accuracy. The free-surface condition is thus always satisfied and no flux normal to the boundary enters the air domain.

Another question that needs to be addressed is the validity of the free-surface condition during the initialisation of the wave field in the domain. Indeed, a ramp function is usually used to initiate the wave field in the domain. The wave field variables are multiplied by a ramp coefficient r in order to introduce the wave field as growing bumps into the domain. But the kinematic boundary is not satisfied when multiplying all the variables by r:

$$\begin{aligned} & r \times h_t + (r \times h_x)(r \times u_{\text{orbital}}) + (r \times h_y)(r \times v_{\text{orbital}}) - r \times w_{\text{orbital}} \\ & \neq r \times (h_t + h_x u_{\text{orbital}} + h_y v_{\text{orbital}} - w_{\text{orbital}}) \\ & \neq 0 \end{aligned} \tag{3.51}$$

During the initialisation stage, it has been decided to reconstruct the vertical velocity w_{orbital} using the free-surface condition on the modified variables $(h_t, h_x, h_y, u_{\text{orbital}}, v_{\text{orbital}})$ as illustrated in Figure 3.6:

$$w_{\text{orbital}} = r \times h_t + (r \times h_x)(r \times u_{\text{orbital}}) + (r \times h_y)(r \times v_{\text{orbital}}). \tag{3.52}$$

At the end of the ramp, LES uses w_{orbital} from HOS since the HOS model satisfies the free-surface condition and negligible artificial error is introduced while spatially discretising the condition in the air domain.

3.3.2.2 Time-stepping and update in HOS

In the LES model, the time advancement is a fully explicit RK3 scheme that uses a dynamic time stepping with a fixed CFL number. It employs a fractional step method to enforce the incompressibility constraint. In the HOS model, the free surface elevation and the velocity potential at the free surface are advanced in time through a RK4 scheme with an adaptive step size control.

The LES model imposes its time stepping to the HOS model. Indeed, the adaptive step size control of the HOS model allows the model to deal with the time advancement as needed. If a bigger time step is imposed by LES, then several iterations in time will occur in HOS for one LES time step as the HOS model will adapt its time advancement. If a smaller time

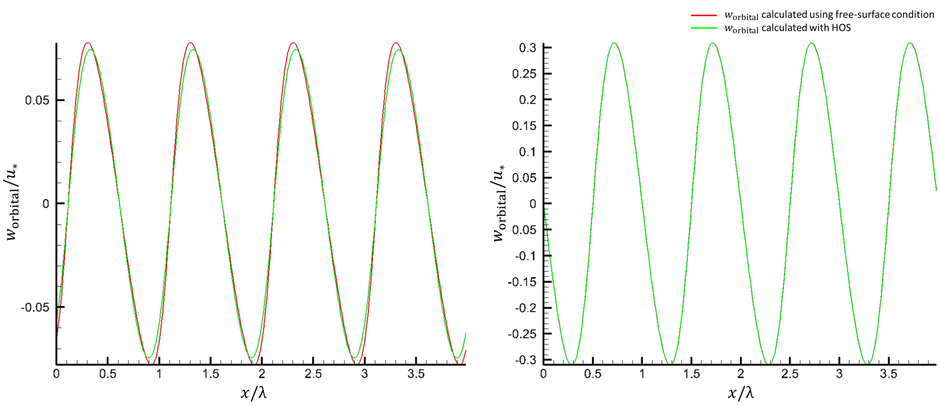

Figure 3.6: Vertical orbital velocity at the free surface. (*Left*) During the ramp initialisation, w_{orbital} is imposed using the free-surface condition (red line) and is different from the velocity calculated in HOS (green). (*Right*) After the initialisation, w_{orbital} corresponds to the variable calculated in HOS. The HOS solution satisfies the free-surface condition. *Note that the magnitude of the velocity is smaller in the upper graph since growing waves are gradually introduced in the domain during the initialisation stage.*

step is imposed by LES, the HOS model will take this LES time step as its own. For example, the air simulation will approximately need 50 time steps per wave period for an airflow propagating above a wave of period $T = 8$ s, wave steepness $ak = 0.1$ and wave age $C_p/u_* = 100$ (swell propagating in light winds) whereas the HOS model will need between 50 and 70 time steps per wave period depending on the discretisation of the spectrum and the order of resolved non-linearities. On the other hand, for a smaller wave age $C_p/u_* = 10$ with a wave of period 1.3 s and a steepness of 0.2 (i.e. a case of wind forcing), the air simulation will need around 300 time steps per wave period, compared to 80-110 time steps for the HOS model.

The main key issue in this coupling procedure lies in the time advancement of the geometric conservation law (GCL) presented in Equation (3.37). The GCL is satisfied using the same time advancement scheme as for the velocity in Equation (3.40). The whole process of GCL time advancement lies in the fact that the wave field $h(x, y, t)$ is known at current and future time steps $(n-1, n)$. Jacobians $\mathcal{J}^{(n-1,n)}$ are then built using the transformation metrics in Equation (3.35). The future grid speed $z_t^{(n)}$ is then calculated so that the GCL is obeyed discretely:

$$\left.\frac{\partial z_t}{\partial \zeta}\right|^{n-1} = \frac{1}{\alpha_n \Delta t}\left[\left.\frac{1}{\mathcal{J}}\right|^{n} - \left.\frac{1}{\mathcal{J}}\right|^{n-1} - \Delta t \beta_n \left.\frac{\partial z_t}{\partial \zeta}\right|^{n-2}\right]. \tag{3.53}$$

In Sullivan et al. (2014), the grid was stored at three time levels at each RK3 stage. In our case, a subtlety has been introduced in the HOS code: at time $t = t^{(n-1)}$, the wave field is known. During the time advancement from $t = t^{(n-1)}$ to $t^{(n)} = t^{(n-1)} + \Delta t_{\text{LES}}$, the LES code asks for the wave field at t_{stage} and $t_{\text{stage}+1}$, with the subscript *stage* being the current stage of the RK3 scheme. This is needed to get the position of the grid nodes in the mesh and to determine how rapidly they move to their new location. During this whole procedure, the atmospheric pressure at the free surface at time $t^{(n-1)}$ will be sent to the HOS code and HOS will conduct its computation without updating the wave field at the end. At the end of the three RK3 stages, the atmospheric pressure has been solved at the new time $t^{(n)}$, but the HOS simulation needs to update its wave field: the global time step Δt_{LES} and the pressure at time $t^{(n-1)}$ are sent to HOS and the wave field will be updated from time $t^{(n-1)}$ to $t^{(n)}$. Thus, Figure 3.7 illustrates that, for one time step in LES (i.e. three inner iterations), HOS will conduct six iterations without updating the wave field (and a certain number of inner iterations depending of the wave field steepness, the discretisation and the order of resolved non-linearities) and one final iteration where the wave field will be updated.

Two arguments support the implementation of this procedure:

1. as stated before, the water density being much larger than the air density, the time scale for the wave to evolve under the wind forcing is much larger than the advection and turnover time scales of the turbulent eddies

2. the wave is more affected by the wind pressure forcing when the wave age is small. In case of small wave age, the aforementioned example shows that the number of time steps per wave period needed in the LES calculation is way bigger than the actual number of time steps needed to solve for the propagation of a sea state in HOS. When the wave age is large ($C_p/u_* >> 20$), the ratio between the time steps needed in LES and in HOS decreases but, under this wind-wave ratio, the wind impact on the wave tends to be negligible and the wave begins to force the wind.

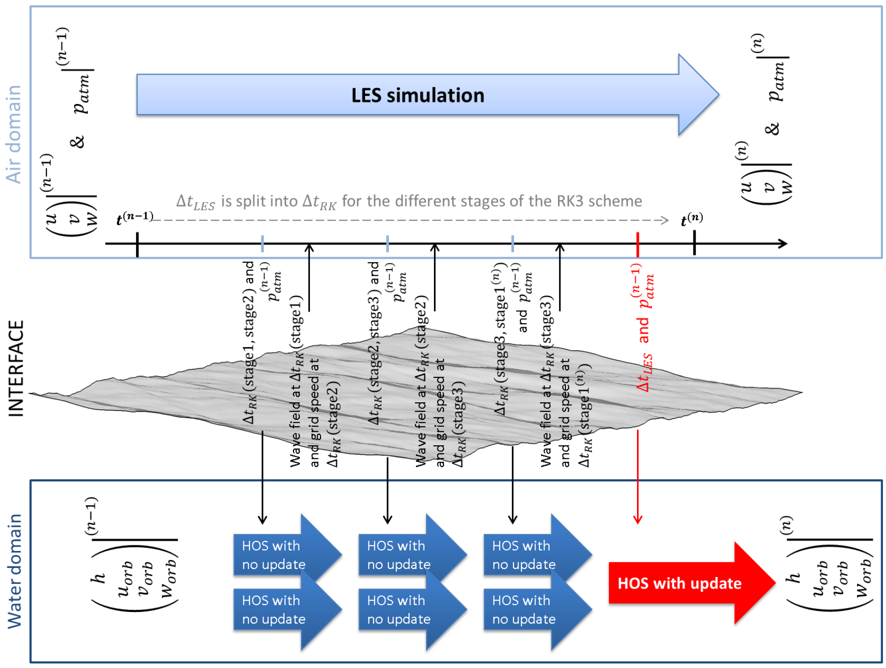

Figure 3.7: Illustrative sketch of the coupling procedure during the different stages of the RK3 scheme.

3.3.2.3 Interpolation

For simplicity reasons, it has been chosen to work with the same surface grid in LES and in HOS. In HOS, the spatial discretisation $N_x \times N_y$ has an impact on the resolution of the wave spectrum since the spatial domain is related to the wavenumber domain through Fourier transforms.

The HOS order M describes the resolved non-linearities. Nevertheless, the number of modes has to be sufficient in order to describe these non-linearities. In a domain of one wavelength, the M harmonics will be correctly solved for if the following relationship between the number of modes N and the HOS order M is satisfied:

$$M = \frac{N}{2} - 1 \tag{3.54}$$

This relationship can be adapted in a domain of x_λ wavelengths:

$$M = \frac{N/2}{x_\lambda} - 1 \tag{3.55}$$

where $k_{\max} = N/2$ is the cut-off wavenumber and comes from the Nyquist-Shannon theorem. Figure 3.8 shows the discretisation of the wave elevation spectrum: it illustrates the influence of the spatial discretisation N_x on the cut-off wavenumber. For a given k_p and a spatial discretisation $N_x = 32$, the spectrum is solved until $k_{\max} = 0.25$ whereas for $N_x = 64$, it will be solved until 0.5. The x_λ-component in the spectral discretisation represents the wavenumber at the peak k_p.

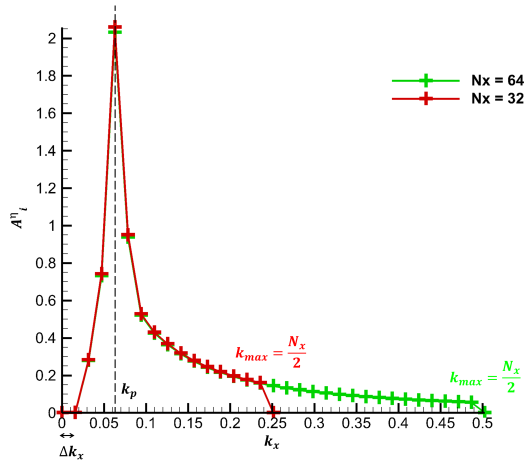

Figure 3.8: Discretisation of a JONSWAP spectrum for a wave of period $T_p = 8$ s and significant height $H_s = 4.5$ m (i.e., steepness of $k_pA = 0.1$). In the spatial domain are modelled four wave periods. Red symbols represent a spatial discretisation $N_x = 32$ whereas for green symbols $N_x = 64$. *Note: these are discrete spectra, lines are plotted for a better visualisation.*

Ducrozet (2007) studied the influence of the HOS order on the phase shift during the propagation of a monochromatic wave (direct propagation and then reverse propagation) over 1000 wave periods. He showed that the observed phase shift is less than 3^o for $M \geq 7$ which proves the convergence of the result.

In our case, typical simulations are conducted over a domain representing four wavelengths discretised by 256 points in the x-direction. If the previous relationship is applied, this configuration will allow to solve for 31 orders of non-linearities, which is going to introduce numerical instabilities at the tail of the spectrum, hence, the necessity of decreasing the number of modes. In order to keep the same surface grid between both simulations, an interpolation is implemented in the frequency domain. The resolution of the HOS system will be done with 32 or 64 modes in the frequency domain and the resolved wave spectrum will be completed with zero padding before being transformed by inverse FFT into the physical domain. Figure 3.9 illustrates the impact of the zero-padding in the spectral domain on the resolution of the wave elevation in the physical domain. A lower discretisation leads to a decrease in the resolution of the wave elevation but this can be overcome with the interpolation process implemented in the frequency domain.

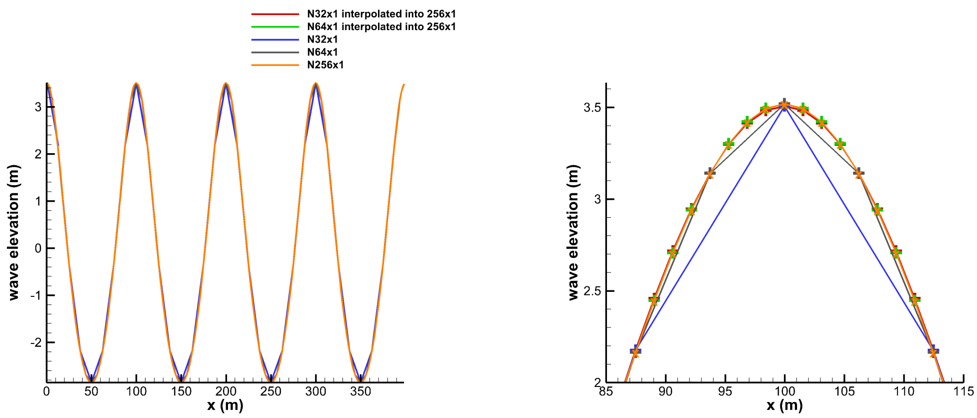

Figure 3.9: Wave elevation over position for a monochromatic wave of period $T = 8$ s and steepness $ak = 0.2$.

3.3.3 Pressure forcing at the free surface

The coupling relies on the exchange of information between the wave field and the airflow in the vicinity of the free surface. In order to take into account the influence of the wind on the sea state, the atmospheric pressure is needed as shown in Equation (3.5) where the last term p'_{atm}/ρ_w represents the wind pressure forcing. In order to evaluate the atmospheric pressure fluctuations at the free surface, one recall the procedure to get the ghost pressure in Equation (3.47): the time advancement of the contravariant velocity W_f

$$W_f\Big|^n = \hat{W}_f\Big|^{n-1} - \Delta t \alpha_n \left(\frac{\zeta_x^2 + \zeta_y^2 + \zeta_z^2}{\mathcal{J}} \frac{\partial p^*}{\partial \zeta} + \frac{\zeta_x}{\mathcal{J}} \frac{\partial p^*}{\partial \xi} + \frac{\zeta_y}{\mathcal{J}} \frac{\partial p^*}{\partial \eta} \right)^n \tag{3.56}$$

is rearranged at $\zeta = 0$ and solved using an iterative method where the superscript i denotes the iteration index:

$$\left[\frac{\zeta_x^2+\zeta_y^2+\zeta_z^2}{\mathcal{J}}\frac{p^*\left(\xi,\eta,\frac{\Delta\zeta}{2}\right)-p^*\left(\xi,\eta,\zeta=0\right)}{\frac{\Delta\zeta}{2}}\right]^i = \frac{\hat{W}_f - W_f(\zeta=0)}{\Delta t \alpha_n} - \left(\frac{\zeta_x}{\mathcal{J}}\frac{\partial p^*}{\partial \xi}+\frac{\zeta_y}{\mathcal{J}}\frac{\partial p^*}{\partial \eta}\right)^{i-1}. \quad (3.57)$$

The pressure at the free surface is then reconstructed and its value is sent at each time step to the HOS computation in order to take into account the wind forcing on the sea state propagation. When one-dimensional monochromatic waves are considered, the mean pressure at the free surface is calculated in the y-direction in the LES code in order to get a 1D pressure signal forcing the 1D monochromatic wave. In Figure 3.10 are plotted the wave elevation and its modal amplitude for a 1D monochromatic wave of period $T = 0.39$ s and steepness $ak = 0.2$. Four periodic waves are modelled in the domain and the domain has a surface resolution of $N_x \times N_y = 128 \times 128$. The red line represents the case where the HOS code propagates the sea state without any pressure forcing consideration. The coupling with an overlying airflow is represented by the green line: a case with a strong wind forcing is considered as the ratio between wind and wave velocity is very small (i.e. wave age $C_p/u_* = 1.58$). The pressure term is implemented in the dynamic free surface boundary condition in the HOS code, hence the sea state evolves under the pressure forcing. These curves correspond to the free surface elevation and its modal amplitude after half a wave period from the moment when the pressure coupling has been activated between the two codes. At this stage, where no dissipation is introduced into the wave model, the solution instantaneously diverges at high frequencies (around $k_x = 200 - 400$ m^{-1}).

This first test indicates that it seems unrealistic to couple the two codes without any parametrisation of the dissipation into the wave model. There is ongoing research about this thematics in LHEEA laboratory (Seiffert and Ducrozet, 2016). Filtering the atmospheric pressure signal at the free surface appears to be an alternative for dissipation into the wave model, though it is not a physical solution.

The first idea is then to filter the pressure signal in order to select the low frequencies that will force the wave spectrum and to get rid of these high

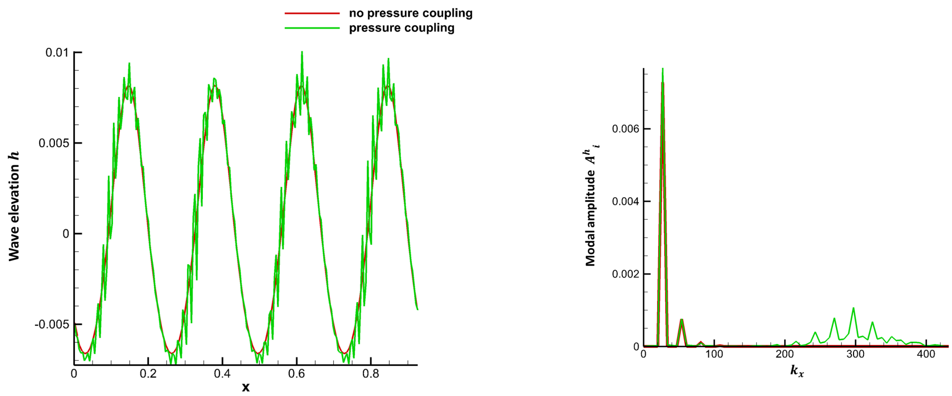

Figure 3.10: Wave elevation and its modal amplitude for a 1D monochromatic wave of period $T = 0.39$ s and wave steepness $ak = 0.2$. Red line represents a case where the pressure term is not active whereas the pressure forcing is active for the green line.

frequencies that appear in the spectrum. Two tests have been conducted: firstly, a filter $n_{\text{filter\_pressure}} = N_x/2$ is applied to the pressure signal. The results are the same as the case with no filtering, i.e. high frequencies are developing in the wave elevation spectrum. A second filter is applied to the pressure signal, $n_{\text{filter\_pressure}} = N_x/8$: the coupled computation crashes after 25 wave periods from the moment when the pressure coupling has been activated between the two codes. Figure 3.11 illustrates the impact of the atmospheric pressure filtering on the evolution of the sea state.

The effect of the pressure filtering has to be cautiously considered: indeed, the transfer of energy from wind to the waves occurs at high frequencies, so a certain amount of energy might be filtered while applying this filter to the pressure signal. Two exploratory cases on this two-way coupling will be carried out in the following chapter.

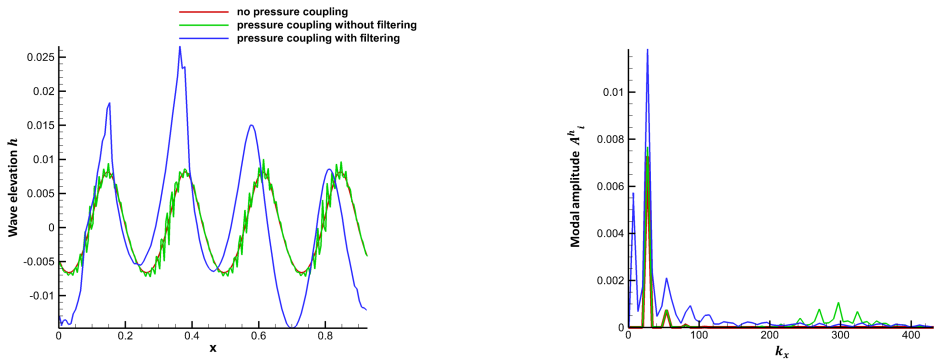

Figure 3.11: Wave elevation and its modal amplitude for a 1D monochromatic wave of period $T = 0.39$ s and wave steepness $ak = 0.2$. Red line and green line represent cases without pressure coupling and with pressure coupling but without filtering. Blue line is a case with pressure coupling and pressure filtering at $N_x/8$.

Résumé du chapitre 4

Un couplage numérique a été introduit entre un code atmosphérique modélisant les grandes échelles et un modèle HOS résolvant l'évolution et la propagation d'un état de mer. Ce couplage repose sur un échange d'informations entre les deux codes. Le couplage unilatéral (one-way coupling) est défini par l'envoi des informations de l'état de mer (élévation de surface libre, ses dérivées et la vitesse orbitale) du code HOS au code LES, tandis que le couplage bilatéral (two-way coupling) est défini par l'échange bilatéral d'informations entre les deux codes, ce qui signifie pour ce couplage que l'état de mer évolue sous le forçage par la pression du vent. On néglige les effets de stratification et de flottabilité. Les flux de quantité de mouvement de sous-maille tiennent compte des longueurs d'onde non-résolues à l'intérieur de la première maille au-dessus de la surface de l'eau: ils sont paramétrés à l'aide d'une loi logarithmique basée sur une longueur de rugosité constante.

L'influence de l'état de mer sur l'écoulement atmosphérique a été étudiée à travers trois cas de couplage unilatéral: un cas de forçage du vent au-dessus de petites vagues, un cas de houle se propageant dans une zone de faible vent et un dernier cas de génération d'un jet de vent induit par la houle. Pour le premier cas de forçage du vent avec un âge de vague $C_p/u_* < 10$, l'influence de la discrétisation du maillage est étudiée, ainsi que l'influence de la hauteur du domaine atmosphérique: l'influence est plus importante sur les profils de pression et de quantité de mouvement même si les valeurs sont similaires proche de la surface libre. Cette influence est due au fait que le domaine atmosphérique est modélisé comme une soufflerie et que des conditions de gradient de vitesse non-nul sont imposées sur la frontière supérieure plate. La hauteur n'a presque pas d'impact sur les profils moyens de vent et de traînée de forme. L'influence du contenu spectral de l'état de mer est aussi étudiée: un état de mer avec un contenu spectral plus important tend à ralentir de façon plus significative l'écoulement d'air. Pour le deuxième cas où une houle monochromatique non-linéaire se propage dans un vent faible (âge de vague $C_p/u_* = 60$), l'influence de la hauteur du domaine sur les profils moyens est plus frappante que pour le cas précédent. Une accélération plus importante semble survenir dans la soufflerie la moins haute et cette accélération est corrélée à une contrainte de pression plus importante qui va agir comme une poussée plus importante sur le vent. En effet, le vent et les vagues échangent de la quantité de mouvement et de l'énergie à travers la traînée de forme et cet échange influence directement la croissance de la vague. La notion de forçage est ainsi caractérisée par le paramètre de taux de croissance β, qui repose sur la traînée de forme adimensionnelle due à la pression et à la cambrure de la vague. La différence majeure entre les deux cas réside dans le signe de ce coefficient qui est directement basé sur le signe de la traînée de forme à la surface. Dans le cas des jeunes vagues sous-jacentes à un vent fort (âge de vague $C_p/u_* < 10$), les vagues agissent comme une traînée sur le vent et $\beta > 0$. Dans le cas d'une houle rapide se propageant dans une zone de faible vent, les vagues agissent comme une poussée sur le vent et $\beta < 0$. Une autre façon de représenter ces phénomènes est que le premier cas est considéré comme un cas de forçage par le vent, alors que le second cas est un cas de forçage par les vagues.

Un paramètre de taux de croissance négatif n'implique pas la génération d'un vent induit par la vague. En effet, aucun jet de vent n'est observé dans l'écoulement atmosphérique pour un âge de vague $C_p/u_* = 60$. Un troisième cas est donc modélisé avec un âge de vague $C_p/u_* = 120$ où une houle monochromatique très rapide se propage dans une zone de très faible vent. Dans de telles conditions, un jet de vent est observé autour de 50-100 m au-dessus de la surface de l'eau. La présence de ce vent induit par la vague est corrélée à un flux de quantité de mouvement positif: un transport de quantité de mouvement ascendant est observé, invalidant les modèles océan-atmosphère actuels qui n'autorisent que des flux descendants. Cependant, l'état de mer n'est pas vraiment réaliste pour ce cas avec une amplitude de 12.7 m. Trois états de mer avec des plus petites cambrures sont ensuite considérées. Pour les plus petits états de mer, aucun jet de vent n'est observé dans le profil de vent, le vent est même décéléré au-dessus de la vague au cours du temps. Ce comportement appuie l'influence de la cambrure de la vague et de l'énergie du spectre de vague sur l'écoulement atmosphérique. Pour ces cas de petites cambrures, la traînée de forme légèrement positive ne contrebalance pas suffisamment le flux de quantité de mouvement négatif: le transfert global reste donc négatif et il n'y a pas de jet de vent dans le profil de vitesse.

Avec le couplage unilatéral, on signale le fait que l'évolution naturelle du système vent-vague est déformée car l'état de mer n'évolue pas sous le forçage de la pression, amenant ainsi une quantité d'énergie quasiment infinie dans le domaine atmosphérique. Deux cas supplémentaires ont été implémentés afin d'étudier le couplage bilatéral. Comme aucun modèle de dissipation n'existe dans le modèle HOS, l'état de mer ne supporte pas le forçage de la pression. Il a été décidé de filtrer le signal de pression atmosphérique afin de ne considérer que le forçage des plus petites composantes spectrales, soit des plus grandes longueurs d'onde. Ce faisant, on retarde le moment où la dissipation entre en jeu. Néanmoins, ce procédé n'est pas physique et la paramétrisation de la dissipation de l'énergie constitue l'élément clé de la compréhension des interactions du système vent-vagues. Ce sujet fait actuellement l'objet de nombreuses recherches au LHEEA (Seiffert and Ducrozet, 2016).

Chapter 4

Wind-wave interactions: application case studies

This chapter examines the perspectives within that coupling between the atmospheric LES code (Sullivan et al., 2014) and the HOS wave model (Ducrozet, 2007) presented in the previous chapter. This coupling is based on a communication procedure that has been implemented so that the two codes exchange information as illustrated in Figure 3.5. The atmospheric code needs the sea-surface elevation h at each time step, so that the mesh in the air domain evolves in time, and its orbital velocity $\mathbf{u}_{\text{orbital}}$ as boundary conditions. In return, the sea state is evolving within the HOS model, propagating and growing under the wind pressure forcing. Throughout the rest of the document, a distinction is drawn within the numerical definition of "coupling". The one-way coupling is defined as the forcing from the wave model on the atmospheric model, meaning that the wave information (i.e. the wave elevation and its derivatives and the orbital velocities) is sent from the HOS code to the LES code without any feedback on the wave model. The two-way coupling is defined as a physical coupling, meaning that there is an exchange of information between the two codes and that the sea state will evolve under the wind pressure forcing.

The chapter is organised in three sections: firstly the one-way coupling is validated through a comparative case based on laboratory wind waves. Then, the influence of a sea state on the overlying airflow will be numerically investigated through three cases: wind forcing over young waves, a swell underlying a light wind and a case of generation of a wave-induced wind.

Finally, an exploratory study will be conducted on the two-way coupling where the atmospheric pressure is sent back to the HOS code so that the sea state evolves under wind forcing.

4.1 Implementing a one-way coupling

In a first stage, the pressure coupling is not activated. This means that for small wave ages (i.e. $C_p/u_* < 15 - 20$) where the wind forcing prevails, the sea state will not evolve under the pressure forcing. The first idea is to compare a one-way coupled simulation with a simulation from the original code which contains a simplified wave propagation model as stated in the previous chapter (i.e. the wave is reconstructed using the initial FFTs and a single phase velocity). A file with tank data has been provided by Peter Sullivan from the National Center for Atmospheric Research, CO, USA. This case is compared with a case with a non-linear monochromatic wave and a case with an irregular sea state: in both cases, the wave propagation is computed with the HOS code based on similar characteristics as the laboratory wind wave (i.e. same wavelength, similar wave steepness and same wave age), and the wave elevation and its orbital velocities are sent to the LES code through the one-way coupling.

4.1.1 Airflow above a simplified wave model

A first simulation has been computed on the original code: a monochromatic wave train described by a wavelength $\lambda = 23.2780$ cm and a wave steepness $ak \approx 0.226$ is propagated in a wave tank with the speed ratio $C_p/u_* = 1.6$. The LES code initially reads the tank data and FFTs are computed in order to build the sea state at $t > 0$. Figure 4.1 shows the wave elevation and the orbital velocities of the tank data. This corresponds to a case of young waves propagating under a strongly forced condition with no wave breaking.

This set of data constitutes the information that are needed at the lower boundary, i.e. the mesh deformation, its vertical speed and the velocity boundary condition. In the original code, the file with tank data is read during the initialisation of the simulation and a Fourier transform is performed leading to a memory storage of the Fourier coefficients of the wave elevation and the horizontal orbital velocity. Each time wave information is needed,

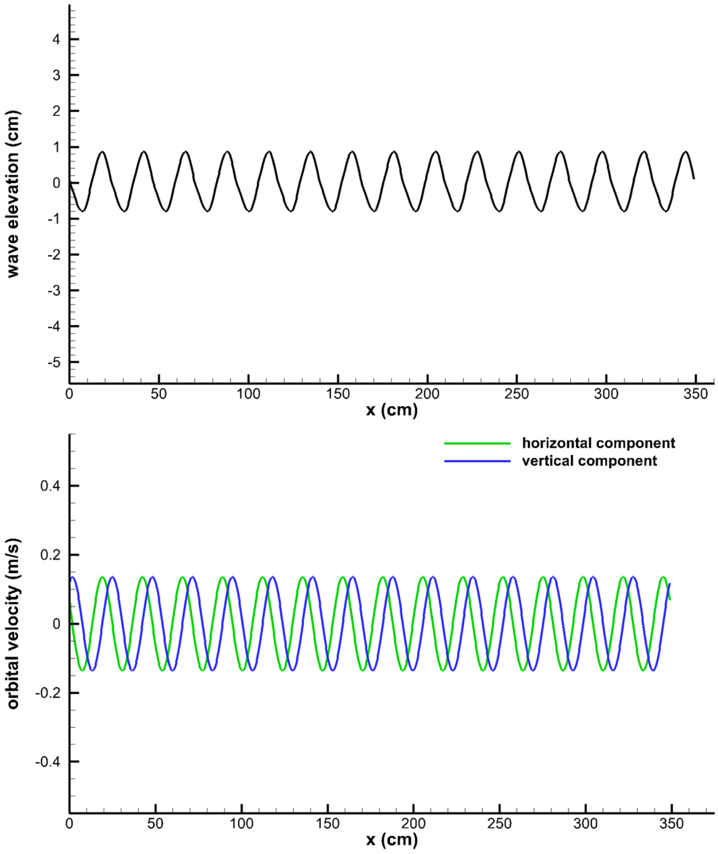

Figure 4.1: Data from a tank experiment with no wave breaking. (*Top*) The wave elevation (cm) is plotted over the position (cm). The wavelength is 23.2780 cm. (*Bottom*) The orbital velocities (m.s^{-1}) are plotted over the position (cm).

the signal in physical space is reconstructed and advanced in time using the Fourier coefficients and assuming that the wave moves with uniform phase speed, here $C_p = 0.602861$ m.s^{-1}. The vertical orbital velocity is reconstructed using the free-surface condition imposing that no flux normal to the surface crosses the free surface. As a one-dimension wave field is considered, Equation (3.44) becomes:

$$w_{\text{orbital}} = h_t + h_x \times u_{\text{orbital}}. \tag{4.1}$$

Figure 4.2 illustrates the influence of the reconstruction of the vertical orbital velocity w_{orbital} so that the free-surface condition is satisfied.

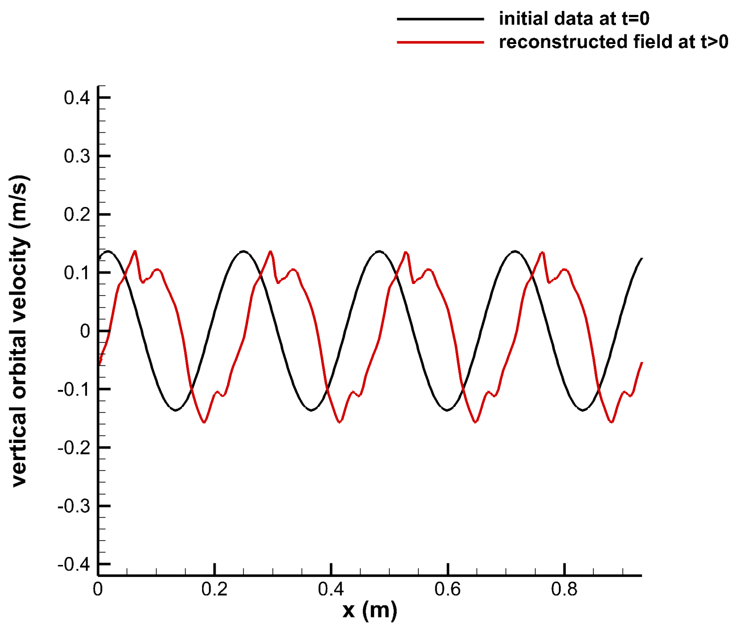

Figure 4.2: Influence of the free-surface condition on the vertical orbital velocity w_{orbital}. Black line is the initial wave field data set and red line represents the reconstructed vertical orbital velocity at $t > 0$.

Now that the wave field has been introduced, the numerical model of the air domain is detailed. Governing equations have been presented in the previous chapter. The main assumption of the model is that the air domain represents a wind tunnel with neutral atmosphere, meaning that no buoyancy effects are taken into consideration. Moreover, a wall-type boundary condition is considered at the top of the domain, where a no-flux boundary condition is implemented. The complete set of spatially filtered LES equations (3.38) is solved in computational coordinates (ξ, η, ζ) under a time-dependent surface-following mapping (3.33). The size of the air domain is $(L_x, L_y, L_z) = (4\lambda, 4\lambda, 1\lambda)$, λ being the wavelength of the wave field, here $\lambda = 0.23278$ m. The discretisation of the domain uses $(N_x, N_y, N_z) = (256, 256, 128)$ grid points. The horizontal grid spacing is thus $\Delta\xi = \Delta\eta = 0.0156\lambda = 3.64 \times 10^{-3}$ m and the first vertical level is located $0.0065\lambda = 1.51 \times 10^{-3}$ m above the free surface. The vertical grid distribution is non-uniform and is generated by a smooth algebraic stretching: the spacing ratio between two adjacent grid points is $\Delta\zeta_{i+1}/\Delta\zeta_i \approx 1.0028$. As specified in the previous chapter, the subgrid-scale model parametrises the small eddies in the turbulent flow. The filter length scale Δ is computed from the averaging volume $\Delta^3 = (3/2)^2(\Delta\xi\Delta\eta\Delta\zeta/\mathcal{J})$ with $\mathcal{J}$ the Jacobian of the mapping transformation (3.33) and the factor 3/2 accounting for dealiasing. Therefore, the resolution near the surface is fine leading to a reduced reliance on the SGS model. Concerning the unresolved surface waves, they are simply modelled by a fixed surface roughness $z_0 = 1 \times 10^{-4}$ m. The bulk aerodynamic formula (i.e. Monin-Obukhov similarity theory) is applied point by point along the wavy boundary with the surface roughness in order to compute the surface momentum as described in the previous chapter. The initial wind forcing is applied by the external pressure gradient $\partial\mathcal{P}/\partial x$ (3.26) that yields a surface stress $\tau_{\text{surface}} = (\partial\mathcal{P}/\partial x)\,\lambda$ and a surface friction velocity $u_* = |\tau_{\text{surface}}|^{1/2}$. Here the ratio between the wind and the wave field is initially imposed with the wave age $C_p/u_* = 1.6$ which is a strongly forced condition. These wind-wave settings are typical for dominant wind waves in laboratory conditions. It can also represent small-scale waves in the open ocean.

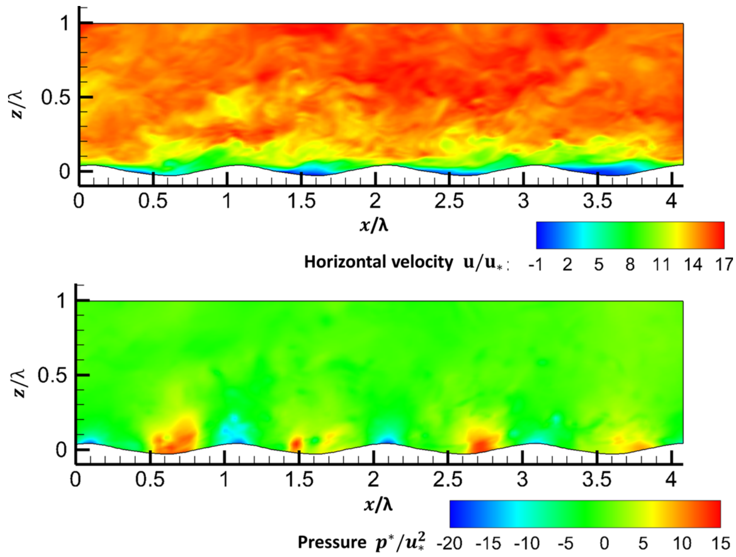

Figure 4.3: Instantaneous contours in a $x-z$ plane of dimensionless horizontal velocity (*top*) and pressure (*bottom*) for a LES simulation of a strongly forced condition with wave tank data. The laboratory wave has a wavelength $\lambda = 0.23$ m and a steepness $ak = 0.226$ and the wind-wave speed ratio is defined by the wave age $C_p/u_* = 1.6$.

The results of the LES simulation are presented in Figure 4.3. Coherent patterns are observed in the horizontal velocity and pressure fields. The velocity field shows a cat's eye pattern on the lee side of the wave crest. A detailed view of the lee side is illustrated in Figure 4.4 and the streamlines clearly show a closed pattern. The pressure plot shows that the maximum pressure is located downwind the wave trough, which contributes to the air-water momentum flux in the way that the high pressure acts on the positive wave slope and pushes the wave in the direction of the wave propagation. Hara and Sullivan (2015) conducted similar numerical simulations and their results show that the enhanced wave-induced stress very close to the free surface reduces the turbulent stress, which is correlated with a reduction in the TKE viscous dissipation rate. They demonstrated that this weakening of turbulence in the vicinity of the water surface is related to the modification of the mean wind profile and the increase of the equivalent surface roughness.

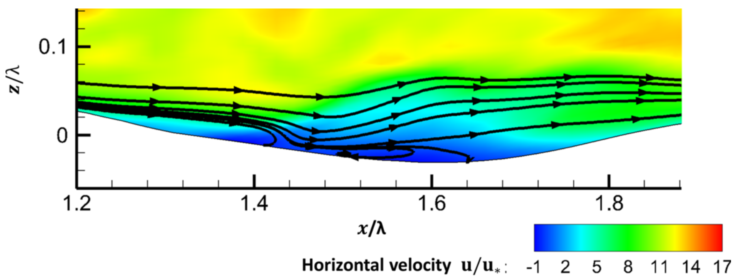

Figure 4.4: Detailed view of the cat's eye pattern in the horizontal velocity field.

This case represents the modelling of strongly forced conditions (i.e. the wave age is $C_p/u* = 1.6$) where a strong wind overlies really small waves generated in a laboratory tank (wavelength $\lambda = 0.23278$ m and wave steepness $ak = 0.226$). A similar case where an Airy wave with a wavelength $\lambda = 23.278$ cm underlies a strong wind with $C_p/u_* = 1.6$ is also conducted. The main difference lies in the wave steepness, $ak = 0.2$, in order to get a comparative element for the following cases that will treat waves with a wave steepness of 0.2. The cat's eye pattern is also present in the trough of the Airy wave. Instantaneous plots can be found in Appendix A. This Airy case conducted with the original code constitutes a basis for comparison with the two other one-way coupled cases that will be presented in the next section.

4.1.2 Airflow over non-linear monochromatic and irregular waves

After the implementation of the coupling between the HOS wave model and the LES atmospheric code, the validation of the numerical developments is needed: to this end, wind-wave conditions similar to the previous Airy wave are tested. The propagation of monochromatic and irregular sea states is modelled with the HOS wave model. Compared to the original code, HOS solves for the complete non-linear free surface boundary conditions. HOS method will model either non-linear monochromatic waves using the Rienecker&Fenton initialisation or an irregular sea state based on a JONSWAP spectrum. In order to make qualitative comparisons, the characteristics of the sea states are similar to the previous case: sea states of small waves are considered with a wavelength $\lambda = 0.23278$ m (λ_p for the irregular sea state) and a wave steepness $ak = 0.2$. For the irregular sea state, the wave spectrum is defined by the significant wave height and the peak period (H_s, T_p) where H_s can be related to the amplitude of the corresponding monochromatic wave, a, by the following relationship:

$$H_s = 4\sqrt{E} \approx 4\sqrt{\frac{1}{2}a^2}. \tag{4.2}$$

The energy spectrum of the monochromatic wave being discrete with one main energy peak at $k = 2\pi/\lambda$, it is difficult to compare it with the continuous energy spectrum of the irregular sea state where the energy is distributed over a spectral domain. In order to have a reference point between the two sea states, a large peak enhancement factor γ of the JONSWAP spectrum (cf Equation (3.19)) is considered. This factor is related to the concentration of energy around the peak of the spectrum. For example, a JONSWAP spectrum with $\gamma = 3.3$ will concentrate 49% of the total energy around the peak in a range of $[0.75k_p; 1.25k_p]$ whereas a JONSWAP spectrum with $\gamma = 10.0$ will concentrate 58% of the total energy in the same range. We thus considered a sea state defined by $H_s = 0.02$ m, $T_p = 0.39$ s and $\gamma = 10.0$.

The airflow is modelled under the same considerations as the previous simulation: a wind tunnel of neutral atmosphere has a dimension of $(4\lambda, 4\lambda, 1\lambda)$ and is discretised with $(256, 256, 128)$ grid points. The first vertical point is located $0.0065\lambda = 1.51 \times 10^{-3}$ m above the free surface. The mesh follows the free surface elevation with the mapping transformation (3.33). The vertical grid distribution is non-uniform and is generated by the same stretching with a ratio of 1.0028. In the vicinity of the free surface, a wave is thus horizontally discretised by 64 points and $9-10$ cells are vertically distributed between the trough and the crest of the wave. The same ratio between wind and wave velocities is imposed with the wave age $C_p/u_* = 1.6$.

Figure 4.5 shows the wave elevation and orbital velocities for the different sea states. It illustrates the different features specific to each wave input: the non-linear regular wave (green line) has steeper crests and flatter troughs compared to the Airy wave (red line) with the same wave steepness $ak = 0.2$.

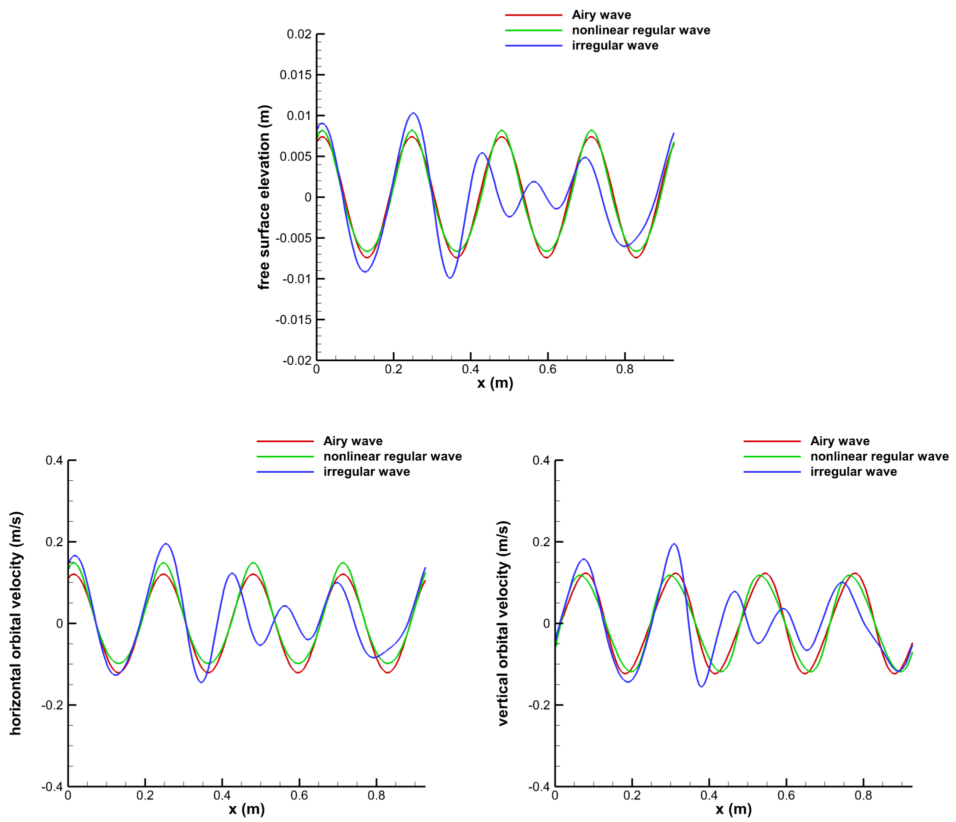

Figure 4.5: Distribution of wave elevation (*top*) and orbital velocities (*bottom*) along the x dimension of the domain for various wave fields.

Concerning the irregular sea state, results have to be cautiously considered. Indeed, the solution of the HOS method for the ($H_s = 0.02$m, $T_p = 0.39$s) sea state is not reliable, because the breaking limit seems to be exceeded for this sea state. In order to overcome this limit, the high frequencies of the tail of the spectrum are not taken into account anymore: the cut-off wavenumber k_{max} is decreased from 64 to 8 (i.e. $k_{max} = 32k_p$ decreased to $k_{max} = 2k_p$), which means that fewer non-linearities will be solved. It is clearly an ideal case but the idea is to qualitatively compare similar sea states with similar wave elevation. The only uncompromising aspect must be the validity of the free-surface condition (cf Equation (3.44)) for each sea state, so that no flux normal to the lower boundary crosses the free surface. As specified in the previous section, the vertical orbital velocity is reconstructed so that the free-surface boundary condition is satisfied for the Airy wave case.

Figure 4.6 and Figure 4.7 display the instantaneous contours of the horizontal velocity and pressure fields in a $x-z$ plane for the cases of a non-linear monochromatic wave and an irregular wave coupled to the airflow simulation. In both cases, the cat's eye pattern on the lee side of the wave crests can be observed in the velocity field. For the irregular sea state in Figure 4.7, it does not occur where the crest is quite flat: typically, no sheltering effect is observed after the second crest, around $x/\lambda = 1.5$. Another phenomenon can also be related to this surface "flatness" between $x/\lambda = 0.86$ and $x/\lambda = 3.4$: the airflow seems to be less accelerated above this part of the surface compared to the other cases. Actually, it can be noted that, instantaneously, the acceleration of the wind occurs closer to the free surface above the first cat's eye pattern. In the pressure field, the maximum pressure is also located downwind the wave trough, even if this coherent pattern has a smaller amplitude for the irregular wave sea state where crests and troughs are quite flat.

All these considerations have been made on instantaneous plots. Spatial averages are computed by area averaging over $\xi - \eta$ surfaces because of horizontal periodicity. Figure 4.8 illustrates the temporal evolution of the friction velocity and the vertical flux of horizontal momentum at the first cell above the free surface for the four different cases. Time evolution is globally the same in the three cases: after a period of stabilisation after the initialisation, the plots converge around a mean value, which seems to be the same for the cases with the non-linear regular wave and irregular waves. The case where an Airy wave is imposed at the lower boundary of the air domain (red

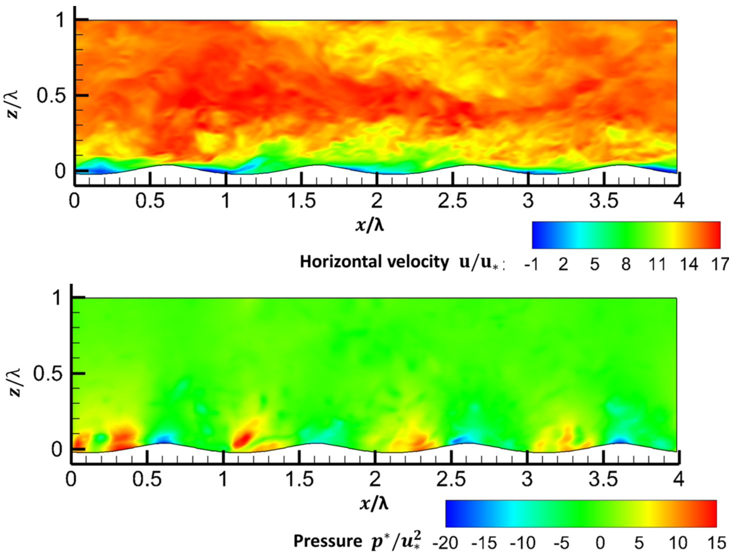

Figure 4.6: Instantaneous contours in a $x-z$ plane of dimensionless horizontal velocity (*top*) and pressure (*bottom*) for a one-way coupled simulation of a non-linear monochromatic wave underlying a strong airflow. The non-linear regular wave has a wavelength $\lambda = 0.23$ m and a steepness $ak = 0.2$ and the wind-wave speed ratio is defined by the wave age $C_p/u_* = 1.6$.

plot) seems to have a slightly bigger friction velocity at the first cell above the free surface which is correlated to the slightly bigger momentum flux (in amplitude) at the free surface.

The spatial averages allow to compute statistics down to the free surface, especially between and below the wave crests. These resulting vertical profiles are further averaged in time (Sullivan et al., 2014). The airflow is then averaged over 50 wave periods from the moment the quantities converge (i.e. the boundary layer is quasi stationary). Figure 4.9 shows the vertical profile of the average wind speed and the average pressure for the four simulations. A slightly larger wind velocity is observed in the case with the Airy wave (red plot). Concerning the vertical profile of the pressure, for the one-way coupled case with the irregular wave (blue plot), the magnitude of the pressure is bigger around $\zeta = 0.025$ m compared to the other cases. This can be related to the vertical extension of the negative pressure above the large wave crest in Figure 4.7, which seems to be larger in this case than in the other three cases.

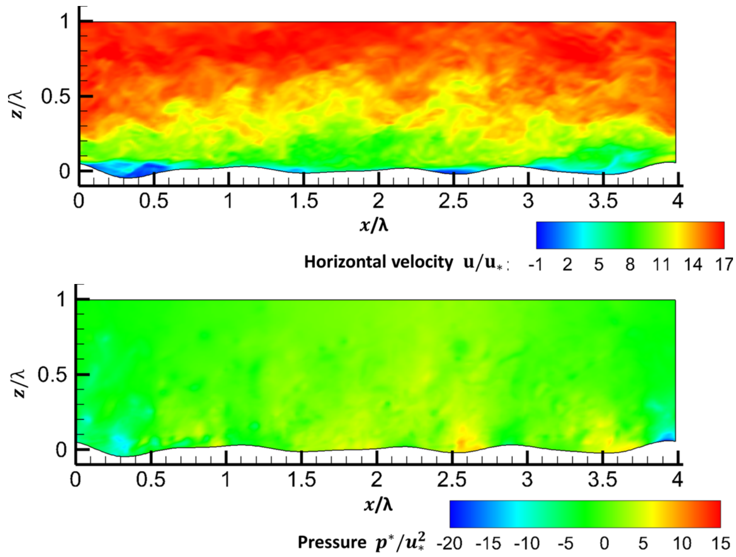

Figure 4.7: Instantaneous contours in a $x-z$ plane of dimensionless horizontal velocity (*top*) and pressure (*bottom*) for a one-way coupled simulation of an irregular wave underlying a strong airflow. The irregular wave has a wavelength $\lambda = 0.23$ m and a steepness $ak = 0.2$ and the wind-wave speed ratio is defined by the wave age $C_p/u_* = 1.6$.

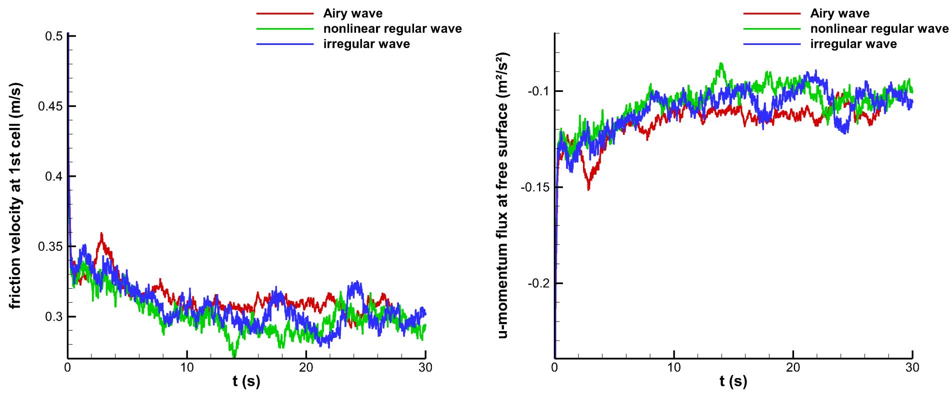

Figure 4.8: Time evolution of the friction velocity (*left*) and the vertical flux of horizontal momentum (*right*) at the first cell above the free surface for various wave fields.

Figure 4.10 shows the vertical profile of the average vertical flux of horizontal momentum and the average form drag for the four simulations. On the left plot, the momentum flux is decomposed into the resolved part and

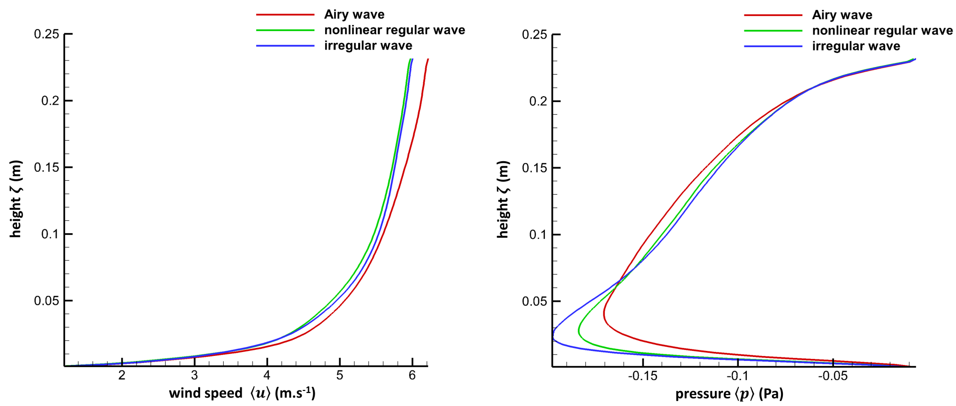

Figure 4.9: Vertical profiles of average wind speed (*left*) and pressure (*right*) for various wave fields.

the subgrid-scale part. The high contribution of the SGS part can be noticed near the free surface due to the bulk aerodynamic formula which computes the surface stress and the effect of the unresolved surface waves. However, the fine resolution of the mesh leads to a reduced reliance on the SGS model. This contribution of the SGS model to the total momentum flux decreases with height. The behaviour is quite the same in the four simulations. The values at the free surface, lying between -0.09 and -0.1 kg.m^{-1}.s^2, can be aligned to the values of the u-momentum fluxes at the free surface in Figure 4.8. The pressure stress (i.e. $p\partial h/\partial x$) is also similar in the four cases: the behaviour of the pressure above the highest crest/trough in the irregular wave case may be smoothed by the rest of the free surface where the x-derivative of the wave elevation is smaller. The negative form drag and momentum flux contribute to a downward momentum flux: the waves impart drag on the winds. It is coherent with the wind-wave conditions that have been imposed, i.e. strongly forced conditions.

In conclusion, the numerical implementation of the coupling between the LES atmospheric code and the sea state propagation code has been validated by comparing four cases with similar sea state and airflow characteristics. A wave field with a wavelength $\lambda = 0.23278$ m (i.e. a phase velocity $C_p = 0.603$ m.s^{-1}) is considered in both cases and underlies an airflow with the exact same wave age $C_p/u* = 1.6$. A first case with a wave field extracted from tank data (with a wave steepness $ak \approx 0.226$) has been running with the original

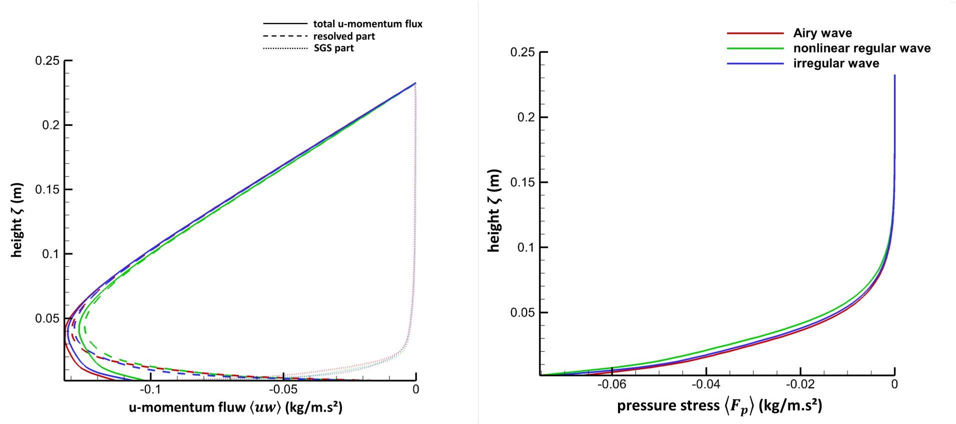

Figure 4.10: Vertical profiles of average vertical flux of horizontal momentum (*left*) and form drag (*right*) for various wave fields.

atmospheric code. A second case with an Airy wave (i.e. linear regular wave) with a wave steepness similar to the first case, $ak = 0.2$, has also been run with the original atmospheric code. In the two other cases, the coupling has been activated with the HOS code. HOS solves for a non-linear regular wave of wave steepness $ak = 0.2$ with the Rienecker&Fenton initialisation method, and for an irregular sea state. This irregular sea state appears to be quite unrealistic since HOS resolution only takes into account the lower frequencies of the wave spectrum, but it has been retained in order to make comparisons and validations. Despite small deviations, instantaneous contours in a $x-z$ plane of the velocity and the pressure, temporal evolutions and vertical profiles of average quantities show the same patterns in the four simulations. The validation is also strengthened by some numerical markers: time steps and pressure errors are similar regarding the order of magnitude (between 3×10^{-4} and 2×10^{-4} for the time steps and 1.5×10^{-10} and 5×10^{-11} for the pressure error) and the maximum of the velocity divergence is even smaller in the coupled cases (5×10^{-20} for non-coupled simulation and 4×10^{-23} for coupled simulations). Now that the implementation of the coupling has been tested against previous test cases and validated, further simulations can be conducted in order to investigate the applications of this LES-HOS coupling.

4.2 Numerical investigation of the impact of a sea state on the overlying airflow

A more suitable description of the MABL requires to go beyond the statistical formalism normally used in the modelling of the ocean-atmosphere interactions both as regards in meteorology and in climate science (Chen et al. (2015), Fan et al. (2012)). A better description of the processes related to the momentum flux exchanges requires a specific description of the airflows evolution at their own time and spatial scales. Moreover, the outstanding questions within the simple description of the wind-wave coupling are numerous, e.g. the vertical extension of the MABL directly impacted by the underlying waves, the role of the wave, the correlation between winds and waves for various sea states... The single mechanism of wave growth under wind forcing is a point of considerable discussion.

The wave effects are commonly thought to be confined within a small region above the water surface and are usually considered as an aerodynamic roughness length. However, field observations and numerical modelling have shown that the atmospheric surface layer can be strongly disturbed by waves, especially waves generated non-locally. One of the crucial differences for an airflow over waves compared to a flow over a usual rough surface is the dynamic motion of the sea surface. Under wind forcing, wind and wave exchange momentum and energy mainly through form drag (Sullivan and McWilliams, 2010), so the knowledge of this quantity is of importance because it directly influences wave growth (Belcher and Hunt, 1998). The growth rate parameter β is related to the wind forcing through:

$$\beta = \frac{2F_p}{(ak)^2}, \tag{4.3}$$

where F_p is the dimensionless form drag, or form stress, per unit area due to the pressure p^*:

$$F_p = \frac{1}{\lambda}\int_0^{\lambda} p^* \frac{\partial h}{\partial x}\mathrm{d}x. \tag{4.4}$$

For an irregular sea state, Yang et al. (2013) define a growth rate parameter related to the wave mode k with:

$$\beta\,(k) = \frac{2F_p\,(k)}{(a(k)k)^2}.$$

Throughout the rest of the chapter, the resolved form stress (i.e., the drag or thrust) of the underlying wave is expressed in the wave-following coordinates system through the mapping transformation (3.33):

$$p^*_{\text{comp}}\frac{\zeta_x}{\mathcal{J}} = -p^*_{\text{phys}} z_\xi. \tag{4.5}$$

Thus, in accordance with the mapping transformation between the physical space coordinates and the computational curvilinear coordinates, a negative form drag means that the surface form stress acts as a drag on the surface winds, and vice versa, a positive form drag will act as a thrust on the surface winds.

Sullivan et al. (2000) among others demonstrated that the wave-induced momentum flux shows a strong dependence on the wave age C_p/u_*. Hence various wind-wave configurations have been investigated and are further detailed: cases with strongly forced wave conditions, cases with a swell propagating in light wind and cases of generation of a wave-induced wind.

4.2.1 Wind forcing over young waves

Firstly, various wind-wave configurations have been investigated within the framework of a strong wind overlying young waves. Table 4.1 presents the four cases that have been implemented. Three wave ages are considered: $C_p/u_* = 1.6$, 5 and 10 which are smaller than the wind-wave equilibrium $C_p/u_* \approx 15 - 20$. For the largest wave age, two wave steepness have been tested, $ak = 0.2$ and 0.16, in order to investigate the influence of the wave steepness of the wind-wave interactions.

A study similar to the study presented in the previous section has been conducted. Appendix B lists the instantaneous contours in a $x - z$ plane of u, w and p^* for cases WA1, WA5 and WA10 (a). The cat's eye pattern that has been observed in the previous section for case WA1 is still present for case WA5 but has a smaller magnitude and spatial extension. When the wave age increases, this sheltering effect occurring on the lee side of the wave crests tends to disappear: indeed this pattern is not observed in the velocity field of case WA10.

		Case WA1	Case WA5	Case WA10 (a)	Case WA10 (b)
Wind-wave ratio	wave age C_p/u_*	1.6	5	10	10
Wave parameters	wavelength λ (m)	0.23	0.70	2.78	2.78
	amplitude a (m)	0.007	0.022	0.088	0.071
	steepness ak	0.2	0.2	0.2	0.16
	phase velocity C_p (m.s^{-1})	0.60	1.04	2.08	2.08
Wind parameters	initial friction velocity u_* (m.s^{-1})	0.38	0.21	0.21	0.21
	$U_{10\mathrm{m}}$ calculated from log law (m.s^{-1})	11.0	6.0	6.0	6.0

Table 4.1: Characteristics of the wave field and the initial wind imposed for various cases with young waves propagating in strong wind conditions.

In the literature, β is often parametrised as a function of wave age C_p/u_*. This dependence is illustrated in Figure 4.11. β increases, reaches its maximal value around $C_p/u* = 5$ and then decreases as C_p/u_* increases further. At small C_p/u_*, our results fall in the middle of various theoretical predictions. Miles and Janssen theories are based on the critical-layer theory in which the air is assumed to be inviscid and the turbulence is only considered to provide a mean shear profile. The growth rate is due to the resonant interaction between the wave-induced pressure fluctuations and the free surface waves in the critical layer. Cohen and Belcher (1999) considered more details of the wind turbulence structure through their rapid distortion theory. The non-separated sheltering mechanism complements Miles' theory for the growth of slow waves ($C_p/u_* < 11$) and they introduced the concept of damping of fast waves under wind forcing ($C_p/u_* > 20$). Our coupled LES-HOS results agree well with the one-way coupled HOS-LES results of Yang et al. (2013), where cases CU6 and CU10 correspond to different parameters of JONSWAP spectra (i.e., $C_p/u_* = 6$ and 10). But they are quite far from the DNS results of Sullivan et al. (2000) and Yang and Shen (2010) who obtain values superior to 30 for small wave ages. Nevertheless, it should be noted that Sullivan et al. (2000) studied monochromatic waves of small wave steepness

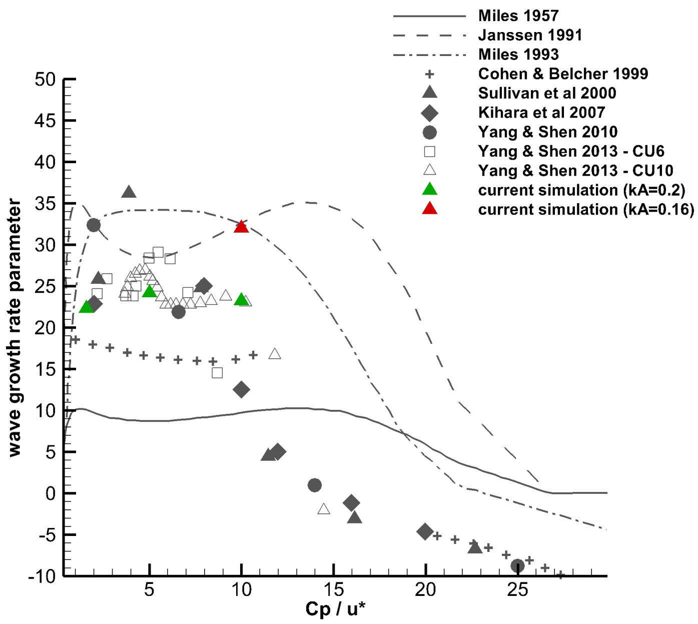

Figure 4.11: Dependence of wave growth rate parameter β on wave age C_p/u_*. Values predicted by theories are identified by lines. Results from previous numerical studies are indicated by symbols and current results are indicated by coloured symbols.

$ak << 0.1$. The influence of the wave steepness can be observed in our results at wave age $C_p/u_* = 10$ where β is about 30% larger for case WA10 (b) ($ak = 0.16$) compared to case WA10 (a) ($ak = 0.2$). This trend has also been observed by Yang and Shen (2010): they developed DNS of a stress-driven turbulent Couette flow over waving surfaces, such as Airy and Stokes waves with and without wind-induced surface drift, as well as stationary wavy wall and vertically waving walls for comparison. They considered two wave steepness values, $ak = 0.1$ and 0.25, and three wave ages, $C_p/u_* = 2$, 14 and 25. Turbulent flow structure was found to be strongly dependent on wave age. For slow waves ($C_p/u_* = 2$), the geometric effect of the wave on turbulence dominates, whereas for intermediate and fast waves ($C_p/u_* = 14$ and 25), the kinematic effect of the wave on turbulence dominates over the geometric effect. Their analysis showed that the wind-induced growth rate parameter of slow waves decreases as the wave steepness increases: the wave tends to influence distributions of turbulent quantities and the larger ak the further the influence extends into the bulk flow.

	Stokes wave ($ak = 0.16$)		Stokes wave ($ak = 0.2$)	
C_p/u_*	F_p	β	F_p	β
1.6	-	-	-0.44	22
5	-	-	-0.48	24
10	-0.41	32	-0.46	23

	Airy wave ($ak = 0.1$)		Stokes wave ($ak = 0.25$)	
C_p/u_*	F_p	β	F_p	β
2	-0.161	32	-0.540	17.27
14	-0.005	1	0.0001	-0.004

Table 4.2: Form drag and wave growth parameter for various underlying waves (our current results (*left*) are compared to DNS results from Yang and Shen (2010) (*right*)). Note that the DNS results from Yang and Shen (2010) are expressed in the wave-following coordinates system (4.5).

The numerical simulations by Yang and Shen (2010) provide some points of comparison for our set of simulations. Table 4.2 shows the dimensionless form drag and the wave growth rate parameter for our four cases in comparison with DNS results by Yang and Shen (2010). A negative form stress acts as a drag on the surface winds, which is the case for the results of Yang and Shen (2010). Case WA1 lies in their results, but cases WA10 (a) and (b) seem far from their values, since they obtained a reverse in the sign of the form drag, meaning that their waves act as a thrust on the surface winds. In our case, even if the wave age is smaller ($C_p/u_* = 10$), the trend does not seem to lead to a reverse sign so quickly.

While looking at the instantaneous pressure contours of the one-coupled simulation with wave age $C_p/u_* = 10$ in Figure 4.12, bumps can be observed at the top of the domain, below the upper boundary. A convergence study is thus needed in order to quantify the influence of the height of the domain on the airflow near the surface.

4.2.1.1 Convergence study on the mesh and the height of the air domain

When increasing the wave age, the ratio between irrotational motions and turbulence is changing. As formerly mentioned, successive bumps of positive and negative magnitude are observed in the pressure field in Figure 4.12, below the upper boundary, in the case of a non-linear monochromatic wave of wavelength $\lambda = 2.78$ m and steepness $ak = 0.2$ underlying an airflow characterised by a wave age $C_p/u_* = 10$.

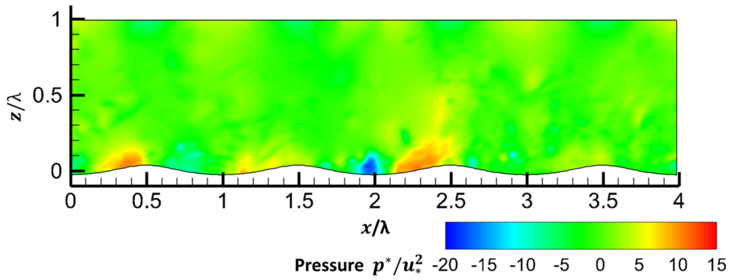

Figure 4.12: Instantaneous contours in a $x - z$ plane of dimensionless pressure for a one-way coupled simulation of a non-linear monochromatic wave underlying a strong airflow. The non-linear regular wave has a wavelength $\lambda = 2.78$ m and a steepness $ak = 0.2$ and the wind-wave speed ratio is defined by the wave age $C_p/u_* = 10$.

These bumps are the consequence of the incompressible assumption and the zero-gradient boundary conditions of the domain. Any pressure disturbance at the free surface will immediately be seen throughout the domain. Due to the remeshing process, the geometric conservation law must be satisfied by the numerical discretisation so that the entire scheme is conservative as stated in Equation (3.37):

$$\frac{\partial}{\partial t}\left(\frac{1}{\mathcal{J}}\right) = -\frac{\partial z_t}{\partial \zeta}. \tag{4.6}$$

Having a fine mesh and small time steps, the Jacobian is approximately 1 especially at the upper boundary and its time derivative is thus 0 approximately. The time derivative of the grid speed z_t is then constant in the ζ direction (i.e. the vertical direction). The grid speed is imposed at the lower boundary in order to get a "no normal flux" condition at the free surface and is set to the time derivative of the free surface elevation, h_t. Thus, at the upper boundary, as the top is flat, the imposed "no flux normal to the boundary "condition implies $W_f = w = z_t \neq 0$ when a moving wavy surface is considered. The pressure bumps are negligible when dealing with small waves but, when increasing the wave amplitude, these bumps prevail over the amplitude of the bumps developing above the free surface. The fix would be to have no remeshing (i.e., a stationary wave at the bottom of the domain) or to have a wavy top boundary. However, these modifications of the code (Sullivan et al., 2014) are out of the scope of this thesis: the influence of the pressure bumps is maintained far enough from the zone of interest by increasing the height of the domain, so that they do not interfere with the turbulent structures developing near the free surface. A convergence study on the influence of the height of the computational domain is thus needed.

	Dimensions	Discretisation	Height of first cell	Stretching factor
Case WA10 (i)	$4\lambda \times 2\lambda \times 1\lambda$	$256 \times 128 \times 80$	5×10^{-3}	1.02
Case WA10 (ii)	$4\lambda \times 2\lambda \times 1\lambda$	$256 \times 128 \times 113$	5×10^{-3}	1.009
Case WA10 (iii)	$4\lambda \times 2\lambda \times 2\lambda$	$256 \times 128 \times 110$	5×10^{-3}	1.02
Case WA10 (iv)	$4\lambda \times 2\lambda \times 2\lambda$	$256 \times 128 \times 167$	5×10^{-3}	1.009
Case WA10 (v)	$4\lambda \times 2\lambda \times 5\lambda$	$256 \times 128 \times 152$	5×10^{-3}	1.02
Case WA10 (vi)	$4\lambda \times 2\lambda \times 5\lambda$	$256 \times 128 \times 253$	5×10^{-3}	1.009

Table 4.3: Characteristics of the different meshes for the convergence study on the influence of the height of the air domain.

Six meshes have been compared in order to study the influence of the height of the domain, and the influence of the vertical stretching. Three heights are tested, 1λ (previous case), 2λ and 5λ, combined with two vertical stretching factors, 1.02 and 1.009. The vertical stretching factor 1.009 corresponds to the spacing ratio tested in Sullivan et al. (2014), but this vertical discretisation leads to heavy meshes, hence the desire of decreasing this factor. The following wind-wave configuration is implemented: a non-linear monochromatic wave characterised by a wavelength $\lambda = 2.78$ m and a wave steepness $ak = 0.2$ propagates in a horizontal domain of dimension $4\lambda \times 2\lambda$ discretised by 256×128 grid points. Periodicity is implemented in $x-$ and $y-$directions. The first cell is located at $5 \times 10^{-3}\lambda$ above the free surface for all the cases. The propagation of the wave is solved at each time step by the HOS model and quantities such as wave elevation, orbital velocities and time derivative of the elevation are sent back to the air simulation through the one-way coupling. The air is considered as neutral and the lower and upper boundaries satisfy the "no flux normal to the boundary" condition. The speed ratio between the airflow and the wave is imposed through the initial wave age $C_p/u_{*_{\text{initial}}} = 10$, which mimics soft forced conditions compared to the previous cases with $C_p/u_* = 1.6$. Details about the mesh are found in Table 4.3.

Figure 4.13 illustrates the temporal evolution of the dimensionless friction velocity $u_*/u_{*_{\text{initial}}}$ for the six aforementioned cases. It can be noticed that, after a time period of approximately $20 - 25$ dimensionless time units, the friction velocity seems to converge for all cases. Statistics are obtained by a combination of space and time averages in order to increase the efficiency of these averaging operations. Spatial averages are conducted over $\xi - \eta$ surfaces since the domain is horizontally periodic. The resulting vertical profiles (e.g. Figure 4.14) are then averaged in time: time averaging is taken over a time period when the boundary layer is quasi stationary. An average of the quantities is then computed from $t = 20$ until the end of each simulation in order to get statistics. Note that case WA10 (iii) has not been run long enough (until $t = 22$), so the results should be treated with caution.

Statistics are computed on the vertical profile of the wind speed, the pressure, the momentum flux and the pressure stress. The influence of the height of the air domain is nearly negligible on the vertical profile of the horizontal velocity (Figure 4.14). Small differences occur at the top of each box, but near the free surface, for $\zeta < 2$ m, the results agree very well with each other. The green dashed curve (case WA10 (iii)) is slightly different but this is certainly due to the fact that the statistics were run on a time period of 2 compared to 50 at least for the other cases. Concerning the pressure, the height of the box has a significant impact on the vertical profile. This is due to the fact that the boundary conditions on the pressure are gradient conditions at the top of the domain. But the maximum value (in magnitude) in the vertical profile occurs at the same height for all the cases and the value is similar for cases WA10 (iii) to WA10 (vi).

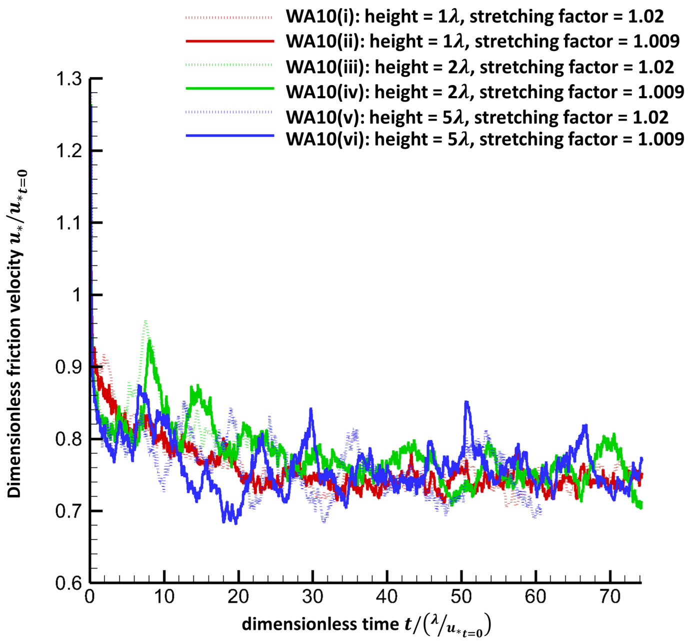

Figure 4.13: Temporal evolution of the dimensionless friction velocity at the first cell above the free surface for a same sea state and various heights and vertical stretching of the mesh of the air domain. The non-linear regular wave has a wavelength $\lambda = 2.78$ m and a steepness $ak = 0.2$ and the wind-wave speed ratio is defined by the wave age $C_p/u_* = 10$.

Figure 4.15 shows the vertical profiles of the average vertical flux of horizontal momentum (resolved and SGS contributions) and pressure drag. The vertical profile of the u-momentum flux corresponds to the expected momentum profile for a turbulent planetary boundary layer over a rough surface (Sullivan et al., 2008): it is negative with positive vertical divergence. Once again, the significant influence of the height on the momentum flux is observed, even if the values in the vicinity of the free surface are similar. The signature of the pressure stress shows the same tendency: at the wavy surface, the waves impart a negative drag on the wind of the same order. In other words, there is, as expected, a significant momentum transfer from the atmosphere to the ocean. The vertical profile of the pressure drag is in fairly good agreement for all the cases.

In conclusion, the height of the domain has a significant impact on the

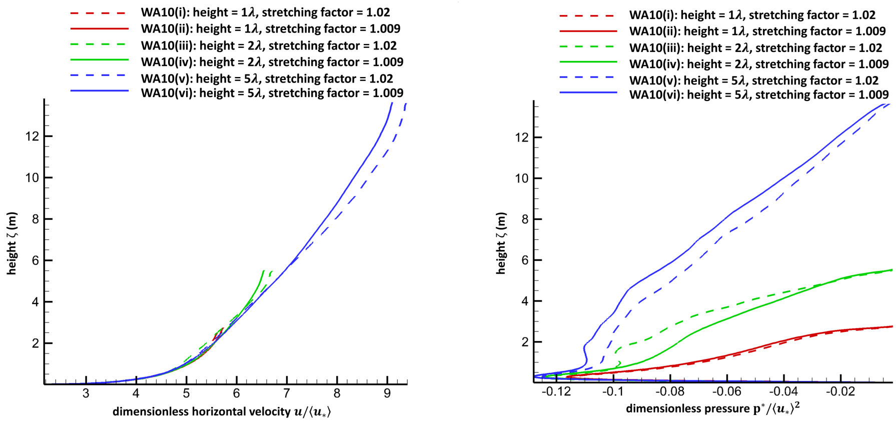

Figure 4.14: Vertical profiles of average dimensionless wind speed (*left*) and pressure (*right*). The non-linear regular wave has a wavelength $\lambda = 2.78$ m and a steepness $ak = 0.2$ and the wind-wave speed ratio is defined by the wave age $C_p/u_* = 10$.

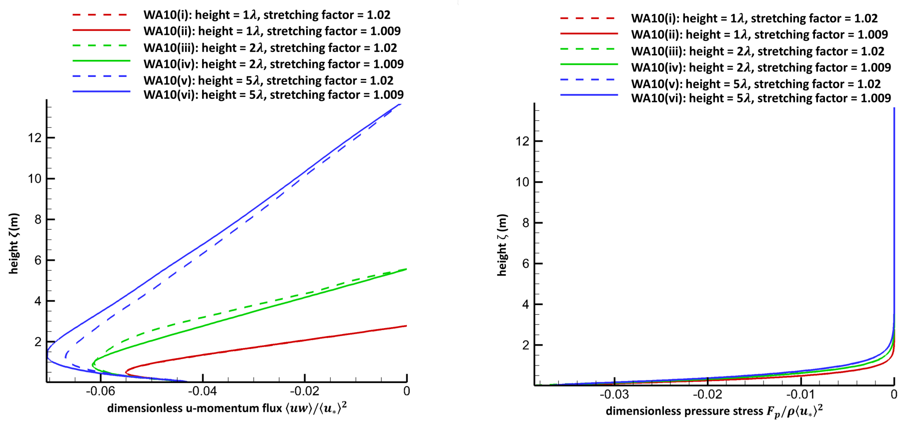

Figure 4.15: Vertical profiles of average dimensionless vertical flux of horizontal momentum (*left*) and pressure drag (*right*). The non-linear regular wave has a wavelength $\lambda = 2.78$ m and a steepness $ak = 0.2$ and the wind-wave speed ratio is defined by the wave age $C_p/u_* = 10$.

pressure and the momentum flux profiles, even if the values in the vicinity of the free surface are quite similar. This influence is due to the fact that the air domain is modelled as a wind channel and gradient conditions are imposed at the flat upper boundary. However, the height has nearly no impact on the wind and the pressure drag profiles.

4.2.1.2 Influence of the wave spectrum content

At the beginning of this section, the comparative study of cases WA10 (a) and (b) showed that the wave steepness has an impact on the wind-induced growth rate parameter for waves with same wavelength ($\lambda = 2.78$ m) and wave age ($C_p/u_* = 10$). This section sets out to take a practical look at the influence of the wave spectrum content on the overlying airflow.

The same case with a wave age $C_p/u_* = 10$ is considered here. It represents a case where the wind slightly forces the sea state. Two parameters have been tested:

1. the sea state type, i.e. non-linear regular waves are compared to irregular sea states,

2. the distribution of the energy in the wave spectrum, i.e. simulations with similar total wave energy are compared to simulations with similar wave energy at the peak.

A specific wave steepness is introduced, $A_s k_p$, with A_s the amplitude related to the total energy in the wave spectrum. For a regular sea state, $A_s = a$, whereas for an irregular sea state, $A_s = \frac{H_s}{2\sqrt{2}}$.

	Wave type	Steepness $A_s k_p$	Energy at the peak	Total linearised energy
Case 1 (red symbols)	regular	0.2	3.74×10^{-3}	3.78×10^{-3}
Case 2 (orange symbols)	irregular ($\gamma = 3.3$)	0.2	1.57×10^{-3}	3.90×10^{-3}
Case 3 (green symbols)	irregular ($\gamma = 10.0$)	0.2	2.46×10^{-3}	3.90×10^{-3}
Case 4 (grey symbols)	irregular ($\gamma = 10.0$)	0.249	3.8×10^{-3}	6.06×10^{-3}
Case 5 (blue symbols)	regular	0.16	2.46×10^{-3}	2.47×10^{-3}

Table 4.4: Characteristics of the different wave fields depending on the composition of the wave spectrum.

Definition of the total linearised energy

The peak energy is the energy at the peak of the wave spectrum, i.e. $\frac{1}{2}a(k_p)^2/\Delta k$, and the total energy represents the sum of the energy at each wavenumber k_i. Δk is related to the spatial discretisation of the domain of the sea state. Here, the concept of total energy defined as $\sum_i \frac{1}{2}\frac{a(k_i)^2}{\Delta k}$ is based on the linearisation of the energy. Indeed, if a linear monochromatic wave is considered, the amplitude spectrum is composed of one single peak. Due to the non-linear nature of surface water waves, free waves interact among themselves: a non-linear monochromatic wave will have an amplitude spectrum composed of one major peak, i.e. the free wave, and secondary peaks, i.e. the bound waves resulting from the wave-wave interactions among free waves. The same remark stands for an irregular sea state: if non-linearities are solved, the spectrum is composed of free waves and bound waves. Eventually, all the sea states will be solved with an order of non-linearities $M = 3$ and will have the same spatial discretisation leading to $\Delta k = 0.56$ m^{-1}.

Description of the sea states

Five sea states have been implemented. Table 4.4 shows the wave characteristics of the different sea states considered in this study. The reference case, case 1, represents the non-linear regular wave presented in the previous section. Case 2 is an irregular sea state (i.e. a JONSWAP spectrum with $\gamma = 3.3$) with the same wave steepness as case 1: the total energy is approximately the same as case 1, but since it represents an irregular case with a continuous distribution of the energy over various wavelengths k_x, the energy at the peak is smaller. Case 3 is the same case as case 2 but the concentration of energy around the peak of the spectrum is larger ($\gamma = 10.0$ instead of 3.3 for case 2). The total linearised energy is thus the same as case 2 but with a bigger component at the peak. Case 4 also represents an irregular sea state and the energy at the peak is of the same order as the energy at the peak in case 1. This leads to a modification of the wave steepness, $A_s k_p = 0.249$, and to a larger total energy. The last case, case 5, represents a non-linear regular wave whose energy at the peak is the same as case 3: the wave steepness of this wave is thus smaller, $A_s k_p = ak = 0.16$. It is important to note that all the wave simulations, especially for the irregular sea states, are based on the same discretisation of the spectral space: indeed the initialisation of the JONSWAP spectrum is based on a imposed energy density of the wavefield (i.e., $H_s \approx 4\sqrt{E}$) and the wavefield spectrum is initially constructed by a superposition of linear components based on the spectral discretisation k_x which is related to the discretisation of the physical domain.

Figure 4.16 illustrates the linearised wave energy spectrum for each case previously described. The peaks of the wave spectra are located at $k_p = 2\pi/\lambda_p$, with $\lambda_p = 2.78$ m for all the simulations.

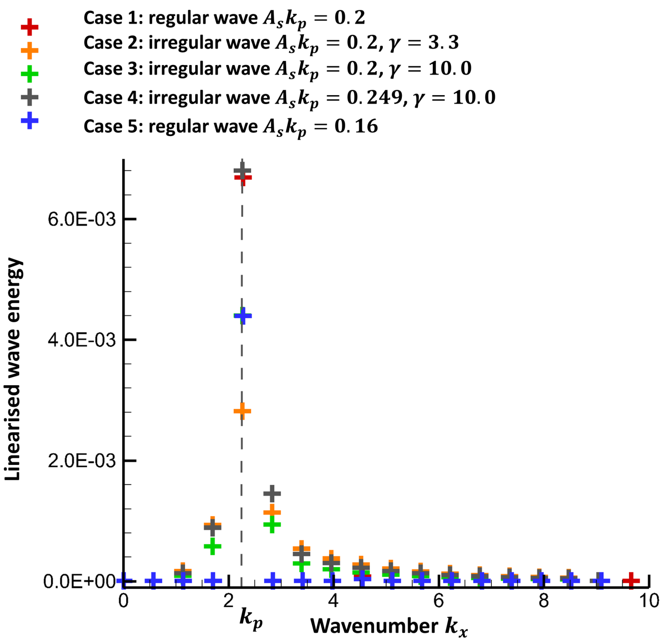

Figure 4.16: Linearised energy spectrum for five sea states with wavelength $\lambda_p = 2.78$ m and wave age $C_p/u_* = 10$. The vertical dashed line is the value of $k_p = 2\pi/\lambda_p$.

Description of the airflow simulation

Concerning the airflow simulations, we consider a computational domain of dimensions $4\lambda \times 2\lambda \times 1\lambda$ with the wavelength of the sea state $\lambda = 2.78$ m. The domain is discretised using $256 \times 128 \times 113$ grid points with the first cell located at 1.4×10^{-2} m above the free surface. The horizontal grid spacing is $\Delta\xi = \Delta\eta = 4.3 \times 10^{-2}$ m and the spacing ratio between two vertical cells is 1.009. This discretisation leads to a vertical distribution of approximately 6 cells between the trough and the crest of the wave. The unresolved surface waves are modelled by a fixed surface roughness $z_0 = 2 \times 10^{-4}$ m. The air domain is represented by a wind tunnel where the air is considered as neutral (i.e., no buoyancy effect) and there is no net flow across the lower and upper boundaries. The speed ratio between wind and wave velocities is initially imposed with the wave age $C_p/u_* = 10$.

Temporal evolution of the friction velocity and the growth rate parameter

Figure 4.17 shows the temporal evolution of the friction velocity at the first cell centre above the free surface for the five cases previously described. This first cell centre is located at the same height for all the cases since the mesh is the same. Three groups can be identified. Case 5 (blue) has the highest friction velocity (i.e. more wind near the free surface): it is the case with the smallest wave steepness and the smallest total energy. Cases 1 (red), 2 (orange) and 3 (green) have more or less the same trend. Case 4 (grey) has the smallest friction velocity (i.e. less wind, or a wind being slowed down): it is the case with the largest wave steepness and the largest total energy and energy at the peak.

Figure 4.18 illustrates the temporal evolution of the wave growth rate parameter β. One can notice the large fluctuation in the temporal evolution of β for irregular sea states compared to regular waves. This is due to the fact that all the contributions of the wavelengths of the irregular sea states are taken into account in the computation of the form drag and thus in β. The wave steepness related to the total energy is used in the calculation of β:

$$\beta = \frac{2F_{p_{\text{global}}}}{(A_s k_p)^2}.$$

Comparison of global statistics

Statistics are obtained by a combination of space and time averages in order to increase the efficiency of these average operations. Here the time average is computed from approximately 250 s until the end of the simulation. Figure 4.19 shows the vertical profiles of the average wind speed. The dashed line illustrates the initial mean wind, i.e. before the surface waves are introduced in the domain and after the initialisation of the simulation over a flat lower boundary during which the initialisation simulation runs until the turbulence is in near statistical equilibrium. One can notice the low-level jet due to the heat flux imposed at the surface during the initialisation in order to activate

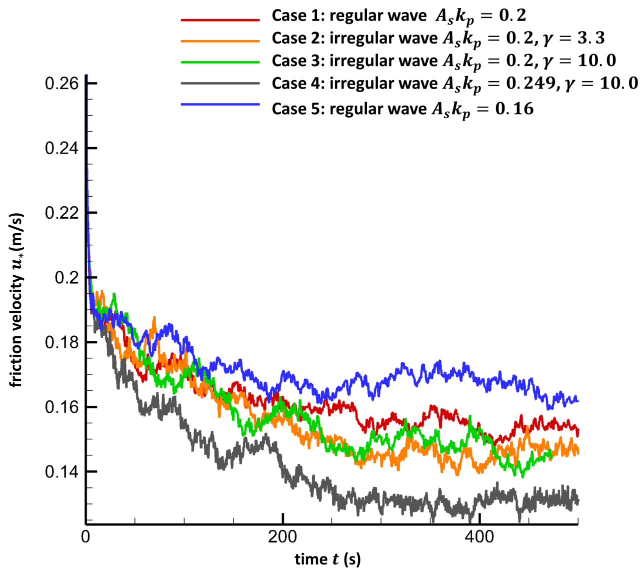

Figure 4.17: Friction velocity at the first cell for sea states with various spectral composition. Sea states have the same wavelength $\lambda_p = 2.78$ m and wave age $C_p/u_* = 10$.

the turbulence. The three groups previously identified are also present in this figure: case 5 (blue) with a wind profile that has been less slowed down compared to the initial wind profile, cases 1 (red), 2 (orange) and 3 (green) with quite similar results for the two irregular cases (which only differ from each other with the value of γ in the JONSWAP spectrum), and, finally, case 4 (grey) with a slower wind profile. These results are strengthened by the temporal evolution of the friction velocity at the first cell in Figure 4.17 where the same trend has been observed. We emphasise the fact that the speed ratio between wind and wave is the same in all simulations with a wave age $C_p/u_* = 10$. A sea state with a larger spectral content tends to slow down the wind more notably .

Figure 4.20 shows the vertical profiles of the average vertical flux of horizontal momentum (resolved and SGS contributions) and pressure drag. The vertical profile of the u-momentum flux is as expected for a turbulent planetary boundary layer over a rough surface (Sullivan et al., 2008): it is negative with positive vertical divergence. The signature of the pressure stress shows

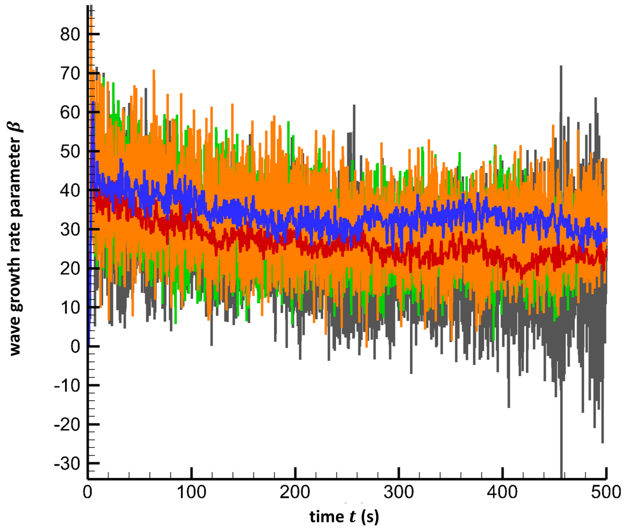

Figure 4.18: Temporal evolution of the wave growth rate parameter for various sea states.

the same tendency: at the wavy surface, the waves impart a negative drag on the wind. In other words, there is, as expected, a significant momentum transfer from the atmosphere to the ocean.

Comparison of statistics at $t = 50$, 100 and 200 T_p

In order to observe the temporal evolution of the quantities, statistics have been computed over 20 wave periods at different time instants (50, 100 and 200 T_p). Figure 4.21 shows the temporal evolution of the average wave growth rate parameter and form drag at the free surface. As previously specified, the form drag is negative at the free surface, meaning that the wind is thrusting the wave, or the wave is dragging the wind: the behaviour is as expected since the imposed condition is a forced condition with an initial wave age $C_p/u_* = 10$. The three groups are also identified in the pressure drag plot: case 5 (blue) is the less energetic wave with a smaller steepness (and thus a smaller amplitude) and has the smallest form drag in magnitude at the free surface, whereas case 4 (grey) is the most energetic wave and has the largest form drag. In between are cases 1 (red), 2 (orange) and 3 (green) with a similar total wave energy. Over time, the form drag decreases in magnitude for all the cases, but the trend is more significant for case 4. This

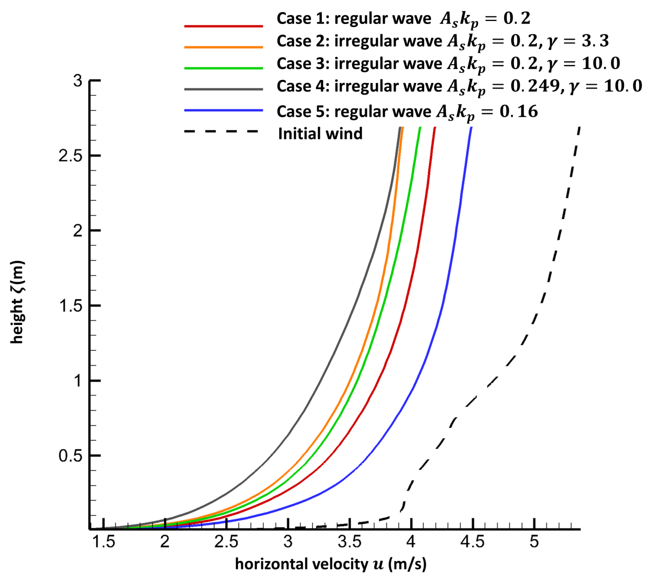

Figure 4.19: Vertical profiles of average wind speed for sea states with various spectral composition. Sea states have the same wavelength $\lambda_p = 2.78$ m and wave age $C_p/u_* = 10$.

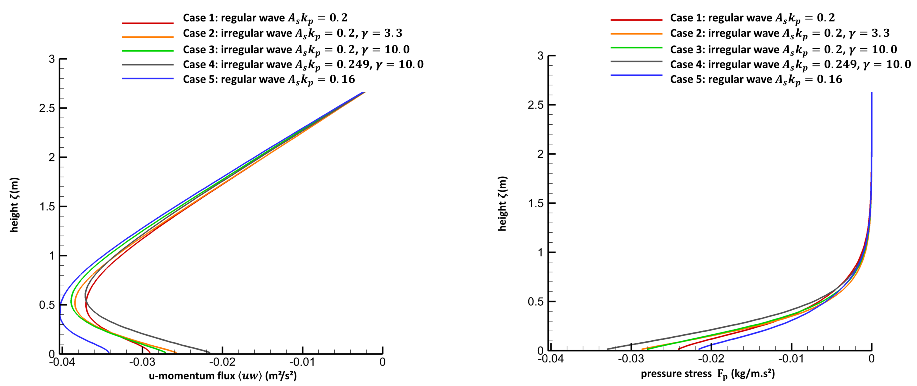

Figure 4.20: Vertical profiles of average vertical flux of horizontal momentum (*left*) and pressure drag (*right*). Sea states have the same wavelength $\lambda_p = 2.78$ m and wave age $C_p/u_* = 10$.

time evolution for the form drag is linked to the time evolution of the wave growth: $\beta > 0$ for all cases, we consider a situation of wave growth. This wave growth is hypothetical since the coupling of the pressure from the air simulation to the HOS model is not activated: instead of observing physically a wave growth, the wave field parameters remain constant. The same trend is observed on the time evolution of the wave growth rate parameter: it decreases over time, and a larger spectral content leads to a smaller wave growth and vice versa. The influence of the spectral content near the peak is more noticeable as case 2, which has the same total energy but a smaller distribution of energy at the peak than case 3, feels a larger wave growth.

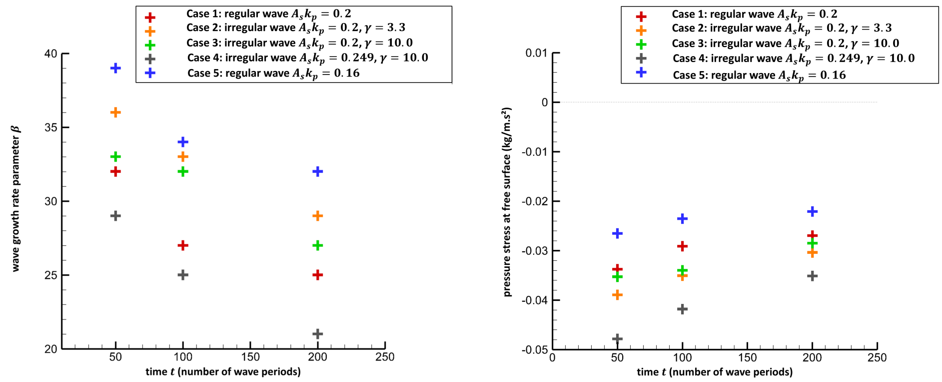

Figure 4.21: Temporal evolution of the mean wave growth rate parameter (*left*) and pressure drag at free surface (*right*). The temporal axis is expressed in terms of number of wave periods. Sea states have the same wavelength $\lambda_p = 2.78$ m and wave age $C_p/u_* = 10$.

Another way to look at the wave growth rate parameter is illustrated in Figure 4.22. β is plotted over the effective wave age with the friction velocity at the first cell averaged over the time period. The decrease in β is correlated with the increase of the effective wave age. The same trend is observed: the less energetic case, case 5 (blue), has a wave growth rate $\beta \approx 40$ at $t = 50\ T_p$ which is related to a small wave age $C_p/u_* = 11.5$, whereas the most energetic case, case 4 (grey), has a growth rate close to 20 at $t = 200\ T_p$ for a wave age $C_p/u_* = 16$. Moreover, it can be noticed that the temporal evolution of the wave age is larger when irregular sea states are considered compared to regular waves. This is due to the fact that the growth rate parameter is calculated using the global form drag for the cases with irregular sea states, i.e. we consider β and not $\beta(k)$.

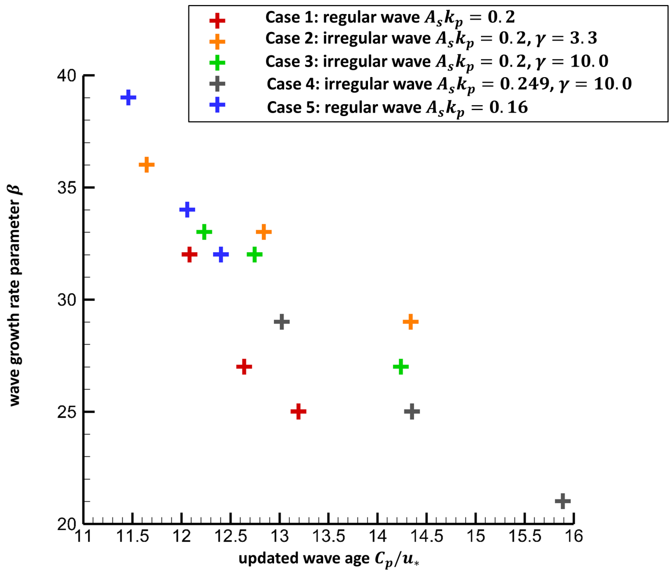

Figure 4.22: Wave growth rate parameter over wave age calculated with the mean friction velocity over specified time periods.

4.2.2 Swell underlying a light wind

Turbulent flow is found to be strongly dependent on wave age. For a small wave age, the geometric effect of the surface wave on turbulence dominates. Yang and Shen (2010) demonstrated that for intermediate wave $C_p/u_* = 14$ and fast wave $C_p/u_* = 25$, the kinematic effect of the surface wave on turbulence dominates the geometric effect. In Table 4.2, the form drag at the free surface reverses sign and the wave growth rate parameter β becomes negative: the form stress begins acting as a thrust on the surface wind. Indeed, field observations and numerical modelling have shown that the atmospheric surface layer can be strongly disturbed by waves, especially nonlocally generated waves (i.e. swell). Air-sea interactions in the swell regime have been mentioned in the first chapter. One can remember the most striking effect of the swell on the MABL, the presence of a low-level wave driven wind jet above the water surface. This wave-driven wind is correlated to an upward transport of momentum from water to air, corresponding to a negative drag coefficient C_D. Often considered as an exotic case, the upward momentum transfer is now associated with the swell regime correlated to a light-wind-speed regime (Grachev and Fairall (2001), Högström et al. (2013)).

Within this framework, a case with one-way coupled simulation between LES and HOS is investigated. The wave age is initially set to 60, and we consider a non-linear monochromatic wave, the characteristics of which are detailed in Table 4.5. As a reminder, the wind-wave equilibrium corresponds to a wave age $C_p/u_* \approx 15-20$. The air domain is still modelled as a wind channel where the air is considered to be neutral (i.e. no buoyancy effects). The mesh follows the free surface elevation given by the HOS code through the mapping transformation (3.33) and a non-uniform vertical grid distribution. The HOS model gives the free surface elevation and its orbital velocity at each time step, and special care is taken so that the lower boundary condition of the air domain satisfies a "no flux normal to the boundary" condition. More information about the mesh is given in the next section as a mesh convergence study is carried out.

Three studies have been carried out on:

- the influence of the initialisation of the air simulation,
- the influence of the spatial discretisation in horizontal and vertical directions,
- the influence of the height of the domain.

Indeed, in the previous case with a wave $\lambda = 2.78$, $ak = 0.2$ and $C_p/u_* = 10$, pressure bumps have been observed below the upper boundary. These bumps are the consequence of the incompressible assumption and the zero-gradient boundary conditions. Hence, a higher domain is considered in this case, where an upward transfer momentum from the waves to the airflow is expected. The starting point for the height of the domain is set to 5λ.

4.2.2.1 Influence of the initialisation

Firstly, the influence of the initialisation of the air simulation is investigated. We consider a box of dimensions $4\lambda \times 2\lambda \times 5\lambda$ discretised by $256 \times 128 \times 80$ grid points. The first cell is located at $5.2 \times 10^{-3}\lambda$ m and the vertical stretching factor is 1.05. With this discretisation, there are approximately 12 cells from the wave trough to the wave crest. The initialisation procedure is activated on the same mesh and domain as for the wind-wave simulation, but on a flat bottom. A constant heat flux is imposed at the bottom of the domain, and the temperature and buoyancy effects are activated during this initialisation. Two parameters have been identified to play with: the value of the heat flux (here, set to 30 K.m.s^{-1}) and the height of the boundary layer inversion. The top of the MABL, z_i, is marked by a steep stable gradient in the potential temperature. When considering a box of 1λ-height with 128 vertical points, z_i was set to $z(100)$, i.e. $z(0.8N_z)$. Here, since a box of 5λ-height is considered, a first case with z_i located at approximately 4λ is implemented. This case is compared to a second one where z_i is located around 0.8λ: the inversion layer is located at the same height as if we had a case with a 1λ-height

		Case WA60
Wind-wave ratio	wave age C_p/u_*	60
Wave parameters	wavelength λ (m)	100.0
	amplitude a (m)	3.18
	steepness ak	0.2
	phase velocity C_p (m.s^{-1})	12.5
Wind parameters	initial friction velocity u_* (m.s^{-1})	0.21
	$U_{10\text{m}}$ calculated from log law (m.s^{-1})	6.0

Table 4.5: Characteristics of the wave field and the initial wind imposed for a case of a swell propagating in light wind conditions ($C_p/u_* = 60$).

box.

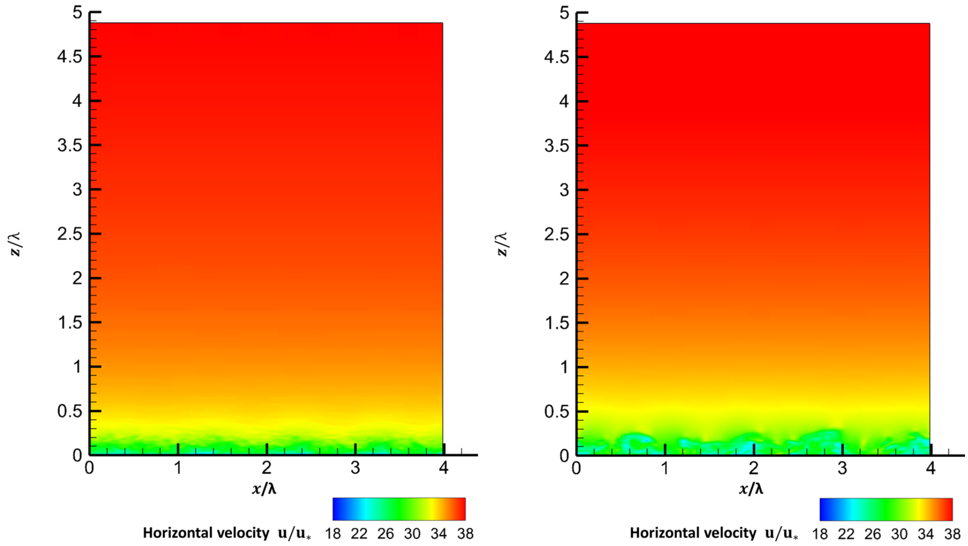

Figure 4.23: Initial instantaneous contours in a x_z plane of dimensionless horizontal velocity for a one-way coupled simulation with a wave age $C_p/u_* = 60$. The air domain has been initialised with a configuration where z_i is located at 0.8λ (*left*) and 4λ (*right*).

Figure 4.23 shows the initial instantaneous contours of the dimensionless horizontal velocity, just after the initialisation procedure and before the introduction of the wave through the ramp into the domain. The turbulence is in near statistical equilibrium at the end of the initialisation. Here we note that the layer near the free surface seems to be more turbulent and seems to extend higher in the domain for the case where z_i is located at 4λ, whereas z_i being located closer to the surface (0.8λ) seems to compress the turbulence near the surface. Since we consider neutral conditions thereafter, we initially want to get rid of the effects due to a too low inversion boundary layer. Hence, we would like to choose the case where the inversion layer is as high as possible in the initialisation run so that it does not influence the wind near the free surface.

Statistics are computed at different times over 100 wave periods in order to observe the temporal evolution of quantities such as wind speed, pressure, momentum flux and pressure stress and to evaluate the influence of the initialisation on this temporal evolution. Statistics are computed at successive time periods and not on a whole simulated time because this case of wave age C_p/u_* is expected to represent a case of a wave forcing the airflow. Indeed the wave age is larger than the equilibrium range values $(15-20)$. As the pressure coupling from the air to the ocean simulation is not activated, the sea state does not evolve with the pressure at the interface. The wave brings a continuous amount of energy to the wind and the wind-wave equilibrium may take a long time to occur. Hence, the statistics are computed over 100 wave periods at $t = 500\ T_p$, $1000\ T_p$ and $1500\ T_p$. The time evolutions of the dimensionless mean horizontal velocity, pressure, u-momentum flux and pressure stress are plotted in Figure 4.24.

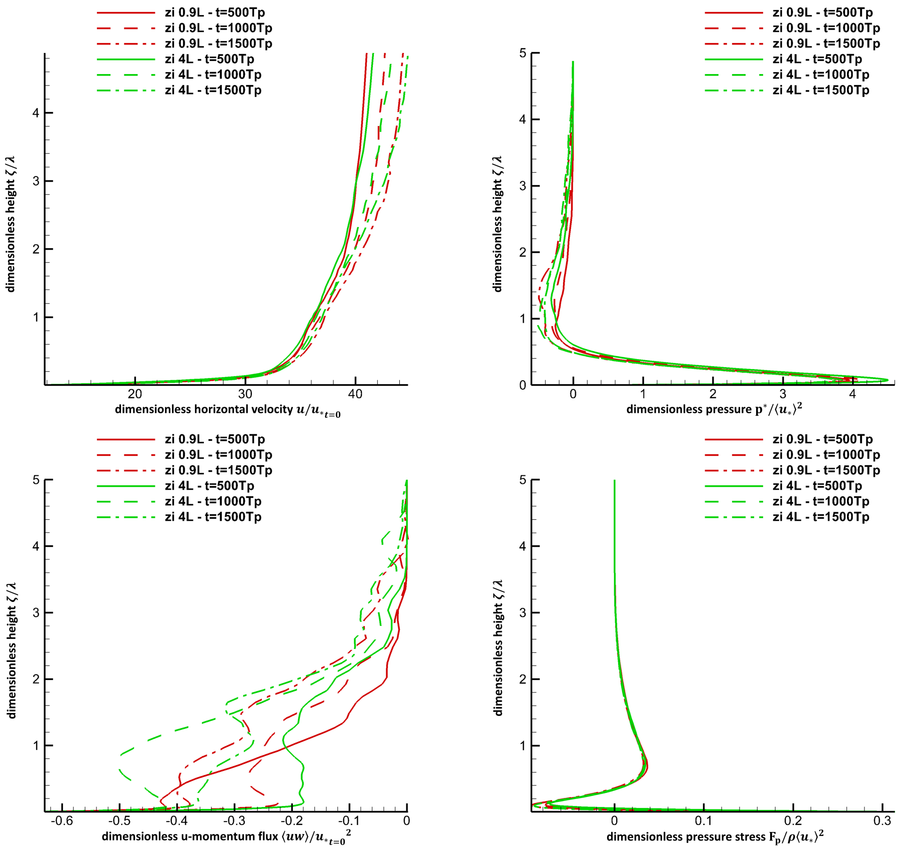

Figure 4.24: Time evolution of the vertical profiles of the average wind speed (*top left*), pressure (*top right*), u-momentum flux (*bottom left*) and pressure stress (*bottom right*) for two initialisations of a wind-wave simulation with wave age $C_p/u_* = 60$.

The comparison of the profiles of velocity, pressure and pressure stress shows that the value of z_i does not have a real impact on the vertical profile. The impact is more significant for the vertical profile of the momentum flux. Its evolution is quite fluctuating, but it seems to converge for the profile at $t = 1500\ T_p$. We notice that the momentum flux is still negative, whereas the pressure stress reverses sign at the free surface (i.e., becomes positive compared to previous cases with smaller wave ages). The profile becomes negative around $\zeta/\lambda = 4 \times 10^{-2}$ and reverses sign again around $\zeta/\lambda = 0.4$ and has its maximum value around $\zeta/\lambda = 0.75$. Nevertheless, if the pressure stress and the momentum flux are added, it is not sufficient to get a positive total flux, and thus a positive upward transfer of momentum. To conclude on the influence of the initialisation, the height of the inversion layer has an impact until a time period equivalent to 1500 wave periods, but no upward momentum transfer is observed in any case.

4.2.2.2 Influence of the spatial discretisation

The study is carried out on the same case, i.e. a wave of wavelength $\lambda = 100$ m, wave steepness $ak = 0.2$ propagating in an air domain with a wave age $C_p/u_* = 60$. The air domain is modelled as a wind channel, with $(4\lambda, 2\lambda, 5\lambda)$ dimensions, and the air is considered as neutral. The study focuses on the spatial discretisation, in $x-$ and $y-$directions and in $z-$direction. The aspect ratio at the free surface is set to $\Delta x/\Delta z_0 = 3$ which is considered a reasonable number. Firstly, we impose the spatial discretisation in the horizontal directions as a power of 2 since spatial derivatives in the (ξ, η) computational coordinates are estimated using pseudospectral approximations based on FFT. Three discretisations are chosen, $N_x = 128$, 256 and 512, corresponding to a first vertical cell $\Delta z_0 = 1.04 \times 10^{-2}\lambda$ m (i.e. 6 vertical grid points from wave trough to wave crest), $5.2 \times 10^{-3}\lambda$ m (i.e. 12 vertical grid points from wave trough to wave crest) and $2.6 \times 10^{-3}\lambda$ m (i.e. 24 vertical grid points from wave trough to wave crest) respectively. Three vertical stretching factors are tested: 1.08, 1.05 and 1.02.

	Number of points per wave height	N_x	N_y	N_z	Stretching factor
WA60 (a)	6	128	64	67	1.05
WA60 (b)	12	256	128	57	1.08
WA60 (c)	12	256	128	80	1.05
WA60 (d)	12	256	128	152	1.02
WA60 (e)	24	512	256	94	1.05

Table 4.6: Spatial discretisation of a wind-wave simulation with wave age $C_p/u_* = 60$ for a mesh convergence study.

Statistics are computed over 100 wave periods at $t = 500\ T_p$ and 1000 T_p. The time evolutions of the dimensionless mean horizontal velocity, pressure, u-momentum flux and pressure stress are plotted in Figure 4.25. The case with the smallest horizontal discretisation (i.e. $N_x = 128$), WA60 (a), is illustrated by red lines, cases with $N_x = 256$ are depicted by lines with shades of green, and the case with $N_x = 512$, WA60 (e), is illustrated by blue lines. Solid and dashed lines correspond respectively to statistics computed

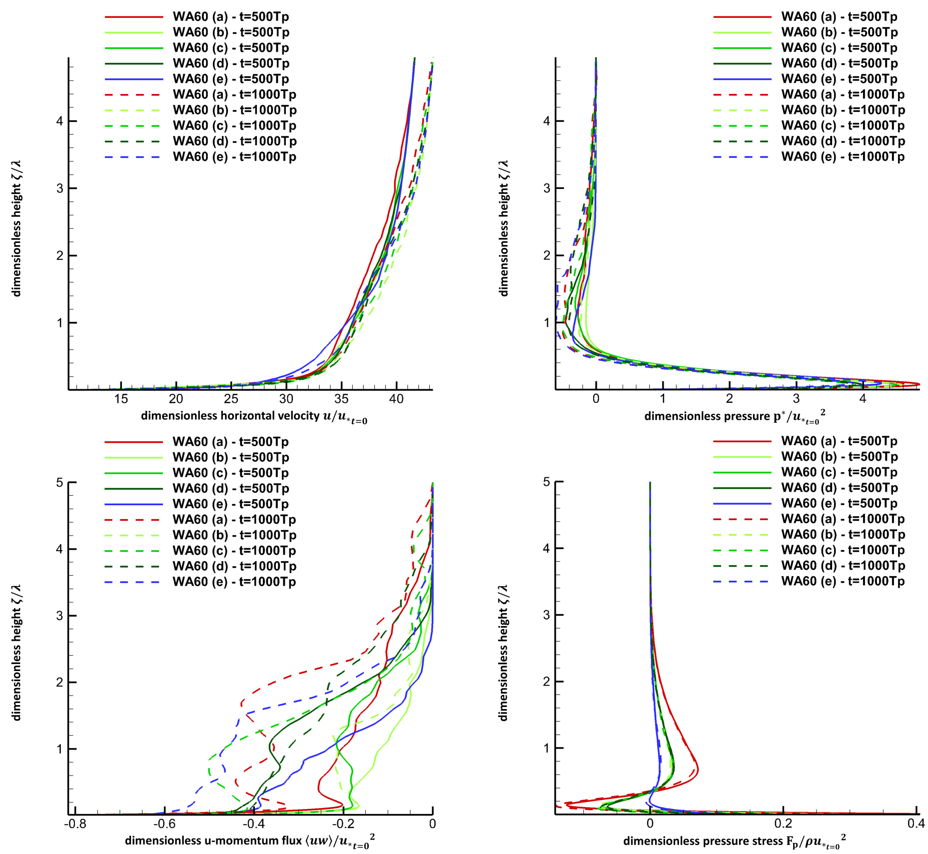

Figure 4.25: Time evolution of the vertical profiles of the average wind speed (*top left*), pressure (*top right*), u-momentum flux (*bottom left*) and pressure stress (*bottom right*) for various mesh discretisation for a wind-wave simulation with wave age $C_p/u_* = 60$.

at $t = 500\ T_p$ and $1000\ T_p$.

First of all, we notice that the horizontal discretisation has an impact on each quantity. For the velocity profile, small deviations are observed with the wind being slowed down or less accelerated around $\zeta/\lambda = 0.6$ for case WA60 (e) at $t = 500\ T_p$. But the wind profile in this highly discretised case then tends to be similar to other cases at $t = 1000\ T_p$. For the pressure profile, the horizontal discretisation has an influence on the maximum value around $\zeta/\lambda = 0.2$, with the smallest discretisation leading to a larger value whereas this maximum value tends to decrease and to converge for the other cases with $N_x = 256$ and 512. For the u-momentum flux, it is difficult to observe any trend in the profile. The only observation that can be made is about the height from which the profile tends to zero: the finer the horizontal discretisation is, the smaller is the height where the momentum flux tends to zero. Over time, this height tends to become higher. Moreover, for all cases, the momentum flux is negative, corresponding to a downward transfer from the atmosphere to the ocean. A small jet is observed in the momentum flux profile near the wavy surface (the maximum value is still negative but this may lead to a wind jet over time or if the wave age increases), but for case WA60 (e), this maximum value is quite smaller compared to the other cases. Concerning the pressure stress, the time evolution is quasi-constant. Moreover, the influence of the horizontal discretisation is quite striking: a minimum value is observed close to the wavy surface (at the same height where a maximum value in the momentum flux profile has been observed), this value decreases while the horizontal discretisation increases. The same trend is observed for the maximum value around $\zeta/\lambda = 0.6$: this maximum tends to decrease in amplitude while the horizontal discretisation increases. Thus, from a profile where positive values are observed in the vicinity of the free surface, then negative values around $\zeta/\lambda = 0.6$ acting as a drag on the wind, and finally positive values acting as a thrust on the wind, the increase in the horizontal discretisation leads to a positive profile with very small variations over height for case WA60 (e). Moreover, the form drag at the free surface is quite smaller for case WA60 (e) compared to the other cases.

The influence of the vertical discretisation on the averaged profiles, except for the momentum flux profile, is quasi negligible compared to the influence of the horizontal discretisation. In conclusion, for the meshes with $N_x = 128$ and 256 with different vertical stretching factors, an influence is observed on the profiles. However, for the simulation with $N_x = 512$, even if the "physical" quantities such as the pressure and velocity seem to converge, the behaviour of the pressure drag and the u-momentum flux is quite different near the free surface. A smaller pressure drag is also noticed at the free surface. This specific case needs further investigations and will be set aside in this study.

4.2.2.3 Influence of the height of the domain

Two cases with the same horizontal discretisation, size of the first cell and vertical stretching factor, but with different vertical heights are compared. The first case is the case WA60 (c) with a box of dimensions $(4\lambda, 2\lambda, 5\lambda)$ discretised by $256 \times 128 \times 80$ grid points and a first cell size value $\Delta z_0 = 5.2 \times 10^{-3}\lambda$ m and a stretching factor of 1.05. The second case has a box of dimensions $(4\lambda, 2\lambda, 10\lambda)$ discretised by $256 \times 128 \times 94$ grid points and a first cell size value $\Delta z_0 = 5.2 \times 10^{-3}\lambda$ m and a stretching factor of 1.05.

In order to evaluate the influence of the height, statistics are computed at successive time periods, $t = 500\ T_p$, $1000\ T_p$, $1500\ T_p$ and $2000\ T_p$ over 100 wave periods for each time period. Figure 4.26 shows the evolution in time of the vertical profile of mean velocity, pressure, momentum flux and pressure stress. These quantities are dimensionless, by using the mean friction velocity at the first cell corresponding to each time period. A global acceleration of the wind can be noticed for both cases, despite the fact that the wind first decelerates between $t = 500\ T_p$ and $1000\ T_p$ for the case with a 5λ-height. Globally, the wind is stronger when the height of the air domain is smaller. Concerning the pressure and pressure stress profiles, evolutions in time of these values are not really significant. We note that the maximum value close to the free surface is smaller for the 5λ-high case, which correspond to a smaller drag close to the surface, whereas around $\zeta \approx 0.75 - 1\lambda$, the pressure is more negative, which means that the pressure stress acts as a thrust with a larger value on the wind when considering the 5λ-high case. But minimum and maximum values are globally reached at the same heights in both cases. Concerning the profile of the momentum flux, the time evolution of this quantity is quite disparate in both cases. It can be noted that, despite different heights, the flux is negative and becomes zero around the same height $\zeta \approx 4 - 5\lambda$ in both cases. The flux is globally larger for the 5λ-high case.

Thus, a larger acceleration of the airflow overlying a non-linear monochromatic wave with a wave age $C_p/u_* = 60$ seems to occur for the smallest wind tunnel. This acceleration is correlated to a larger pressure stress which acts as a larger thrust on the wind.

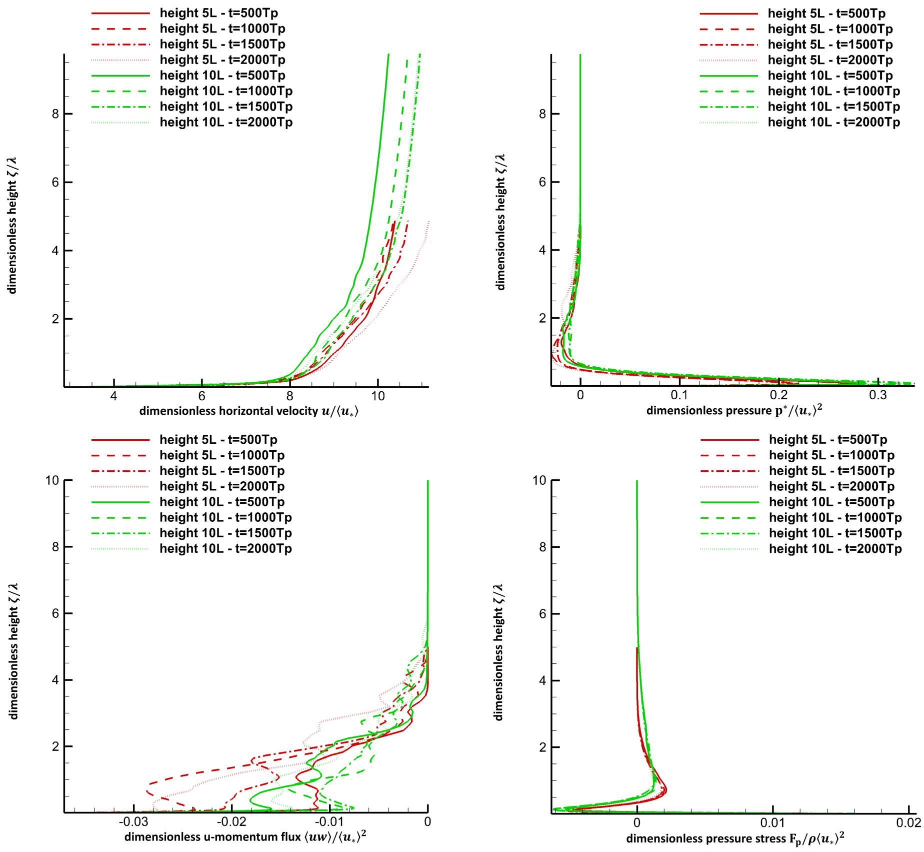

Figure 4.26: Time evolution of the vertical profiles of the average wind speed (*top left*), pressure (*top right*), u-momentum flux (*bottom left*) and pressure stress (*bottom right*) for two heights of the air domain for a wind-wave simulation with wave age $C_p/u_* = 60$.

4.2.3 Wave-induced wind

The previous case with a wave age $C_p/u_* = 60$ tends to show that the wave starts to act as a thrust on the wind, but the total momentum flux does not reverse sign and there is no generation of wind jet in the wind vertical profile. Further analysis has subsequently been undertaken by extending the wave age to $C_p/u_* = 120$. The corresponding wave has a wavelength value $\lambda = 400$ m, a wave period $T \approx 16$ s and a wave steepness $ak = 0.2$. Note that this case was firstly considered as an exploratory case study. Indeed, such a wave would have an amplitude $a = 12.7$ m which is quite enormous and does not represent a realistic sea state. We chose to model this sea state as a non-linear monochromatic wave: this would not be unrealistic for such a swell to have a prevailing frequency in its spectrum and a quite unidirectional direction of propagation.

Once again, the air domain is modelled by a computational box of dimensions $(4\lambda, 2\lambda, 5\lambda)$ discretised by $256 \times 128 \times 80$ grid points. The first vertical cell is located $5.2 \times 10^{-3}\lambda$ above the free surface. This corresponds to a vertical distribution of 12 points from the wave trough to the wave crest. The air is considered as neutral, and no flow across the upper and lower boundaries is imposed.

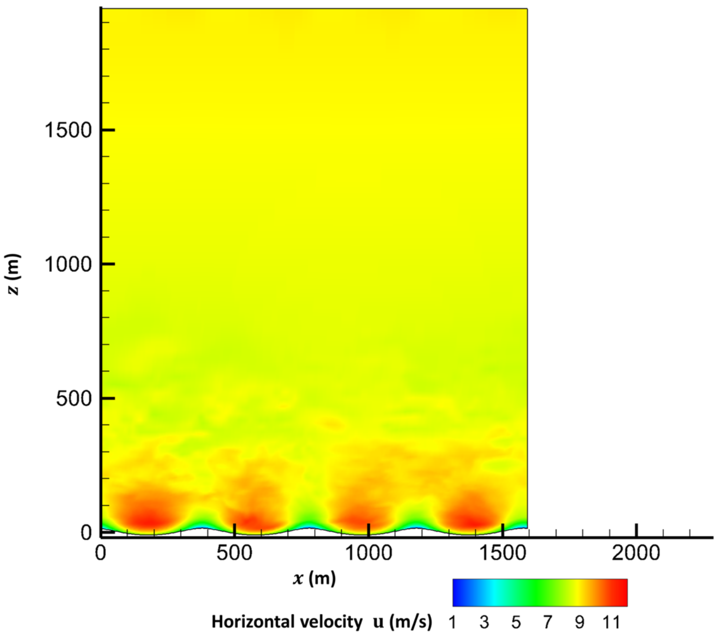

Figure 4.27: Instantaneous contours in a $x - z$ plane of the horizontal wind speed overlying a fast wave ($\lambda = 400$ m, $ak = 0.2$ and $C_p/u_* = 120$).

Figure 4.27 illustrates the instantaneous contours in a $x - z$ plane of the horizontal velocity of the airflow. The image clearly shows an acceleration in the wind speed above the wave troughs until $\zeta = 200$ m. Instantaneous contours of dimensionless horizontal and vertical velocities and pressure are listed in Appendix B. Compared to the case with wave age $C_p/u_* = 60$, the airflow is clearly accelerated above the wave troughs. The location of the minimum and the maximum of the vertical velocity is similar to the case with wave age 60, and the amplitude is larger. A similar observation can be made on the pressure field. The pressure field amplitude is quite significant and pressure bumps of non-negligible amplitude are observed below the top boundary. This must have an impact as mentioned in the previous section, but no quantification has been carried out since this case is quite an unrealistic case. This case is compared to more realistic wave fields.

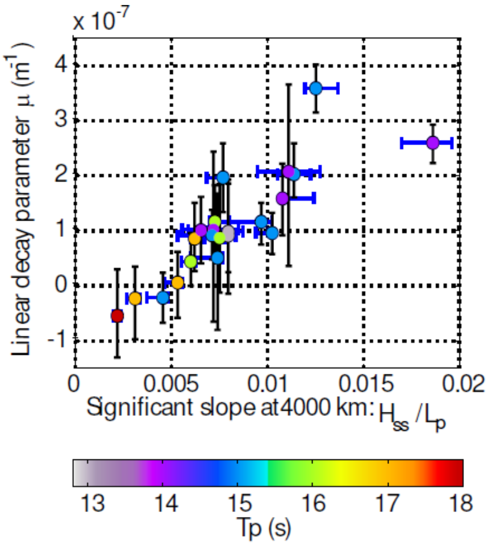

Figure 4.28: Estimated linear attenuation coefficient as a function of the initial significant wave height and peak wavelength taken 4000 km from the storm centre for a variety of peak swell periods (colours) (Ardhuin et al., 2009).

Figure 4.28 illustrates the swell dissipation for 22 events (Ardhuin et al., 2009). The estimated linear attenuation coefficient μ (cf Equation 2.8) is plotted over the initial significant slope H_s/λ_p, taken 4000 km from the storm centre, for a variety of peak swell periods. For a wave of period $T \approx 16$ s (green circles), the maximum significant slope is $H_s/\lambda_p \approx 0.0075 - 0.01$. In our case where we consider a non-linear monochromatic wave with the upper range of the maximum significant slope: this corresponds to a wave steepness $ak = 0.022$. Two intermediates cases are considered, $ak = 0.044$ and $ak = 0.1$. The characteristics of these cases are detailed in Table 4.7.

Statistics are computed for different time periods (100 T_p, 500 T_p, 1000 T_p and 1500 T_p when the simulation was long enough to compute statistics) over

		Case WA120 (i)	Case WA120 (ii)	Case WA120 (iii)	Case WA120 (iv)
Wind-wave ratio	wave age C_p/u_*	120	120	120	120
Wave parameters	wavelength λ (m)	400.0	400.0	400.0	400.0
	amplitude a (m)	12.7	6.4	2.8	1.4
	steepness ak	0.2	0.1	0.0444	0.022
	phase velocity C_p (m.s^{-1})	25.0	25.0	25.0	25.0
Wind parameters	initial friction velocity u_* (m.s^{-1})	0.21	0.21	0.21	0.21
	$U_{10\mathrm{m}}$ calculated from log law (m.s^{-1})	6.0	6.0	6.0	6.0

Table 4.7: Characteristics of the wave field and the initial wind imposed for cases of a swell propagating in very light wind conditions ($C_p/u_* = 120$).

100 wave periods. Figure 4.29 illustrates the time evolution of the mean vertical profile of horizontal velocity, pressure, momentum flux and form drag.

A wind jet is observed for the cases WA120 (i) and (ii): its amplitude is larger for WA120 (i) and located around $\zeta \approx 40$ m whereas it is slightly higher for WA120 (ii) with $\zeta \approx 60$ m. Over time, this wind jet increases in magnitude and in vertical extension, and its maximum value moves up: compared to cases with smaller wave steepness, the vertical profile of the wind speed deviates on the lowest 260 m of the MABL at $t = 100\ T_p$, 600 m at $t = 500\ T_p$ and 850 m at $t = 1000\ T_p$. The ratio of the maximum velocity of the wind jet over the wind speed at the top of the domain $U_{\mathrm{max}}/U_{\mathrm{top}}$ becomes larger than 1 for case WA120 (i) at $t = 500\ T_p$ and stabilises around $1.08 - 1.09$ for statistics around 1000 and 1500 T_p. This wind speed ratio does not exceed 1 for case WA120 (ii), even if it reaches 0.97 at $t = 1000\ T_p$. The wind jet is not observed for the more realistic cases WA120 (iii) and (iv). Their wind profiles have the same trend at $t = 500\ T_p$, but the wind profile is more decelerated over time for the case WA120 (iv) with the smallest wave steepness. For the pressure profile, the same trend as the trend in the wind profiles is observed with a larger amplitude for the case with the

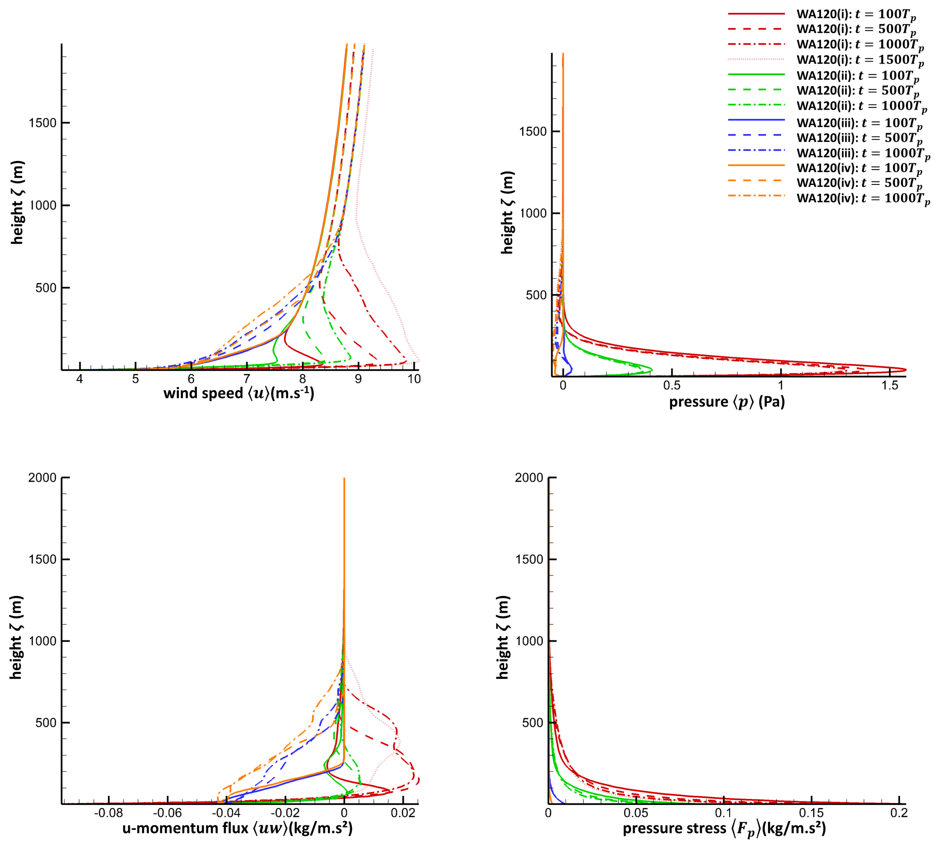

Figure 4.29: Time evolution of the vertical profiles of the average wind speed (*top left*), pressure (*top right*), u-momentum flux (*bottom left*) and pressure stress (*bottom right*) for fast sea states with various wave steepness underlying very light wind conditions. The initial wave age is $C_p/u_* = 120$.

largest wave steepness. The pressure profile is positive over height for cases WA120 (i), (ii) and (iii) at $t = 100\ T_p$, but negative for case WA120 (iv) with the smallest wave steepness. The maximum is reached just below the wind jets observed previously. The amplitude of this maximum decreases over time and the profiles become negative around $\zeta = 300$ for cases WA120 (i) and (ii) and around $\zeta = 120$ m for case WA120 (iii).

Concerning the form drag profiles and momentum flux profiles, the trend is similar for cases WA120(i) and (ii) even if the amplitude is larger for case WA120(i): the pressure stress is always positive over height and decreases slightly over time. The momentum flux has a positive maximum value for case WA120 (i) (slighlty positive for case WA120 (ii)), and over time, this maximum increases in magnitude and in vertical extension as for the wind jet observed in the wind profile. We recall that a positive flux-value means an upward momentum transfer. This upward transfer is reinforced by the positive form drag. For the cases with smaller wave steepness, cases WA120 (iii) and (iv), the momentum flux remains negative over time. But the waves create a contribution in the transfer process as a result of the correlation of wind pressure and wave slope which competes with the turbulence-supported stress. The total momentum flux (i.e. the sum of the turbulent momentum flux and the form drag) is plotted in Figure 4.30: the presence of the wind jet is correlated to the positive sign of the total momentum flux, meaning that an upward momentum transfer occurs in the wind-wave system. For cases WA120 (iii) and (iv), the slightly positive form drag is not strong enough to counteract the negative turbulent momentum flux, the overall momentum transfer remains negative and no wind jet is present in the velocity profile.

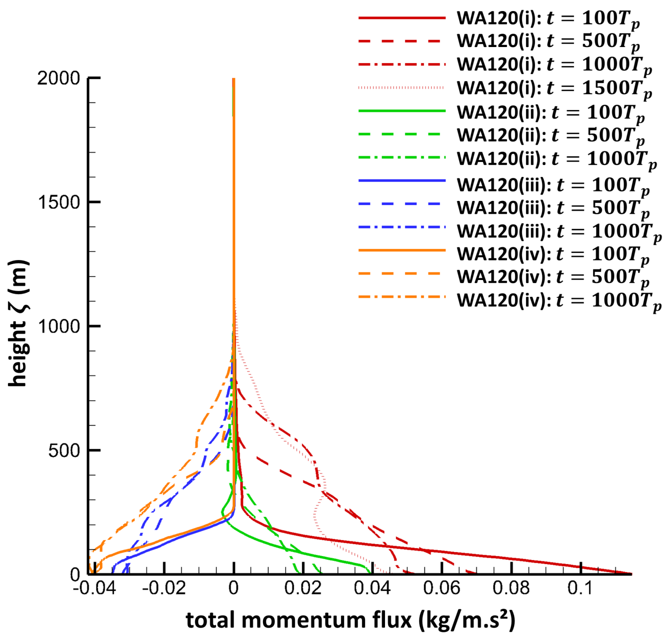

Figure 4.30: Time evolution of the vertical profiles of the average total momentum flux for fast sea states with various wave steepness underlying very light wind conditions. The initial wave age is $C_p/u_* = 120$.

Contrary to the previous cases where a young wave was propagating under strong wind conditions, the wave growth rate parameter, which is calculated from the dimensionless form drag at the free surface, is negative as illustrated in Figure 4.31. The form drag at the free surface is positive which means that the pressure stress acts as a thrust on the overlying airflow in all the cases, and its magnitude is directly correlated to the wave steepness (and thus to the wave energy spectrum). Concerning the time evolution of the wave growth rate parameter, two trends are observed as mentioned previously: the cases with a large wave steepness (cases WA120 (i) and (ii)) have a negative wave growth rate parameter β which tends to decrease in magnitude over time, whereas for the two other cases, β tends to increase quite slightly in magnitude.

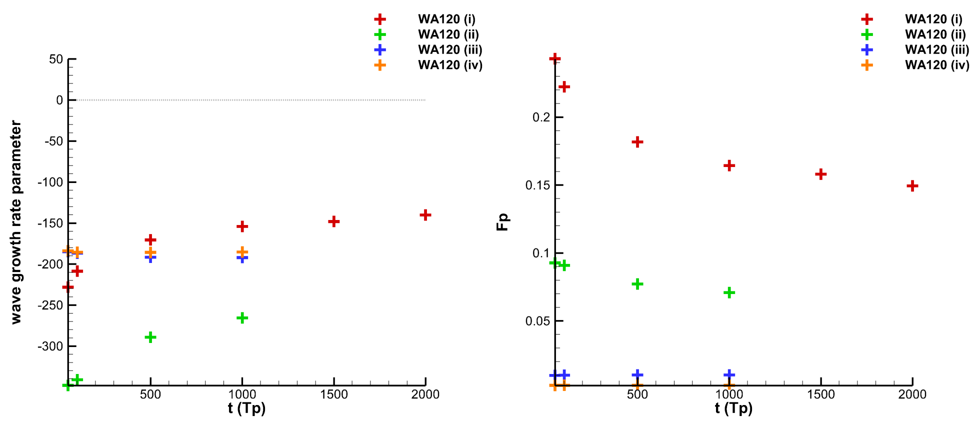

Figure 4.31: Temporal evolution of the wave growth rate parameter (*left*) and form drag at the free surface (*right*) with very light wind conditions overlying fast waves with various wave steepness.

As mentioned at the beginning of this section, β can be plotted over the effective wave age C_p/u_* with the mean friction velocity at the first cell averaged over the time period. Firstly, we can notice that the variation in β is large for the cases with large wave steepness (cases WA120 (i) and (ii)) whereas the variation in the updated wave age is small. The opposite trend occurs for the small wave steepness (cases WA120 (iii) and (iv)). Comparing these cases to the cases with the small wave ages detailed at the beginning of the section (WA1, WA5, WA10), we note that the cases with larger wave steepness (WA120 (i) and (ii)) have an opposite trend: β increases over time (becomes less negative) while C_p/u_* decreases (a first increase is observed for case WA120 (ii) but then it decreases). This seems rather evident to have opposite trends since the two groups of cases are located before and after the wind-wave equilibrium state which is around $C_p/u_* \approx 15-20$: the wind-wave system will tend to this equilibrium state by increasing its actual wave age for cases WA1, 5 and 10 (i.e. decreasing the wind speed above the wave since the wave does not evolve under the wind pressure forcing) and decreasing its actual wave age for cases WA120 (i.e. increasing the wind speed above the wave, which is observed through the occurrence of the wind jet). For the cases with smaller wave steepness (cases WA120 (iii) and (iv)), β tends to slightly decrease with time which is correlated to an increase in the effective wave age (i.e. a decrease in the wind speed above the wave): indeed, no wind jet has been observed in the wind speed profile for these two cases, the wind is decelerated above the wave over time. This behaviour supports the study that has been carried out on the influence of the wave steepness (therefore the energy of the wave spectrum) on the overlying airflow for an initial wave age $C_p/u_* = 10$.

We emphasize the fact that the natural evolution of the system is distorted: the sea state does not evolve under the wind pressure forcing and brings an infinite amount of energy into the air domain. Moreover, the influence of the stratification of the atmosphere is not considered here, whereas the bibliographical study showed that such a light-wind-speed regime correlated to a swell regime occurs when the MABL is generally unstable (i.e. convective). Upward momentum fluxes have been reported during the field campaigns with smaller sea states: Drennan et al. (1999) observed an upward momentum flux for $H_s = 1.11-1.45$ m and Grachev and Fairall (2001) reported a value of $H_s \approx 0.5$ m during the SCOPE experiment. The difference in H_s values may be due to the fact that SCOPE data correspond to open ocean swells, whereas Drennan et al. (1999) values reflect waves in an enclosed lake. Cases WA120 (iii) and (iv) are characterised by larger amplitudes than those for which upward momentum fluxes have been observed in the aforementioned experiments, and no upward transfers have been observed in the computations.

The coupling between an atmospheric LES code and a pseudo-spectral code solving for the sea state propagation has been implemented and var-

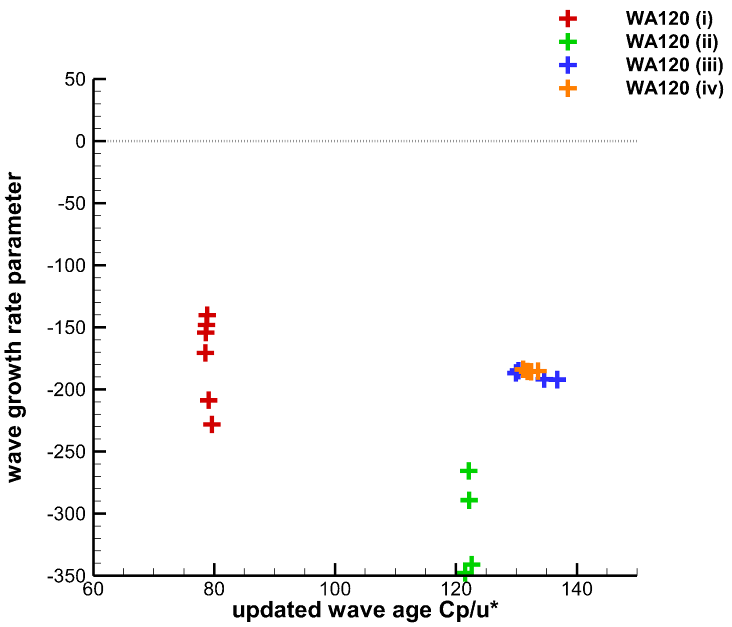

Figure 4.32: Wave growth rate parameter over wave age calculated with the mean friction velocity over specified time periods. The initial wave age is $C_p/u_* = 120$.

ious cases have been tested with the activated information exchange from the HOS code to the LES code (i.e., the wave elevation, its orbital velocity and its time and spatial derivatives): cases where young waves propagate into strongly forced wind conditions and cases where a swell propagates into light and very light wind conditions. Very strong sea states have shown the existence of wind jet above the free surface. All the simulations have been carried out considering that the sea state does not evolve under the wind pressure forcing. We now introduce two cases where the pressure forcing is activated during the coupling.

4.3 Exploratory study on the two-way coupling

The evolution of a sea state is mainly affected by non-linear wave interactions, wind forcing and dissipation from wave breaking. Their parametrisation is for instance a current bottleneck in state-of-the-art phase averaged global wave models. In order to have a better description with finely resolved spatial and temporal details of the wave field and the overlying airflow, i.e. a deterministic description, the wave phases need to be solved. Liu et al. (2010) introduced a coupling between a HOS method and a DNS for wind turbulence in a phase-resolved context. They investigated broadband waves to gain insight into wind forcing for phase-resolved wave field simulation. They found that for long wave components, the wave growth parameter can be approximated by the value of the corresponding monochromatic waves, whereas for short waves, stochastic modelling for wind input is called for. They mentioned that their wave breaking dissipation model was still at an early age of development and that more work in the modelling would be needed. Chalikov and Rainchik (2011) developed a coupled numerical modelling of wind and waves based on a RANS wave boundary-layer (WBL) model and their non-stationary conformal wave model. They introduced an algorithm of the breaking parametrisation based on smoothing of the interface: it is designed to prevent the development of the breaking instability by highly selective high-frequency smoothing of the interface. They showed that the wind profile in the lowest part of the WBL deviates considerably from the logarithmic form. They also investigated the dependence of the drag coefficient C_D on the wind speed and on the wave spectrum shape.

In our current coupling, the pressure coupling is introduced after 100 000 iterations (at $t \approx 80\lambda/u_*$ s) during which the HOS code sends the wave information to the LES without evolving under the pressure forcing. From this time (it = 100 000), the atmospheric pressure signal interpolated at the free surface is sent to the HOS code using the procedure outlined in the previous chapter: during inner iterations due to the RK scheme, HOS does not update its solution, and at the end of the three RK stages, HOS evolves by updating its solution and taking into account the pressure term into its own equations. The pressure acts as a forcing (actually, as a thrust or a drag depending on the speed ratio between wind and wave) on the sea state through the form drag that has been previously defined in Equation (4.4). Along with the surface pressure, the tangential stress is responsible for the formation of a stress layer in the MABL, however this shear stress cannot be assimilated in the wave model due to the hypothesis of potential flow for the water. As mentioned in the previous chapter, the HOS code does not take into account any dissipation model, whereas the pressure forcing brings energy into the wave system. Without introducing any dissipation in the system, the HOS code crashes immediately after taking into account the pressure forcing: the pressure forcing introduces energy at high frequencies in the wave spectrum as shown by the green line in Figure 3.11. This energy input at high frequencies is not counterbalanced in the HOS model due to the lack of dissipation such as wave breaking, viscosity... There is ongoing research about this thematics in LHEEA laboratory (Seiffert and Ducrozet, 2016). As a workaround, it has been decided to filter the atmospheric pressure signal. This filtering is an alternative to the energy dissipation as specified in the previous chapter: we only consider the growth of "not-so-steep" waves. Note that in-depth tests need to be carried out on this filtering since the parametrisation of the energy dissipation constitutes the whole key of the understanding of the interactions in the coupled wind-wave system. This thematics has been identified as out of scope of this thesis and will be expanded in further works.

Two cases have been implemented. The first one corresponds to the first case presented in the previous section with a non-linear monochromatic wave of wavelength $\lambda = 0.23$ m and a wave steepness $ak = 0.2$ and an initial wave age $C_p/u_* = 1.6$. This case corresponds to a case where a very young monochromatic wave propagates into strongly forced wind conditions: this is an idealised case with a sea state representing by a discrete spectrum with a major peak and secondary peaks. The second case represents a case close to the wind-wave equilibrium with wave age $C_p/u_* = 15$. Characteristics are detailed in Table 4.8.

Figure 4.33 illustrates the time evolution of the wave spectrum and the corresponding free surface elevation for case WA1 (i.e. strongly forced wind conditions). The graphs on the left represent the sea state when the pressure forcing starts whereas the graphs on the right represent the sea state at $t = 17\ T_p$ (i.e. $t \approx 6.6$ s) after the numerical activation of the pressure forcing. Although the pressure signal has been numerically filtered at high frequencies, a transfer of energy is observed in the tail of the wave spectrum. Energy is also observed at low frequencies, around the peaks of higher order of non-linearities, and especially on the left of the principal peak with the presence of a peak. With this filtered pressure signal, the growth acts on the first free components of the spectrum that create harmonics. But the

		Case WA1	Case WA15
Wind-wave ratio	wave age C_p/u_*	1.6	15
Wave parameters	wavelength λ (m)	0.23	20.0
	amplitude a (m)	0.007	0.31
	steepness ak	0.2	0.2
	phase velocity C_p (m.s^{-1})	0.6	5.6
Wind parameters	initial friction velocity u_* (m.s^{-1})	0.28	0.37
	$U_{10\text{m}}$ calculated from log law (m.s^{-1})	11.0	10.7

Table 4.8: Characteristics of the wave field and the initial wind imposed for cases where the atmospheric pressure forcing on the sea state is activated ($C_p/u_* = 1.6$ and 15).

non-physical dissipation makes the evolution of the wave spectrum hard to analyse.

A second case with a wind-wave simulation close to the wind-wave equilibrium is investigated. Three time periods are observed in Figure 4.34, when the pressure coupling has just been activated (top graphs), at $t = 45\ T_p$ and, just before the crash, at $t = 90\ T_p$ (i.e. $t \approx 322$ s). Firstly, we note that it takes a longer time for the simulation to crash compared to the previous case. Secondly, the wave spectrum slightly evolves between the initial time and $t = 45\ T_p$ where the amplitude of the principal peak is slightly bigger resulting in a slightly larger wave amplitude. This must be due to the fact that this specific case corresponds to a case where wind and waves are close to the equilibrium, so the pressure wind forcing, i.e. the wind input, does not prevail in the HOS equation. But the simulation ends up crashing at $t = 90\ T_p$. The same conclusion as in the previous case can be made: the numerical

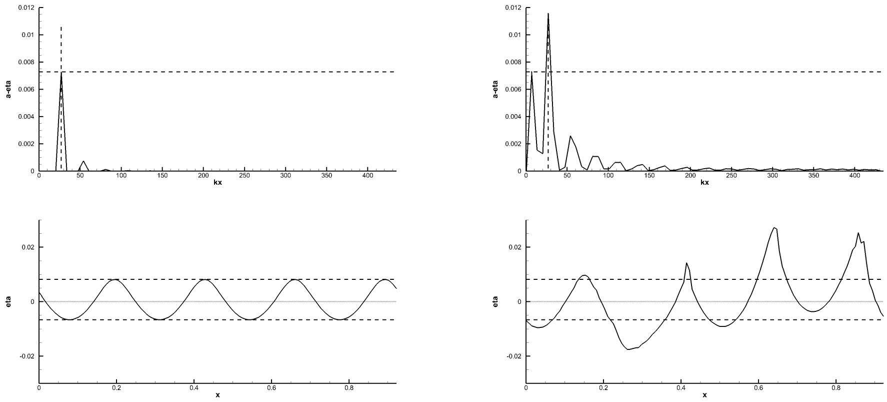

Figure 4.33: Wave spectrum over wavenumber (*top*) and the corresponding wave elevation over position(*bottom*) for a wind-wave coupled simulation with a non-linear monochromatic wave underlying an airflow with an initial speed ratio $C_p/u_* = 1.6$. Graphs on the left represent the sea state when the pressure forcing is just activated and graphs on the right show the evolution of the sea state at $t = 17\ T_p$ after the activation of the pressure forcing, just before the crash. Dashed lines mark the amplitude of the wave elevation and the spectral peak at the time when the pressure coupling is activated.

filtering of the pressure signal induces a forcing of the lowest frequencies in the wave spectrum, but this is non-physical and it is hard to evaluate if the evolution of the energy distribution is due to an energy transfer from the wind input, non-linear interactions or simply numerical instabilities.

This analysis indicates that the dissipation is essential into the coupled model. A first attempt has been introduced by filtering the high frequencies of the atmospheric pressure signal, limiting by this means the forcing on the low frequencies of the wave spectrum. But the physical dissipation of the energy into the sea state becomes a key to the coupling. Wave energy is dissipated through wave breaking, and in the generation of currents and turbulence: the parametrisation of local dissipation through wave breaking is an ongoing research topic at LHEEA (Seiffert and Ducrozet, 2016). Global dissipation can also be introduced through the linearisation of dissipation terms derived from the parametrisation of spectral models (Perignon et al., 2011).

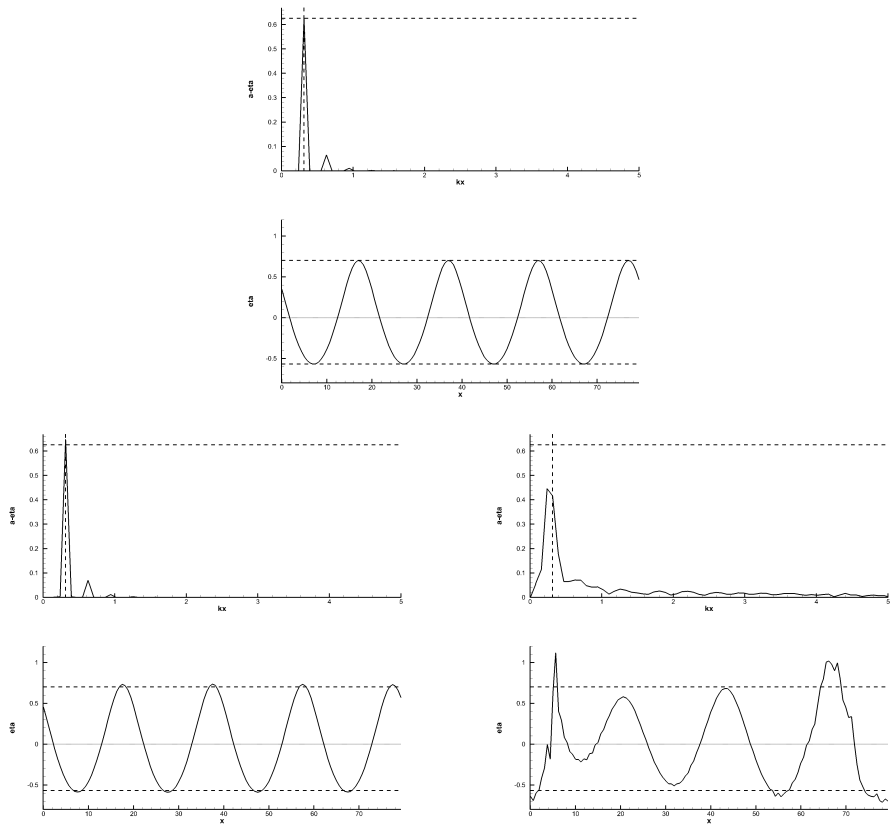

Figure 4.34: Wave spectrum over wavenumber and the corresponding wave elevation over position for a wind-wave coupled simulation with a non-linear monochromatic wave underlying an airflow with an initial speed ratio $C_p/u_* = 15$. Graphs at the top represent the sea state when the pressure forcing is just activated, graphs on the left show the evolution of the sea state at $t = 45\ T_p$ after the activation of the pressure forcing and on the left at $t = 90\ T_p$, just before the crash. Dashed lines mark the amplitude of the wave elevation and the spectral peak at the time when the pressure coupling is activated.

4.4 Conclusion

A numerical coupling has been introduced between an LES atmospheric code (Sullivan et al., 2014) and a HOS wave model that solves the evolution and propagation of a sea state. This numerical coupling is based on an exchange of information between the two codes. The one-way coupling has been defined as the wave information (i.e. wave elevation and its derivatives and the orbital velocities) being sent from the HOS code to the LES code, whereas the two-way coupling is defined as an exchange of information between the two codes (meaning that the sea state evolves under wind pressure forcing). The numerical assumptions are the following: the atmosphere is considered as a wind tunnel with no atmospheric stratification (i.e. neutral air). The SGS momentum fluxes accounting for the unresolved wavelengths at the first cell above the water surface are parametrised using a logarithmic law based on a fixed roughness length.

The influence of the sea state on the overlying airflow has been numerically investigated through three one-way coupled cases: wind forcing over young waves, a swell underlying a light wind and a case of generation of a wave-induced wind jet. For the first case of a wind forcing over young waves with wave age $C_p/u_* < 10$, the influence of the mesh discretisation is studied, as well as the influence of the height of the air domain: the influence is larger on the pressure and momentum flux profiles even if the values in the vicinity of the free surface are quite similar. The influence is due to the fact that the air domain is modelled as a wind channel and gradient conditions are imposed at the flat upper boundary. The height has nearly no impact on the mean wind and pressure drag profiles. The vertical discretisation has a negligible impact considering that the first cell satisfies $\Delta x/\Delta_z \approx 3$. The influence of the spectral content of the sea state (monochromatic vs. irregular sea states) is also investigated: a sea state with a larger spectral content tends to more notably slow down the airflow. For the second case where a monochromatic non-linear swell underlies a light wind (wave age $C_p/u_* = 60$), the influence of the height on the mean profiles is more striking than the previous case. A larger acceleration of the airflow seems to occur for the smallest wind tunnel and this acceleration is correlated to a larger pressure stress which acts as a larger thrust on the wind. Indeed, wind and wave exchange momentum and energy mainly through form drag and this exchange directly influences the wave growth. The notion of forcing is thus characterised by a coefficient β, the wave growth rate parameter, which is related to the dimensionless form drag per unit area due to the pressure and the wave steepness. A major difference between the two cases lies in the sign of the wave growth rate parameter which is directly related to the sign of the form drag at the free surface. For the case of young waves underlying a strong wind (i.e. $C_p/u_* < 10$), the waves act as a drag on the wind and

$\beta > 0$. For the case of a fast swell underlying a light wind, the waves act as a thrust on the wind and $\beta < 0$. A different way to look at this is that the first case can be considered as a wind forcing whereas the second case is a wave forcing. If the two-way coupling were active (i.e. the pressure forcing active in the HOS wave model), the young waves would grow whereas the swell would "decrease".

A negative growth rate parameter does not imply the generation of a wave-induced wind. Indeed, no wind jet is observed in the airflow for the case with a wave age $C_p/u_* = 60$. Hence, a third case has been investigated with a wave age $C_p/u_* = 120$ where a fast monochromatic swell propagates in a very light airflow. Under these conditions, a wind jet is observed around $50 - 100$ m above the wavy surface. The presence of this wave-induced wind is correlated to a positive momentum flux: an upward transport of momentum from water to air is observed, invalidating the current ocean-atmosphere models that only allow the momentum transfer to be directed from the atmosphere to the ocean. However, the sea state is not really realistic for this case with an amplitude of 12.7 m. Three waves with smaller wave steepness are then considered. For the smallest sea states, no wind jet has been observed in the wind speed profile, the wind is decelerated above the wavy surface over time. This behaviour supports the influence of the wave steepness and the energy of the wave spectrum on the overlying airflow. For cases with small wave steepness, the slightly positive form drag is not strong enough to counteract the negative momentum flux in the tested conditions: the overall momentum transfer remains negative and no wind jet is thus observed in the velocity profile.

With the one-way coupling, we emphasize the fact that the natural evolution of the wind-wave system is distorted since the sea state does not evolve under the wind pressure forcing, hence it brings a quasi constant amount of energy into the air domain. Two additional cases are implemented in order to investigate the two-way coupling. As no dissipation model exists in the HOS wave model, the HOS code crashes instantly under the wind pressure forcing. As a workaround, the atmospheric pressure signal is filtered, which acts as a mitigation of the forcing, restricted to the main components (i.e. the most stable components in the spectrum). The parametrisation of the energy dissipation constitutes the whole key of the understanding of the interactions in the coupled wind-wave system: further work needs to be expanded on this thematics. For now, two cases are investigated. On one hand, a small wave age where young waves are forced by a strong wind is tested. The HOS code crashes at 17 T_p after the activation of the pressure forcing. Energy appears in the tail of the wave spectrum and at low frequencies, but the non-physical dissipation makes the evolution of the wave spectrum hard to analyse. On the other hand, a wind-wave simulation close to the wind-wave equilibrium is investigated. The HOS code crashes at 90 T_p after the activation of the pressure forcing. This may be due to the fact that the pressure forcing does not prevail in the HOS equation. These two simulations are obviously preliminary studies that have been conducted on this subject. In-depth tests will need to be carried out once the dissipation model will be available in the HOS model.

The next chapter is a small chapter of pre-conclusion that will question the use of the parametric laws in the international governing standards based on the comparisons of the mean velocity profiles derived from the previous LES-HOS simulations.

Résumé du chapitre 5

L'objectif de ce chapitre de pré-conclusion est de situer les études numériques développées au cours de cette thèse dans le contexte des normes régissant l'industrie de l'éolien offshore. En effet, ces normes et directives internationales reposent sur des méthodologies qui ont été mises en place pour l'éolien terrestre, avec notamment l'utilisation de la loi logarithmique pour prédire le profil de vent. Néanmoins, ce profil issu de la loi logarithmique n'est valide que dans la couche de surface dans des conditions de stratification atmosphérique neutres, ce qui est rarement le cas au-dessus de l'océan. De plus, des campagnes d'observations en mer et des simulations numériques ont révélé que les effets des vagues, notamment la rugosité de la surface de la mer qui n'est pas fixe, sont un facteur majeur perturbant l'écoulement atmosphérique au-dessus de l'océan.

Ainsi, quatre profils moyens de vent provenant des précédentes simulations vont être comparés à différents profils issus de la loi logarithmique. On rappelle que le domaine atmosphérique est modélisé par un écoulement d'air neutre dans des conditions de soufflerie. Les cas sélectionnés sont caractérisés par des âges de vague $C_p/u_* = 1$ et 10 (i.e. cas de forçages du vent), 60 (i.e. houle rapide se propageant dans une zone de vent faible) et 120 (i.e. génération d'un jet de vent induit par la houle). Pour les cas de petits âges de vague, la loi log ne représente pas le profil de vent issu de la CFD et surestiment la vitesse du vent près de la surface libre. Pour les deux autres cas, la loi log a tendance à sous-estimer le profil de vent issu de la CFD et elle ne prédit pas du tout le jet de vent qui apparaît autour de 100 m.

Une dernière comparaison est réalisée à partir du coefficient de traînée C_D et de la vitesse prise à la hauteur de référence U_{10}. Le choix de cette vitesse de référence a un impact sur les propriétés qualitatives et quantitatives de C_D, et on note que la hauteur 10 m se trouve dans la zone d'influence de la vague. De nombreuses études ont montré que le coefficient de traînée pouvait subir une variation non négligeable due à la stabilité de l'atmosphère et à l'état de mer. Deux valeurs de C_D, correspondant aux valeurs extrêmes trouvées dans la littérature, ont été choisies. On remarque que la valeur du coefficient de traînée a un impact non négligeable sur le profil issu de la loi log, mais il ne représente toujours pas le jet de vent. L'influence du choix de la hauteur de référence sur la dynamique de la couche limite atmosphérique marine demeure assez vague, et malgré des efforts considérables, l'éparpillement des données expérimentales est assez significatif de la difficulté à paramétrer de façon correcte le coefficient de traînée C_D.

Chapter 5

Why the logarithmic wind profile should be cautiously considered in offshore wind energy?

This pre-conclusive chapter aims to place into perspective the logarithmic wind profile commonly used to predict the vertical wind profile in the governing standards. Indeed, the governing standards and international guidelines for the offshore wind industry rely on standards and methodologies that have been first addressed to the onshore wind industry (see details of IEC 61400 in Chapter 1). Chapter 1 illustrated that the waves interact with the wind and affects its profile. Moreover, the logarithmic wind profile is only valid in the surface layer under neutral atmospheric stratification. Field experiments and numerical simulations have revealed that atmospheric stability and wave effects, including the dynamic sea surface roughness, are two major factors affecting flow over ocean.

Chapter 3 introduced the numerical coupling that has been implemented between an atmospheric LES code (Sullivan et al., 2014) and a high-order spectral (HOS) potential code solving the sea state propagation. The CFD code developed by Sullivan et al. (2014) has tremendous applications, but requires large computational resources. With the aim of simplification and in order to provide a first tool to study the coupling between those two codes, a neutral atmosphere has been considered: considering independently the atmospheric stratification and wave effects constitutes a first step in the understanding of the ocean-atmosphere interactions. Another point that has been discussed in Chapters 3 and 4 is that the two-way coupling is not directly usable as the dissipation model in the HOS code is still a work-in-progress in the LHEEA laboratory. A workaround on the atmospheric pressure filtering has shown some potential, any further investigation has been limited.

Four cases have been selected among the simulations that have been carried out and detailed in Chapter 4. All these simulations refer to cases where a neutral airflow in a wind tunnel modelled by the LES code is forced by a non-linear monochromatic wave solved by the HOS code. Table 5.1 summarises the wave and airflow properties. Cases WA1 and 10 represent young waves in strongly forced wind conditions, whereas cases WA60 and 120 depict swell underlying light wind conditions, with the formation of a wave-induced wind jet in case WA120. The swell in this particular case has a wave steepness $ak = 0.1$ leading to an amplitude $a = 6.4$ m which is more realistic than the case WA120 (i) in the previous chapter with its amplitude $a = 12.7$ m.

For cases WA1 and 10, statistics are computed over a time period from $20\lambda/u_*$ s to $100\lambda/u_*$ s, whereas for cases WA60 and 120 for which the wind conditions are light and the wave has a strong impact on the wind profile, statistics are computed over 100 wave periods around $t = 500\ T_p$. From these statistics, wind profiles are indicated by black lines in Figure 5.1. Red lines illustrate the log law plotted from the surface friction velocity computed with the LES-HOS simulation.

As a reminder, the logarithmic law is (red lines in Figure 5.1):

$$U(z) = \frac{u_*}{\kappa} \ln\left(\frac{z}{z_0}\right). \tag{5.1}$$

The wind estimation computed with this surface friction velocity show two trends: for cases with small wave ages (WA1 and 10), the log law does not represent the CFD wind profile and overestimates the wind speed near the wavy surface, whereas for larger wave ages, the log law tends to underestimate the CFD wind profile. For case WA120, the log law has a general shape which is very close to the CFD wind profile but is not able to capture the wind jet around 100 m. We note that for a better comparison, the log

		Case WA1	Case WA10	Case WA60	Case WA120
Wind-wave ratio	wave age C_p/u_*	1.6	10	60	120
Wave parameters	wavelength λ (m)	0.23	2.78	100.0	400.0
	amplitude a (m)	0.007	0.088	3.18	6.4
	steepness ak	0.2	0.2	0.2	0.1
	phase velocity C_p (m.s^{-1})	0.6	2.08	12.5	25.0
Wind parameters	initial friction velocity u_* (m.s^{-1})	0.28	0.21	0.21	0.21
	$U_{10\mathrm{m}}$ calculated from log law (m.s^{-1})	11.0	6.0	6.0	6.0

Table 5.1: Characteristics of the wave field and the initial wind imposed for various wave ages ($C_p/u_* = 1.6$, 10, 60 and 120).

profile should be calculated from global quantities such as the friction velocity calculated from a constant-flux layer and roughness length computed from the Charnock relation (Equation (1.22)). But in the previous chapter, the vertical profiles of momentum flux showed that, for some cases it seems to exist a constant-flux layer really close to the surface, but the values of the fluxes are quite fluctuating. Longer simulations with longer statistics should be computed in order to get proper values. Sullivan et al. (2014) demonstrated that the total flux is approximately constant in the marine surface layer but individual flux components vary markedly with wave age.

The surface friction velocity is a dimensionless quantity which is not measured directly from a wind gauge on a mast for example. Other wind profiles have been reconstructed from the wind speed measured at a certain height in our numerical simulations. In all the simulations, except for case WA1,

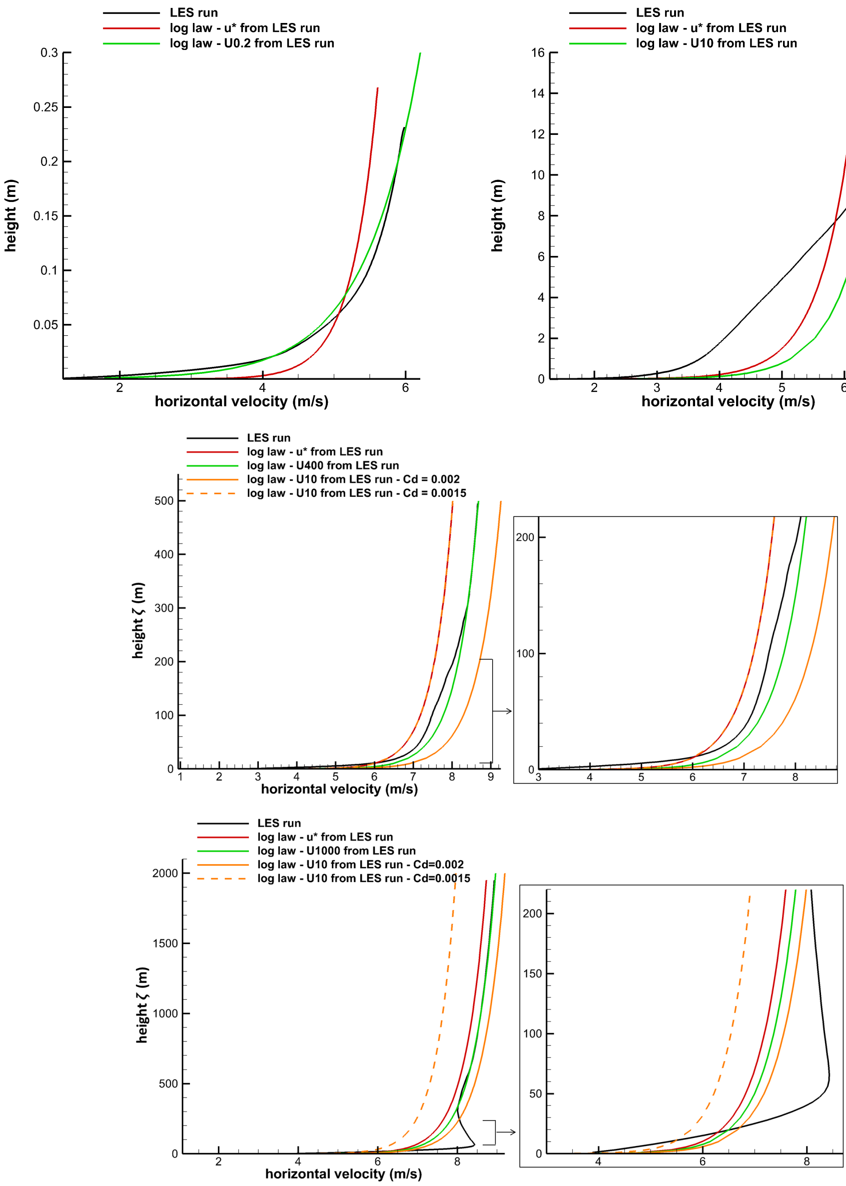

Figure 5.1: Wind profile and various corresponding log laws for cases WA1 (*top left*), WA10 (*top right*), WA60 (*middle*) and WA120 (*bottom*).

the wind profile computed from the numerical simulation does not look like a log profile: near the free surface a disturbed zone is observed due to the presence of the wave. The height for the comparison has been chosen to be out of this disturbed zone (note that it seems easy to locate this zone of disturbance since we can observe the whole wind profile, which is not the case if the measure was obtained from a wind gauge located at a fixed height, independent of the underlying sea state). The wind speed has been measured at 0.2 m above the mean water level for case WA1, 10 m for case WA10, 400 m for case WA60 and 1000 m for case WA120. These heights of reference, which are established as reference by our own criteria, are various and depend on the wind-wave properties imposed in the numerical simulations. Green lines in Figure 5.1 are the wind profiles computed from the log law and a measured value of the wind speed at a reference height. The log law is reconstructed so that its formula satisfies (green lines in Figure 5.1):

$$U\left(z_{\text{ref}}\right)=\frac{u_{*\text{unknown}}}{\kappa}\ln\left(\frac{z_{\text{ref}}}{z_0}\right). \tag{5.2}$$

For all cases, black and green lines match at the height identified as the reference height (0.2 m for WA1, 10 m for WA10, 400 m for WA60 and 1000 m for WA120). Moreover, this log law computed from a measured wind speed at a reference height seems to be in better agreement than the log law computed from the surface friction velocity (red line), except for case WA10 where the wind profile seems to be decelerated compared to log law profiles. For the case with the smallest wave age $C_p/u_* = 1.6$, the log law profile is in accordance with the profile from the CFD. For larger wave ages, the log law fits very well with the top of the wind profile but misses the wind jet in case WA120 and its signs in case WA60.

Eventually, a last comparison is made with another way of writing the log law based on the wind speed at 10 m and the drag coefficient C_D (orange lines in Figure 5.1):

$$U\left(z\right)=\frac{\sqrt{C_D}U_{10}}{\kappa}\ln\left(\frac{z}{z_0}\right). \tag{5.3}$$

The reference height 10 m is a reference in many publications (see Chapter 1). Here, the value of the wind speed at 10 m, U_{10}, is measured from the CFD. The choice of the reference wind speed has an impact on the quantitative and qualitative properties of C_D. For a fixed wind speed at 10 m height, Donelan (1982) found that the drag coefficient may vary by a factor 2 depending on the sea state. Based on the work of Kara et al. (2007) on the wind stress drag coefficient over the ocean, $C_D \geq 1.5 \times 10^{-3}$ is prevalent over North Pacific and North Atlantic, whereas due to the air stability, an increase of more than 20% can be observed compared to neutral situations.

Here two values for the drag coefficient are chosen, $C_D = 1.5 \times 10^{-3}$ and $C_D = 2.0 \times 10^{-3}$ which represent the quite high range of the observed drag coefficients. The idea is to illustrate the impact of the C_D value on the log profile. Solid and dashed orange lines in Figure 5.1 show the influence of the drag coefficient on the wind profile for the cases WA60 and 120. First of all, we can notice the large discrepancy between the dashed and solid lines: a small deviation in the drag coefficient leads to a quite different wind profile. Moreover, these wind profiles are based on a log law. This log law is supposed to be valid under neutral atmospheric conditions inside the surface layer and it is based on a fixed roughness length over a fixed surface. Therefore the wind jet can not be predicted with this empirical law. Last but not least, our C_D values were chosen based on the literature. However, for case WA120, it has been shown in the previous chapter that the wave acts as a thrust on the airflow, so we expect a negative drag coefficient. Figure 1.9 shows that the majority of the values of the drag coefficient are lower than the standard TOGA COARE parametrisation in case of wave ages and that for light winds with an underlying fast-moving swell, C_D can be negative. The dynamic understanding of the reference height in the MABL is rather vague and despite enormous efforts, the scatter of experimental data is very significant and a consistent parametrisation for $C_{D_{10}}$ has not been established yet.

Conclusion

The ocean-atmosphere system is a complex system governed by numerous interactions and the assessment of the offshore wind resource must be put into consideration within the whole coupled system. The offshore environment addresses very specific problems: two major factors have been identified in the literature as key drivers in ocean-atmosphere interactions. Indeed, the atmospheric stratification due to the large heat capacity of the ocean (Kristjansson et al., 2011) and the wave-induced effects (especially the dynamic roughness of the oceanic surface) have an impact on the marine atmospheric boundary layer. Ocean waves are often considered to act as a drag on the surface wind, which is related to a downward momentum transferred from the atmosphere into the waves. IEC 61400-3 standard, *Wind Turbines Part 3: Design Requirements for Offshore Wind Turbines*, relies on parametric relationships of the wind profile and the surface roughness that are commonly used for the onshore wind industry. However, field experiments and numerical modelling have observed upward momentum transfers causing the surface wind to accelerate under light-wind-speed regimes correlated to a fast-swell regime. The existence of low-level wave-driven winds is the evidence that the marine atmospheric boundary layer is influenced by the dynamic oceanic surface. According to Semedo et al. (2011), the presence of swell-dominated sea states is higher than 70% almost everywhere in the global oceans, and the light-wind-speed regime occurs about 16 % of the time in the equatorial west Pacific Ocean (Grachev and Fairall, 2001). Despite numerous studies, our current understanding of the mechanisms governing the wind-wave interactions remains quite incomplete, and, under specific conditions, sparse field observations contradict the usual theoretical, empirical and stochastic models. The present PhD work is part of the overall framework of ocean-atmosphere interactions and is based on a multidisciplinary approach that includes hydrodynamics, atmospheric sciences and computing science.

In this PhD thesis, numerical tools have been developed in order to study the coupling between an atmospheric airflow and a sea state. The bibliographical study in Chapter 1 has shown that the aforementioned atmospheric stratification and waves have an impact on the marine atmospheric boundary layer. However, the work has focused on the wave effects: considering independently these effects constitutes a first step in the understanding of the ocean-atmosphere interactions. A preliminary study lies in the intention of developing an effective and evolving tool that would be able to address an increasing complexity of the representation of a part of the ocean-atmosphere physics. A RANS computational model developed in the LHEEA laboratory, ICARE, has been modified to investigate the swell dissipation by induced atmospheric shear stress in the case of no mean wind. The properties of the flow under stationary conditions have been studied within a periodic domain along the wave direction. The study has shown a dependence on the Reynolds number of this wave-induced airflow. The computed shear work has revealed a small deviation compared to the Dore analytical expression under laminar conditions, but a transitional state appears, leading to a fully turbulent boundary layer where the shear work increases. A parametrisation of this increase has been expressed through the viscous dissipation coefficient calculated from the mean work of the shear stress over a wavelength. For the most turbulent case, the increase reaches less than $3.5\mu_{\mathrm{Dore}}$ which corresponds to a e-folding decay $(1/\mu)$ of the order of 20 000 km for an oceanic swell. This is way smaller than the observed dissipation of about $56\mu_{\mathrm{Dore}}$ from Ardhuin et al. (2009). Both the effect of the mean wind or thermal and roughness effects have been neglected in the model. Therefore, to date, other mechanisms involved in the swell dissipation still remain to be investigated.

Considering a proper atmospheric circulation and its actual interaction with the swell remains a challenge within the current computational tools. A focus on wind-wave interactions was proposed with the development of a deterministic numerical model for the study of the coupling between an airflow and the underlying sea state. To this end, a collaboration has been initiated with Peter Sullivan from the National Center for Atmospheric Research in order to couple his atmospheric LES code with a spectral code (i.e. HOS model) that solves the non-linear evolution of a sea states developed in the LHEEA laboratory. The numerical coupling is based on an exchange of information between the two codes: the HOS code forces the lower boundary of the air domain in the LES code with the wave information (i.e. wave elevation, its derivatives and the orbital velocities). In return, the atmospheric pressure at the free surface can be sent to the HOS code leading to a two-way coupling between the two codes. The major assumption of this work concerns the atmospheric stratification: the air domain has been modelled as a wind tunnel with no atmospheric stratification (i.e. neutral air). Moreover, the SGS momentum fluxes accounting for the unresolved wavelengths at the first cell above the water surface are parametrised using a logarithmic law based on a fixed roughness length.

The influence of the sea states on the overlying airflow has been numerically investigated through three one-way coupled cases (i.e. the sea state does not evolve under wind pressure forcing as the atmospheric pressure is not exchanged): wind forcing over young waves, a swell underlying a light wind and a case of generation of a wave-induced wind jet. Different numerical features have been examined, such as the influence of the mesh discretisation, the height of the air domain and the initialisation of the LES simulation. The notion of forcing is characterised by the wave growth rate parameter,β, which is related to the dimensionless form drag per unit area due to the pressure at the water surface and the wave steepness. For the case of young waves underlying a strong wind, the waves acts as a drag on the wind and $\beta > 0$. For the case of a fast swell underlying a light wind, the waves act as a thrust on the wind and $\beta < 0$. However, a negative growth rate parameter does not imply the generation of a wave-induced wind. The presence of a wave-induced wind is correlated to a positive momentum flux: an upward transport of momentum from water to air is observed for a case where the speed ratio C_p/u_* measuring the force balance between the waves and the wind is very high (here, a wave age $C_p/u_* = 120$ has been tested with a wave characterised by $\lambda = 400$ m and $a = 12.7$ or 6.4 m), whereas the wind-wave equilibrium is around 15-20). However, for more realistic sea states ($\lambda = 400$ m and $a = 2.8$ or 1.4 m), the slightly positive form drag was not strong enough to counteract the negative momentum flux: no wind jet has been observed. This behaviour supports the fact that it is not only the wave age that characterises the wind-wave interactions, but the wave steepness and the energy content of the wave spectrum have also an influence on the overlying airflow.

This work aimed at placing into perspective the logarithmic wind profile commonly used to predict the vertical wind profile in the governing standards. One should recall that this log profile is only valid in the surface layer under neutral stratification. Here, the air has been considered as neutral, but the numerical simulations have shown that the common reference height (i.e. 10 m) often lies within the disturbed MABL. A set of numerical wind-wave configurations have illustrated that the log law profile is in accordance with the CFD profile for small wave age, but for larger wave ages, the log law profile tends to overestimate the wind speed in the first 10 m above the water surface. But the most striking effect occurring during a light-wind regime correlated to a fast-swell regime, the wave-driven wind jet, invalidates the use of such a law for up to $300 - 500$ m above the water surface. It has also been demonstrated that the influence of the parametrisation of the drag coefficient C_D is non negligible on the wind profile, supporting the evidence that a consistent parametrisation for $C_{D_{10}}$ has not been established yet despite enormous efforts.

We emphasise that the natural evolution of the wind-wave system has been distorted in the aforementioned simulations since the sea state has not evolved under the wind pressure forcing, hence it brought an infinite amount of energy into the air domain. Two additional cases have been implemented in order to investigate the wind-wave coupling. Along with the surface pressure, the tangential stress is responsible for the formation of a stress layer in the MABL, however this stress can not be assimilated in the wave model due to the hypothesis of potential flow for the water. Nevertheless, the HOS calculation crashed instantly when the pressure forcing brought energy into the wave energy balance at high frequencies, since this energy input was not counterbalanced in the HOS model due to the lack of dissipation such as wave breaking, viscosity... This question goes well beyond the content of this thesis and there is still active research and discussions on this topic in the oceanographic and hydrodynamics communities. As a workaround, the atmospheric pressure signal has been filtered at high frequencies, preventing the steepest waves to grow: this filtering acts as a mitigation of the forcing, restricted to the main components. However, in-depth tests will need to be carried out on this filtering as the parametrisation of the energy dissipation constitutes the whole key of the understanding of the interactions in the coupled wind-wave system.

The outlook for this PhD thesis lies in the addition of an increasing complexity of the representation of a part of the ocean-atmosphere physics into the numerical coupled model. Indeed, the major assumption of neutral air does not stand under very-light wind regimes to which the unstable atmospheric stratification seems to be correlated. The wave-induced wind jet may disturb the wind measurements at a mast for example and may not represent the wind resource above. Moreover, the Coriolis forces appear to be important under stable conditions, affecting the wind direction with height. An other challenge lies in the boundary conditions that are needed at the surface: the wall function modelling can not be departed, but in this PhD work, the roughness length has been considered as constant in the calculation of the surface fluxes. This procedure does not take into account the dynamic presence of any wavelets. Yang et al. (2013) proposed a dynamic modelling of a sea-surface roughness. Finally, more wind-wave configurations should be tested as most of the aforementioned cases were characterised by winds following a non-linear monochromatic sea state, especially irregular sea states and wind-wave misalignment.

Appendix A

Airflow over various waves in various wind conditions

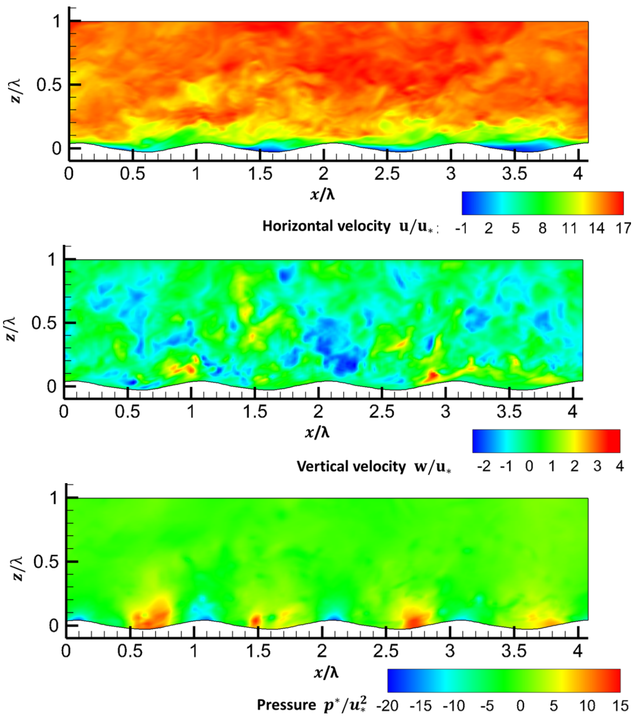

Figure A.1: Instantaneous contours in a $x-z$ plane of dimensionless horizontal velocity (*top*), vertical velocity (*middle*) and pressure (*bottom*) for a LES simulation of a strongly forced condition with wave tank data. The initial wave age is $C_p/u_* = 1.6$.

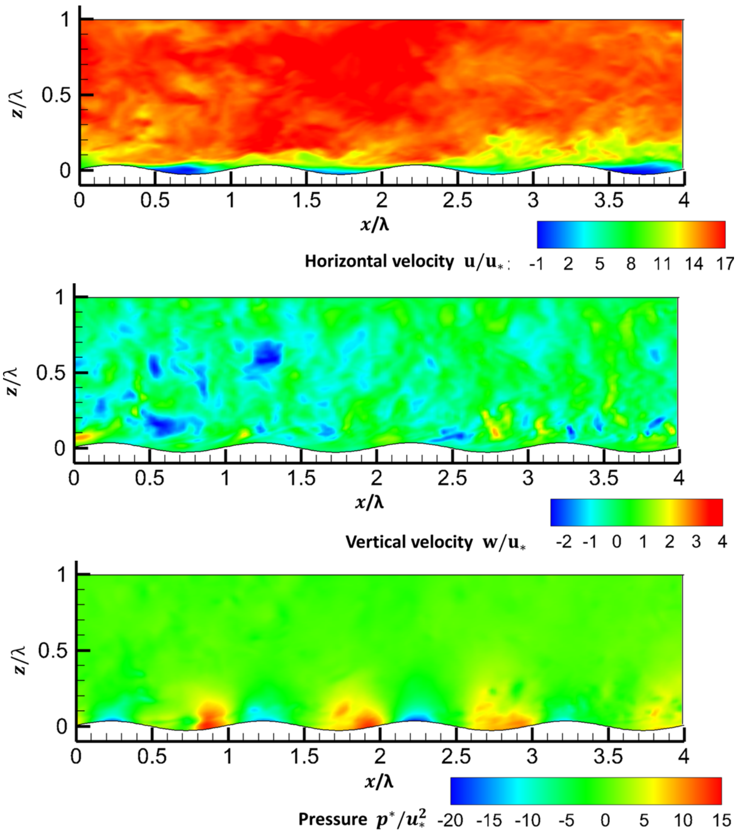

Figure A.2: Instantaneous contours in a $x - z$ plane of dimensionless horizontal velocity (*top*), vertical velocity (*middle*) and pressure (*bottom*) for a LES simulation of a strongly forced condition with an Airy wave. The initial wave age is $C_p/u_* = 1.6$.

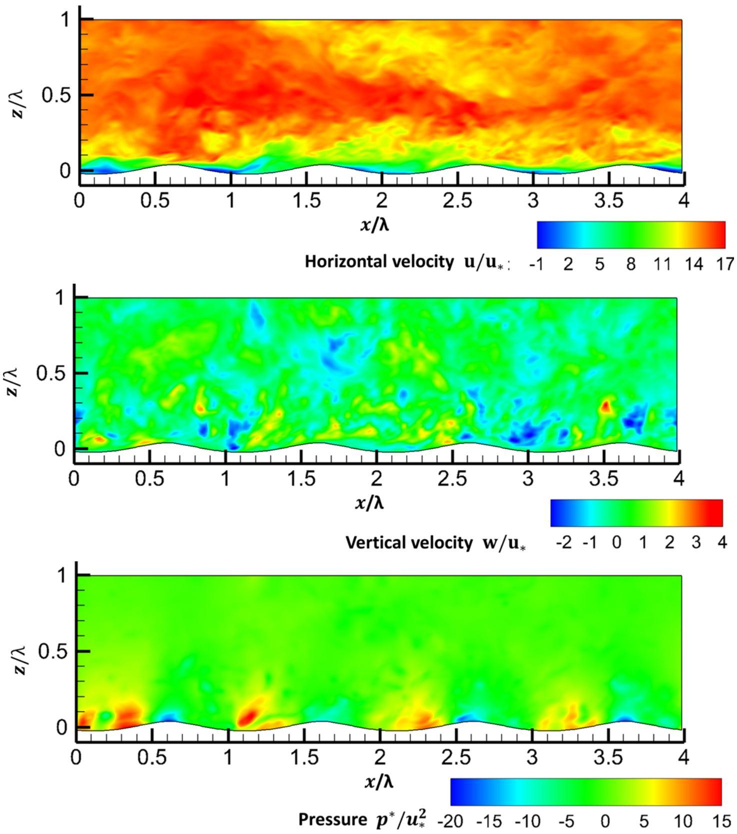

Figure A.3: Instantaneous contours in a $x - z$ plane of dimensionless horizontal velocity (*top*), vertical velocity (*middle*) and pressure (*bottom*) for a one-way coupled simulation of a non-linear monochromatic wave underlying a strong airflow. The initial wave age is $C_p/u_* = 1.6$.

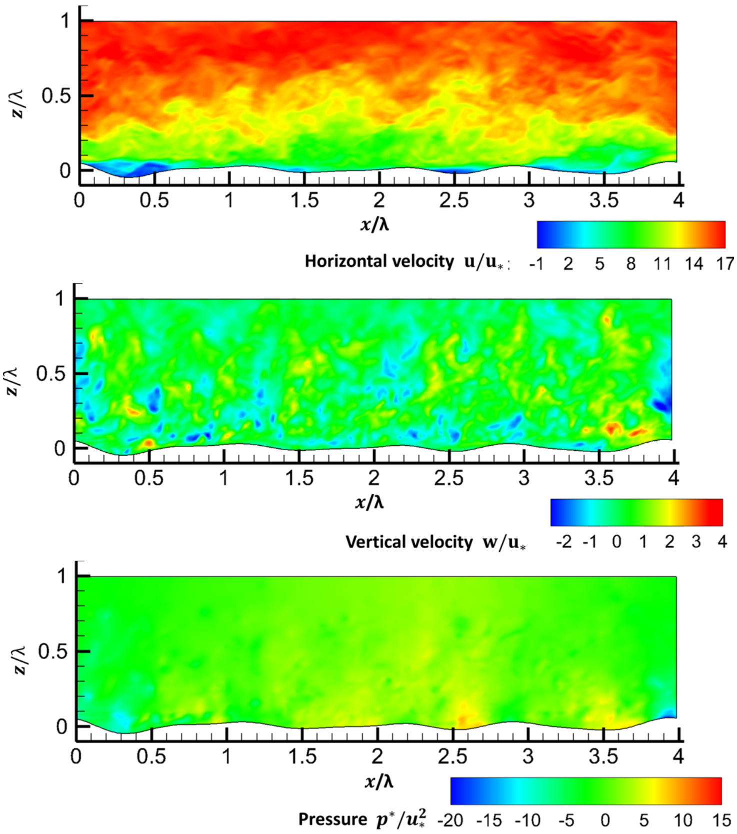

Figure A.4: Instantaneous contours in a $x - z$ plane of dimensionless horizontal velocity (*top*), vertical velocity (*middle*) and pressure (*bottom*) for a one-way coupled simulation of an irregular wave underlying a strong airflow. The initial wave age is $C_p/u_* = 1.6$.

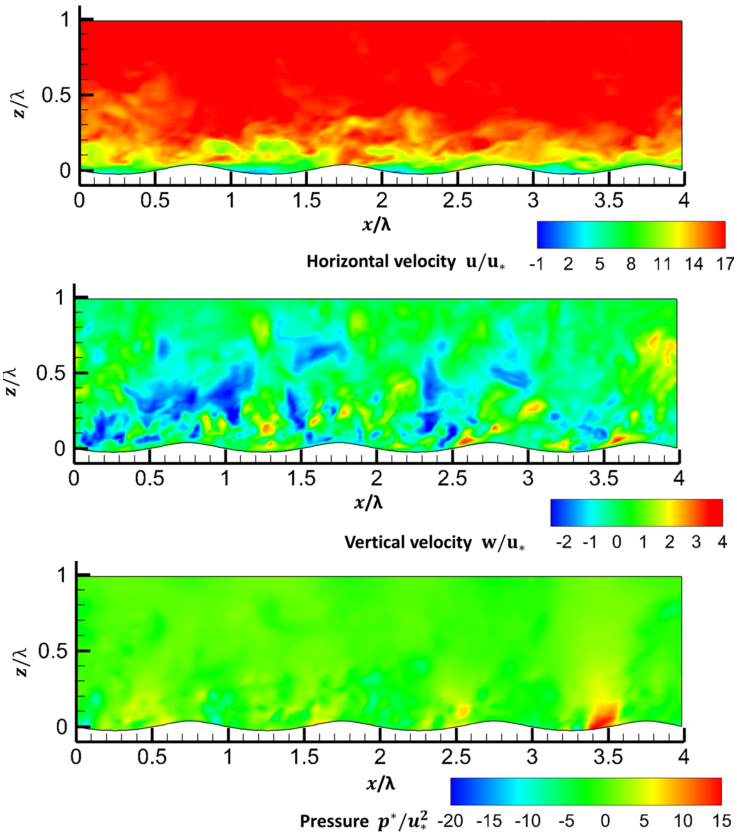

Figure A.5: Instantaneous contours in a $x - z$ plane of dimensionless horizontal velocity (*top*), vertical velocity (*middle*) and pressure (*bottom*) for a one-way coupled simulation of a non-linear monochromatic wave underlying an airflow. The initial wave age is $C_p/u_* = 5$.

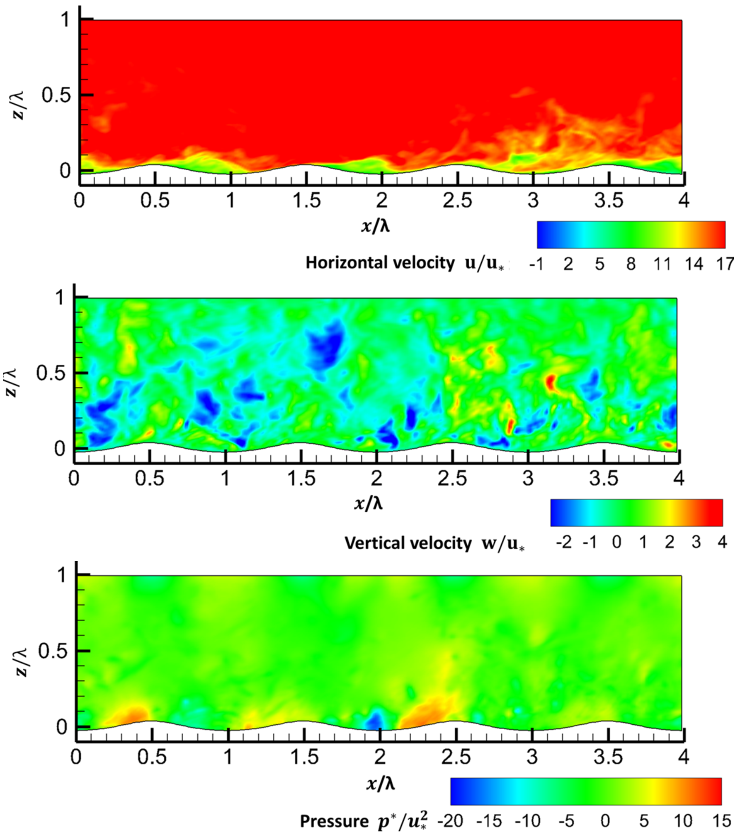

Figure A.6: Instantaneous contours in a $x - z$ plane of dimensionless horizontal velocity (*top*), vertical velocity (*middle*) and pressure (*bottom*) for a one-way coupled simulation of a non-linear monochromatic wave underlying an airflow. The initial wave age is $C_p/u_* = 10$.

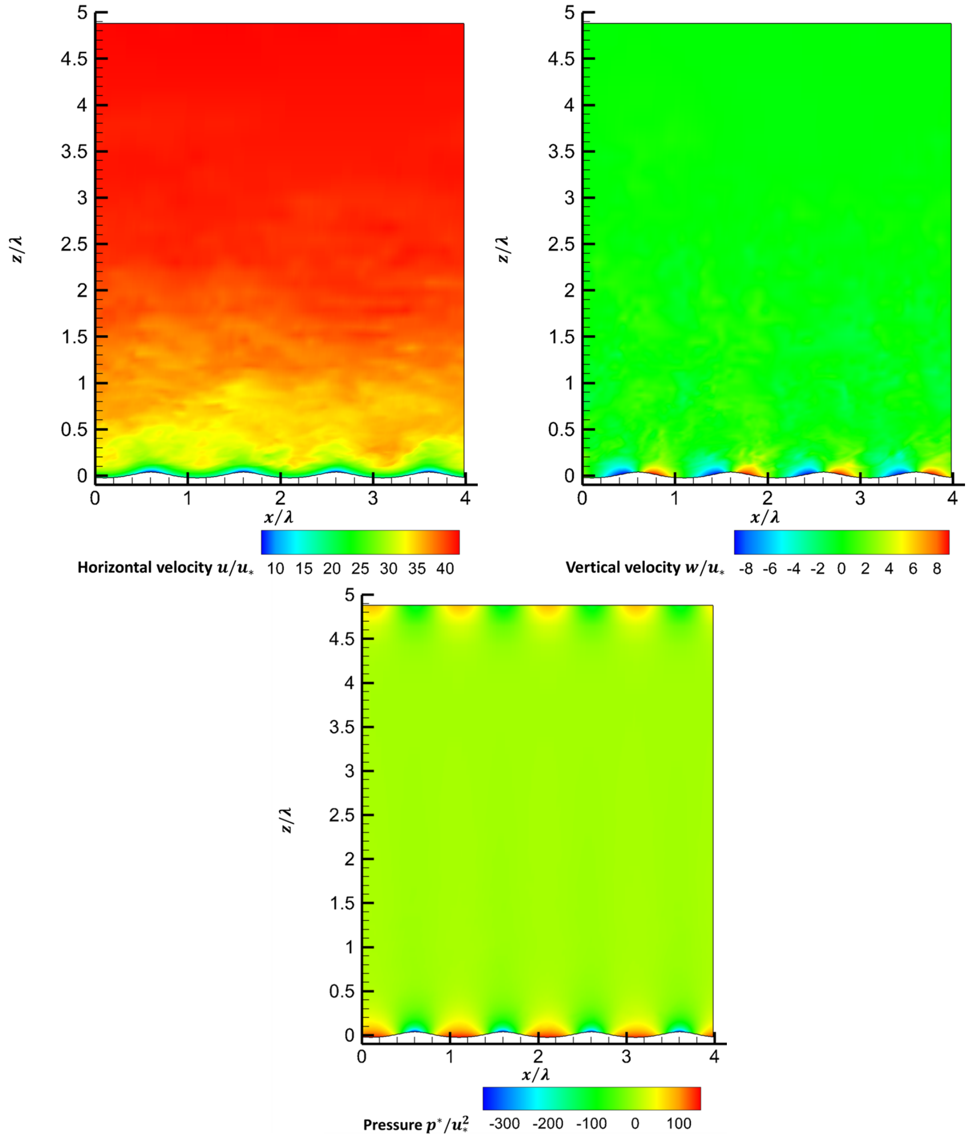

Figure A.7: Instantaneous contours in a $x - z$ plane of dimensionless horizontal velocity (*top*), vertical velocity (*middle*) and pressure (*bottom*) for a one-way coupled simulation of a non-linear monochromatic wave underlying a light airflow. The initial wave age is $C_p/u_* = 60$.

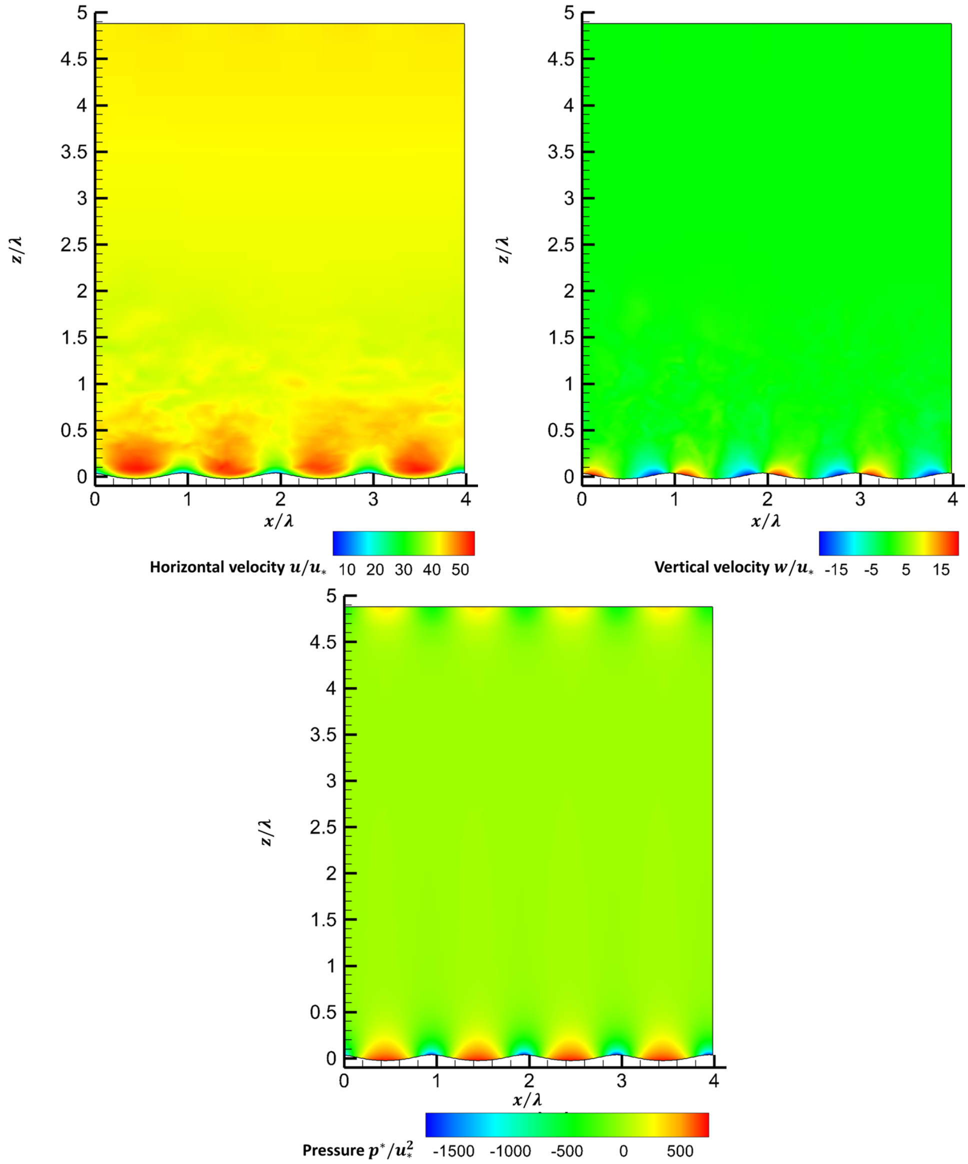

Figure A.8: Instantaneous contours in a $x - z$ plane of dimensionless horizontal velocity (*top*), vertical velocity (*middle*) and pressure (*bottom*) for a one-way coupled simulation of a non-linear monochromatic wave underlying a very light airflow. The initial wave age is $C_p/u_* = 120$.

Bibliography

B. Alessandrini and G. Delhommeau. A fully coupled Navier-Stokes solver for calculation of turbulent incompressible free surface flow past a ship hull. *International Journal for Numerical Methods in Fluids*, 29:125–142, 1999.

A. AlSam, R. Szasz, and J. Revstedt. The Influence of Sea Waves on Offshore Wind Turbine Aerodynamics. *Journal of Energy Resources Technology*, 137, 2015.

D. Anderson, J. Tannehill, and R. Pletcher. *Computational Fluid Mechanics and Heat Transfer*. McGraw-Hill, 1984.

F. Ardhuin. Cours - les vagues: un compartiment important du système terre. 2012.

F. Ardhuin, B. Chapron, and F. Collard. Observation of swell dissipation across oceans. *Geophysical Research Letters*, 36, 2009.

A. Babanin, M. Onorato, and F. Qiao. Surface waves and wave-coupled effects in lower atmosphere and upper ocean. *Journal of Geophysical Research*, 117, 2012.

G. Batchelor and I. Proudman. The effect of rapid distortion on a fluid in a turbulent motion. *The Quarterly Journal of Mechanics and Applied Mathematics*, 7:83–103, 1954.

S. Belcher and J. Hunt. Turbulent shear flow over slowly moving waves. *Journal of Fluid Mechanics*, 251:109–148, 1993.

S. Belcher and J. Hunt. Turbulent air flow over hills and waves. *Annual Review of Fluid Mechanics*, 30:507–538, 1998.

R. Benoit. On the integral of the surface layer profile-gradient functions. *Journal of Applied Meteorology*, 16:859–860, 1977.

F. Bonnefoy, G. Ducrozet, D. Le Touzé, and P. Ferrant. *Advances in numerical simulations of nonlinear water waves*, chapter Time-domain simulation of nonlinear water waves using spectral methods, pages 129–164. World Scientific, 2010.

J. Businger, J. Wyngaard, Y. Izumi, and E. Bradley. Flux Profile Relationships in the Atmospheric Surface Layer. *Journal of the Atmospheric Sciences*, 28:181–189, 1971.

I. Calmet. Cours - hydrologie et atmosphère urbaine. 2015.

B. Carlsson, A. Rutgersson, and A.-S. Smedman. Impact of swell on simulations using a regional atmospheric climate model. *Tellus Series A*, 61: 527–538, 2009.

D. Chalikov. The numerical simulation of wind-wave interaction. *Journal of Fluid Mechanics*, 87:561–582, 1978.

D. Chalikov and S. Rainchik. Coupled numerical modelling of wind and waves and the theory of the wave boundary layer. *Boundary-Layer Meteorology*, 138:1–41, 2011.

H. Charnock. Wind stress on a water surface. *Quarterly Journal of the Royal Meteorological Society*, 81:639–640, 1955.

S. Chen, M. Flatau, T. Jensen, T. Shinoda, J. Schmidt, P. May, J. Cummings, M. Liu, P. Ciesielski, C. Fairall, R. Lien, D. Baranowski, N. Chi, S. de Szoeke, and J. Edson. A study of CINDY/DYNAMO MJO suppressed phase. *Journal of Atmospheric Sciences*, 72(10):3755–3779, 2015.

J. Cohen and S. Belcher. Turbulent shear flow over fast moving waves. *Journal of Fluid Mechanics*, 386:345–371, 1999.

F. Collard, F. Ardhuin, and B. Chapron. Routine monitoring and analysis of ocean swell fields using a spaceborn SAR. *Journal of Geophysical Research*, 114 (C7), 2009.

J. Deardorff. The use of subgrid transport equations in a three-dimensional model of atmospheric turbulence. *Journal of Fluids Engineering*, 95:429–438, 1973.

D. Dommermuth. The initialization of nonlinear waves using an adjustement scheme. *Wave motion*, 32:301–317, 2000.

D. Dommermuth and D. Yue. A high-order spectral method for the study of nonlinear gravity waves. *Journal of Fluid Mechanics*, 184:267–288, 1987.

M. Donelan. The dependence of the aerodynamic drag coefficient on wave parameters. In *Proceedings of the First International Conference on Meteorological and Air/Sea Interaction of the Coastal Zone, 10-14 May 1982, the Hague, the Netherlands*, pages 381–387, Boston, Massachusetts, 1982. American Meteorological Society.

M. Donelan. *The Sea: Ocean Engineering Science*, volume 9, chapter Air-Sea Interaction. John Wiley, 1990.

M. Donelan. *Physical Processes in Lake and Oceans*, volume 54, chapter Air-water exchange processes, pages 19–36. J. Imberger, 1998.

M. Donelan, M. Skafel, H. Graber, P. Liu, D. Schwab, and S. Venkatesh. On the growth rate of wind-generated waves. *Atmosphere Ocean*, 30:457–478, 1992.

M. Donelan, W. Drennan, and K. Katsaros. The air-sea momentum flux in conditions of wind sea and swell. *Journal of Physical Oceanography*, 27: 2087–2099, 1997.

B. Dore. Some effects of the air-water interface on gravity waves. *Geophysical and Astrophysical Fluid Dynamics*, 10:215–230, 1978.

W. Drennan, H. Graber, and M. Donelan. Evidence for the effects of swell and unsteady winds on marine wind stress. *Journal of Physical Oceanography*, 29:1853–1864, 1999.

W. Drennan, P. Taylor, and M. Yelland. Parameterizing the sea surface roughness. *Journal of Physical Oceanography*, 35:835–848, 2005.

G. Ducrozet. *Modélisation des processus non-linéaires de génération et de propagation d'états de mer par une approche spectrale*. PhD thesis, Ecole Centrale de Nantes, 2007.

A. Dyer. A review of flux-profile relations. *Boundary Layer Meteorology*, 1: 363–372, 1974.

J. Edson. Review of air-sea transfer processes. In *ECMWF workshop on ocean-atmosphere interactions*, pages 7–24, 2008.

L. Eliassen, J. Jakobsen, and C. Obhrai. The effect of atmospheric stability on fatigue life of offshore wind turbines. *The 22nd International Ocean and Polar Engineering Conference*, 2012.

S. Emeis. *Atmospheric Physics for Wind Power Generation*, chapter 5. Springer, 2013.

C. Fairall, E. Bradley, D. Rogers, J. Edson, and G. Young. Bulk parameterization of air-sea fluxes for tropical ocean-global atmospher coupled-ocean atmosphere response experiment. *Journal of Geophysical Research*, 101: 3747–3764, 1996.

C. Fairall, E. Bradley, J. Hare, A. Grachev, and J. Edson. Bulk parameterization of air-sea fluxes: updates and verifications of the COARE algorithm. *Journal of Climate*, 16:571–591, 2003.

Y. Fan, S. Lin, I. Held, Z. Yu, and H. Tolman. Global ocean surface wave simulation using a coupled atmosphere-wave model. *Journal of Climate*, 25(18), 2012.

P. Ferrant. Simulation of strongly-nonlinear wave generation and wave-body interaction using a 3D MEL model. In *Proc. 21st ONR Symp on Naval Hydrodynamics*, pages 93–109, Trondheim, Norway, 1996.

P. Ferrant. Cours - méthodes spécifiques aux problèmes à surface libre. 2013.

J. Garratt. *The atmospheric boundary layer*. Cambridge University Press, 1994.

P. Gent and P. Taylor. A numerical model of the airflow above water waves. *Journal of Fluid Mechanics*, 77:105–128, 1976.

M. Gouin, G. Ducrozet, and P. Ferrant. Development and validation of a non-linear spectral model for water waves over variable depth. . *European Journal of Mechanics - B/Fluids, Elsevier*, 57:115–128, 2016.

A. Grachev and C. Fairall. Upward momentum transfer in the marine boundary layer. *Journal of Physical Oceanography*, 31:1698–1710, 2001.

M. Gundogdu and M. Carpinlioglu. Present state of art on pulsatile flow theory. *JSME Int.*, 42:398–410, 1999.

K. Hanley and S. Belcher. Wave-driven wind jets in the marine atmospheric boundary layer. *Journal of the Atmospheric Sciences*, 65:2646–2660, 2008.

T. Hara and P. Sullivan. Wave boundary layer turbulence over surface waves in a strongly forced condition. *Journal of Physical Oceanography*, 45:868–883, 2015.

J. Hare, T. Hara, J. Edson, and J. Wilczak. A similarity analysis of the structure of airflow over surface waves. *Journal of Physical Oceanography*, 27:1018–1037, 1997.

D. Harris. The wave-driven wind. *Journal of the Atmospheric Sciences*, 23:688–693, 1966.

K. Hasselmann, T. Barnett, E. Bouws, H. Carlson, D. Cartwright, K. Enke, J. Ewing, H. Gienapp, D. Hasselmann, P. Kruseman, A. Meerburg, P. Mller, D. Olbers, K. Richter, W. Sell, and H. Walden. Measurements of wind-wave growth and swell decay during the Joint North Sea Wave Project (JONSWAP). *Ergnzungsheft zur Deutschen Hydrographischen Zeitschrift Reihe*, 8:95, 1973.

U. Högström, A.-S. Smedman, and H. Bergström. A case study of two-dimensional stratified turbulence. *Journal of the Atmospheric Sciences*, 56:959–976, 1999.

U. Högström, A.-S. Smedman, E. Sahleé, W. Drennan, K. Kahma, H. Pettersson, and F. Zhang. The atmospheric boundary layer during swell: A field study and interpretation of the turbulent kinetic energy budget for high wave ages. *Journal of the Atmospheric Sciences*, 66:2764–2779, 2009.

U. Högström, A. Rutgersson, E. Sahlée, A.-S. Smedman, T. Hristov, W. Drennan, and K. Kahma. Air–Sea Interaction Features in the Baltic Sea and at a Pacific Trade-Wind Site: An Inter-comparison Study. *Boundary-Layer Meteorology*, 147:139–163, 2013.

P. Hwang. Influence of the wavelength on the parameterization of drag coefficient and surface roughness. *Journal of Oceanography*, 60:835–841, 2004.

IEC 61400-1. Wind turbines - Part 1: Design Requirements. Standard, International Electrotechnical Commission, 2005.

IEC 61400-3. Wind turbines - Part 3: Design Requirements for Offshore Wind Turbines. Standard, International Electrotechnical Commission, 2009.

S. Jacobs. An asymptotic theory for the turbulent flow over a progressive water wave. *Journal of Fluid Mechanics*, 174:69–80, 1987.

P. Janssen. Wave-induced stress and the drag of air flow over sea waves. *Journal of Physical Oceanography*, 19:745–754, 1989.

P. Janssen. *The Interaction of Ocean Waves and Wind*. Cambridge University Press, 2004.

H. Jeffreys. On the formation of water waves by wind. *Proc. Roy. Soc. London*, 107:189–206, 1925.

A. Jenkins, M. Paskyabi, I. Fer, A. Gupta, and M. Adakudlu. Modelling the Effect of Ocean Waves on the Atmospheric and Ocean Boundary Layers. *Energy Procedia*, 24:166–175, 2012.

B. Jensen, B. Sumer, and J. Fredsoe. Turbulent oscillatory boundary layer at high reynolds numbers. *Journal of Fluid Mechanics*, 206:265–297, 1989.

S. Kalvig, O. Gudmestad, and N. Winther. Exploring the gap between 'best knowledge' and 'best practice' in boundary layer meteorology for offshore wind energy. *Wind Energy*, 17:161–171, 2014.

A. Kara, A. Wallcraft, E. Metzger, H. Hurlburt, and C. Fairall. Wind Stress Drag Coefficient over the Global Ocean. *Journal of Climate*, 20:5856–5864, 2007.

G. Katul, A. Konings, and A. Porporato. Mean velocity profile in a sheared and thermally stratified atmospheric boundary layer. *Physical Review Letters*, 2011.

G. Komen, P. Janssen, V. Makin, and W. Oost. On the sea state dependence of the charnock parameter. *Global Atmosphere-Ocean System*, 5:367–388, 1998.

J. Kristjansson, I. Barstad, T. Aspelien, I. Fore, O. Godoy, O. Hov, E. Irvine, T. Iversen, E. Kolstad, T. Nordeng, H. McInnes, R. Randriamampianina, J. Reuder, O. Saetra, M. Shapiro, T. Spengler, and H. Olafsson. The Norwegian IPY-THORPEX: polar lows and Arctic fronts during the 2008 Andoya campaign. *Bulletin of the American Meteorological Society*, 92 (11):1443–1466, 2011.

V. Kudryavtsev and V. Makin. Impact of Swell on the Marine Atmospheric Boundary Layer. *Journal of Physical Oceanography*, 34:934–949, 2004.

B. Lange, S. Larsen, J. Hojstrup, and R. Barthelmie. Importance of thermal effects and sea surface roughness for offshore wind resource assessment. *Journal of Wind Engineering and Industrial Aerodynamics*, 92:959–988, 2004.

D. Le Touzé. *Méthodes spectrales pour la modélisation non-linéaires d'écoulements à surface libre instationnaires.* PhD thesis, Ecole Centrale de Nantes, 2003.

M. Lighthill. Physical interpretation of the mathematical theory of wave generation by wind. *Journal of Fluid Mechanics*, 14:385–398, 1962.

S. Liu, K. Hendrickson, X. Dong, L. Shen, and D. Yue. Numerical investigation of coupled boundary layers air-sea transfer (CBLAST) at small scales. In *16th Symposium on Boundary Layers and Turbulence*, 2003.

Y. Liu, D. Yang, X. Guo, and L. Shen. Numerical study of pressure forcing of wind on dynamically evolving water waves. *Physics of fluids*, 2010.

V. Makin and V. Kudryavtsev. Coupled sea surface-atmosphere model. 1. wind over waves coupling. *Journal of Geophysical Research*, 104:7613–7623, 1999.

V. Makin, V. Kudryavtsev, and C. Mastenbroek. Drag of the sea surface. *Boundary Layer Meteorology*, 73:159–182, 1995.

C. Mastenbroek, V. Makin, M. Garat, and J. Giovanangeli. Experimental evidence of the rapid distortion of turbulence in the air flow over water waves. *Journal of Fluid Mechanics*, 318:273–302, 1996.

J. Miles. On the generation of surface waves by shear flows. *Journal of Fluid Mechanics*, 3:185–204, 1957.

H. Moeng. A large-eddy simulation for the study of planetary boundary layer turbulence. *Journal of the Atmospheric Sciences*, 41:2052–2062, 1984.

M. Moeng, A. Le Mone, M. Khairoutdinov, S. Krueger, P. Bogenschutz, and D. Randall. The tropical marine boundary layer under a deep convection system: A large-eddy simulation study. *Journal of Advances in Modeling Earth Systems*, 1(16), 2009.

L. Moskowitz. Estimates of the power spectrums for fully developed seas for wind speeds of 20 to 40 knots. *Journal of Geophysical Research*, 69: 5161–5179, 1964.

M. Motta, R. Barthelmie, and P. Volund. The influence of non-logarithmic wind speed profiles on potential power output at danish offshore sites. *Wind Energy*, 8:219–236, 2005.

W. Musial and B. Ram. Large scale offshore wind power in the united states: assessment of opportunities and barriers. Technical report, National Renewable Energy Laboratory, 2010.

E. Nickerson and V. Smiley. Surface layer and energy budget parameterizations for mesoscale models. *Journal of Applied Meteorology*, 14:297–300, 1975.

E. Nilsson, A. Rutgersson, A.-S. Smedman, and P. Sullivan. Convective boundary-layer structure in the presence of wind-following swell. *Quarterly Journal of the Royal Meteorological Society*, 138:1476–1489, 2012.

C. Obhrai, S. Kalvig, and O. Gudmestad. A review of current guidelines and research on win modeling for the design of offshore wind turbines. *The 22nd International Ocean and Polar Engineering Conference*, June 17-22 2012.

A. Obukhov. Turbulence in an atmosphere with a non-uniform temperature. *Boundary-Layer Meteorology*, 2:7–29, 1971.

W. Oost, G. Komen, C. Jacobs, and C. van Oort. New evidence for a relation between wind stress and wave age from measurements during ASGAMAGE. *Boundary-Layer Meteorology*, 103:409–438, 2002.

E. Patton, P. Sullivan, and C. Moeng. The influence of idealized heterogeneity on wet and dry planetary boundary layers coupled to the land surface. *Journal of Atmospheric Sciences*, 62:2078–2097, 2005.

C. Paulson. The mathematical representation of wind speed and temperature in the unstable atmospheric surface layer. *Journal of Applied Meteorology*, 9:857–861, 1970.

Y. Perignon, F. Bonnefoy, G. Ducrozet, and P. Ferrant. Wind forcing and dissipation in a High Order Spectral deterministic wave model. In *21st International Offshore and Polar Engineering Conference*, Maui, Hawaii, USA, 19-24 June 2011.

Y. Perignon, F. Ardhuin, M. Cathelain, and M. Robert. Swell dissipation by induced atmospheric shear stress. *Journal of Geophysical Research*, 119 (10):6622–6630, 2014.

O. Phillips. On the generation of waves by turbulent wind. *Journal of Fluid Mechanics*, 2:417–445, 1957.

O. Phillips. A note on the tubulence generated by gravity waves. *Journal of Geophysical Research*, 66(9):2889–2893, 1961.

O. Phillips. *The Dynamics of the upper ocean.* Cambridge University Press, 1966.

W. Pierson and L. Moskowitz. A proposed spectral form for fully developed wind seas based on the similarity theory of s. a. kitaigorodskii. *Journal of Geophysical Research*, 69:181–190, 1964.

H. Potter. Swell and the drag coefficient. *Ocean Dynamics*, 65:375–384, 2015.

L. Prandtl. Zur Turbulenten Strömung in Rohren und längs Platten. *Ergeb. Aerod. Versuch Göttingen*, IV(4), 1932.

L. Prandtl. Bericht über Untersuchungen zur ausgebildeten Turbulenz. *Zeitschrift für angewandte Mathematik und Mechanik*, 5(2):136–139, 1961.

C. Rhie and W. Chow. Numerical study of the turbulent flow past an airfoil with trailing edge separation. *AIAA Journal*, 21:1525–1532, 1983.

M. Rienecker and J. Fenton. A fourier approximation for steady water waves. *Journal of Fluid Mechanics*, 104:119–137, 1981.

A. Rutgersson and P. Sullivan. The effect of idealized water waves on the turbulence structure and kinetic energy budgets in the overlying airflow. *Dynamics of Atmospheres and Oceans*, 2005.

B. Seiffert and G. Ducrozet. Deep water wave-breaking in a High-Order Spectral model. In *International Workshop on Water Waves and Floating Bodies IWWWFB2016*, 2016.

M. Sekioka. Application of kelvin-helmholtz instability to clear air turbulence. *Journal of Applied Meteorology*, 1970.

A. Semedo, K. Suselj, A. Rutgersson, and A. Sterl. A global view on the wind sea and swell climate and variability from ERA-40. *Journal of Climate*, 24:1461–1479, 2011.

S. Sirnivas, W. Musial, B. Bailey, and M. Filippelli. Assessment of Offshore Wind System Design, Safety, and Operation Standards. Technical report, National Renewable Energy Laboratory, 2014.

A.-S. Smedman, M. Tjernström, and U. Högström. The Near-Neutral Marine Atmospheric Boundary Layer with No Surface Shearing Stress : A Case Study. *Journal of the Atmospheric Sciences*, 51:3399–3411, 1994.

A.-S. Smedman, U. Högström, H. Bergström, A. Rutgersson, K. Kahma, and H. Pettersson. A case study of air-sea interaction during swell conditions. *Journal of Geophysical Research*, 104:25833–25851, 1999.

A.-S. Smedman, X. Guo Larsén, U. Högström, K. Kahma, and H. Pettersson. Effect of sea state on the momentum exchange over the sea during neutral conditions. *Journal of Geophysical Research*, 108, 2003.

S. Smith. Coefficients for sea surface wind stress, heat flux and wind profiles as a function of wind speed and temperature. *Journal of Geophysical Research*, 93:15467–15472, 1988.

S. Smith, R. Anderson, W. Oost, C. Kraan, N. Maat, J. DeCosmo, K. Katsaros, K. Davidson, K. Bumke, L. Hasse, and H. Chadwick. Sea surface stress and drag coefficients: the HEXOS results. *Boundary Layer Meteorology*, 60:109–142, 1992.

C. Solliec. Mécanique des fluides générale. ecole des mines de nantes. •, 2013.

P. Spalart and B. Baldwin. Direct simulation of a turbulent oscillating boundary layer. *Turbulent shear flows*, 6:417–440, 1989.

R. Stull. *An Introduction to Boundary Layer Meteorology*, volume 13. Springer Netherlands, 1988.

P. Sullivan and J. McWilliams. Dynamics of winds and currents coupled to surface waves. *Annual Review of Fluid Mechanics*, 42:19–42, 2010.

P. Sullivan, J. McWilliams, and C. Moeng. Simulation of turbulent flow over idealized water waves. *Journal of Fluid Mechanics*, 80:535–559, 2000.

P. Sullivan, J. Edson, T. Hristov, and J. McWilliams. Large-eddy simulations and observations of atmospheric marine boundary layers above non-equilibrium surface waves. *Journal of the Atmospheric Sciences*, 65: 1225–1245, 2008.

P. Sullivan, J. McWilliams, and E. Patton. Large-Eddy Simulation of Marine Atmospheric Boundary Layers above a Spectrum of Moving Waves. *Journal of the Atmospheric Sciences*, 71:4001–4027, 2014.

P. Taylor and M. Yelland. The dependence of sea surface roughness on the height and steepness of the waves. *Journal of Physical Oceanography*, 31: 572–590, 2001.

P. Thomas and C. Lombard. Geometric conservation law and its application to flow computations on moving grids. *American Institute of Aeronautics and Astronautics Journal*, 17:1030–1037, 1979.

A. Townsend. Flow in a deep turbulent boundary layer over a surface distorted by water waves. *Journal of Fluid Mechanics*, 55:719–735, 1972.

C. van Duin and P. Janssen. An analytic model of the generation of surface gravity waves by turbulent air flow. *Journal of Fluid Mechanics*, 236: 197–215, 1992.

Y. Volkov. Turbulent flux of momentum and heat in the atmospheric surface layer over a disturbed sea-surface. *Izv. Acad. Sci. USSR, Atmos. Oceanic Phys. (Engl. Transl.)*, 6:770–774, 1970.

B. West, K. Brueckner, R. Janda, M. Milder, and R. Milton. A new numerical method for surface hydrodynamics. *Journal of Geophysical Research*, 92: 11803–11824, 1987.

J. Wyngaard. *Turbulence in the Atmosphere*. Cambridge University Press, 2010.

D. Yang and L. Shen. Direct-simulation-based study of turbulent flow over waving boundaries. *Journal of Fluid Mechanics*, 650:131–180, 2010.

D. Yang and L. Shen. Simulation of viscous flows with undulatory boundaries. Part II: coupling with other solvers for two-fluid computations. *Journal of Computational Physics*, 230:5510–5531, 2011.

D. Yang, C. Meneveau, and L. Shen. Dynamic modelling of sea-surface roughness for large-eddy simulation of wind over ocean wavefield. *Journal of Fluid Mechanics*, 726:62–99, 2013.

D. Yang, C. Meneveau, and L. Shen. Large-eddy simulation of offshore wind farm. *Physics of Fluids*, 26, 2014.

V. Zakharov. Stability of periodic waves of finite amplitude on the surface of a deep fluid. *Journal of Applied Mechanics and Technical Physics*, pages 190–194, 1968.

l'université nantes angers le mans

PÔLE DE RECHERCHE ET D'ENSEIGNEMENT SUPÉRIEUR

Centrale Nantes

Thèse de Doctorat

Marie CATHELAIN

Développement d'un modèle de simulation déterministe pour l'étude du couplage entre un écoulement atmosphérique et un état de mer.

Development of a deterministic numerical model for the study of the coupling between an atmospheric flow and a sea state.

Résumé

La physique de la couche limite atmosphérique en domaine océanique est principalement régie par les processus couplés liés au vent, à l'état de mer local, et à des effets de flottabilité. Leur compréhension reste néanmoins parcellaire et leurs descriptions théoriques et stochastiques sont pour le moins lacunaires, lorsqu'elles ne sont tout simplement pas mises à mal par les rares observations.

Dans un contexte d'exploitation croissante de la ressource éolienne offshore, la mise en place de méthodes numériques visant à une description plus fine des propriétés turbulentes de cette couche limite sera une étape déterminante dans la réduction des coûts et l'optimisation des structures pour des rendements de récupération d'énergie améliorés. Ainsi, un outil numérique a été mis en place afin d'étudier le couplage entre un écoulement atmosphérique et l'état de mer. Un code Large-Eddy Simulation massivement parallèle pour la simulation des écoulements atmosphériques incompressibles développé par P. Sullivan au *National Center for Atmospheric Research* est couplé à un code spectral d'états de mer non-linéaires développé au *Laboratoire de recherche en Hydrodynamique, Energétique et Environnement Atmosphérique*.

De nombreuses configurations de vents et d'états de mer sont modélisées. On montre que les lois semi-empiriques souvent utilisées pour représenter la distribution verticale de la vitesse moyenne du vent sont une bonne approximation dans les situations où un petit état de mer est soumis à un fort vent. Néanmoins, dans le cas de houles très rapides se propageant dans des zones de faible vent, la création d'un jet de vent par la houle invalide ces lois semi-empiriques.

Mots clés
Mécanique des fluides, Hydrodynamique, Couche limite atmosphérique marine, Interactions vent-vague, Jet de vent induit par la vague, Large-eddy simulation, Méthode High-order spectral, Couplage.

Abstract

Modelling the dynamic coupling of ocean-atmosphere systems requires a fundamental and quantitative understanding of the mechanisms governing the wind-wave interactions: despite numerous studies, our current understanding remains quite incomplete and, in certain conditions, sparse field observations contradict the usual theoretical and stochastic models.

Within the context of a growing exploitation of the offshore wind energy and the development of metocean models, a fine description of this resource is a key issue. Field experiments and numerical modelling have revealed that atmospheric stability and wave effects, including the dynamic sea surface roughness, are two major factors affecting the windfield over oceans. A numerical tool has been implemented in order to study the coupling between an atmospheric flow and the sea state. A massively parallel large-eddy simulation developed by P. Sullivan at the *National Center for Atmospheric Research* is then coupled to a High-Order Spectral wave model developed at the *Hydrodynamics, Energetics & Atmospheric Environment Laboratory* in Ecole Centrale de Nantes.

Numerous configurations of wind and sea states are investigated. It appears that, under strongly forced wind conditions above a small sea state, the semi-empirical laws referred to as standards in the international guidelines are a good approximation for the vertical profile of the mean wind speed. However, for light winds overlying fast-moving swell, the presence of a wave-induced wind jet is observed, invalidating the use of such logarithmic laws.

Key Words
Fluid mechanics, Hydrodynamics, Marine atmospheric boundary layer, Wind-wave interactions, Wave-induced wind jet, Large-eddy simulation, High-order spectral wave model, Coupling.

L'Université Nantes Angers Le Mans